Dynamic Measures of Human Protein Metabolism with Stable Isotopes and Mass Spectrometry

By

Matthew Jaconelli

BSc (Honours)

Submitted to the University of Nottingham for the degree, Doctor of Philosophy, September 2023.

Table of Contents

COVID-19 IMPACT STATEMENT

PRESENTATIONS ARISING FROM THIS THESIS

POSTER PRESENTATIONS
ORAL PRESENTATIONS

PUBLICATIONS ARISING FROM THIS THESIS

ABSTRACTS
PAPERS

TRAINING COURSE ATTENDANCE

DECLARATION

ACKNOWLEDGEMENTS

CHAPTER I:

THE SYSTEMIC EFFECTS OF SURGICAL TRAUMA ON PROTEIN METABOLISM

1. INTRODUCTION

1.1 THE METABOLIC RESPONSE TO SURGICAL TRAUMA
1.2 THE PERIOPERATIVE STRESS RESPONSE
1.3 THE EFFECTS OF GLUCOCORTICOIDS ON METABOLISM: IMPACTS FOR SKELETAL MUSCLE AND THE PATHOGENESIS OF INSULIN-RESISTANCE
1.4 NUTRIENT-SENSING AND ENERGY STATUS: REGULATION OF MUSCLE PROTEIN TURNOVER
1.5 THE EFFECTS OF IMMOBILISATION ON SKELETAL MUSCLE
1.6 THE INFLAMMATORY RESPONSE TO SURGICAL TRAUMA
1.7 THE IMPACTS OF SURGERY ON SKELETAL MUSCLE CATABOLISM
1.8 REFERENCES

2. THE EFFECTS OF ELECTIVE ABDOMINAL SURGERY ON PROTEIN TURNOVER: A META-ANALYSIS OF STABLE ISOTOPE TECHNIQUES TO INVESTIGATE POSTOPERATIVE CATABOLISM

2.1 INTRODUCTION
2.2 METHODS
2.3 RESULTS
2.4 DISCUSSION
2.5 CONCLUSION
2.6 SUPPLEMENTARY MATERIALS
2.7 REFERENCES

CHAPTER II:

USE OF DEUTERIUM-OXIDE STABLE ISOTOPE TRACER TO STUDY HUMAN METABOLISM

1. INTRODUCTION

1.1 DEUTERIUM-OXIDE STABLE ISOTOPE TRACER
1.2 ASSESSING CELL PROLIFERATION THROUGH ^{2}H-LABELLING OF DNA

1.3 KINETIC MEASUREMENTS OF THE CELLULAR PROTEOME WITH DEUTERIUM-OXIDE
1.4 REFERENCES

2. PROTEOME-WIDE TURNOVER MEASUREMENTS IN DIFFERENTIATING M1- AND M2-LIKE MACROPHAGES *EX VIVO*

2.1 INTRODUCTION
2.2 METHODS
2.3 RESULTS
2.4 DISCUSSION
2.5 REFERENCES

3. INVESTIGATIONS INTO CELLULAR PROLIFERATION AND PROTEIN TURNOVER IN HUMAN IMMUNE CELL POPULATIONS USING DEUTERIUM-OXIDE *IN VIVO*: A PILOT STUDY

3.1 INTRODUCTION
3.2 METHODS
3.3 RESULTS
3.4 DISCUSSION
3.5 CONCLUSIONS
3.6 APPENDIX
3.7 REFERENCES

4. DEUTERIUM BRAIN IMAGING AT 7T DURING DEUTERIUM-OXIDE DOSING

4.1 INTRODUCTION
4.2 METHODS
4.3 RESULTS
4.4 DISCUSSION
4.5 CONCLUSION
4.6 REFERENCES

CHAPTER III:

TECHNICAL CONSIDERATIONS AND PROSPECTS FOR SINGLE-CELL PROTEOMICS

1. REVIEW

1.1 INTRODUCTION
1.2 SAMPLE PROCESSING
1.3 CHEMICAL LABELLING VS LABEL-FREE APPROACHES
1.4 DATA ACQUISITION
  1.41 DDA OR DIA
  1.42 OPTIMISING DATA ACQUISITION
  1.43 NANOFLOW LIQUID CHROMATOGRAPHY
  1.44 ION MOBILITY SPECTROMETRY
  1.45 LINEAR ION TRAPS
1.5 DATA PROCESSING AND ANALYSIS
1.6 SUMMARY
1.7 REFERENCES

COVID-19 IMPACT STATEMENT

The COVID-19 pandemic had a significant impact on the work of this PhD thesis, which was originally to be centred around a study assessing the effects of major abdominal surgery on skeletal muscle protein turnover and immune cell dynamics. The first lockdown in March 2020 prevented laboratory access for a period of 6-months, at a time when the study had been in the process of receiving ethical approval. Upon return to the laboratory after 6-months (October 2020), all human research was further suspended until April 2021. This prevented several human physiology studies which I was set to be involved in from commencing. Throughout and after this time, from October 2020-October 2021, laboratory access was restricted to 50% capacity, with significant backlogs in general lab and cell culture consumables limiting progress on alternative research outputs. Additionally, throughout this 18-month period (March 2020-October 2021), access to surgical patients was restricted to primary care staff only, preventing my primary PhD study from commencing once restrictions on human research eventually lifted, end-April 2021.

Once apparent that the original PhD was not possible, in November 2021 my PhD was altered to focus on the development of stable isotope tracer techniques using deuterium-oxide (D_2O), for *ex vivo* and *in vivo* human applications. This necessitated a *de facto* transfer from the University of Nottingham's, Queen's Medical Centre campus, to the stable isotope mass spectrometry facility located at Royal Derby Hospital, UoN. Around the time of this transfer, increased demand within Derby's facility for untargeted metabolomics and proteomics (which was relatively new to the facility at the time) increased, partially due to sample backlogs as a result of the COVID-19 pandemic, which resulted in a change of LC-MS instrumentation used for proteomics. Unfortunately, this change in instrumentation led to persistent issues regarding both maintenance and performance of the LC-MS system over the remaining 18-months of my research time, ultimately leading to the instrument being unavailable for approximately 1-year of my remaining PhD research. Expectedly, this had a significant impact on the remainder of my PhD, which as a result became even more experimentally limited and substantially reduced my research output. While I utilised this time to pursue external training in both clinical, laboratory and bioinformatic techniques wherever possible, I hope that these mitigating circumstances are taken into consideration during the assessment of this PhD thesis.

PRESENTATIONS ARISING FROM THIS THESIS

POSTER PRESENTATIONS

1. Jaconelli, M., Lord, J.M., Greenhaff, P.L., Atherton, P.J., Lobo, D.N. & Brook, M.S. **Declines in muscle protein synthesis are a primary metabolic feature of post-operative catabolism: A systematic review and meta-analysis.** European Society of Parenteral and Enteral Nutrition Virtual Annual Congress, September 2020.

ORAL PRESENTATIONS

1. Jaconelli, M., Greenhaff, P.L., Atherton, P.J., Lobo, D.N. & Brook, M.S. **The effects of elective abdominal surgery on protein turnover: A meta-analysis of stable isotope techniques to investigate postoperative catabolism.** Surgical Research Society Annual Meeting, East Midlands Conference Centre, Nottingham, March 2022.

PUBLICATIONS ARISING FROM THIS THESIS

ABSTRACTS

1. Jaconelli, M., Lord, J.M., Greenhaff, P.L., Atherton, P.J., Lobo, D.N. & Brook, M.S. **Declines in muscle protein synthesis are a primary metabolic feature of post-operative catabolism: A systematic review and meta-analysis.** *Clin. Nutr. ESPEN* **40**, 623 (2020).

2. Jaconelli, M., Greenhaff, P.L., Atherton, P.J., Lobo, D.N. & Brook, M.S. **O104 The effects of elective abdominal surgery on protein turnover: a meta-analysis of stable isotope techniques to investigate postoperative catabolism.** *Br. J. Surg.* **109** (2022).

PAPERS

1. Jaconelli, M., Greenhaff, P.L., Atherton, P.J., Lobo, D.N. & Brook, M.S. **The effects of elective abdominal surgery on protein turnover: A meta-analysis of stable isotope techniques to investigate postoperative catabolism.** *Clin. Nutr.* **41**, 709–722 (2022).

2. Cocking, D., Damion, R.A., Franks, H., Jaconelli, M., Wilkinson, D., Brook, M.S., Auer, D.P. & Bowtell, R. **Deuterium brain imaging at 7T during D2O dosing.** *Magn. Reson. Med.* **89**, 1514-1521 (2023).

TRAINING COURSE ATTENDANCE

EXTERNAL

- SYSMIC M1 (certificate of distinction): 2020-2021.
- Metabolomics Data Processing and Data Analysis: Birmingham Metabolomics Training Centre, Feb. 2021.
- Quality Assurance and Quality Control in Metabolomics: Birmingham Metabolomics Training Centre, Mar. 2021.
- LC-MS Based Metabolomics and Metabolite Identification with the Q-Exactive Plus and Orbitrap ID-X Tribrid: Birmingham Metabolomics Training Centre, May 23-26th 2022.
- Research Software Development in Python: Alan Turing Institute, 31st Oct-11th Nov 2022.
- Basic Phlebotomy, *Understanding and Applying Phlebotomy Skills and Techniques*, Phlebotomy Training Services, Nottingham, UK: 20-21st Feb. 2021.
- Cannulation Theory, Department of Research and Education, Emergency and Acute Medicine (DREEAM), Nottingham University Hospitals – NHS Trust: 15th Dec. 2021.

INTERNAL

- Research Integrity: Comprehensive – The University of Nottingham: 1st October 2019.
- Biomedical Imaging in Research – The University of Nottingham: 13th November 2019.
- Surface Analysis with X-ray Photoelectron Spectroscopy (XPS) and Time of flight Secondary Ion Mass Spectrometry (ToF SIMs) – The University of Nottingham: 20th November 2019.
- Introduction to Flow Cytometry – The University of Nottingham: 28th November 2019.
- A question of Ethics: The Use of Humans and Animals in Biomedical Research – The University of Nottingham: 14th February 2020.
- Basics of MATLAB – The University of Nottingham: 18th February 2020.
- Flow Cytometry Data Analysis – Basic Concepts and use of Kaluza: May 2020.

DECLARATION

I, Matthew Jaconelli, declare that all of the work contained within this thesis, submitted to the University of Nottingham for the degree, Doctor of Philosophy, September 2023, is my own work; except in several instances where I must also acknowledge the assistance of several collaborators, who have contributed to the research contained within this thesis:

Foteini Patera – who performed the cell culture macrophage differentiation in *Chapter II, section 2.1*, and who performed the majority of cell isolations, including MACs and FACs in *Chapter II, section 3*.

Anna Malecka – who performed the remaining cell isolations, including MACs and FACs in *Chapter II, section 3*.

And, Dr. Robin Damion and Daniel Cocking, who performed the MRI measurements contained in *Chapter II, section 4*, including MRI data analysis and presentation, as part of the collaborative publication enclosed within this section, performed as an appendage to the primary study detailed in *Chapter II*.

Sincerely,

ACKNOWLEDGEMENTS

I would like to thank all those who have supported the work of this PhD thesis:

Prof. Dileep Lobo for his support and guidance in the drafting and revision of the meta-analysis manuscript accepted for publication in *Clinical Nutrition*, presented in *Chapter I, section 2*.

My primary supervisor, Dr. Matthew Brook, for accepting me onto this PhD programme and for his willingness to involve me in a variety of additional research projects, including the pilot study funded by CRUK - which ultimately provided the majority of data presented within this thesis. His support during numerous applications for additional training opportunities has been invaluable to not only my development as a scientist, but in enabling me to secure a prestigious post-doctoral position within a leading research institute.

I would like to extend a special thank you to Dr. Daniel Wilkinson, who has always made time to assist and guide my research, and answer my many (many) questions relating to mass spectrometry.

My secondary supervisors, Prof. Paul Greenhaff and Prof. Philip Atherton, for their assistance in securing an alternate research direction following the inability to complete my original PhD project.

The staff of QMC; in particular Sara Brown, Dr. Jo Mallinson and Dr. Scott Cooper for their support during my PhD research, as well as the staff of Royal Derby Hospital; with special acknowledgement to Dr. Paula Scaife and Dr. Debbie Rankin.

I would like to extend a special thank you to, Dr. Natalie Shur, for her guidance during the collection of biological samples from surgical theatre and for her feedback during preparation of presentations for upcoming conferences.

Those researchers who contributed to the data presented in chapter II of this thesis; Foteini Patera, Anna Malecka, Dr. Robin Damion, Daniel Cocking and Dr. Hester Franks.

The PhD students of QMC and Royal Derby Hospital.

I would like to extend several special thanks to:

Dr. Simon Platt, for his continued support throughout my PhD studies and in securing my post-doctoral position. He has been both a great mentor and friend.

Dr. Iain Gallagher, for his unwavering support and guidance throughout both my undergraduate and postgraduate degree programmes. His wisdom has been invaluable in enabling me to achieve success and further myself as a scientist, as well as a person.

Dr. D Lee Hamilton, for believing in me and providing me with the opportunity to start this journey into the realm of human physiology research. I am fortunate to have begun my education and career under his guidance.

All staff of the Physiology, Exercise and Nutrition research group at the University of Stirling, for providing me with a strong base from which to develop throughout this PhD program, and for their continued support over the course of my postgraduate studies.

Finally, I would like to extend a deep thank you to my family and friends for their continued support throughout this process, in particular that of my parents and brother, with whom I am thankful to have been able to share this unique experience.

This thesis is dedicated to,

Sonia,

My flower in the rock.

CHAPTER I:

THE SYSTEMIC EFFECTS OF SURGICAL TRAUMA ON PROTEIN METABOLISM

1. INTRODUCTION

1.1 The Metabolic Response to Surgical Trauma

Surgical trauma is known to lead to the development of various metabolic pathologies. These lead to post-surgical complications, increased rates of mortality, as well as the prolongment of the duration of clinical care required for successful patient recovery. The perioperative care of patients is therefore crucial in optimising not only patient health and recovery, but also the efficient use of clinical resources. Through further understanding the metabolic consequences of surgery and the mechanisms underlying their development, we may inform perioperative care strategies and improve clinical outcomes.

Early research in this field by Sir David Cuthbertson [1,2], whose work examined patients with tibial fractures, illustrated the occurrence of two distinct phases in the response to injury; the ‘ebb’ and ‘flow’ phases. The ‘ebb’ phase is characterised by depressed metabolic activity, hyperglycaemia and hypotension. For those that survive the ebb phase, it is followed by the ‘flow’ phase; characterised by maximal protein catabolism, increased metabolic rate, heat generation and salt and water retention. In later years, these stages were further expanded by Moore [3], who included an ‘anabolic’ phase which consists of accelerated healing, returned appetite, restored anabolic metabolism and normalised salt and water excretion. Although by Cuthbertson’s classical works it appeared lessened compared to the initial traumatic injury, it was noted in patients who underwent subsequent surgical procedures that these metabolic phases also occurred as a consequence of surgical trauma [1]. This was further defined by Moore, whose work on the metabolic responses to surgical trauma supported these observations and led to the inclusion of the ‘anabolic’ phase during recovery.

Both classical authors noted that protein catabolism and metabolic rate were strongly affected surgical parameters. As skeletal muscle is an important glucose sink and a major energy reserve, this tissue is heavily implicated in the metabolic response to surgical trauma and poses as the predominant site of catabolism. These metabolic effects are also likely contributed to by the periods of disuse that often occur in conjunction with traumatic injury and surgery. Early work by Cuthbertson acknowledged the relevance of this input and displayed that healthy immobilised controls displayed a similar yet less acute response to bed-rest and lower limb immobilisation [4]. Further and more recent studies have confirmed these observations, displaying immobilisation to cause suppressions in muscle protein synthesis and induce overall muscle wasting [5]. However, it is evident that the metabolic responses to surgery and trauma are influenced by other factors that lead to a much greater overall metabolic response.

The influence and input of hormonal signalling, primarily through the action of the adrenal glands, has long been associated with the perioperative stress response, particularly in the ‘ebb’ or now more commonly referred to, ‘acute’ phase. Cuthbertson observed adrenal-hormone-dependent nitrogen loss in early murine studies [6]. They attributed causation of this to the systemic presence of these hormones; demonstrating this in adrenalectomized rats which received ‘maintenance’ dosages of cortical hormones following operative trauma and consequently displayed nitrogen excretion comparable to control specimens. Through their experiments they also suggested that the priming or sensitisation of molecular pathways was an important factor in this response, and as such was not an ‘all or nothing’ effect limited to adrenal inputs.

The concept of inflammation following trauma being dangerous, yet crucial to the development of metabolic responses that enable healing, has existed for millennia. Historically, Hippocrates suggested inflammation to be an important part of the healing process, but when unchecked could lead to severe consequences [7]. This concept was elegantly iterated many centuries later by John Hunter, within his work “A Treatise on the Blood, Inflammation and Gunshot Wounds” [8], wherein he stated; “There is a circumstance, attending accidental injury which does not belong to disease, namely that the injury done has in all cases a tendency to produce both the disposition and means of cure”. Over the last century, research has greatly expanded our understanding of inflammatory mechanisms; with studies specifically focused on surgically-induced inflammation starting to elucidate the underlying mechanisms that occur during this metabolic state.

This review will focus on physiological processes central to the perioperative metabolic response; with particular attention to neuro-hormonal signalling, inflammation, the metabolic implications for skeletal muscle and the regulation of skeletal muscle mass following surgical trauma.

1.2 The Perioperative Stress Response: The Regulation of HPA Axis and Cortisol Metabolism

Trauma from surgery initiates alterations in the neuro-hormonal signalling axis, which is believed to drive the early stress response. This predominantly occurs through the hypothalamic-pituitary-adrenal (HPA) signalling axis [9], and this response is known to be relative to the intensity and duration of traumatic insult [10]. Afferent signals from the site of surgical trauma invoke an increased release of hormones from the pituitary gland, mediated through altered hormonal regulation at the site of the hypothalamus, centrally the paraventricular nucleus (PVN) [11]. This promotes the release of glucocorticoids and catecholamines from the adrenal glands into the circulation, which have various metabolic effects. A significant example of this process is the increased hormonal secretion of corticotrophin-releasing hormone (CRH) from the hypothalamus and the consequent increase in release of corticotrophin (ACTH) from the anterior pituitary. This results in the subsequent production of the glucocorticoid stress hormone, cortisol, from the adrenal cortex thus completing the HPA signalling axis. Production of cortisol along this signalling axis is further enhanced through the simultaneous release of anti-diuretic hormone (ADH, also known as arginine vasopressin (AVP)) from the posterior pituitary, following its prohormone peptide synthesis in the hypothalamus. This concomitant release of ADH has shown to be most pronounced following major abdominal surgery, and exerts significant additional impacts on fluid balance regulation [12–14]. Together, these processes have

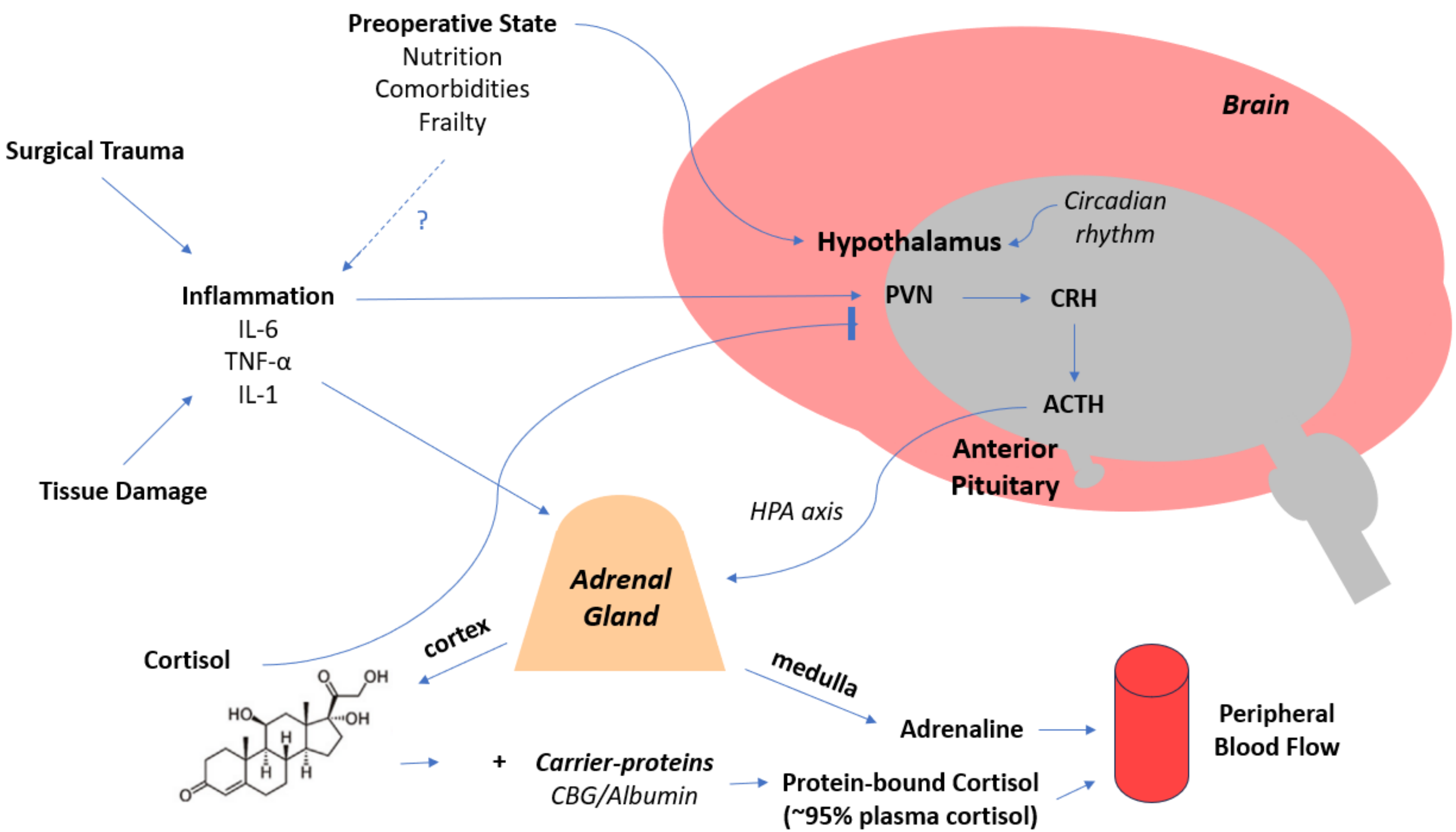

Figure 1: *Impacts of surgery on the regulation of the hypothalamic-pituitary-adrenal (HPA) axis.* ***PVN****; paraventricular nucleus,* ***CRH****; corticotrophin-releasing hormone,* ***ACTH****; corticotrophin,* ***CBG****; corticosteroid-binding globulin,* ***TNF-α****; tumour necrosis factor alpha,* ***IL****; interleukin. Figure adapted from* Manou-Stathopoulou, et al. 2019[11].

shown to result in ACTH production higher than physiologically required for maximal adrenocortical stimulation within minutes of the onset of surgery [15]. Under homeostatic conditions, levels of cortisol provide negative feedback on ACTH production, thus modulating hormone levels within this signalling axis. However, following surgical insult this regulatory feedback loop fails, with ACTH and cortisol levels in blood remaining in an elevated state for a significant period following surgery. This is believed to primarily occur due to prolonged disruption of the inherently pulsatile release of cortisol via ACTH, relative to circadian rhythm; with increased pulsatile activity being shown to occur following cardiac surgery, displaying elevated ACTH and cortisol levels that persist for approximately 8 and 24 hours respectively [16]. A meta-analysis of cortisol serum levels following surgery has further expounded that more invasive procedures can produce elevated cortisol levels for as long as 7 days compared to healthy controls [10]. However, the exact mechanisms that drive this disproportionate persistence of cortisol levels relative to ACTH is unknown. This imbalanced relationship is likely influenced by various external factors, with several parameters implicated in the regulation of cortisol levels within blood and tissues.

Within plasma, cortisol travels bound to the carrier-proteins, corticosteroid-binding globulin (CBG) and albumin. This results in only ~5% of total cortisol freely circulating within the blood [17]. Due to this binding, only freely circulating cortisol is capable of migrating into tissues and diffusing across cell membranes through its lipophilic structure to exert its regulatory effects. It is therefore commonly accepted that cortisol (and similar steroid hormones) exist in an inactive form when bound to their carrier-proteins. Following increased cortisol levels there is reduced availability of these carrier-proteins, which enables more cortisol to freely circulate and diffuse into tissue cells. This is complemented at sites of inflammation, whereby activated neutrophils cleave CBG and further promote local active cortisol concentrations [18,19]. Carrier-protein-glucocorticoid interactions are therefore an important means of glucocorticoid regulation, and further modifications have been displayed in response to inflammatory stress. This includes the down-regulation of CBG following stress and chronic illness, resulting in increased active glucocorticoid within blood plasma [18].

Once able to successfully diffuse across cell membranes, cortisol binds intracellular receptors. Glucocorticoids, such as cortisol, interact with two distinct receptor types; mineralocorticoid receptors (MRs) and glucocorticoid receptors (GRs) [20,21]. Following receptor binding, both receptors translocate to the nucleus whereby they influence gene expression, either to repress or promote transcription via interactions with DNA and transcription factors. The GR further regulates intracellular signalling pathways via non-genomic, G-protein second messenger signalling transduction [22]. Many of these signalling pathways directly modulate metabolism and are present in tissues throughout the body.

The expression of the MR and GR receptors is also influenced by metabolic stress. Oxidative stress has been shown to down-regulate GR expression [23] and up-regulate MR expression [24,25], while increased cellular cAMP (cyclic adenosine monophosphate) has shown to increase the expression of both receptors [21,26]. Surgical trauma often results in oxidative stress within both damaged and highly active metabolic tissues, primarily as a result of inflammation and the subsequent generation of reactive-oxygen-species (ROS). Surgery has also been shown to induce blood plasma increases in second-messenger cAMP (which is involved in various metabolic signalling pathways) [27–29]. It has been shown that elevations in plasma cAMP are associated with activation of β-adrenergic receptors from adrenaline [30], and that this relationship is observed within surgically-induced elevations in both adrenaline and cAMP [27]. This would therefore suggest that adrenaline-driven responses aid in promoting the upregulation of glucocorticoid-GR signalling and thus would amplify the metabolic response to stress from this pathway. The interaction of both glucocorticoids and adrenaline are also associated with early immune responses along this axis. In a study of blunt trauma it was observed that trauma-induced increases in both adrenaline and cAMP were significantly correlated with plasma neutrophil counts [31]. This study hypothesised that this may be a result of adrenaline-induced increases in neutrophil intracellular cAMP, resulting in the promotion of neutrophil demargination and their subsequent release into the bloodstream. However, it is also probable that associated increases in neutrophil count following trauma are mainly attributed to the glucocorticoid-driven responses of demargination and enhanced maturation process [32]. Regardless, it would appear that both cortisol and adrenaline separately coordinate and together amplify metabolic stress responses following trauma and contribute to the early neutrophilia observed following trauma.

Another important parameter in understanding the role of the primary human glucocorticoid, cortisol in the perioperative stress response is the regulation of cortisol’s removal from the blood. As there exists a large pool of cortisol bound to carrier proteins, which thus allows for rapid fluctuations in freely existing cortisol within plasma, cortisol degradation is very important in controlling net cortisol levels. This is largely achieved through the activity of the hepatic and adipose tissue reductases, which breakdown cortisol via 5α-reductase and 5β-reductase. Additionally, cortisol is broken down into its inactive cortisone counterpart within kidney tissue by 11β-hydroxysteroid dehydrogenase type 2 (11β-HSD2) [33]. In a study investigating cortisol metabolism in critically ill ICU patients [34], it was shown that clearance of plasma cortisol was reduced by over 50% compared to surgical controls, through measurement of infused deuterated-cortisol disappearance in patients. This occurred in paradigm to a poor correlation between elevated cortisol and comparably low ACTH levels, strongly suggesting that the increased circulating cortisol was due to decreased metabolic breakdown. This was further demonstrated by greater suppression of cortisol clearance in non-survivors when compared to survivors, suggesting this alteration in cortisol metabolism likely occurs as a protective mechanism to reduce metabolic demand. The downregulation of cortisol breakdown was also apparent at the tissue level. Patient liver showed over 75% decreased mRNA expression of 5α-reductase, and over 80% decreased mRNA expression of 5β-reductase, compared to controls. 5β-reductase mRNA expression positively correlated with protein expression and negatively correlated cortisol levels, with over 50% reduced enzymatic activity also present as a likely consequence of increased circulating bile acids [33]. Together, these findings strongly suggest decreased cortisol breakdown as a mechanism to maintain elevated cortisol levels during persistent clinical stress responses.

It is likely similar mechanisms occur following elective surgery and may be involved in the persistence of stress responses within tissues, even when cortisol levels have returned to baseline levels. Similar cortisol dynamics could also pose as an explanation for the observed imbalance between ACTH and cortisol levels demonstrated following surgery [16]. In two perioperative studies of cardiac surgery [35,36], surgery resulted in decreased cortisol – cortisone conversion, which was hypothesised by the authors to be the result of exhausted 11β-HSD2 enzymatic activity following surgically elevated cortisol. Although plausible, these studies did not directly measure 11β-HSD2 activity or expression, and as such these interpretations are limited. There exists another regulator central to cortisol metabolism, which may also present a cause of elevated cortisol levels following surgical trauma, particularly in its pathogenesis within tissues. 11β-hydroxysteroid dehydrogenase type 1 (11β-HSD1) controls the conversion of cortisone to cortisol. This process happens readily in the liver, but also within various other tissues. As plasma cortisol often returns to near baseline levels following 24hr post-surgery [10], yet the effects of what is largely attributed to be cortisol-driven stress responses may persist in tissues for much longer, dysregulation of 11β-HSD1 is a potential cause for the continued stress pathology present in these tissues. Following minor elective surgery, skeletal muscle has demonstrated elevated 11β-HSD1 activity up to 6 days after the procedure, while plasma cortisol levels were shown to return to baseline levels after 24 hours [37]. This upregulation was remote to the site of surgery (*vastus lateralis* biopsy following abdominal surgery), and as such suggests 11β-HSD1 as a viable regulator of systemic stress within tissues.

1.3 The Effects of Glucocorticoids on Metabolism: Impacts for Skeletal Muscle and the Pathogenesis of Insulin-Resistance

Glucocorticoids are hormones originating from steroid precursors synthesised by the zona fasciculata of the adrenal cortex that exert potent effects on carbohydrate, protein and fat metabolism. Glucocorticoids and GRs play an important role in maintaining sufficient gluconeogenesis production in the liver; which is crucial during times of fasting to ensure sufficient glucose availability and is thought to partially explain their circadian cycle of release [38]. Glucocorticoids further act to ensure sufficient circulating glucose levels by suppressing pancreatic β-cell secretion of the glucose storage hormone, Insulin, and within skeletal muscle can significantly reduce the translocation of GLUT4, the glucose membrane transporter required for the uptake of glucose into muscle [39–41]. This activity is largely dependent on GR expression and availability, as well as local glucocorticoid levels. Glucocorticoids can further facilitate increases in gluconeogenesis by providing gluconeogenic substrates for metabolism in the liver from amino acids mobilised from peripheral skeletal muscle through increasing rates of protein breakdown. Dysregulation of these processes is heavily implicated in the pathogenesis of insulin-resistance that is observed in various conditions; such as type 2 diabetes, the metabolic syndrome and as a result of surgical trauma.

Hyperglycaemia is pronounced following surgical trauma and manifests rapidly, usually peaking within 24 hours following surgery [42,43]. The suppression of glucose storage via insulin-dependent mechanisms and the upregulated production of glucose in the liver provides a protective mechanism to enable sufficient energy availability in times of physiological stress, and thus would appear to provide an initial benefit during surgery. However, persistent hyperglycaemia post-surgery can have negative metabolic impacts and is associated with increased rates of mortality [44–46]. This is suggested to be contributed to by the various metabolic and biochemical impacts of prolonged hyperglycaemia [42]. These present greater risks of infection and sepsis post-surgery, likely through hyperglycaemic immunomodulatory effects. These include abnormalities in monocyte and neutrophil functional capacity; primarily the reduction of neutrophil phagocytic function. In studies of both diabetic and non-diabetic cardiac patients [47,48] maintenance of normoglycaemic levels via insulin treatment provided improved neutrophil and monocyte post-operative immune function compared to controls, along with protection from infectious complications compared to controls. A recent meta-analysis on the potential benefits of glycaemic control following surgical trauma supported these observations [49], demonstrating reductions in infection and sepsis in patients who undertook post-operative glycaemic control. They also displayed post-operative glycaemic control to result in reduced short-term mortality, further conveying the metabolic importance of glycaemic regulation in clinical outcomes.

Skeletal muscle is an essential post-prandial glucose sink and fuel store, consisting of up to 50% of human body mass. It therefore poses as a crucial metabolic tissue and as such, effects of metabolic dysregulation here are substantial. The development of insulin-resistance within skeletal muscle is thus of great consequence to metabolic whole-body function following traumatic insult, and elucidating the mechanistic action and consequences of skeletal muscle insulin-resistance is critical. 11β-HSD1 has been implicated as a causative mechanism of cortisol-induced insulin resistance within peripheral tissues. As levels of cortisol within tissues are highly regulated by the active conversion of cortisone to cortisol via 11β-HSD1 activity, 11β-HSD1 has been studied as a mechanistic target of glucocorticoids metabolic effects. In C2C12 myotubes it has been shown that glucocorticoid-mediated insulin-resistance was dependent on 11β-HSD1 activity, and when 11β-HSD1 inhibitors were introduced, the antagonistic effects of cortisol on insulin were negligible [50]. This has been further supported in both murine and human primary skeletal muscle cell lines, which showed 11β-HSD1 to possess an integral role in modulating glucocorticoid-induced insulin-resistance [51]. As previously mentioned, surgical trauma has been shown to lead to increased 11β-HSD1 activity in skeletal muscle for up to 6 days post-surgery [37] which supports 11β-HSD1 as a potential effector of peripheral insulin-resistance. However, other metabolic processes are also known to impact insulin and its signalling effects within skeletal muscle.

Free-fatty acids (FFA) are an important source of energy within skeletal muscle and are the predominant fuel source under fasting conditions. The use and generation of

FFAs within skeletal muscle is regulated by various hormones including both insulin and glucocorticoids. Glucocorticoids have been shown to increase FFA availability through modulation of catecholamine receptors, GR-mediated mechanisms and promotion of lipolysis [52]. In a study of primary human skeletal muscle cell lines [53], the introduction of cortisone and cortisol reduced myocyte glucose uptake and glycogen synthesis, while increasing palmitate oxidation and pyruvate dehydrogenase kinase 4 (PK4). This illustrates a mechanistic shift in metabolism similar to that observed in the skeletal muscle of type 2 diabetes patients who exhibit high expression of PDK4 in conjunction with impaired glucose utilisation [54]. When PDK4 was inhibited it prevented the cortisol-driven metabolic responses, suggesting it to be a central effector in this process. However, when myocytes were stimulated with insulin the effects of cortisol were prevented within this study. This is likely due to insulin exerting its own regulatory effects on PDK4, with insulin levels demonstrating an inverse correlation with PDK4 expression [55].

In murine skeletal muscle it has been shown that during a lipid-induced insulin-resistant state, the capabilities of insulin to suppress PDK4 expression decrease by 2-3 fold [56]. This study also observed that insulin-resistance following intralipid infusion resulted in decreased insulin signalling via Akt and FOXO1 signalling pathways, implicating fatty acids to suppress insulin regulation of PDK4 via alterations in insulin signalling. Under normal homeostatic (post-prandial) conditions, insulin acts to increase glucose uptake and promote growth in skeletal muscle through binding its tyrosine-kinase receptor and inducing a signalling cascade. Activation of the insulin receptor results in the intracellular tyrosine phosphorylation of various associated proteins, with insulin-receptor-substrate 1 (IRS1) being the major docking protein. This phosphorylation mediates the activation of PI3K and the generation of second messenger PIP_3 at the plasma membrane. PIP_3 activates Akt (also known as protein kinase B), which is a central regulator of insulin-mediated effects on metabolism and growth [57]. Akt is now capable of phosphorylating substrate, AS160, a Rab GTPase-activating protein which activates Rab GTPases required for the translocation of GLUT4 vesicles to the cell membrane, which enables the subsequent uptake of glucose into skeletal muscle [58]. Human studies have aimed to further define the mechanisms of fatty acid inhibition on insulin signalling in skeletal muscle through nuclear magnetic resonance spectroscopy (NMRS) [59]. These studies have illustrated that increased fatty acids cause defects in IRS1 phosphorylation and its associated activation of PIP_3 in skeletal muscle. This suggests that the availability of fatty acids may be the driving force in the development of insulin-resistance in skeletal muscle, with glucocorticoids actions inhibiting glucose uptake into skeletal muscle and initiating the promotion of fatty acid oxidation augmenting this process.

Therefore, post-operative hyperglycaemia may also be attributed to increases in circulating FFAs which dysregulate the insulin signalling pathway and promote insulin-resistance. As surgery has been shown to result in increased plasma FFA in conjunction with hyperglycaemia [60], it is possible that increased release of FFA contributes to the pathology of insulin resistance following surgical trauma. This hypothesis was examined in a study of patients who underwent elective major open abdominal surgery [61]. Surgery resulted in increased plasma FFA and hyperglycaemia.

This was in tandem with a 4-fold increase in PDK4 mRNA expression and a greater than 50% decrease in pyruvate dehydrogenase complex activity within the *vastus lateralis* of patients post-surgery. This supports that surgical trauma initiates a local upregulation of fat oxidation in skeletal muscle, and these effects occur in the periphery remote to the site of traumatic insult. Although these observations support this hypothesis, this study lacked further molecular measures to substantiate the molecular underpinnings of their observations. Regardless, there appears to be a strong association between increased FFA availability and the development of insulin-resistance in skeletal muscle following surgical trauma, which is likely augmented via the metabolic actions of glucocorticoids.

1.4 Nutrient-Sensing and Energy Status: Regulation of Muscle Protein Turnover

Under homeostatic conditions, the regulation of muscle synthesis and breakdown is primarily controlled via energy status. As the metabolic demands of skeletal muscle are highly fluctuant due to its inherent role in locomotion, as well as its essential role as a metabolic store and regulator of whole-body metabolism, the ability of skeletal muscle to sense changes in both nutrient and energy status is of the upmost importance. Energy sensing is controlled through the combined action of both peripheral and central mechanisms.

The arcuate nucleus (ARC) of the hypothalamus is a group of neurons located at the bottom of the third ventricle of the brain, in close proximity to the median eminence. The median eminence is a structure of the blood-brain-barrier, and due to its proximity, enables the ARC to sense nutritional and hormonal changes within the blood. This site is thus capable of monitoring peripheral energy signals that are carried within the blood, and responding with centrally-driven responses that act through effector neuro-hormonal signals that in turn modulate systemic, and tissue specific, metabolism. This enables the regulation of energy status through central mechanisms, with the ARC consisting of two major regulatory neuron groups: those that produce neuro-peptide Y (NPY) and Agouti-related protein (AgRP), and those neurons that produce the pro-opiomelanocortin (POMC) and cocaine-and amphetamine-related transcript (CART) [62]. The former group are termed orexigenic and promote feeding behaviour, while also presenting inhibitory synaptic effects via release of gamma amino-butyric acid (GABA) and are known inverse-agonists for the melanocortin receptors [63,64]. POMC and CART are anorexigenic neurons, with POMC capable of both excitatory and inhibitory transmission via glutamate and GABA release, as well as releasing post-translational products of POMC peptide which include; α-, β-, γ-melanocyte-stimulating hormone (MSH) and the adrenocorticotropic hormone (ACTH). Together, the neuron groups of the ARC modulate systemic energy responses via synaptic transmission that target secondary effector neurons which consequently release energy hormones into the circulation.

An important secondary neuron structure downstream of the ARC is the PVN. During the fed state, release of α-MSH from the POMC initiates the catabolic melanocortin signalling cascade via the G-protein-coupled melanocortin receptors (MCR). This acts to decrease food intake and increase energy expenditure through positive regulation of the HPA axis [62]. This response is subject to intra-PVN competition with AgRP and inhibition of the POMC via GABA secreted from the intermingled orexigenic neuron groups. Neuronal projections of the PVN are also capable of influencing sympathetic and parasympathetic activation through interaction with the dorsal motor nucleus of the vagus nerves (DMX) and the intermedio-lateral cell column (IML), with sympathetic tone being an important mechanism of increased lipolysis, liver gluconeogenesis and decreased insulin secretion. This is partly achieved through innervation of many peripheral tissues, such as adipose tissue, from the autonomic nervous system (ANS).

In murine studies, central manipulation of the melanocortin signalling cascade has been shown to cause changes in peripheral tissue metabolism, irrespective of nutrient intake [65,66]. Overall, these changes promoted shifts towards lipid metabolism, with increased mobilisation and storage in white adipose tissue while causing decreases in glucose metabolism within skeletal muscle. These shifts have been suggested as potential causes of metabolic syndrome in peripheral tissues and have been implicated as such within studies that have demonstrated selective peripheral metabolic changes following ablation of NPY/AgRP to result in obesity irrespective of dietary intake [67,68].

Surgery is known to cause defects in HPA-axis signalling, as well as the development of insulin-resistance in peripheral tissues with associated alterations in fat metabolism. However, whether these changes are affected by inputs from the ARC during surgery is relatively unknown, largely due to the methodological difficulty of measures within humans. Alteration to ARC pathways may however pose explanations for some of the metabolic changes observed following surgery, and research should be conducted in this field to investigate these parameters.

It is also common following surgery for patients to feel incapable of eating or to experience suppressed hunger. This complicates recovery, and in turn can contribute to increased catabolism in the days following surgery. If ARC dysregulation does in fact occur following surgery, it could also provide a causative mechanism for the lack of hunger observed in patients. This would further support ARC signalling as a potential therapeutic target in minimising the detrimental impacts of surgical trauma on whole-body metabolism. At this stage however, any potential alterations in the ARC signalling axis following surgical trauma is largely speculative.

Within skeletal muscle, the ability to sense local changes in cellular energy demands is important in ensuring the continued supply of energy required for both mechanical function and metabolism. An important sensor of this process within skeletal muscle is AMP-activated protein kinase (AMPK). ATP is the body’s cellular energy currency, and demand for ATP within skeletal muscle can increase by up to 1000-fold during intense exercise [69]. In order to maintain ATP requirements, skeletal muscle rapidly generates ATP through the coordinated action of the skeletal muscle energy systems: the phosphagen, glycolytic and mitochondrial respiratory. However, during times of cellular energy stress, there can still present a decrease in available ATP and a concomitant increase in cellular AMP. Increased cellular AMP activates AMPK, which has various metabolic effects that promote catabolism and inhibit anabolism.

These aim to ensure sufficient ATP demand within tissues, with AMPK posing as one of the most pivotal regulators of this metabolic switch. AMP activates AMPK through inducing a conformational change that enables phosphorylation, and subsequently inhibits dephosphorylation, of Thr172 within the AMPK activation-loop [70]. AMPK can additionally be activated by decreased inhibitory action from glycogen, which is suggested to be mediated via alleviated inhibitory kinase activity towards AMPK. The production of ROS, which commonly occurs during various inflammatory settings such as that following surgical trauma, are also known to both directly and indirectly activate AMPK [70].

Once activated, AMPK inhibits mTORC1 (the central promoter of protein synthesis) through both direct inhibitory phosphorylation of the raptor mTORC1 subunit, as well as upstream activation of tuberous sclerosis complex 2 (TSC2) which also inhibits mTORC1. With the inhibition of mTORC1, AMPK is now capable of exerting inhibition on both transcription and translation machinery within cells [71,72]. AMPK is also known to directly promote autophagy, mitophagy and mitochondrial fission; all of which are known to contribute to skeletal muscle wasting [70,73–78]. Combined, these processes strongly promote catabolism and suggest AMPK to be an integral regulator of protein turnover within skeletal muscle.

Perioperatively, it is common for patients to have reduced dietary intake due to either medically recommended restriction of fluid and food or from the common side effects of nausea, reduced appetite and abdominal discomfort following operation [79]. These often result in negative energy balance during the days following surgery, when skeletal muscle catabolism is known to be most prevalent. It has been shown that hypocaloric nutrition alone for several days can induce insulin-resistance in healthy volunteers [80] and therefore likely also contributes to its pathogenesis following surgery. Insufficient caloric intake is therefore a culpable mechanism of skeletal muscle catabolism both in the period directly before and in the days following surgical trauma, and additionally may contribute to the development of insulin-resistance. This is supported by studies that display decreased catabolism, as well as reduced insulin-resistance, in patients that received pre- and/or post-surgical supplementation with carbohydrates and amino acids compared to placebo and control patients who did not [81–91]. Regarding catabolism, these studies have shown that fasting before surgery and reduced intake after, both promote MPB and reduce MPS compared to when supplementation protocols are utilised. However, it should be noted that these studies have utilised heterogenous, and often minimal, methods of measuring muscle protein turnover. This conveys the need to carry out more comprehensive and sensitive measurements of muscle protein turnover following surgical trauma. These would likely benefit from recent advances in the use of stable isotope techniques to measure muscle synthetic rates, in combination with other methods that can quantify the activation of these synthetic and degradative pathways within skeletal muscle [92].

The direct activity of nutrient-sensing regulators of muscle protein turnover within skeletal muscle, such as AMPK, have to the authors knowledge, not been assessed following surgical procedures. However, the regulation of these energy-sensing mediators is likely affected and involved in the catabolic processes that ensue surgical trauma. With increased insulin-resistance as a result of surgery, there will consequently be decreased uptake of glucose into skeletal muscle via GLUT4-dependent mechanisms and decreased glycogen synthesis. This would relieve inhibitory action on AMPK from glycogen, enabling greater activation of AMPK within skeletal muscle. Traumatic insult is also known to induce systemic inflammation, which together with the concerted activation of neutrophils, leads to increased ROS production. ROS are capable of activating AMPK both indirectly through increases in cellular AMP [93], as well as through direct modulation of AMPK phosphorylation [70]; however in skeletal muscle cell lines this direct interaction is yet to be elucidated [94]. These mechanisms could both pose as possible means of AMPK activation following surgery, but research in this field is needed to substantiate these hypotheses. AMPK is also known to interact with central mechanisms in the hypothalamus that regulate hunger, with the gastric hunger-promoting hormone, Ghrelin, being known to promote AMPK-induced inhibition of mTORC1. Ghrelin also acts to increase AgRP levels, which has been shown to occur in an AMPK-dependent manner, but which can be offset by increased insulin-mTORC1 signalling [95]. The impacts of fasting or reduced calorie intake pre- and post-surgery likely impact these signalling pathways, and may promote AMPK-activation through both central and peripheral mechanisms. Future research should assess the relevancy of these pathways following surgical trauma, and their influence on the improved metabolic outcomes that have thus far been associated with carbohydrate and amino acid supplementation in patients perioperatively.

1.5 The Effects of Immobilisation on Skeletal Muscle

Immobilisation is known to induce loss of muscle mass and insulin-resistance in healthy humans. Immobilisation-induced loss of muscle mass is a consequence of dysregulated muscle protein turnover, although the mechanisms underlying this process are still to be mechanistically defined. Rodent models of acute limb immobilisation for 6 and 24 hour periods have shown decreases in MPS and increases in MPB, when measured using *in vivo* stable isotope tracer methodologies [96,97]. Further research of muscle synthetic and degradative pathways during several days of cast-limb immobilisation in rodents has suggested protein breakdown to be the driving factor of the associated muscle atrophy [98]. This is due to observed increases in mRNA expression of the ubiquitin-ligases, muscle atrophy F-box (MAFbx) and muscle RING-finger 1 (MuRF1), whose peak expression at day 3 of immobilisation was in parallel to the plateaued decrease of muscle wet weight (12% decrease in gastrocnemius muscle) also observed at day 3. This suggestion of MPB driving the observed muscle atrophy was further supported by *in vivo* administration of the proteasome inhibitor, Velcade, which reduced the observed hindlimb atrophy of the gastrocnemius muscle by approximately 50% at day 3 of immobilisation.

In humans however, the progression of muscle atrophy following immobilisation is primarily believed to stem from suppressions in MPS [99]. Various tracer studies utilising immobilisation models of both lower-limb cast [100,101] and bed-rest [102–105] in humans have displayed decreased synthetic rates in skeletal muscle. In a study by de

Boer et al. [101], the authors measured post-absorptive decreases in myofibrillar synthetic rates of ~50%. They highlighted this could plausibly account for the decline in muscle cross-sectional area (CSA) alone, without the need for additional upregulation of degradative pathways. Although these measures were limited to muscle synthetic responses in the basal (fasted) state, such drastic suppressions in MPS could very well account for the changes in quadricep CSA across the measurement period of 10 days in these young, healthy volunteers. Although few studies have measured changes in muscle protein breakdown in skeletal muscle following immobilisation [102,105], these have illustrated negligible input from MPB during the development of atrophy in humans, or have illustrated adaptive declines in MPB following immobilisation. It is due to these observations, in paradigm with the substantial decreases in MPS, that it is widely believed suppressions in MPS are culpable for the progression of skeletal muscle atrophy during periods of immobilisation. However, it should be noted that there is a significantly reduced number of MPB studies that utilise tracer methodologies compared to those that have measured MPS, and as such we cannot discredit a potential role for these degradative pathways in the pathogenesis of skeletal muscle atrophy following periods of immobilisation.

It has been shown that immobilisation alters the expression of mRNA and protein components of several muscle degradative pathways [101,106–111], with the ubiquitin-proteasome pathway most heavily implicated. Although the ubiquitin-proteasome system is unable to degrade intact myofibrils (first requiring preparatory degradation from other systems), it is generally believed to be the primary mediator of coordinated net skeletal MPB [112,113]. Alterations in the activity of this pathway are therefore palpable in the development of atrophy, and in human immobilisation models, have generally shown increases during the early stage (first 3-5 days) of immobilisation. As such, it is possible that increased MPB provides a transient mechanism for promoting skeletal muscle atrophy during the initial stages of inactivity. Early increases in MPB following disuse have also been displayed by increases in 3-methylhistidine excretion following 72 hours of unilateral lower-limb suspension [114]. With currently few reliable studies utilising tracer methodologies to assess the contributions of MPB to muscle atrophy during early disuse in humans, the influence of these pathways in the pathology of immobilisation-induced skeletal muscle atrophy remains to be understood.

Although the underlying cellular mechanisms that direct skeletal muscle atrophy during immobilisation are yet to be fully understood, there are several candidate explanations. As it most likely that alterations in MPS are driving immobilisation-induced atrophy, especially over longer periods when notable declines in muscle CSA begin to occur, dysregulation of muscle synthetic pathways is a probable cause of this process. Initiation of protein translation, characterised by association of mRNA transcripts with ribosomal machinery, is upregulated during periods of increased amino acid availability and muscular contraction. Research has shown this to be an important point of regulation for MPS, even during times of reduced MPS rates such as those observed during sepsis [115–117]. Within rodent models, nutrient- and contractile- induced activation of translation initiation has shown to be centred around the activity and phosphorylation status of the Akt/mTORC1/p70S6k signalling axis. This is primarily due to rodent studies that have illustrated electrical-stimulation of skeletal muscle to induce hypertrophy with associated increases in the phosphorylation of these proteins along this signalling axis [118], as well as that overexpression of this signalling axis in transgenic mice results in significant hypertrophy [119]. However, studies of this signalling pathway in human models of atrophy do not support the relevancy of this axis. It has been shown that neither phosphorylation state nor content of Akt, p70S6K, 4E-BP1 or eIF-4E were drastically altered in the post-absorptive state following either 10 or 21 days of immobilisation that resulted in ~5 and 10% reductions in quadricep CSA respectively [101]. In an immobilisation study across 14 days which investigated changes in MPS during both the post-absorptive and post-prandial state following amino acid infusion, the authors noted that although immobilisation blunted muscle protein synthesis in response to amino acid provision in the immobilised vs control limb, these effects were not reflected in the phosphorylation status of the Akt/mTORC1/p70S6k signalling axis [100]. Other studies of immobilisation in humans have produced similar findings [108,109], although one study following 48-hours of unilateral immobilisation displayed decreases in the phosphorylation status of the Akt-signalling axis in the immobilised compared to the contralateral control limb [107]. This supports the previously suggested role of this axis in contributing to muscle atrophy, but to date, overall evidence suggests that alterations in the Akt/mTORC1/p70S6k signalling axis is not the driving mechanism of muscle atrophy during immobilisation in humans.

Immobilisation and bed-rest are also known to induce insulin-resistance in healthy volunteers. This occurs as a whole body response, as indicated by increases in plasma glucose and insulin concentrations, and more importantly by reduced clearance of glucose following infusion with hyperinsulinemic-euglycaemic clamp [120,121]. Insulin-resistance can occur as early as 3-5 days following immobilisation [122], and due to its presence also being observed in the limbs, it is interpreted that insulin-resistance additionally manifests itself in skeletal muscle during periods of immobilisation. Studies have further illustrated that reducing ambulation alone is sufficient to cause reductions in insulin-sensitivity [123,124], indicating that decreases in the contractile activity of skeletal muscle are involved in these metabolic changes. However, the potential mechanisms behind this process are, as of yet, unclear.

Due to the sequential and seemingly concomitant manifestation of insulin-resistance and skeletal muscle atrophy following periods of reduced activity or immobilisation, insulin-resistance has been implicated as a causative mechanism of immobilisation-induced atrophy. This is generally believed to occur via alterations in the insulin, IRS1-Akt signalling axis, which is an important pathway for nutrient-hormonal signalling regulation of mTORC1 complex and the consequent upregulation of MPS. This is supported by rodent models that have shown reductions in IRS1 protein expression and Akt activity following hindlimb immobilisation [125], as well as bed-rest models in humans that have illustrated suppressions in insulin-stimulated phosphorylation of Akt [124,126,127]. Interference in insulin-signalling would also explain the reductions in GLUT-4 translocation observed with immobilisation following 7-19 days of bed-rest [128–130], and the consequent increase in plasma glucose concentrations.

Further implications of insulin-signalling disruption have been illustrated by both reduced hexokinase activity and glycogen synthase activity in skeletal muscle following 7 days of immobilisation in healthy, young men [130,131]. However, whether these responses drive or occur as a consequence of immobilisation is still unknown. With it being suspected that reductions in contractile activity drive these responses, we do not yet know the intrinsic mechanisms that sense and regulate internal metabolic activity within skeletal muscle as a product of inactivity. AMPK activity has shown to be unchanged following 9 days of bed-rest even though several AMPK subunits were upregulated [127], and it has been shown that exercise following a period of 7 days bed-rest abolishes activation of AMPK suggesting that this target and/or pathway is directly affected from skeletal muscle inactivity. Again, it is unknown whether these effects are driving or consequential to immobilisation-induced insulin-resistance. Regarding physical inactivity; it has been illustrated that a model of dry-immersion (a simulation of micro-gravity) invokes a 6-fold increase in neural-cell-adhesion-molecule (NCAM) association with muscle fibres (which is typically indicative of a denervation process) [132], with this occurring in skeletal muscle after only 3 days. The implications for skeletal muscle denervation in the pathogenesis of both insulin-resistance and muscular atrophy are yet to be fully explored, but it should be noted that dry-immersion is an intense model of immobilisation; with a separate study reporting a decrease of ~10% in *vastus lateralis* myofiber CSA after only 3 days of dry-immersion [133]. As such this model may not be indicative of immobilisation that is more applicable to everyday life scenarios that require bed-rest or limb-immobilisation, e.g. limb injury and surgical recovery.

Another important consideration in the pathogenesis of insulin-resistance (as discussed previously in section: *The Effects of Glucocorticoids on Metabolism…*) is the input from increased plasma FFA and increased lipid presence in peripheral tissues. Within skeletal muscle, it has been shown that 28-days of bed-rest leads to accumulation of intramyocellular lipid (IMCL) content [134], with this occurring in a less pronounced manner after 7-days of bed-rest [120]. Increased skeletal muscle IMCL may arise as a result of decreased basal fat oxidation from physical inactivity and the associated reductions in metabolic rate, likely augmented by the concomitant positive energy intake increasing circulating FFA availability. This hypothesis is supported by studies that have illustrated bed-rest to decrease lipid oxidation [135–137], which was shown to occur irrespective of positive energy balance and in association with insulin-resistance. These changes have been observed after as little as 7 days of bed-rest, suggesting that these effects manifest rapidly following reduced physical activity. As use of the lipid-lowering agent, Acipimox, has been shown to simultaneously lower plasma FFA and IMCL in healthy adults, while simultaneously improving insulin-sensitivity in correlation to these reductions [138]; alterations in IMCL could potentially be driving the development of insulin-resistance following immobilisation or reduced physical activity. IMCL accumulation in skeletal muscle would expectedly lead to increases in intracellular fatty acid metabolites; such as long-chain fatty acyl CoAs, acylcarnitines and diacylglycerols. Accumulation of these metabolites would inhibit pyruvate dehydrogenase activity, as well as blunt insulin-signalling, and together these would suppress glucose metabolism in skeletal muscle. Whether increased IMCL and the associated alterations in metabolic signalling are driving insulin-resistance or occurring as a consequence of it during periods of immobilisation is currently unknown. Furthermore, the greater implications that these processes may have on muscle atrophy is yet to be comprehensively understood in the context of human immobilisation.

An alternative explanation for immobilisation-driven changes in metabolic substrate utilisation is the activity and content of mitochondria. A microarray analysis revealed both 2- and 14-days of immobilisation heavily impacted the expression of genes related to mitochondrial bioenergetics and carbohydrate metabolism; downregulating the activity of these pathways, with these changes present by 2-days of immobilisation and persisting until 14-days [139]. Whereas these changes occurred early and were maintained throughout immobilisation, significant changes in protein synthesis and degradation (which were down- and up-regulated respectively) only occurred following 14-days of immobilisation. As such, it is plausible that these early metabolic changes in mitochondrial function may influence the later changes in muscle protein metabolism observed later on in the immobilisation period [140]. Further to this, 14-days of immobilisation has been shown to elicit declines in quadricep mitochondrial respiratory capacity and protein content in both men and women [139], and for men this has been shown to occur to a comparable extent in both younger and older participants [141]. This is believed to stem from decreased mitochondrial content, due to analysis of respiratory capacity revealing restoration to baseline levels once values were normalised to citrate synthase activity (a marker of total mitochondrial content). Supportive of this was the fact that exercise training after the period of immobilisation restored both mitochondrial respiratory capacity in unison with citrate synthase activity [141]. Changes in mitochondrial content are regulated through both mitochondrial biogenesis; primarily regulated through the signalling of PGC1-α, and mitophagy; the specific degradation of mitochondria via autophagy. In humans, 7-days of immobilisation has been shown to affect the regulation of both these pathways, causing decreases in mRNA and protein expression of mitochondrial biogenesis-related proteins and inversely increasing mitophagy-related mRNA and protein expression [142]. This suggests immobilisation induces early changes in the regulation of mitochondrial synthetic and degradative pathways in a fashion that would reduce total cellular mitochondrial content, which would support previous observations of decreased respiratory capacity in skeletal muscle cells being related to reduced mitochondrial protein. Future studies should utilise measurements of autophagy/mitophagy flux, in addition to microscopy techniques, to thoroughly assess both the direct action of these pathways and any alterations that may occur in mitochondria number and quality.

In summary, immobilisation is known to induce metabolic changes that are of great consequence to whole body metabolism and skeletal muscle mass. With many patients following elective surgical procedures being bed-ridden for varying periods during recovery, there is undoubtedly great importance in understanding the metabolic implications of immobilisation and their progression in order to provide efficient medical care in the recovery period. When attempting to elucidate the mechanisms driving the metabolic responses to surgical trauma, it is of the upmost importance to understand the physiological context, and how other parameters such as nutrition, energy intake and immobilisation impact upon these responses. Although there is available literature on how the modulation of nutrition affects various physiological parameters in the perioperative period, there is very little research on the potentially augmented effects immobilisation may have on post-operative conditions; namely the pathogenesis of insulin-resistance and muscle atrophy. There is a need for further work in this field that is capable of assessing these parameters and broadening our understanding of the interactional effects these various clinical procedures and circumstances likely have on patient health and recovery.

1.6 The Inflammatory Response to Surgical Trauma

Surgery is known to induce both local and systemic inflammatory responses. These tend to originate at the site of trauma, but may also progressively manifest in tissues throughout the body. Inflammation can result from either the release of intracellular components as a direct result of tissue damage (known as sterile inflammation) or alternatively from microbial infection, which can lead to complications such as sepsis. Both inflammatory responses are known to lead to the increased release of cytokines, altered immune responses and immune cell activation, the production of ROS, and the consequent development of various ailments that negatively influence clinical outcomes. Although surgical trauma typically induces an inflammatory response via sterile inflammation [11], up to 10% of patients who undergo elective surgery develop an infection [143]. These combined can lead to a severe inflammatory state and the development of sepsis, which is strongly correlated to increased patient mortality [144].

In addition to its impacts on immune function and the development of sepsis following surgery, inflammation is known to influence muscle homeostatic regulation and signalling pathways involved in atrophy [5]. Within rodent models, several pro-inflammatory cytokines have been implicated in atrophy [145,146], with these cytokines being shown to increase MPB through increased activation of the ubiquitin-proteasome system. Notable examples of this are that the infusion of TNF-α *in vivo* has been shown to induce upregulation of E3-ligases, MAFbx and Murf-1 in rodents [147], while the interleukins-1 and -6 (IL-1, IL-6) have been demonstrated to increase myofibrillar protein breakdown [148,149]. IL-6 may be a target of particular interest, as both TNF-α and IL-1 are known to induce production of IL-6 by a variety of cell types [150]. However, although direct induction of IL-6 into rats elicited the increased release of 3-methylhistidine and tyrosine within skeletal muscle (suggestive of increased MPB), when IL-6 was introduced directly to rat skeletal muscle *in vitro* this did not affect MPB [148]. This disparity between *in vivo* and *in vitro* analyses has been additionally noted for TNF-α in other work by this author [151], as well as in other studies [152–154], and thus suggests that regulation of skeletal muscle protein metabolism by cytokines is likely mediated via other effectors within these pathways.

In humans, septic patients in ICU constitute a significant proportion of critically-ill patients, with the most common infections stemming from abdominal cavity, urinary tract and lung surgery [155]. Mortality rates in these patients is high (approx. 30-50%), with a study of septic shock in Danish ICUs showing abdominal infection to have the highest incidences of mortality [156]. However, many patients in ICU display systemic inflammatory profiles without a known site of origin (often termed, systemic inflammatory response syndrome or SIRS) as a result of surgical trauma, which is also related to poorer clinical outcomes [157]. In patients with chronic inflammation (both septic and non-septic), muscle loss occurs rapidly [158] and is an independent predictor of mortality both within clinical care [159] and during periods of recovery thereafter [160]. These patients present high levels of circulating cytokines (namely IL-6), increased production of the hepatic C-reactive protein (CRP) and modulated immune responses with particularly notable impacts on neutrophil kinetics and functions [161–165].

There are limited data that detail the effects inflammatory responses have on skeletal muscle metabolism following surgical trauma. Since early work in this field, such as that of Sir David Cuthbertson [1,4], it has been understood that trauma elicits declines in muscle mass and that the progression of this anomaly is linked to perturbations in homeostatic regulation from the inflammatory response that accompanies this condition. Yet, since recent advances in measurements of muscle protein metabolism over the last 20 years [92], our understanding of these responses is largely limited to less reliable measures of urinary nitrogen and 3-methylhistidine excretion [166–169], as well as non-labelled amino acid observations and ribosome counts [170,171]. Of the limited studies available utilising stable isotope tracers, it appears that surgery elicits immediate declines in MPS and increased rates of MPB. Studies of elective abdominal surgery have illustrated decreases in MPS of approximately 25-30% within the first 24-hours following the procedure [172–175], irrespective of total parental nutrition [173]. A further study has shown decreases in MPS of up to 50% after 3-days, also irrespective of nutritional support [176]. Furthermore, a study utilising stable isotope [15N2]urea to assess protein breakdown within skeletal muscle observed an approximate 25% increase in MPB among their surgical control group [177]. The relative importance of these measures in the regulation of skeletal muscle mass has been aptly illustrated in a study of tumour resection among colorectal cancer patients [178]. This study demonstrated that after early exacerbation of muscle atrophy following surgery (as highlighted by a decline in muscle mass of approximately 7% as quantified by DEXA), recovery of muscle mass was strongly correlated to that of normalised post-prandial MPS responses. Although perioperative nutrition strategies have been shown to provide clinical benefits [179], they do not appear to effectively combat declines in MPS or increases in MPB following surgery among these studies. There is some evidence to suggest that the use of epidural blockade prevents hyperglycaemia and elevated cortisol levels following surgery [175,180] and may minimise the development of catabolism through attenuation of MPB levels post-operation [177,181]. However, these studies have not shown epidural blockade to provide any attenuation for the declines in MPS observed following surgical trauma, which appears to largely contribute to post-surgery net catabolism. As the effects of epidural blockade are mainly attributed to attenuations in neuro-hormonal signalling and reduced sympathetic drive, it would appear that dysregulation of muscle synthetic responses is being controlled by other mechanisms following surgical trauma.

It should, however, be noted that many of these studies are limited to short sampling periods that are only reflective of one post-operative timepoint for MPS, relative to pre-operative baseline values. As such, there is great need to accurately define surgically-induced alterations in MPS across longer periods in order to comprehensively examine the impacts of surgery on muscle synthetic responses. This would likely benefit from the use of deuterium-oxide (D2O), which has been shown to precisely measure fractional synthetic rates of muscle protein across extended study periods [182], and would thus provide a more comprehensive assessment of these responses throughout the immediate periods of recovery following operative procedures.

The role of inflammation in regulating skeletal muscle mass and metabolic function during chronic inflammatory states and as a result of trauma is becoming increasingly apparent [5]. Inflammation may therefore represent the driving mechanism behind the post-operative suppressions of MPS. ICU patients have demonstrated elevated levels of the muscle cytokines, IL-6 (6.5-fold) and TNF-α (2-fold) when compared to healthy volunteers [183]. In conjunction with these increases, patients demonstrated dephosphorylation (inactivation) of MPS signalling proteins (Akt, GSK3α/β, mTOR, p70S6K and 4E-BP1). The authors additionally noted upregulation of muscle specific E3-ligases, MAFbx and Murf-1, which displayed increased levels of mRNA (4.5-fold, 2.5-fold) and protein (5-fold, 4.5-fold) respectively. This study also observed increases in mRNA and protein of 20S proteasome (5-fold, 2.5-fold) and myostatin (3-fold, 8.5-fold) in patients vs controls. This suggests inflammatory states to simultaneously downregulate MPS while promoting MPB. The Akt/FOXO signalling pathway is a likely controller of this process, and has been implicated as such in a rodent model of endotoxemia involving 24-hour infusion of lipopolysaccharide (LPS) [184]. This study demonstrated endotoxemia to produce expected increases in TNF-α and IL-6 (8.9-fold, 8.4-fold) in association with reductions in IRS-1 mRNA expression and Akt protein, while increasing dephosphorylation (activation) of FOXO1 and FOXO3 protein. These changes coincided with notable increases in muscle MAFbx (mRNA 5.5-fold, protein 2-fold), as well as PDK4 mRNA and protein expression (15-fold, 1.6-fold respectively) and a 56% reduction in pyruvate dehydrogenase activity. With similar reductions in glucose metabolism via these mechanisms being displayed in patients following major abdominal surgery [61], as well as in ICU and septic patients [183,185], cytokine-driven alterations in the regulation of the Akt/FOXO signalling pathway are a probable cause of the skeletal muscle metabolic dysregulation and catabolism observed during these inflammatory conditions. In support of this, further research conducted with animal models of endotoxemia [186,187] have illustrated *in vivo* strategies to minimise the inflammatory-mediated increase in circulating cytokines results in the attenuation of muscle atrophy and glucose dysregulation, through improved Akt/FOXO signalling and pyruvate dehydrogenase activity.

A study on the inflammatory impacts of major abdominal surgery has illustrated operative trauma to result in increased muscle cytokine levels both local and remote to the site of surgery, with elevated cytokine levels persisting in plasma for 48-hours thereafter [188]. This was characterised by increases in *rectus abdominus* (RA) as well as *vastus lateralis* (VL) mRNA levels for TNF-α (16.5-fold, 5.8-fold respectively) and IL-6 (1058-fold, 126-fold respectively). This was in addition to increased mRNA expression of FOXO1 (10.5-fold RA, 2.5-fold VL), MAFbx (11.5-fold RA, 6.4-fold VL) and PDK4 (7.8-fold RA, 4.1-fold VL). Overall, this illustrated that the inflammatory response local to the site of surgical trauma also manifested itself in a similar pattern within skeletal muscle remote to the site of surgery (albeit in a reduced capacity). With the metabolic changes observed similar to those previously described in animal models of inflammation, it seems plausible that these alterations are driven by surgically-induced inflammation. Of particular note are the drastic increases in IL-6 at both the site of surgery (RA), as well as in peripheral skeletal muscle (VL).

IL-6 has been otherwise shown to reduce myofiber size and induce metabolic dysregulation in skeletal muscle. It has been shown that introduction of IL-6 to rodents *in vivo* initiates MPB [148], with IL-6 augmented upregulation of CRP posing as an indirect mechanism of suppressing MPS signalling in human myotubes [189]. In this study of human myotubes, suppressed MPS signalling occurred in conjunction with the activation of AMPK. This has been further illustrated within both *in vitro* and *in vivo* rodent models, as well as in C2C12 myotubes [190], which have shown increased activation of AMPK in association with increases in glycogen breakdown and fat oxidation following exposure to IL-6. These findings suggest another causative link between surgical-induced cytokine release and the observed decline in skeletal muscle glycogen content, increased PDK4 expression, as well as the observed activation of FOXO-mediated proteolysis as a potential consequence of AMPK-dependent signalling [188]. IL-6 has been further implicated in the maintenance of corticosteroid responses during inflammation and infection, irrespective of CRH-ACTH-dependent signalling, suggesting this cytokine to be capable of direct interactions with the adrenal glands [191]. Although research is currently tentative, these interactions may also be involved in the disparity between pulsatile-secretion of CRH-ACTH (especially during the early stages of traumatic insult) with TNF-α, IL-6 and AMPK all being known to interact and regulate hypothalamic processes [95,192,193]. Cytokines have additionally been inferred as important activators of centrally-driven catabolic responses to chronic inflammatory conditions, such as cancer cachexia [192], further emphasising their importance as a potential link between inflammation and post-surgical catabolism.

Together, these observations strongly implicate the potent ramifications of increased cytokine release (in particular IL-6) and their role in mediating metabolic dysregulation following surgery. Although the study of major abdominal surgery by Varadhan et al. [188] effectively measured the presence of candidate inflammatory cytokines, their measures of skeletal muscle protein turnover were limited to the observed increases in proteolytic genes (FOXO1, MAFbx). Further research would benefit from assessing how elevated cytokine levels might modulate human skeletal muscle protein turnover *in vivo* in perioperative periods via the use of stable isotope measurements of MPS and MPB. Additionally, with the production of cytokines being largely attributed to various immune cell types, and neutrophils being by far the most abundant of these, measurements of neutrophil migration and activation may also be useful in ascertaining the pathogenesis of systemic inflammation following surgery.

1.7 The Impacts of Surgery on Skeletal Muscle Catabolism

Within skeletal muscle, one of the most significant alterations that occurs during the metabolic response to trauma is skeletal muscle catabolism and the accompaniment of muscle atrophy. As previously described, this occurs commonly in the 'flow' phase of the metabolic response following trauma, with increased availability of glucose and FFAs preceding this development. Muscle catabolism is a probable result of various inputs, of which the most culpable are: energy demand, disruption of muscle signalling pathways via metabolic dysregulation, inflammation and the requirements for accelerated protein turnover synonymous with muscle healing. It is likely the pathogenesis of skeletal muscle atrophy following surgical trauma during the 'flow' phase is also augmented by the consequent immobilisation of patients post-surgery, which is known to independently suppress muscle metabolism. As post-surgical loss of skeletal muscle mass is associated with complications and mortality [194,195], gaining knowledge of the mechanisms that drive these processes is important in improving clinical outcomes.

Skeletal muscle mass is maintained via the balance between muscle protein breakdown (MPB) and muscle protein synthesis (MPS); with the balance between these processes referred to as muscle protein turnover. These processes are regulated via neuro-endocrine and local regulatory signalling pathways, which are responsive to energy status, mechanical load and physiological stress. MPB within skeletal muscle occurs through several degradative pathways; the autophagal-lysosomal, the ubiquitin-proteasome, as well as the calpain and caspase systems. The activity of these pathways is often integrated, with the ubiquitin-proteasome pathway generally being attributed to be the requisite degradative pathway within skeletal muscle. Skeletal muscle synthetic responses are primarily mediated through activation of mammalian target of rapamycin complex 1 (mTORC1), which through its downstream effectors enables increased MPS transcription and translation events.

Measurements of protein turnover by mass spectrometry have traditionally utilised either whole body or tissue-specific tracer methodologies [196]. These commonly involve administering amino acids containing the stable isotopes; ^{13}C, ^{15}N or ^{2}H, across a constant 'steady-state' period or via a 'flooding' supraphysiological dose [197]. Following equilibrium of the exogenous tracer with the intracellular amino acid (AA) pools (arterial, venous, intracellular/extracellular spaces); changes in either whole body or tissue-specific protein turnover can be determined [198].

Perioperative measurements of protein turnover have typically utilised one of three methodological approaches. Arterio-venous (AV) tracer measurements, which reflect whole-body (or limb-specific) protein turnover, whereby tracer and tracee are measured in both arterial (or more commonly arterialised-venous) and venous blood. This allows for rates of disappearance to be determined from arterial blood, which provides a proxy for protein synthesis via uptake of stable isotopically-labelled amino acids into tissue, while dilution of the amino acid tracer within the venous pool by release of endogenous amino acids provides a proxy for protein breakdown. These processes are typically modelled as a two-pool stochastic system, which poses several constraints and has been suggested to in fact reflect amino acid transport opposed to protein turnover *per se* [199]. Extension of this approach to a 3-pool stochastic model is possible by further sampling the intracellular amino acid pool of the specific metabolic tissue of interest, but this approach often requires use of more than one stable isotope to successfully model both protein synthesis and protein breakdown simultaneously, while also being more clinically invasive. Irrespective, arterio-venous approaches require intravenous administration of stable isotopically-labelled amino acids and maintenance of strict physiological conditions to ensure accurate measurements of protein turnover, and therefore are typically employed acutely in clinical settings across the span of several hours.

End-product stable isotope techniques enable amino acid tracers to be employed either intravenously or orally and can be applied for temporal measurements of whole-body protein turnover. Initially developed for minimally-invasive measurement of protein kinetics in paediatric research, these techniques assess the incorporation of stable isotopes into the end products of protein metabolism present in the urine, specifically ammonia and urea [200]. End-product methodology is founded on the principle that the flux or dilution of tracer in urinary end products is reflective of whole-body protein breakdown, with it then being possible to model rates of protein synthesis through the combined knowledge of breakdown rates and tracer dose administered, which again represents a two-pool stochastic model.

These methods are in contrast with direct-incorporation measures, currently considered the ‘gold’ standard for the assessment of protein turnover within skeletal muscle [201]. As tracer enters the intracellular pool and is incorporated into proteins within skeletal muscle, through serial tissue biopsies it is possible to directly determine the incorporation of tracer into skeletal muscle as proteins are synthesised or broken down across time. For measurements of protein synthesis this conforms to a precursor: product model, where isotopic enrichment of the precursor pool (aminoacyl-tRNA being the true precursor pool in skeletal muscle) must be factored into calculations of protein turnover.

While advancements have been made in the application of direct-incorporation methods in recent years, their implementation within studies assessing the impacts of surgical procedures on skeletal muscle metabolism have lagged. With a lack of uniform tracer methodologies being applied across decades of surgical research, as well as the substantial technological advancements in mass spectrometry instrumentation across the last 10-15 years, a comprehensive characterisation of protein kinetics in the surgical patient has yet to be achieved [202]. Furthermore, interpretation of randomised controlled trials assessing the impacts of perioperative care strategies aimed at ameliorating skeletal muscle wasting, as quantified by stable isotope mass spectrometry analysis of amino acid metabolism, are confounded by the variability in methods employed across the span of several decades [196]. This necessitates a synthesis of previous studies and methodologies, as well as future studies employing up-to-date direct-incorporation stable isotope techniques, in order to characterise the underlying kinetics driving skeletal muscle atrophy following surgical insult.

References:

1. Cuthbertson, D. P. OBSERVATIONS ON THE DISTURBANCE OF METABOLISM PRODUCED BY INJURY TO THE LIMBS. *QJM Int. J. Med.* **1**, 233–246 (1932).
2. Cuthbertson, D. P. The Metabolic Response to Injury and other Related Explorations in the Field of Protein Metabolism: An Autobiographical Account. *Scott. Med. J.* **27**, 158–171 (1982).
3. Moore, Francis. D. Metabolic care of the surgical patient. By Francis D. Moore, M.D., Moseley Professor of Surgery, Harvard Medical School. 10¾ × 7¾ in. Pp. 1011 + x, with 14 2illustrations. 1959. Philadelphia and London: W. B. Saunders Co. 140s. *BJS Br. J. Surg.* **47**, 455–455 (1960).
4. Cuthbertson, D. P. The disturbance of metabolism produced by bony and non-bony injury, with notes on certain abnormal conditions of bone. *Biochem. J.* **24**, 1244–1263 (1930).
5. Crossland, H., Skirrow, S., Puthucheary, Z. A., Constantin-Teodosiu, D. & Greenhaff, P. L. The impact of immobilisation and inflammation on the regulation of muscle mass and insulin resistance: different routes to similar end-points. *J. Physiol.* **597**, 1259–1270 (2019).
6. Campbell, R. M., Sharp, G., Boyne, A. W. & Cuthbertson, D. P. Cortisone and the metabolic response to injury. *Br. J. Exp. Pathol.* **35**, 566–576 (1954).
7. Granger, D. N. & Senchenkova, E. *Historical Perspectives*. (Morgan & Claypool Life Sciences, 2010).

8. Hunter, J. A treatise on the blood, inflammation, and gun-shot wounds. 1794. *Clin. Orthop.* **458**, 27–34 (2007).

9. Miller, T., Gibbison, B. & Russell, G. M. Hypothalamic–pituitary–adrenal function during health, major surgery, and critical illness. *BJA Educ.* **17**, 16–21 (2017).

10. Prete, A. *et al.* The cortisol stress response induced by surgery: A systematic review and meta-analysis. *Clin. Endocrinol. (Oxf.)* **89**, 554–567 (2018).

11. Manou-Stathopoulou, V., Korbonits, M. & Ackland, G. L. Redefining the perioperative stress response: a narrative review. *Br. J. Anaesth.* **123**, 570–583 (2019).

12. Goldmann, A. *et al.* Combined vs. Isoflurane/Fentanyl anesthesia for major abdominal surgery: Effects on hormones and hemodynamics. *Med. Sci. Monit. Int. Med. J. Exp. Clin. Res.* **14**, CR445-52 (2008).

13. Furuya, K., Shimizu, R., Hirabayashi, Y., Ishii, R. & Fukuda, H. Stress hormone responses to major intra-abdominal surgery during and immediately after sevoflurane-nitrous oxide anaesthesia in elderly patients. *Can. J. Anaesth. J. Can. Anesth.* **40**, 435–439 (1993).

14. Haas, M. & Glick, S. M. Radioimmunoassayable plasma vasopressin associated with surgery. *Arch. Surg. Chic. Ill 1960* **113**, 597–600 (1978).

15. Burton, D., Nicholson, G. & Hall, G. Endocrine and metabolic response to surgery. *Contin. Educ. Anaesth. Crit. Care Pain* **4**, 144–147 (2004).

16. Gibbison, B. *et al.* Dynamic pituitary-adrenal interactions in response to Cardiac surgery. *Crit. Care Med.* **43**, 791–800 (2015).

17. Lewis, J. G., Bagley, C. J., Elder, P. A., Bachmann, A. W. & Torpy, D. J. Plasma free cortisol fraction reflects levels of functioning corticosteroid-binding globulin. *Clin. Chim. Acta Int. J. Clin. Chem.* **359**, 189–194 (2005).
18. Henley, D. E. & Lightman, S. L. New insights into corticosteroid-binding globulin and glucocorticoid delivery. *Neuroscience* **180**, 1–8 (2011).
19. Hammond, G. L., Smith, C. L., Paterson, N. A. & Sibbald, W. J. A role for corticosteroid-binding globulin in delivery of cortisol to activated neutrophils. *J. Clin. Endocrinol. Metab.* **71**, 34–39 (1990).
20. Ruhs, S., Nolze, A., Hübschmann, R. & Grossmann, C. 30 YEARS OF THE MINERALOCORTICOID RECEPTOR: Nongenomic effects via the mineralocorticoid receptor. *J. Endocrinol.* **234**, T107–T124 (2017).
21. Vandevyver, S., Dejager, L. & Libert, C. Comprehensive overview of the structure and regulation of the glucocorticoid receptor. *Endocr. Rev.* **35**, 671–693 (2014).
22. Tasker, J. G., Di, S. & Malcher-Lopes, R. Minireview: rapid glucocorticoid signaling via membrane-associated receptors. *Endocrinology* **147**, 5549–5556 (2006).
23. Okamoto, K. *et al.* Redox-dependent regulation of nuclear import of the glucocorticoid receptor. *J. Biol. Chem.* **274**, 10363–10371 (1999).
24. Funder, J. W. Mineralocorticoid receptors: distribution and activation. *Heart Fail. Rev.* **10**, 15–22 (2005).
25. Nagase, M. *et al.* Oxidative stress causes mineralocorticoid receptor activation in rat cardiomyocytes: role of small GTPase Rac1. *Hypertens. Dallas Tex 1979* **59**, 500–506 (2012).

26. Wang, J. *et al.* GPR48 increases mineralocorticoid receptor gene expression. *J. Am. Soc. Nephrol. JASN* **23**, 281–293 (2012).

27. Madsen, S. N., Fog-Møller, F., Christiansen, C., Vester-Andersen, T. & Engquist, A. Cyclic AMP, adrenaline and noradrenaline in plasma during surgery. *BJS Br. J. Surg.* **65**, 191–193 (1978).

28. Chiu, R. C.-J. & McArdle, H. A. Levels of plasma cyclic AMP and insulin in cardiac surgery. *J. Thorac. Cardiovasc. Surg.* **75**, 286–289 (1978).

29. Madsen, S. N., Brandt, MR., Engquist, A., Badawi, I. & Khelet, H. Inhibition of plasma cyclic AMP, glucose and cortisol response to surgery by epidural analgesia. - Abstract - Europe PMC. https://europepmc.org/article/med/201331 (1977).

30. Philipsen, E. K. *et al.* The relationship between some beta-adrenergic mediated responses and plasma concentrations of adrenaline and cyclic AMP in man. *Acta Endocrinol. (Copenh.)* **122**, 115–120 (1990).

31. Cocks, R. A., Rainer, T. H., Chan, T. Y., Maycock, P. F. & Lam, N. Y. Increased plasma free cyclic-AMP levels following major trauma and their relevance to the immune response. *Resuscitation* **45**, 105–109 (2000).

32. Ronchetti, S., Ricci, E., Migliorati, G., Gentili, M. & Riccardi, C. How Glucocorticoids Affect the Neutrophil Life. *Int. J. Mol. Sci.* **19**, (2018).

33. Peeters, B., Boonen, E., Langouche, L. & Van den Berghe, G. The HPA axis response to critical illness: New study results with diagnostic and therapeutic implications. *Mol. Cell. Endocrinol.* **408**, 235–240 (2015).

34. Van den Berghe, G., Boonen, E. & Walker, B. R. Reduced cortisol metabolism during critical illness. *N. Engl. J. Med.* **369**, 481 (2013).

35. Vogeser, M., Felbinger, T. W., Röll, W. & Jacob, K. Cortisol metabolism in the postoperative period after cardiac surgery. *Exp. Clin. Endocrinol. Diabetes Off. J. Ger. Soc. Endocrinol. Ger. Diabetes Assoc.* **107**, 539–546 (1999).

36. Vogeser, M., Groetzner, J., Küpper, C. & Briegel, J. The serum cortisol:cortisone ratio in the postoperative acute-phase response. *Horm. Res.* **59**, 293–296 (2003).

37. Jang, C., Obeyesekere, V. R., Alford, F. P. & Inder, W. J. Skeletal muscle 11beta hydroxysteroid dehydrogenase type 1 activity is upregulated following elective abdominal surgery. *Eur. J. Endocrinol.* **160**, 249–255 (2009).

38. Rm, de G., Aj, R. & S, H. Glucocorticoid Hormones and Energy Homeostasis. *Hormone molecular biology and clinical investigation* https://pubmed.ncbi.nlm.nih.gov/25390020/ (2014) doi:10.1515/hmbci-2014-0021.

39. Sp, W., T, P., A, P. & Rs, H. Glucocorticoid-induced Insulin Resistance: Dexamethasone Inhibits the Activation of Glucose Transport in Rat Skeletal Muscle by Both Insulin- And Non-Insulin-Related Stimuli. *Diabetes* https://pubmed.ncbi.nlm.nih.gov/7698514/ (1995) doi:10.2337/diab.44.4.441.

40. Sp, W., Cm, W., A, P. & Sw, C. Dexamethasone Inhibits Insulin-Stimulated Recruitment of GLUT4 to the Cell Surface in Rat Skeletal Muscle. *Metabolism: clinical and experimental* https://pubmed.ncbi.nlm.nih.gov/9440469/ (1998) doi:10.1016/s0026-0495(98)90184-6.

41. Kamba, A. *et al.* Association between Higher Serum Cortisol Levels and Decreased Insulin Secretion in a General Population. *PLOS ONE* **11**, e0166077 (2016).

42. Duncan, A. E. Hyperglycemia and Perioperative Glucose Management. *Curr. Pharm. Des.* **18**, 6195–6203 (2012).

43. S, K. *et al.* Importance of Perioperative Glycemic Control in General Surgery: A Report From the Surgical Care and Outcomes Assessment Program. *Annals of surgery* https://pubmed.ncbi.nlm.nih.gov/23235393/?dopt=Abstract (2013) doi:10.1097/SLA.0b013e31827b6bbc.

44. Ae, D. *et al.* Role of Intraoperative and Postoperative Blood Glucose Concentrations in Predicting Outcomes After Cardiac Surgery. *Anesthesiology* https://pubmed.ncbi.nlm.nih.gov/20216389/ (2010) doi:10.1097/ALN.0b013e3181d3d4b4.

45. Se, C., D, H., K, M., P, P. & Hc, G. Stress Hyperglycemia and Prognosis of Stroke in Nondiabetic and Diabetic Patients: A Systematic Overview. *Stroke* https://pubmed.ncbi.nlm.nih.gov/11588337/ (2001) doi:10.1161/hs1001.096194.

46. Se, C., D, H., K, M. & Hc, G. Stress Hyperglycaemia and Increased Risk of Death After Myocardial Infarction in Patients With and Without Diabetes: A Systematic Overview. *Lancet (London, England)* https://pubmed.ncbi.nlm.nih.gov/10711923/ (2000) doi:10.1016/S0140-6736(99)08415-9.

47. Aj, R. *et al.* Insulin Infusion Improves Neutrophil Function in Diabetic Cardiac Surgery Patients. *Anesthesia and analgesia* https://pubmed.ncbi.nlm.nih.gov/10320160/ (1999) doi:10.1097/00000539-199905000-00008.

48. Aj, R. *et al.* Insulin Increases Neutrophil Count and Phagocytic Capacity After Cardiac Surgery. *Anesthesia and analgesia*

https://pubmed.ncbi.nlm.nih.gov/11973171/ (2002) doi:10.1097/00000539-200205000-00010.

49. Wang, Y. *et al.* Postoperative tight glycemic control significantly reduces postoperative infection rates in patients undergoing surgery: a meta-analysis. *BMC Endocr. Disord.* **18**, 42 (2018).
50. Sy, P., Jh, B. & Ys, C. Cortisone Induces Insulin Resistance in C2C12 Myotubes Through Activation of 11beta-hydroxysteroid Dehydrogenase 1 and Autocrinal Regulation. *Cell biochemistry and function* https://pubmed.ncbi.nlm.nih.gov/24122936/ (2014) doi:10.1002/cbf.3008.
51. Sa, M. *et al.* 11beta-hydroxysteroid Dehydrogenase Type 1 Regulates Glucocorticoid-Induced Insulin Resistance in Skeletal Muscle. *Diabetes* https://pubmed.ncbi.nlm.nih.gov/19675138/ (2009) doi:10.2337/db09-0525.
52. Macfarlane, D. P., Forbes, S. & Walker, B. R. Glucocorticoids and fatty acid metabolism in humans: fuelling fat redistribution in the metabolic syndrome. *J. Endocrinol.* **197**, 189–204 (2008).
53. Salehzadeh, F. *et al.* Glucocorticoid-mediated effects on metabolism are reversed by targeting 11 beta hydroxysteroid dehydrogenase type 1 in human skeletal muscle. *Diabetes Metab. Res. Rev.* **25**, 250–258 (2009).
54. Rm, W. *et al.* Pyruvate Dehydrogenase kinase-4 Structures Reveal a Metastable Open Conformation Fostering Robust Core-Free Basal Activity. *The Journal of biological chemistry* https://pubmed.ncbi.nlm.nih.gov/18658136/ (2008) doi:10.1074/jbc.M802249200.
55. M, M., Km, P., Ra, H., C, B. & M, P. Insulin Downregulates Pyruvate Dehydrogenase Kinase (PDK) mRNA: Potential Mechanism Contributing to Increased Lipid Oxidation in Insulin-Resistant Subjects. *Molecular genetics and*

metabolism https://pubmed.ncbi.nlm.nih.gov/9787110/ (1998) doi:10.1006/mgme.1998.2748.

56. Kim, Y. I., Lee, F. N., Choi, W. S., Lee, S. & Youn, J. H. Insulin regulation of skeletal muscle PDK4 mRNA expression is impaired in acute insulin-resistant states. *Diabetes* **55**, 2311–2317 (2006).
57. Hanada, M., Feng, J. & Hemmings, B. A. Structure, regulation and function of PKB/AKT--a major therapeutic target. *Biochim. Biophys. Acta* **1697**, 3–16 (2004).
58. Abdul-Ghani, M. A. & DeFronzo, R. A. Pathogenesis of Insulin Resistance in Skeletal Muscle. *J. Biomed. Biotechnol.* **2010**, (2010).
59. Petersen, K. F. & Shulman, G. I. Cellular mechanism of insulin resistance in skeletal muscle. *J. R. Soc. Med.* **95**, 8–13 (2002).
60. Mays, E. T. The effect of surgical stress on plasma free fatty acids. *J. Surg. Res.* **10**, 315–319 (1970).
61. Varadhan, K. *et al.* PP015-SUN SURGERY MEDIATED INCREASE IN CIRCULATING FREE FATTY ACIDS MAY BE ASSOCIATED WITH INHIBITION OF MUSCLE GLUCOSE METABOLISM AND THE DEVELOPMENT OF POSTOPERATIVE HYPERGLYCEMIA. *Clin. Nutr. Suppl.* **7**, 31 (2012).
62. Joly-Amado, A. *et al.* The hypothalamic arcuate nucleus and the control of peripheral substrates. *Best Pract. Res. Clin. Endocrinol. Metab.* **28**, 725–737 (2014).
63. Ollmann, M. M. *et al.* Antagonism of central melanocortin receptors in vitro and in vivo by agouti-related protein. *Science* **278**, 135–138 (1997).

64. Shutter, J. R. *et al.* Hypothalamic expression of ART, a novel gene related to agouti, is up-regulated in obese and diabetic mutant mice. *Genes Dev.* **11**, 593–602 (1997).

65. Nogueiras, R. *et al.* The central melanocortin system directly controls peripheral lipid metabolism. *J. Clin. Invest.* **117**, 3475–3488 (2007).

66. Nogueiras, R., López, M. & Diéguez, C. Regulation of lipid metabolism by energy availability: a role for the central nervous system. *Obes. Rev. Off. J. Int. Assoc. Study Obes.* **11**, 185–201 (2010).

67. Joly-Amado, A. *et al.* Hypothalamic AgRP-neurons control peripheral substrate utilization and nutrient partitioning. *EMBO J.* **31**, 4276–4288 (2012).

68. Varela, L. & Horvath, T. L. AgRP neurons: a switch between peripheral carbohydrate and lipid utilization. *EMBO J.* **31**, 4252–4254 (2012).

69. Baker, J. S., McCormick, M. C. & Robergs, R. A. Interaction among Skeletal Muscle Metabolic Energy Systems during Intense Exercise. *J. Nutr. Metab.* **2010**, (2010).

70. Garcia, D. & Shaw, R. J. AMPK: mechanisms of cellular energy sensing and restoration of metabolic balance. *Mol. Cell* **66**, 789–800 (2017).

71. Hoppe, S. *et al.* AMP-activated protein kinase adapts rRNA synthesis to cellular energy supply. *Proc. Natl. Acad. Sci. U. S. A.* **106**, 17781–17786 (2009).

72. Leprivier, G. *et al.* The eEF2 kinase confers resistance to nutrient deprivation by blocking translation elongation. *Cell* **153**, 1064–1079 (2013).

73. Zhang, C.-S. & Lin, S.-C. AMPK Promotes Autophagy by Facilitating Mitochondrial Fission. *Cell Metab.* **23**, 399–401 (2016).

74. Liu, J. *et al.* Depressed mitochondrial biogenesis and dynamic remodeling in mouse tibialis anterior and gastrocnemius induced by 4-week hindlimb unloading. *IUBMB Life* **64**, 901–910 (2012).

75. Egawa, T. *et al.* Involvement of AMPK in regulating slow-twitch muscle atrophy during hindlimb unloading in mice. *Am. J. Physiol.-Endocrinol. Metab.* **309**, E651–E662 (2015).

76. Romanello, V. *et al.* Mitochondrial fission and remodelling contributes to muscle atrophy. *EMBO J.* **29**, 1774–1785 (2010).

77. Tian, W. *et al.* Phosphorylation of ULK1 by AMPK regulates translocation of ULK1 to mitochondria and mitophagy. *FEBS Lett.* **589**, 1847–1854 (2015).

78. Powers, S. K., Wiggs, M. P., Duarte, J. A., Zergeroglu, A. M. & Demirel, H. A. Mitochondrial signaling contributes to disuse muscle atrophy. *Am. J. Physiol. Endocrinol. Metab.* **303**, E31-39 (2012).

79. Nygren, J. The metabolic effects of fasting and surgery. *Best Pract. Res. Clin. Anaesthesiol.* **20**, 429–438 (2006).

80. Svanfeldt, M., Thorell, A., Brismar, K., Nygren, J. & Ljungqvist, O. Effects of 3 days of ‘postoperative’ low caloric feeding with or without bed rest on insulin sensitivity in healthy subjects. *Clin. Nutr. Edinb. Scotl.* **22**, 31–38 (2003).

81. Schricker, T. *et al.* Anticatabolic effects of avoiding preoperative fasting by intravenous hypocaloric nutrition: a randomized clinical trial. *Ann. Surg.* **248**, 1051–1059 (2008).

82. Neuhäuser, M. *et al.* Urinary excretion of 3-methylhistidine as an index of muscle protein catabolism in postoperative trauma: the effect of parenteral nutrition. - PubMed - NCBI. *PubMed* https://www.ncbi.nlm.nih.gov/pubmed/6779092 (1980).

83. Yuill, K. A., Richardson, R. A., Davidson, H. I. M., Garden, O. J. & Parks, R. W. The administration of an oral carbohydrate-containing fluid prior to major elective upper-gastrointestinal surgery preserves skeletal muscle mass postoperatively—a randomised clinical trial. *Clin. Nutr.* **24**, 32–37 (2005).

84. Svanfeldt, M. *et al.* Randomized clinical trial of the effect of preoperative oral carbohydrate treatment on postoperative whole-body protein and glucose kinetics. *Br. J. Surg.* **94**, 1342–1350 (2007).

85. Crowe, P. J., Dennison, A. & Royle, G. T. The effect of pre-operative glucose loading on postoperative nitrogen metabolism. *Br. J. Surg.* **71**, 635–637 (1984).

86. Perrone, F. *et al.* Effects of preoperative feeding with a whey protein plus carbohydrate drink on the acute phase response and insulin resistance. A randomized trial. *Nutr. J.* **10**, 66 (2011).

87. Ljungqvist, O., Thorell, A., Gutniak, M., Häggmark, T. & Efendic, S. Glucose infusion instead of preoperative fasting reduces postoperative insulin resistance. *J. Am. Coll. Surg.* **178**, 329–336 (1994).

88. J, N. *et al.* Preoperative Oral Carbohydrate Administration Reduces Postoperative Insulin Resistance. *Clinical nutrition (Edinburgh, Scotland)* https://pubmed.ncbi.nlm.nih.gov/10205319/?dopt=Abstract (1998) doi:10.1016/s0261-5614(98)80307-5.

89. Dock-Nascimento, D. B. *et al.* Evaluation of the effects of a preoperative 2-hour fast with maltodextrine and glutamine on insulin resistance, acute-phase response, nitrogen balance, and serum glutathione after laparoscopic cholecystectomy: a controlled randomized trial. *JPEN J. Parenter. Enteral Nutr.* **36**, 43–52 (2012).

90. Faria, M. S. M. *et al.* Preoperative fasting of 2 hours minimizes insulin resistance and organic response to trauma after video-cholecystectomy: a randomized, controlled, clinical trial. *World J. Surg.* **33**, 1158–1164 (2009).

91. Wang, Z. G., Wang, Q., Wang, W. J. & Qin, H. L. Randomized clinical trial to compare the effects of preoperative oral carbohydrate versus placebo on insulin resistance after colorectal surgery. *Br. J. Surg.* **97**, 317–327 (2010).

92. Brook, M. S. & Wilkinson, D. J. Contemporary stable isotope tracer approaches: Insights into skeletal muscle metabolism in health and disease. *Exp. Physiol.* (2020) doi:10.1113/EP087492.

93. Hawley, S. A. *et al.* Use of cells expressing gamma subunit variants to identify diverse mechanisms of AMPK activation. *Cell Metab.* **11**, 554–565 (2010).

94. Hinchy, E. C. *et al.* Mitochondria-derived ROS activate AMP-activated protein kinase (AMPK) indirectly. *J. Biol. Chem.* **293**, 17208–17217 (2018).

95. Watterson, K. R. *et al.* Anorexigenic and Orexigenic Hormone Modulation of Mammalian Target of Rapamycin Complex 1 Activity and the Regulation of Hypothalamic Agouti-Related Protein mRNA Expression. *Neurosignals* **21**, 28–41 (2012).

96. Booth, F. W. & Seider, M. J. Early change in skeletal muscle protein synthesis after limb immobilization of rats. *J. Appl. Physiol.* **47**, 974–977 (1979).

97. Kobayashi, H., Kato, H., Hirabayashi, Y., Murakami, H. & Suzuki, H. Modulations of muscle protein metabolism by branched-chain amino acids in normal and muscle-atrophying rats. *J. Nutr.* **136**, 234S–6S (2006).

98. Krawiec, B. J., Frost, R. A., Vary, T. C., Jefferson, L. S. & Lang, C. H. Hindlimb casting decreases muscle mass in part by proteasome-dependent

proteolysis but independent of protein synthesis. *Am. J. Physiol. Endocrinol. Metab.* **289**, E969-980 (2005).

99. Phillips, S. M., Glover, E. I. & Rennie, M. J. Alterations of protein turnover underlying disuse atrophy in human skeletal muscle. *J. Appl. Physiol. Bethesda Md 1985* **107**, 645–654 (2009).

100. Glover, E. I. *et al.* Immobilization induces anabolic resistance in human myofibrillar protein synthesis with low and high dose amino acid infusion. *J. Physiol.* **586**, 6049–6061 (2008).

101. de Boer, M. D. *et al.* The temporal responses of protein synthesis, gene expression and cell signalling in human quadriceps muscle and patellar tendon to disuse. *J. Physiol.* **585**, 241–251 (2007).

102. Ferrando, A. A., Lane, H. W., Stuart, C. A., Davis-Street, J. & Wolfe, R. R. Prolonged bed rest decreases skeletal muscle and whole body protein synthesis. *Am. J. Physiol.-Endocrinol. Metab.* **270**, E627–E633 (1996).

103. Ferrando, A. A., Tipton, K. D., Bamman, M. M. & Wolfe, R. R. Resistance exercise maintains skeletal muscle protein synthesis during bed rest. *J. Appl. Physiol. Bethesda Md 1985* **82**, 807–810 (1997).

104. Kortebein, P., Ferrando, A., Lombeida, J., Wolfe, R. & Evans, W. J. Effect of 10 days of bed rest on skeletal muscle in healthy older adults. *JAMA* **297**, 1772–1774 (2007).

105. Symons, T. B., Sheffield-Moore, M., Chinkes, D. L., Ferrando, A. A. & Paddon-Jones, D. Artificial gravity maintains skeletal muscle protein synthesis during 21 days of simulated microgravity. *J. Appl. Physiol.* **107**, 34–38 (2009).

106. Jones, S. W. *et al.* Disuse atrophy and exercise rehabilitation in humans profoundly affects the expression of genes associated with the regulation of skeletal muscle mass. *FASEB J.* **18**, 1025–1027 (2004).

107. Urso, M. L., Scrimgeour, A. G., Chen, Y.-W., Thompson, P. D. & Clarkson, P. M. Analysis of human skeletal muscle after 48 h immobilization reveals alterations in mRNA and protein for extracellular matrix components. *J. Appl. Physiol. Bethesda Md 1985* **101**, 1136–1148 (2006).

108. Wall, B. T. *et al.* Substantial skeletal muscle loss occurs during only 5 days of disuse. *Acta Physiol.* **210**, 600–611 (2014).

109. Gustafsson, T. *et al.* Effects of 3 days unloading on molecular regulators of muscle size in humans. *J. Appl. Physiol. Bethesda Md 1985* **109**, 721–727 (2010).

110. Reich, K. A., Chen, Y.-W., Thompson, P. D., Hoffman, E. P. & Clarkson, P. M. Forty-eight hours of unloading and 24 h of reloading lead to changes in global gene expression patterns related to ubiquitination and oxidative stress in humans. *J. Appl. Physiol. Bethesda Md 1985* **109**, 1404–1415 (2010).

111. Glover, E. I., Yasuda, N., Tarnopolsky, M. A., Abadi, A. & Phillips, S. M. Little change in markers of protein breakdown and oxidative stress in humans in immobilization-induced skeletal muscle atrophy. *Appl. Physiol. Nutr. Metab. Physiol. Appl. Nutr. Metab.* **35**, 125–133 (2010).

112. Greenhaff, P. L. *et al.* Disassociation between the effects of amino acids and insulin on signaling, ubiquitin ligases, and protein turnover in human muscle. *Am. J. Physiol. Endocrinol. Metab.* **295**, E595-604 (2008).

113. Murton, A. J., Constantin, D. & Greenhaff, P. L. The involvement of the ubiquitin proteasome system in human skeletal muscle remodelling and atrophy. *Biochim. Biophys. Acta* **1782**, 730–743 (2008).

114. Tesch, P. A., von Walden, F., Gustafsson, T., Linnehan, R. M. & Trappe, T. A. Skeletal muscle proteolysis in response to short-term unloading in humans. *J. Appl. Physiol. Bethesda Md 1985* **105**, 902–906 (2008).

115. Vary, T. C. & Kimball, S. R. Sepsis-induced changes in protein synthesis: differential effects on fast- and slow-twitch muscles. *Am. J. Physiol.* **262**, C1513-1519 (1992).

116. Vary, T. C., Jurasinski, C. V., Karinch, A. M. & Kimball, S. R. Regulation of eukaryotic initiation factor-2 expression during sepsis. *Am. J. Physiol.* **266**, E193-201 (1994).

117. Lang, C. H. & Frost, R. A. Sepsis-induced suppression of skeletal muscle translation initiation mediated by tumor necrosis factor alpha. *Metabolism.* **56**, 49–57 (2007).

118. Atherton, P. J. *et al.* Selective activation of AMPK-PGC-1alpha or PKB-TSC2-mTOR signaling can explain specific adaptive responses to endurance or resistance training-like electrical muscle stimulation. *FASEB J. Off. Publ. Fed. Am. Soc. Exp. Biol.* **19**, 786–788 (2005).

119. Bodine, S. C. *et al.* Akt/mTOR pathway is a crucial regulator of skeletal muscle hypertrophy and can prevent muscle atrophy in vivo. *Nat. Cell Biol.* **3**, 1014–1019 (2001).

120. Dirks, M. L. *et al.* One Week of Bed Rest Leads to Substantial Muscle Atrophy and Induces Whole-Body Insulin Resistance in the Absence of Skeletal Muscle Lipid Accumulation. *Diabetes* **65**, 2862–2875 (2016).

121. Sonne, M. P. *et al.* Effect of 10 days of bedrest on metabolic and vascular insulin action: a study in individuals at risk for type 2 diabetes. *J. Appl. Physiol. Bethesda Md 1985* **108**, 830–837 (2010).
122. Smorawiński, J. *et al.* Effects of three-day bed rest on metabolic, hormonal and circulatory responses to an oral glucose load in endurance or strength trained athletes and untrained subjects. *J. Physiol. Pharmacol. Off. J. Pol. Physiol. Soc.* **51**, 279–289 (2000).
123. Olsen, R. H., Krogh-Madsen, R., Thomsen, C., Booth, F. W. & Pedersen, B. K. Metabolic responses to reduced daily steps in healthy nonexercising men. *JAMA* **299**, 1261–1263 (2008).
124. Krogh-Madsen, R. *et al.* A 2-wk reduction of ambulatory activity attenuates peripheral insulin sensitivity. *J. Appl. Physiol. Bethesda Md 1985* **108**, 1034–1040 (2010).
125. Hirose, M., Kaneki, M., Sugita, H., Yasuhara, S. & Martyn, J. A. Immobilization depresses insulin signaling in skeletal muscle. *Am. J. Physiol. Endocrinol. Metab.* **279**, E1235-1241 (2000).
126. Kiilerich, K. *et al.* Exercise-induced pyruvate dehydrogenase activation is not affected by 7 days of bed rest. *J. Appl. Physiol. Bethesda Md 1985* **111**, 751–757 (2011).
127. Mortensen, B. *et al.* Physical inactivity affects skeletal muscle insulin signaling in a birth weight-dependent manner. *J. Diabetes Complications* **28**, 71–78 (2014).
128. Tabata, I. *et al.* Resistance training affects GLUT-4 content in skeletal muscle of humans after 19 days of head-down bed rest. *J. Appl. Physiol. Bethesda Md 1985* **86**, 909–914 (1999).

129. Op ’t Eijnde, B., Ursø, B., Richter, E. A., Greenhaff, P. L. & Hespel, P. Effect of oral creatine supplementation on human muscle GLUT4 protein content after immobilization. *Diabetes* **50**, 18–23 (2001).

130. Biensø, R. S. *et al.* GLUT4 and Glycogen Synthase Are Key Players in Bed Rest–Induced Insulin Resistance. *Diabetes* **61**, 1090–1099 (2012).

131. Ringholm, S. *et al.* Bed rest reduces metabolic protein content and abolishes exercise-induced mRNA responses in human skeletal muscle. *Am. J. Physiol. Endocrinol. Metab.* **301**, E649-658 (2011).

132. Demangel, R. *et al.* Early structural and functional signature of 3-day human skeletal muscle disuse using the dry immersion model. *J. Physiol.* **595**, 4301–4315 (2017).

133. Pagano, A. F. *et al.* Short-term disuse promotes fatty acid infiltration into skeletal muscle. *J. Cachexia Sarcopenia Muscle* **9**, 335–347 (2018).

134. Manini, T. M. *et al.* Reduced physical activity increases intermuscular adipose tissue in healthy young adults. *Am. J. Clin. Nutr.* **85**, 377–384 (2007).

135. Bergouignan, A. *et al.* Effect of Physical Inactivity on the Oxidation of Saturated and Monounsaturated Dietary Fatty Acids: Results of a Randomized Trial. *PLoS Clin. Trials* **1**, (2006).

136. Ritz, P. *et al.* Energy and substrate metabolism during a 42-day bed-rest in a head-down tilt position in humans. *Eur. J. Appl. Physiol.* **78**, 308–314 (1998).

137. Blanc, S. *et al.* Fuel homeostasis during physical inactivity induced by bed rest. *J. Clin. Endocrinol. Metab.* **85**, 2223–2233 (2000).

138. Bajaj, M. *et al.* Sustained reduction in plasma free fatty acid concentration improves insulin action without altering plasma adipocytokine levels in subjects

with strong family history of type 2 diabetes. *J. Clin. Endocrinol. Metab.* **89**, 4649–4655 (2004).

139. Abadi, A. *et al.* Limb Immobilization Induces a Coordinate Down-Regulation of Mitochondrial and Other Metabolic Pathways in Men and Women. *PLoS ONE* **4**, (2009).
140. Romanello, V. & Sandri, M. Mitochondrial Quality Control and Muscle Mass Maintenance. *Front. Physiol.* **6**, (2016).
141. Gram, M. *et al.* Two weeks of one-leg immobilization decreases skeletal muscle respiratory capacity equally in young and elderly men. *Exp. Gerontol.* **58**, 269–278 (2014).
142. Leermakers, P. A. *et al.* Skeletal muscle unloading results in increased mitophagy and decreased mitochondrial biogenesis regulation. *Muscle Nerve* **60**, 769–778 (2019).
143. Torrance, H. D. T., Pearse, R. M. & O'Dwyer, M. J. Does major surgery induce immune suppression and increase the risk of postoperative infection? *Curr. Opin. Anaesthesiol.* **29**, 376–383 (2016).
144. Polat, G., Ugan, R. A., Cadirci, E. & Halici, Z. Sepsis and Septic Shock: Current Treatment Strategies and New Approaches. *Eurasian J. Med.* **49**, 53–58 (2017).
145. García-Martínez, C., López-Soriano, F. J. & Argilés, J. M. Acute treatment with tumour necrosis factor-alpha induces changes in protein metabolism in rat skeletal muscle. *Mol. Cell. Biochem.* **125**, 11–18 (1993).
146. Haddad, F., Zaldivar, F., Cooper, D. M. & Adams, G. R. IL-6-induced skeletal muscle atrophy. *J. Appl. Physiol. Bethesda Md 1985* **98**, 911–917 (2005).

147. Frost, R. A., Nystrom, G. J., Jefferson, L. S. & Lang, C. H. Hormone, cytokine, and nutritional regulation of sepsis-induced increases in atrogin-1 and MuRF1 in skeletal muscle. *Am. J. Physiol. Endocrinol. Metab.* **292**, E501-512 (2007).

148. Goodman, M. N. Interleukin-6 induces skeletal muscle protein breakdown in rats. *Proc. Soc. Exp. Biol. Med. Soc. Exp. Biol. Med. N. Y. N* **205**, 182–185 (1994).

149. Zamir, O., Hasselgren, P. O., von Allmen, D. & Fischer, J. E. The effect of interleukin-1 alpha and the glucocorticoid receptor blocker RU 38486 on total and myofibrillar protein breakdown in skeletal muscle. *J. Surg. Res.* **50**, 579–583 (1991).

150. Akira, S., Hirano, T., Taga, T. & Kishimoto, T. Biology of multifunctional cytokines: IL 6 and related molecules (IL 1 and TNF). *FASEB J. Off. Publ. Fed. Am. Soc. Exp. Biol.* **4**, 2860–2867 (1990).

151. Goodman, M. N. Tumor necrosis factor induces skeletal muscle protein breakdown in rats. *Am. J. Physiol.* **260**, E727-730 (1991).

152. Kettelhut, I. C. & Goldberg, A. L. Tumor necrosis factor can induce fever in rats without activating protein breakdown in muscle or lipolysis in adipose tissue. *J. Clin. Invest.* **81**, 1384–1389 (1988).

153. Moldawer, L. L., Svaninger, G., Gelin, J. & Lundholm, K. G. Interleukin 1 and tumor necrosis factor do not regulate protein balance in skeletal muscle. *Am. J. Physiol.* **253**, C766-773 (1987).

154. Fischer, J. E. & Hasselgren, P. O. Cytokines and glucocorticoids in the regulation of the ‘hepato-skeletal muscle axis’ in sepsis. *Am. J. Surg.* **161**, 266–271 (1991).

155. Angus, D. C. *et al.* Epidemiology of severe sepsis in the United States: analysis of incidence, outcome, and associated costs of care. *Crit. Care Med.* **29**, 1303–1310 (2001).

156. Perner, A. *et al.* [Septic shock in intensive care]. *Ugeskr. Laeger* **172**, 1206–1210 (2010).

157. Chakraborty, R. K. & Burns, B. Systemic Inflammatory Response Syndrome. in *StatPearls* (StatPearls Publishing, 2020).

158. Puthucheary, Z. A. *et al.* Acute skeletal muscle wasting in critical illness. *JAMA* **310**, 1591–1600 (2013).

159. Ali, N. A. *et al.* Acquired weakness, handgrip strength, and mortality in critically ill patients. *Am. J. Respir. Crit. Care Med.* **178**, 261–268 (2008).

160. Dinglas, V. D. *et al.* Muscle Weakness and 5-Year Survival in Acute Respiratory Distress Syndrome Survivors. *Crit. Care Med.* **45**, 446–453 (2017).

161. Rettig, T. C. D. *et al.* Postoperative Interleukin-6 Level and Early Detection of Complications After Elective Major Abdominal Surgery. *Ann. Surg.* **263**, 1207–1212 (2016).

162. Mokart, D. *et al.* Procalcitonin, interleukin 6 and systemic inflammatory response syndrome (SIRS): early markers of postoperative sepsis after major surgery. *Br. J. Anaesth.* **94**, 767–773 (2005).

163. Barbić, J. *et al.* Kinetics of changes in serum concentrations of procalcitonin, interleukin-6, and C- reactive protein after elective abdominal surgery. Can it be used to detect postoperative complications? *Coll. Antropol.* **37**, 195–201 (2013).

164. Drifte, G., Dunn-Siegrist, I., Tissières, P. & Pugin, J. Innate immune functions of immature neutrophils in patients with sepsis and severe systemic inflammatory response syndrome. *Crit. Care Med.* **41**, 820–832 (2013).

165. Lord, J. M. *et al.* The systemic immune response to trauma: an overview of pathophysiology and treatment. *Lancet Lond. Engl.* **384**, 1455–1465 (2014).

166. Wirén, M., Permert, J. & Larsson, J. Alpha-ketoglutarate-supplemented enteral nutrition: effects on postoperative nitrogen balance and muscle catabolism. *Nutr. Burbank Los Angel. Cty. Calif* **18**, 725–728 (2002).

167. Leverve, X., Guignier, M., Carpentier, F., Serre, J. C. & Caravel, J. P. Effect of parenteral nutrition on muscle amino acid output and 3-methylhistidine excretion in septic patients. *Metabolism.* **33**, 471–477 (1984).

168. Carli, F. & Emery, P. W. Intra-operative epidural blockade with local anaesthetics and postoperative protein breakdown associated with hip surgery in elderly patients. *Acta Anaesthesiol. Scand.* **34**, 263–266 (1990).

169. Bérard, M.-P., Pelletier, A., Ollivier, J.-M., Gentil, B. & Cynober, L. Qualitative manipulation of amino acid supply during total parenteral nutrition in surgical patients. *JPEN J. Parenter. Enteral Nutr.* **26**, 136–143 (2002).

170. Hammarqvist, F., Strömberg, C., von der Decken, A., Vinnars, E. & Wernerman, J. Biosynthetic human growth hormone preserves both muscle protein synthesis and the decrease in muscle-free glutamine, and improves whole-body nitrogen economy after operation. *Ann. Surg.* **216**, 184–191 (1992).

171. Wernerman, J., von der Decken, A. & Vinnars, E. Protein synthesis in skeletal muscle in relation to nitrogen balance after abdominal surgery: the effect of total parenteral nutrition. *JPEN J. Parenter. Enteral Nutr.* **10**, 578–582 (1986).

172. Essén, P., McNurlan, M. A., Wernerman, J., Vinnars, E. & Garlick, P. J. Uncomplicated surgery, but not general anesthesia, decreases muscle protein synthesis. *Am. J. Physiol.* **262**, E253-260 (1992).

173. Tjäder, I. *et al.* Muscle protein synthesis rate decreases 24 hours after abdominal surgery irrespective of total parenteral nutrition. *JPEN J. Parenter. Enteral Nutr.* **20**, 135–138 (1996).
174. Essén, P. *et al.* Laparoscopic cholecystectomy does not prevent the postoperative protein catabolic response in muscle. *Ann. Surg.* **222**, 36–42 (1995).
175. Lattermann, R., Carli, F., Wykes, L. & Schricker, T. Epidural blockade modifies perioperative glucose production without affecting protein catabolism. *Anesthesiology* **97**, 374–381 (2002).
176. Essén, P. *et al.* Muscle protein synthesis after operation: effects of intravenous nutrition. *Eur. J. Surg. Acta Chir.* **159**, 195–200 (1993).
177. Lattermann, R., Schricker, T., Wachter, U., Goertz, A. & Georgieff, M. Intraoperative epidural blockade prevents the increase in protein breakdown after abdominal surgery. *Acta Anaesthesiol. Scand.* **45**, 1140–1146 (2001).
178. Williams, J. P. *et al.* Effect of tumor burden and subsequent surgical resection on skeletal muscle mass and protein turnover in colorectal cancer patients. *Am. J. Clin. Nutr.* **96**, 1064–1070 (2012).
179. Awad, S., Varadhan, K. K., Ljungqvist, O. & Lobo, D. N. A meta-analysis of randomised controlled trials on preoperative oral carbohydrate treatment in elective surgery. *Clin. Nutr. Edinb. Scotl.* **32**, 34–44 (2013).
180. Lattermann, R., Belohlavek, G., Wittmann, S., Füchtmeier, B. & Gruber, M. The anticatabolic effect of neuraxial blockade after hip surgery. *Anesth. Analg.* **101**, 1202–1208, table of contents (2005).
181. Schricker, T. *et al.* Postoperative protein sparing with epidural analgesia and hypocaloric dextrose. *Ann. Surg.* **240**, 916–921 (2004).

182. Wilkinson, D. J. *et al.* A validation of the application of D2O stable isotope tracer techniques for monitoring day-to-day changes in muscle protein subfraction synthesis in humans. *Am. J. Physiol. - Endocrinol. Metab.* **306**, E571–E579 (2014).

183. Constantin, D., McCullough, J., Mahajan, R. P. & Greenhaff, P. L. Novel events in the molecular regulation of muscle mass in critically ill patients. *J. Physiol.* **589**, 3883–3895 (2011).

184. Crossland, H., Constantin-Teodosiu, D., Gardiner, S. M., Constantin, D. & Greenhaff, P. L. A potential role for Akt/FOXO signalling in both protein loss and the impairment of muscle carbohydrate oxidation during sepsis in rodent skeletal muscle. *J. Physiol.* **586**, 5589–5600 (2008).

185. Vary, T. C. Down Regulation of Pyruvate Dehydrogenase Complex in Skeletal Muscle during Sepsis: Implications for Sepsis-Induced Hyperlactatemia. *Sepsis* **2**, 303–312 (1999).

186. Crossland, H., Constantin-Teodosiu, D., Greenhaff, P. L. & Gardiner, S. M. Low-dose dexamethasone prevents endotoxaemia-induced muscle protein loss and impairment of carbohydrate oxidation in rat skeletal muscle. *J. Physiol.* **588**, 1333–1347 (2010).

187. Crossland, H., Constantin-Teodosiu, D., Gardiner, S. M. & Greenhaff, P. L. Peroxisome proliferator-activated receptor γ agonism attenuates endotoxaemia-induced muscle protein loss and lactate accumulation in rats. *Clin. Sci. Lond. Engl. 1979* **131**, 1437–1447 (2017).

188. Varadhan, K. K., Constantin-Teodosiu, D., Constantin, D., Greenhaff, P. L. & Lobo, D. N. Inflammation-mediated muscle metabolic dysregulation local and

remote to the site of major abdominal surgery. *Clin. Nutr. Edinb. Scotl.* **37**, 2178–2185 (2018).

189. Wåhlin-Larsson, B. *et al.* Mechanistic Links Underlying the Impact of C-Reactive Protein on Muscle Mass in Elderly. *Cell. Physiol. Biochem. Int. J. Exp. Cell. Physiol. Biochem. Pharmacol.* **44**, 267–278 (2017).
190. Kelly, M., Gauthier, M.-S., Saha, A. K. & Ruderman, N. B. Activation of AMP-activated protein kinase by interleukin-6 in rat skeletal muscle: association with changes in cAMP, energy state, and endogenous fuel mobilization. *Diabetes* **58**, 1953–1960 (2009).
191. Silverman, M. N., Miller, A. H., Biron, C. A. & Pearce, B. D. Characterization of an interleukin-6- and adrenocorticotropin-dependent, immune-to-adrenal pathway during viral infection. *Endocrinology* **145**, 3580–3589 (2004).
192. Burfeind, K. G., Michaelis, K. A. & Marks, D. L. The central role of hypothalamic inflammation in the acute illness response and cachexia. *Semin. Cell Dev. Biol.* **54**, 42–52 (2016).
193. Fuchs, F., Damm, J., Gerstberger, R., Roth, J. & Rummel, C. Activation of the inflammatory transcription factor nuclear factor interleukin-6 during inflammatory and psychological stress in the brain. *J. Neuroinflammation* **10**, 140 (2013).
194. Takahashi, K. *et al.* Prognostic Significance of Skeletal Muscle Loss During Early Postoperative Period in Elderly Patients with Esophageal Cancer. *Ann. Surg. Oncol.* **26**, 3727–3735 (2019).
195. Kudou, K. *et al.* Postoperative Skeletal Muscle Loss Predicts Poor Prognosis of Adenocarcinoma of Upper Stomach and Esophagogastric Junction. *World J. Surg.* **43**, 1068–1075 (2019).

196. Wilkinson, D. J. Historical and contemporary stable isotope tracer approaches to studying mammalian protein metabolism. Mass Spectrom. Rev. 37, 57–80 (2018).

197. Garlick, P. J. et al. Measurement of the rate of protein synthesis in muscle of postabsorptive young men by injection of a 'flooding dose' of [1-13C] leucine. Clin. Sci. Lond. Engl. 1979 77, 329–336 (1989).

198. Wolfe, R. R. & Chinkes, D. L. Isotope Tracers in Metabolic Research: Principles and Practice of Kinetic Analysis. (John Wiley & Sons, 2004).

199. Tipton, K. D., Hamilton, D. L. & Gallagher, I. J. Assessing the Role of Muscle Protein Breakdown in Response to Nutrition and Exercise in Humans. Sports Med. Auckl. Nz 48, 53–64 (2018).

200. Duggleby, S. L. & Waterlow, J. C. The end-product method of measuring whole-body protein turnover: a review of published results and a comparison with those obtained by leucine infusion. Br. J. Nutr. 94, 141–153 (2005).

201. Atherton, P. J., Phillips, B. E. & Wilkinson, D. J. Chapter Four - Exercise and Regulation of Protein Metabolism. in Progress in Molecular Biology and Translational Science (ed. Bouchard, C.) vol. 135 75–98 (Academic Press, 2015).

202. Gillis C, Carli F. Promoting perioperative metabolic and nutritional care. Anesthesiology 2015;123:1455–72.

2. THE EFFECTS OF ELECTIVE ABDOMINAL SURGERY ON PROTEIN TURNOVER: A META-ANALYSIS OF STABLE ISOTOPE TECHNIQUES TO INVESTIGATE POSTOPERATIVE CATABOLISM

Published as a full-text article in *Clinical Nutrition (Edinburgh, Scotland), 41(3), 709–722.*, March 2022.

ABSTRACT

Background & aims: Elective surgery induces skeletal muscle wasting driven by an imbalance between muscle protein synthesis and breakdown. From examination of diverse stable isotope tracer techniques, the dynamic processes driving this imbalance are unclear. This meta-analysis aimed to elucidate the mechanistic driver(s) of postoperative protein catabolism through stable isotope assessment of protein turnover before and after abdominal surgery.

Methods: Meta-analysis was performed of randomized controlled trials and cohort studies in patients undergoing elective abdominal surgery that contained measurements of whole-body or skeletal muscle protein turnover using stable isotope tracer methodologies pre- and postoperatively. Postoperative changes in protein synthesis and breakdown were assessed through subgroup analysis of tracer methodology and perioperative care.

Results: Surgery elicited no overall change in protein synthesis [standardized mean difference (SMD) -0.47, 95% confidence interval (CI): -1.32, 0.39, $p = 0.25$]. However, subgroup analysis revealed significant suppressions via direct-incorporation methodology [SMD -1.53, 95%CI: -2.89, -0.17, $p = 0.03$] within skeletal muscle. Changes of this nature were not present among arterio-venous [SMD 0.61, 95%CI: -1.48, 2.70, $p = 0.58$] or end-product [SMD -0.09, 95%CI: -0.81, 0.64, $p = 0.82$] whole-body measures. Surgery resulted in no overall change in protein breakdown [SMD 0.63, 95%CI: -0.06, 1.32, $p = 0.07$]. Yet, separation by tracer methodology illustrated significant increases in urinary end-products (urea/ammonia) [SMD 0.70, 95%CI: 0.38, 1.02, $p < 0.001$] that were not present among arterio-venous measures [SMD 0.67, 95%CI: -1.05, 2.38, $p = 0.45$].

Conclusions: Elective abdominal surgery elicits suppressions in skeletal muscle protein synthesis that are not reflected on a whole-body level. Lack of uniform changes across whole-body tracer techniques are likely due to contribution from tissues other than skeletal muscle.

Keywords: Meta-analysis; Muscle protein breakdown; Muscle protein synthesis; Postoperative; Stable isotope studies; Surgery.

Abbreviations

AV: Arterio-venous

CI: Confidence interval

DI: Direct-incorporation

EP: End-product

FSR: Fractional synthetic rate

GC-IRMS: Gas chromatography-isotope ratio mass spectrometry

GI: Gastrointestinal

IQR: Interquartile range

RCT: Randomized controlled trial

SD: Standard deviation

SMD: Standardized mean difference

2.1 INTRODUCTION

Skeletal muscle wasting is a key feature of the metabolic response to surgery, known to complicate postoperative recovery and impair clinical outcomes [1]. Although this phenomenon has been observed since early investigations into the metabolic perturbations that occur as a result of trauma and surgery [[2], [3], [4]], the underlying dynamic drivers of these metabolic changes within muscle are yet to be fully defined. Loss of skeletal muscle mass must occur through a chronic imbalance between muscle protein synthesis and muscle protein breakdown, with stable isotope techniques that calculate fractional synthetic rate currently considered a 'gold standard' for the measurement of muscle protein synthesis [5]. These techniques have been employed in the perioperative setting [[6], [7], [8]] and have shown distinct synthetic responses when compared with other stable isotope tracer techniques that quantify arterio-venous protein kinetics within the blood [9,10] or tracer kinetics within urinary end-products [11,12]. Comparisons of protein breakdown rates across tracer methodologies are limited by challenges in the assessment of skeletal muscle protein breakdown due to both underlying assumptions in kinetic modelling [13,14] and protocols ill-suited to clinical populations [14,15]. Hence, there is a paucity of information on fractional breakdown rates in the surgical patient, with stable isotope measures of protein breakdown predominantly reflecting whole-body kinetics. Taken together, the dynamic changes driving postoperative muscle wasting are unclear.

Major abdominal surgery has been shown to elicit systemic metabolic dysregulation within skeletal muscle, including alterations in catabolic and inflammatory signalling pathways [16]. In addition, traditional surgical care for these patients has often prescribed prolonged periods of preoperative fasting [17], putting these patients at great risk of postoperative skeletal muscle wasting through energy deficits [18]. Even in light of enhanced recovery programs aimed at reducing the metabolic stress response to surgery [19], in part through recommendations on the avoidance of preoperative fasting and early resumption of oral nutrition postoperatively [1], a recent audit of UK hospitals has illustrated elective surgical procedures - constituted by approximately 70% upper GI, colorectal or general surgery - to routinely involve preoperative fasting of >12 h for food (73% incidence) and clear fluids (21% incidence) [20]. A synthesis of stable isotope studies quantifying protein kinetics in the patient undergoing abdominal surgery may elucidate the changes in protein turnover driving postoperative catabolism, while informing future care strategies aimed at minimizing skeletal muscle wasting to improve patient outcomes and recovery.

The aims of this meta-analysis were to:

- determine postoperative changes in protein kinetics driving skeletal muscle catabolism, through a synthesis of studies utilizing stable isotope research methodologies across a range of elective abdominal surgical procedures and clinical care.

- assess the impact of perioperative care strategies such as nutritional support, neuraxial blockade and minimally invasive (laparoscopic) surgical approaches, and

- evaluate the postoperative time-course of protein turnover responses.

2.2 METHODS

Search strategy

Electronic searches were performed in PubMed, MEDLINE and Cochrane Library databases to identify suitable articles (i.e. evaluating either whole-body or skeletal muscle protein turnover using stable isotope tracer methodology in adult patients undergoing elective abdominal surgery) published between 01 January 1990 and 08 November 2020. This date restriction was imposed due to the validation of several clinically suitable stable isotope techniques for protein metabolism occurring throughout the 1980s [[21], [22], [23], [24]]; studies which contributed to increased interest into the effects of surgical trauma on protein turnover during the late 1980s [25,26] and to the development of commercially available gas chromatography-isotope ratio mass spectrometers (GC-IRMS) capable of capturing increased signal sensitivity within complex biological matrices [27]. The search terms [“surgery”] AND [“muscle” OR “protein”] AND [“stable isotope” OR “tracer” OR “turnover”] were used to search each database by title and abstract. The bibliographies of all studies which fulfilled the inclusion criteria were manually reviewed to aid in locating additional eligible articles. There were no language restrictions in place during article selection. This meta-analysis was conducted in accordance with the guidance of the PRISMA statement [28] and conforms to AMSTAR-2 guidelines [29].

Study selection

Articles were screened for suitability by title and abstract on two separate occasions by one reviewer (MJ) and verified by a senior reviewer (MSB). Articles were deemed eligible if they described at least one adult patient cohort undergoing elective abdominal surgery, with pre- and postoperative measures of whole-body or skeletal muscle protein turnover through stable isotope tracer methodologies. Postoperative measures were included if they were performed within two weeks of surgery. Patients receiving a variety of nutritional and analgesic regimens were included due to the inherent heterogeneity of surgical care across different hospital settings and procedures. However, any patient cohort that was specified by study authors to be undergoing non-conventional perioperative care or receiving non-standard drug administration or hormone therapy was excluded. Pre- and postoperative measures of protein turnover had to be performed during the same nutritional state for each patient group, specifically; pre- and postoperative measures had to be both in the postabsorptive or postprandial state to enable accurate comparisons of protein turnover within patients, due to the dynamic regulation of muscle protein turnover with feeding [30]. Patients undergoing emergency, transplant or reconstructive procedures or suffering from burns, preoperative trauma, metabolic disorders, prolonged anti-inflammatory or antibiotic medication, organ dysfunction or failure were excluded. Abdominal surgery was defined as general, urological, or gynecologic, with vascular procedures omitted. Only studies on patients undergoing abdominal surgery were included in this analysis to improve homogeneity in postoperative protein turnover responses, as there is evidence to suggest that the catabolic response to surgery is relative to the magnitude of trauma [11,12,31]. Further, ischemia and reperfusion effects have been shown to impact protein turnover rates within an animal model [32], with great variation in postoperative protein turnover responses in humans previously being demonstrated within a heterogenous abdominal surgical cohort containing vascular procedures [33]. Patients were deemed adults if they were 18 years or older, with all pediatric studies being ineligible. Records containing duplication of study results were omitted, with only the primary publication taken forward for inclusion. Duplication of articles eligible for screening were assessed by title using Python programming language (version 3.6.5), with a subsequent manual check to ensure the full removal of duplicate articles. Duplication of study results was checked manually during full-text screening of eligible articles. For any article where fulfilment of the inclusion criteria was unclear, inclusion was discussed by two reviewers (MJ and MSB) and a final decision was made.

Data extraction

Data were extracted by one author (MJ) on two separate occasions and cross-compared to ensure accurate inclusion of article information. These data were then reviewed by a second author (MSB). Where studies contained more than one patient cohort, these cohorts were combined to prevent unit-of-analysis-error in accordance with recommendations from the Cochrane Handbook for Systematic Reviews of Interventions [34]. Data were additionally collected on patient demographics, surgical preparation and underlying conditions necessitating surgical intervention. Where studies did not contain the necessary information, study authors were contacted for retrieval. Where studies did not report the mean and standard deviation of protein turnover measures; median and interquartile ranges were converted to means and standard deviations according to the technique described by Hozo et al. [35]. This technique takes the median as the best estimate of the mean and calculates the SD as follows:

$$\mathrm{SD} = \frac{\text{Upper Limit of IQR} - \text{Lower Limit of IQR}}{1.35}$$

Where relevant, risk of bias for randomized controlled trials (RCTs) was assessed using the Cochrane Collaboration Tool [36]. Publication bias was assessed via funnel plots and tested for via Pustejovsky's and Rodgers' [37] modified test of linear regression for standardized mean difference effect sizes.

Outcome measures

The primary outcome was to detect changes before and after surgery in whole-body or skeletal muscle protein turnover measured via stable isotope tracer methodology. Secondary outcomes aimed to investigate the influence of tracer methodology, severity of trauma (laparoscopic vs. open procedures), nutritional support and anaesthetic regimen on the primary outcome measures. Meta-analysis of these outcomes was achieved through subgroup analyses. The population, intervention, comparator group and outcome (PICO) are summarized in Supplementary Table 1.

Statistical analyses

Data were prepared in Excel spreadsheet format and imported into R programming language (version 4.1.0, The R Foundation for Statistical Computing, http://www.R-project.org). The 'meta' package was used for data analysis. Continuous variables are quoted as standardized mean difference (SMD) with 95% CI and were analysed using a random-effects, inverse-variance model. The DerSimonian-Laird estimator [38] was used to calculate heterogeneity variance, τ2, with Knapp-Hartung adjustments [39] applied in the calculation of confidence intervals around pooled study effects. Forest plots were generated, with statistical significance determined as $p < 0.05$ with 2-tailed testing. Study heterogeneity was assessed by I^2 statistic [40], with <25% representing low heterogeneity, 25–50% representing moderate heterogeneity and >50% representing high heterogeneity. Meta-regression was performed to investigate time as a continuous variable across postoperative sampling timepoints, to determine whether this impacted the assessment of postoperative protein turnover.

Protocol registration

The protocol for this meta-analysis was registered on the Prospero database (www.crd.york.ac.uk/prospero), registration number: CRD42021178987.

2.3 RESULTS

From the 714 studies identified through electronic database searches, 14 studies [[6], [7], [8], [9],11,12,31,[41], [42], [43], [44], [45], [46], [47]] reporting on 190 patients, were included (Fig. 1). Of these, twelve [[6], [7], [8], [9],11,12,[41], [42], [43], [44], [45], [46]] reported measures of protein synthesis (154 patients) and nine [9,11,12,31,[41], [42], [43],46,47] reported measures of protein breakdown (139 patients). From the studies reporting more than one postoperative timepoint [9,11,12,31,42,43], the timepoint closest to surgery was used for analyses, and where differential feeding was involved, its corresponding preoperative baseline value. The full-text from one eligible study [45] was unable to be sourced and attempts to contact the corresponding authors were unsuccessful. However, the abstract contained the necessary information required for inclusion and as such the decision was made between reviewers (MJ and MSB) to include data from this article in the meta-analysis. There were six studies [10,[48], [49], [50], [51], [52]] that fulfilled inclusion criteria but did not contain the necessary information needed for synthesis in the meta-analysis, with the authors being unable to provide the necessary information upon request. These studies were subsequently omitted from the analyses (Supplementary Table 2).

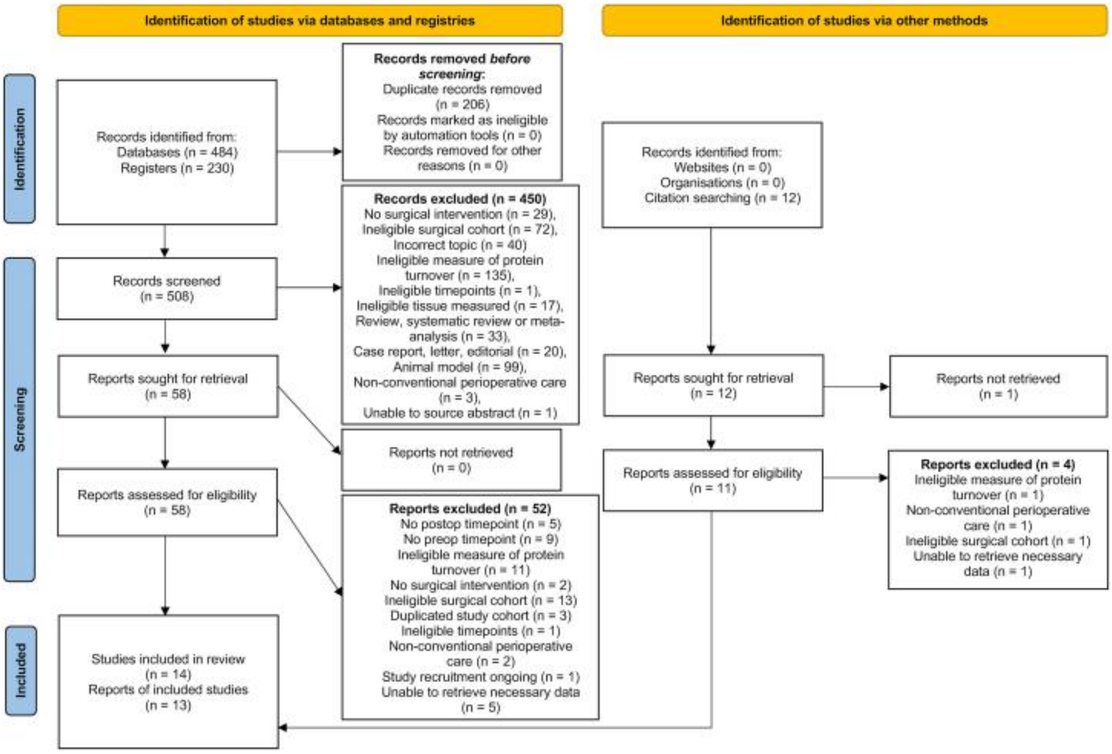

Figure 1: *PRISMA flow-diagram detailing article identification for meta-analysis.*

Risk of bias

Of the 14 studies included in this meta-analysis, eight were RCTs (predominantly investigating parameters related to perioperative catabolism) [6,7,[41], [42], [43], [44], [45],47] and six were cohort studies [8,9,11,12,31,46]. However, none of the RCTs involved randomization of the respective variables of interest within the subgroup analyses performed, with randomized cohorts within these studies thus combined prior to calculation of pooled effect size across studies. Therefore, RCT and cohort studies were not separated throughout this meta-analysis. Additional information on RCT risk of bias can be found in Fig. 2.

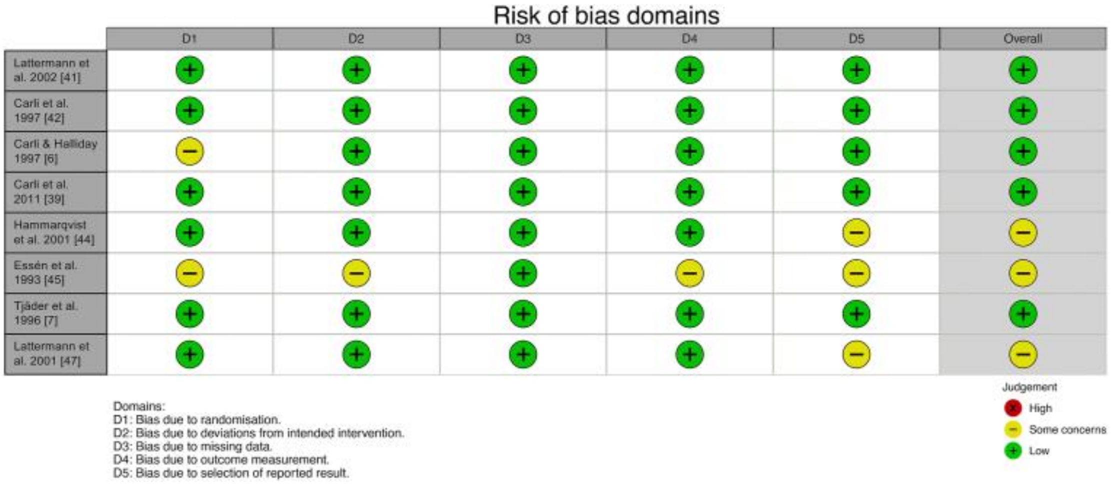

Risk of bias domains

	D1	D2	D3	D4	D5	Overall
Lattermann et al. 2002 [41]	+	+	+	+	+	+
Carli et al. 1997 [42]	+	+	+	+	+	+
Carli & Halliday 1997 [6]	−	+	+	+	+	+
Carli et al. 2011 [39]	+	+	+	+	+	+
Hammarqvist et al. 2001 [44]	+	+	+	+	−	−
Essén et al. 1993 [45]	−	−	+	−	−	−
Tjäder et al. 1996 [7]	+	+	+	+	+	+
Lattermann et al. 2001 [47]	+	+	+	+	−	−

Domains:
D1: Bias due to randomisation.
D2: Bias due to deviations from intended intervention.
D3: Bias due to missing data.
D4: Bias due to outcome measurement.
D5: Bias due to selection of reported result.

Judgement
× High
− Some concerns
+ Low

Figure 2: *Risk of bias of the included randomized controlled trials.*

Publication bias was analysed via funnel plot and Pustejovky's and Rodger's modified test of linear regression [37], for both measures of protein synthesis and protein breakdown across studies (Fig. 3a and b). Neither tests of publication bias for protein synthesis nor protein breakdown were deemed statistically significant ($p = 0.97$ and $p = 0.57$ respectively), although interpretation of these results was limited by the low study numbers included. Several studies in each funnel plot were in range of statistical significance, however due to the high heterogeneity expected across studies due to variation in perioperative care and tracer methodology, all studies were subsequently taken forward for further analyses.

A

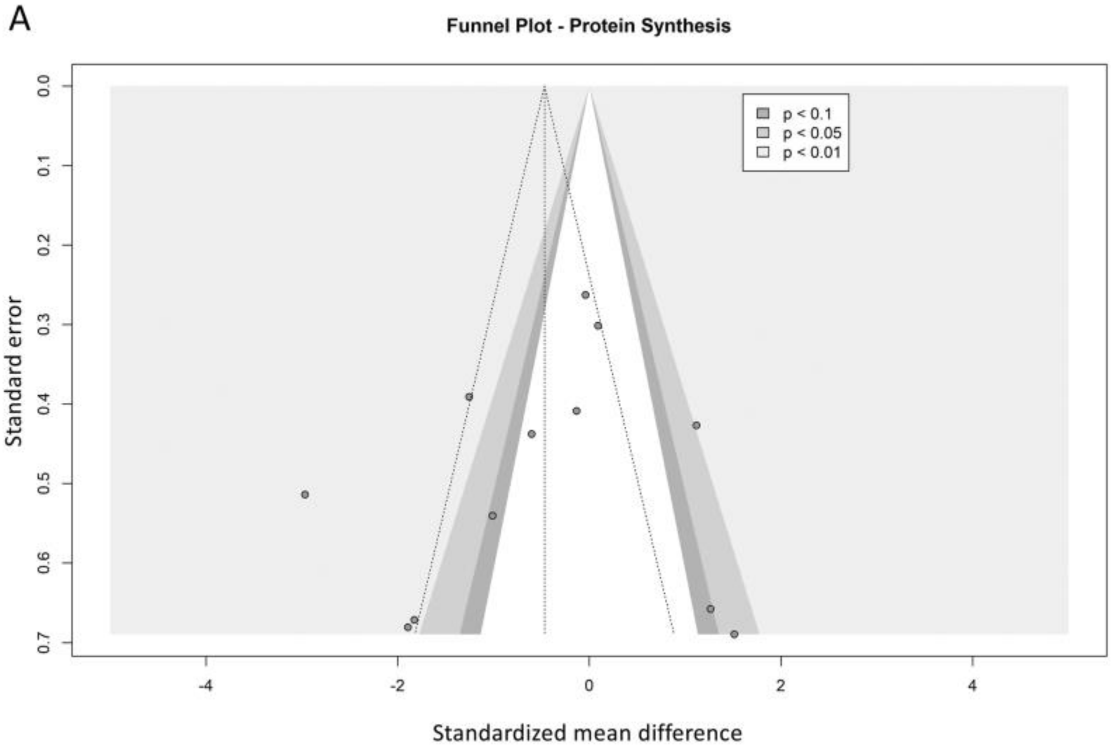

B

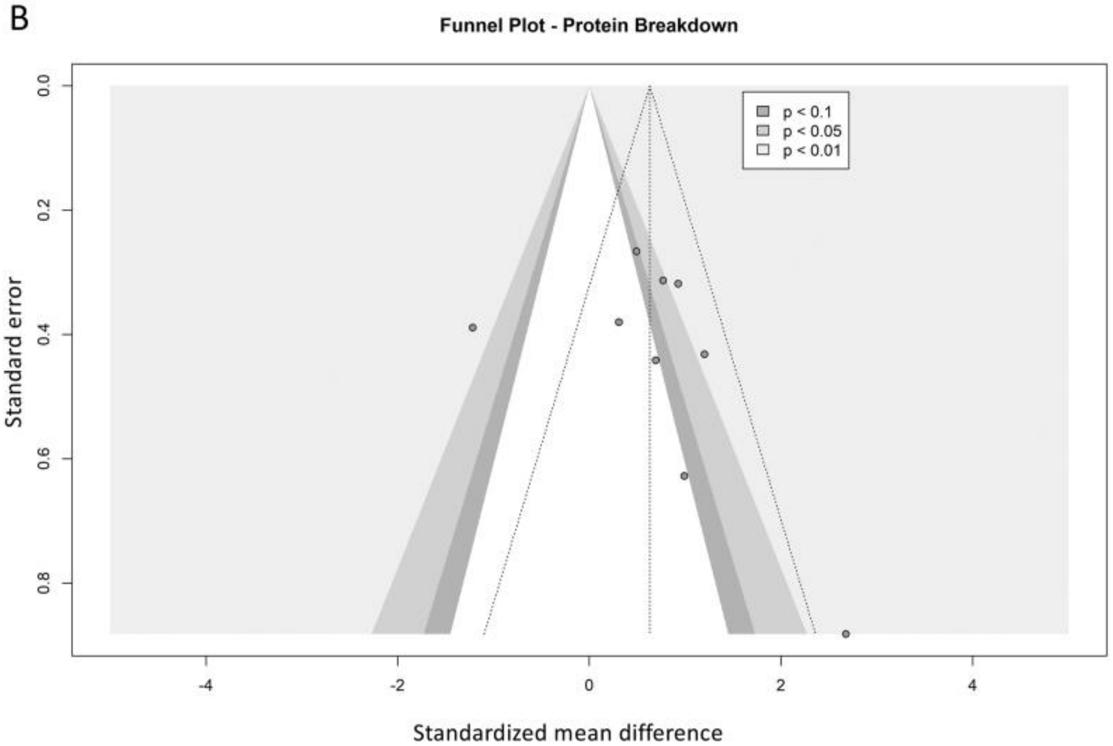

Figure 3: *Contour-enhanced funnel plots of protein synthesis (A) and protein breakdown (B) study effects, with significance represented by contour shading at thresholds of $p < 0.1$, $p < 0.05$ and $p < 0.01$.*

Demographics

Indication for surgery was predominantly colorectal cancer [6,11,12,31,41,42] with the remaining indications a mixture of malignant and benign pathologies [[7], [8], [9],[43], [44], [45], [46], [47]]. Two studies [7,45] included patients having open surgery, with the remaining studies not providing this information [6,8,9,11,12,31,[41], [42], [43], [44],46,47]. A mix of anaesthetic protocols were employed, with five studies [6,41,43,44,47] selectively providing epidural block as part of the anaesthetic regimen (either randomized to patients as part of the study design or based on patient need). Five studies did not provide information on anaesthetic protocol [9,11,12,31,46], with anaesthetic protocol being unknown for one study [45] due to its inclusion based on abstract only. There was varied perioperative nutrition provided to patients across the study period (Table 1), with eight studies [[7], [8], [9],41,[43], [44], [45], [46]] including patient cohorts that underwent a preoperative fast (of approximately 12 h or more overnight) or bowel preparation. Tracer methodology utilized within studies came under three categories; those that assessed the direct incorporation of stable isotopes into skeletal muscle that measure fractional synthetic rate (FSR), those that assessed whole-body protein kinetics in the blood via arterio-venous (AV) measures and those that assessed the whole-body kinetics of stable isotope labelling in excreted total or specific urinary substrates (EP). There were five studies that measured protein synthesis via FSR [[6], [7], [8],44,45], four [9,[41], [42], [43]] via AV, and three [11,12,46] via EP. Studies that utilized direct-incorporation methodology assessed muscle FSR distant from the site of trauma (quadriceps). Five studies [9,[41], [42], [43],47] measured protein breakdown via AV, and four [11,12,31,46] via EP. Postoperative timepoints for measures of protein turnover were predominantly between 24 and 72 h, with only one study's measures [42] being performed later than this range at 144 h.

***Table 1:** Patient demographics of studies included*

Article	**Eligible Patient Cohort**	**Number of Patients (Total)**	**Surgical Procedure**	**Anaesthesia and Analgesia**	**Perioperative Nutrition**	**Stable Isotope Tracer**	**Sampling Timepoints Included (Pre-: Post-operative)**
Tashiro et al. 1991 [11]	Gastric/colorectal surgery	11	Total gastrectomy: 7, hemicolectomy: 3, low anterior resection: 1	Unknown	TPN exclusively, 1.5 g protein/kg/day and 35 kcal/kg/day	[15N] Glycine; EP	Pre: Not specified Post: 72h
Lattermann et al. 2002 [41]	General anaesthesia with epidural block/General anaesthesia only	8/8 (16)	Hemicolectomy/colectomy: 2/5, sigmoid resection: 3/1, anterior resection: 3/1, Ileocolic resection: 0/1	General anaesthesia with patients randomised to either epidural or IV morphine postoperatively	~36h preoperative fast	L-[1-13C] Leucine; AV	Pre: 0h Post: 2h
Carli et al. 1997 [42]	Parenteral nutrition control group	6	All surgery for non-metastatic adenocarcinoma of the rectosigmoid colon	General anaesthesia with postoperative subcutaneous infusion of papaveretum (3-5 mg/h) for 3-4 days	0.1 g nitrogen/kg/day and 20 kcal/kg/day. Nonprotein calories were 60% lipid and 40% carbohydrate. Oral intake was started 6 days before surgery under dietetic supervision, and was then changed to parenteral nutrition at 500mL Vamin 14, 1L Intralipid 10% and 1L dextrose 10% 2 days before surgery and continued for 6 days afterward.	L-[1-13C] Leucine; AV	Pre: 0h Post: 144h
Carli and Halliday 1997 [6]	General anaesthesia with epidural block/general anaesthesia only	6/6 (12)	Paramedian incision for non-metastatic adenocarcinoma of the rectosigmoid colon	General anaesthesia with patients randomised to either; epidural maintained for 48h postoperatively	0.1 g nitrogen/kg/day and 20 kcal/kg/day. Nonprotein calories were 60% fat and 40% carbohydrate. Oral intake commenced 6 days before surgery under dietic	L-[1-13C] Leucine; FSR	Pre: 0h Post: 48h

				supplemented with papaveretum (8–10 mg) given i.m. every 8h or continuous subcutaneous infusion of papaveretum set at 3–8 mg/h	supervision and changed to parenteral nutrition (500ml Vamin 14, 1L Intralipid 10%, 1L dextrose 10%) 2 days before surgery. Discontinued at midnight day before surgery, recommenced at 4h postoperatively and maintained for 2 days after surgery.		
Carli et al. 2011 [43]	Oral Glucose Nutrition/Oral Whey Nutrition	6/7 (13)	Hemicolectomy/colectomy: 4/4, Sigmoid resection: 0/2, Anterior resection: 2/1	General anaesthesia with epidural or intraoperative IV analgesia; postoperative epidural for 2 days or PCA with opioids	Preoperative fast of ~24-36h. Postoperatively, patients were allowed to drink clear fluids unless contraindicated. Clear fluids consisted of a small portion of apple juice (approximately 110 kcal) and Jell-O® (Kraft Foods, Northfield, Illinois) (approximately 70 kcal).	L-[1-13C] Leucine; AV	Pre: -168h Post: 48h
Tashiro et al. 1996 [12]	Gastric or colorectal surgery	22	Total gastrectomy, hemicolectomy or lower anterior resection, and lymph node dissection.	Unknown	Parenteral nutrition providing 1.5 g amino acid/kg/day and energy intake of 35 kcal/kg/day. No fat was provided as an energy source. PN was started 7 days prior to the operation and maintained across the study duration. Doses of protein and energy were maintained strictly the same throughout the study.	[15N] Glycine; EP	Pre: Not specified Post: 72h
Hammarqvist et al. 2001 [44]	Glutamine PN group	8	Colon resection: 4, rectum resection: 3, retroperitoneal resection: 1	General anaesthesia. 3 patients were also provided with epidural blockade,	Postoperative parenteral nutrition containing 0.15 g nitrogen/kg/day including an amino acid solution,	L-[2H5] Phenylalanine; FSR	Pre: 0h Post: 72h

				although this was not provided continuously throughout the study period.	supplemented with 0.28 g glutamine/kg/day. Energy provided as glucose and fat, calculated as 1.2-fold of caloric need as determined by Harris-Benedict formula. 75% of parenteral nutrition dose administered in first day after operation (25% across following 2 days).		
Essén et al. 1993 [45]	Saline/Parenteral nutrition	8/9 (17)	Cholecystectomy	Unable to source full-text article.	Saline or parenteral nutrition for 3 days postoperatively.	L-[1-13C] Leucine; FSR	Pre: Unknown Post: 72h
Tjäder et al. 1996 [7]	Saline	7	Cholecystectomy - subcostal incision	General anaesthesia, with diazepam (5 mg) and pancuronium (0.1 mg/kg) for neuromuscular block, with postoperative IV injections of pethidine (synthetic opioid).	Saline perioperatively 3 ml/kg/h, followed by 35 ml/kg/day postoperatively.	L-[2H5] Phenylalanine; FSR	Pre: 0h Post: 24h
López-Hellín et al. 2004 [46]	Fasted/Parenteral nutrition	21/8 (29)	Left hemicolectomy: 9; right hemicolectomy: 5; front rectum resection: 4; Miles' resection: 1; gastrectomy: 1; sigmoidectomy: 1 (21). Left hemicolectomy: 3; Miles' resection: 2; front rectum resection: 1; right hemicolectomy: 1; gastrectomy: 1 (8).	Unknown	Preoperative hypocaloric parenteral nutrition: CHO (28 kJ/kg/day), Amino acids (1 g/kg/day) - followed by either: preoperative fast and postoperative parenteral nutrition of glucose (28 kJ/kg/day) OR TPN (56.1 kJ/kg/day CHO, 56.1 kJ/kg/day Fat, 1.5 g/kg/day Amino acids) administered	[15N] Glycine; EP	Pre: -72h Post: 24h

					pre- and post-operatively for 24h.		
Essén et al. 1992 [8]	Cholecystectomy patient group	7	Cholecystectomy - subcostal incision	General anaesthesia, with diazepam (5 mg) and pancuronium-bromide (0.1 mg/kg) for neuromuscular block.	Acute fasted study.	L-[1-13C] Leucine; FSR	Pre: 0h Post: Immediately after surgery
Lattermann et al. 2001 [47]	General anaesthesia/General anaesthesia with epidural block	7/7 (14)	Elective cystoprostatectomy - Ileal neobladder: 6/6, Ileal conduit: 1/1	General anaesthesia/General anaesthesia with epidural block. Epidural terminated immediately after surgery – both patient cohorts received IV Piritramide postoperatively.	Parenteral nutrition from 24h postoperatively until 10h before postoperative measurement. 2 g/kg/day xylitol and amino acids, equivalent to 0.15 g of N/kg/day.	[15N2] Urea; AV	Pre: -72h Post: 72h
Tashiro et al. 1996b [31]	Gastric or colorectal surgery	22	Total gastrectomy: 11, Hemicolectomy: 4, Low anterior resection: 6, Miles' operation: 1	Unknown	Parenteral nutrition providing 1.5 g of protein and 40 kcal/kg/day, commenced at least 5 days prior to surgery and maintained throughout study period.	[15N] Glycine; EP	Pre: Not specified Post: 72h
Carli et al. 1990 [9]	Total abdominal hysterectomy	6	Menorrhagia	Unknown	0.1 g of nitrogen/kg body weight and 1200-1400 calories (5021-5858 kJ)/day was commenced 7 days before surgery by oral intake. The same amount of nitrogen and calories was administered intravenously after surgery	L-[1-13C] Leucine: AV	Pre: -48h Post: 48h

					starting 4 h from the end of surgery when the cardiorespiratory conditions were stable. The parenteral nutritional support, based on a mixture of glucose, lipid and amino acids (KabiVitrum), was then continued for 4 days after surgery until patients were able to tolerate the pre-operative oral diet again.		

FSR: fractional synthetic rate; AV: arterio-venous; EP: end-product

Tracer methodology

Protein synthesis

Subgroup analysis of relative changes in protein synthesis (Fig. 4a) pre-post operation illustrated significant suppressions through direct-incorporation methodology (FSR, SMD -1.53, 95%CI: −2.89 to −0.17, p = 0.03). No significant change was observed in whole-body arterio-venous measures (SMD 0.61, 95%CI: −1.48 to 2.70, p = 0.58) or whole-body end-product measures (SMD -0.09, 95%CI: −0.81 to 0.64, p = 0.82). Overall protein synthesis showed a slight trend for suppression, but this did not reach statistical significance (SMD -0.47, 95%CI: −1.32 to 0.39, p = 0.25).

A: Protein synthesis

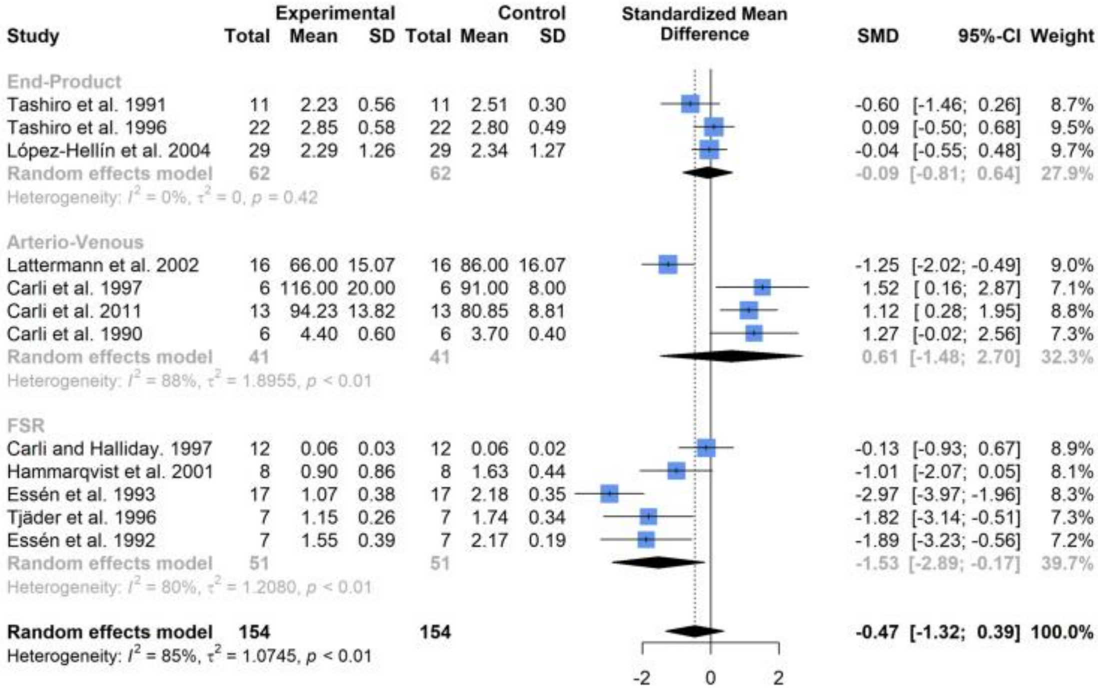

B: Protein breakdown

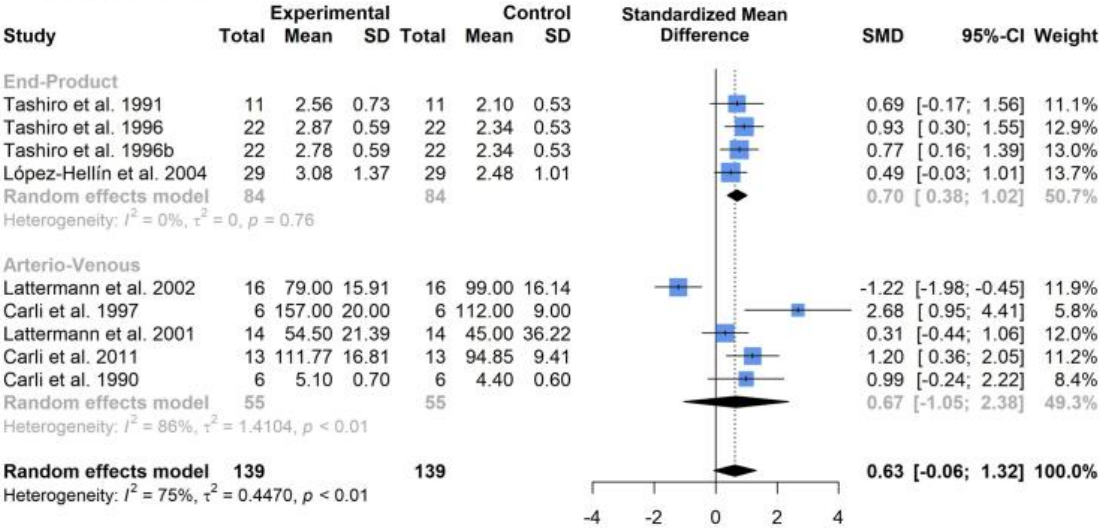

Figure 4: *Forest plot illustrating relative changes in protein synthesis (A) and protein breakdown (B), before and after surgery, with studies separated into subgroups by stable isotope tracer methodology. A random-effects, inverse-variance model was used to conduct the meta-analysis.*

Protein breakdown

Subgroup analysis of relative changes in protein breakdown (Fig. 4b) before and after surgery demonstrated significant increases via whole-body end-product methodology (SMD 0.70, 95%CI: 0.38 to 1.02, $p < 0.001$). No significant effect was observed via whole-body arterio-venous measures (SMD 0.67, 95%CI: −1.05 to 2.38, $p = 0.45$). Overall protein breakdown showed a trend for increase, but this did not reach significance (SMD 0.63, 95%CI: −0.06 to 1.32, $p = 0.07$).

Preoperative fasting

Nutritional support is a key parameter in the metabolic management of the surgical patient, with recent evidence reinforcing the negative consequences of extended periods of caloric and protein deficits in critically-ill surgical patients [53]. Thus, a key component of many current recommendations on clinical nutrition for the surgical patient advocate the avoidance of prolonged periods of preoperative fasting among elective procedures, particularly within gastrointestinal surgery where bowel preparation has traditionally been common practice [1,19].

Protein synthesis

In six studies [[7], [8], [9],41,43,44] measuring protein synthesis within this meta-analysis, patients underwent a preoperative fast as part of conventional perioperative care or bowel preparation. In four studies [6,11,12,42], patients did not undergo a preoperative fast (and were receiving consistent nutritional support prior to operation). One study [46] had to be excluded from subgroup analysis of preoperative fasting due to preoperative study measures of protein synthesis being pooled across two patient cohorts; one of which underwent preoperative fasting and the other avoided preoperative fasting. The study author was unable to provide the necessary information to enable inclusion of these cohorts. Incidence of preoperative fast could not be sourced from a further study [45], due to its inclusion on abstract only, and was consequently excluded from the subgroup analysis. Preoperative fast resulted in no significant changes in protein synthesis (SMD -0.58, 95%CI: −2.07, 0.91, $p = 0.45$, Fig. 5a), although there was high heterogeneity present among studies (I^2: 85%, $p < 0.01$). Avoidance of preoperative fasting also demonstrated no significant changes (SMD 0.07, 95%CI: −1.15, 1.29, $p = 0.92$).

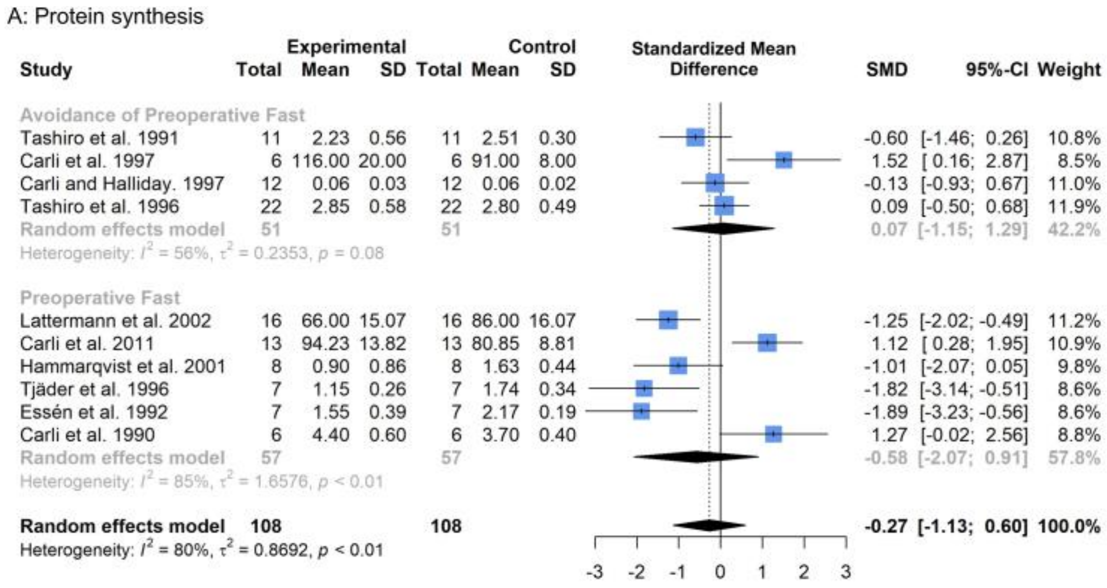

A: Protein synthesis

Study	Experimental Total	Experimental Mean	Experimental SD	Control Total	Control Mean	Control SD	SMD	95%-CI	Weight
Avoidance of Preoperative Fast									
Tashiro et al. 1991	11	2.23	0.56	11	2.51	0.30	-0.60	[-1.46; 0.26]	10.8%
Carli et al. 1997	6	116.00	20.00	6	91.00	8.00	1.52	[0.16; 2.87]	8.5%
Carli and Halliday. 1997	12	0.06	0.03	12	0.06	0.02	-0.13	[-0.93; 0.67]	11.0%
Tashiro et al. 1996	22	2.85	0.58	22	2.80	0.49	0.09	[-0.50; 0.68]	11.9%
Random effects model	51			51			0.07	[-1.15; 1.29]	42.2%
Heterogeneity: $I^2 = 56\%$, $\tau^2 = 0.2353$, $p = 0.08$									
Preoperative Fast									
Lattermann et al. 2002	16	66.00	15.07	16	86.00	16.07	-1.25	[-2.02; -0.49]	11.2%
Carli et al. 2011	13	94.23	13.82	13	80.85	8.81	1.12	[0.28; 1.95]	10.9%
Hammarqvist et al. 2001	8	0.90	0.86	8	1.63	0.44	-1.01	[-2.07; 0.05]	9.8%
Tjäder et al. 1996	7	1.15	0.26	7	1.74	0.34	-1.82	[-3.14; -0.51]	8.6%
Essén et al. 1992	7	1.55	0.39	7	2.17	0.19	-1.89	[-3.23; -0.56]	8.6%
Carli et al. 1990	6	4.40	0.60	6	3.70	0.40	1.27	[-0.02; 2.56]	8.8%
Random effects model	57			57			-0.58	[-2.07; 0.91]	57.8%
Heterogeneity: $I^2 = 85\%$, $\tau^2 = 1.6576$, $p < 0.01$									
Random effects model	**108**			**108**			**-0.27**	**[-1.13; 0.60]**	**100.0%**
Heterogeneity: $I^2 = 80\%$, $\tau^2 = 0.8692$, $p < 0.01$									

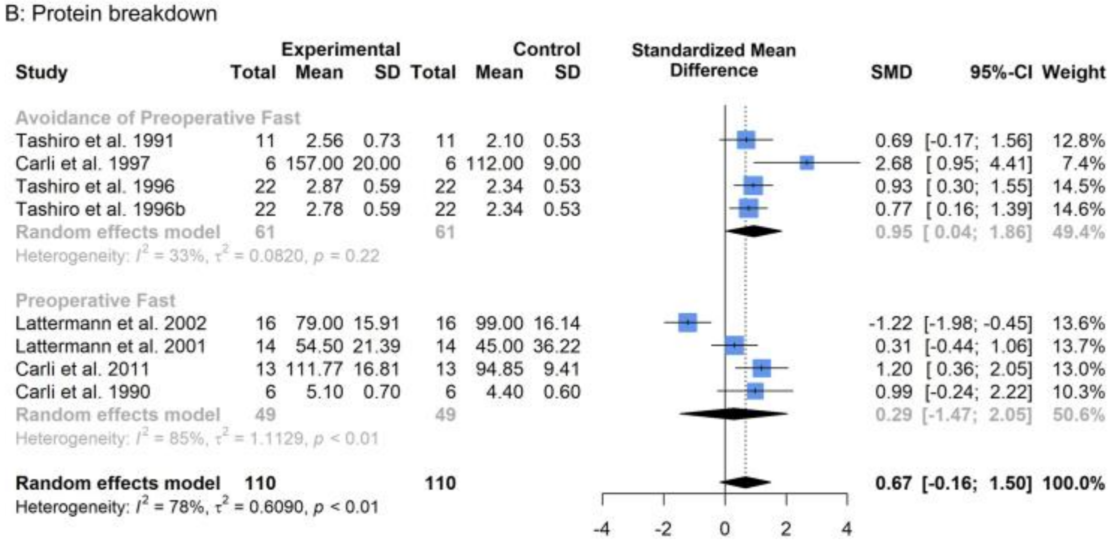

B: Protein breakdown

Study	Experimental Total	Experimental Mean	Experimental SD	Control Total	Control Mean	Control SD	SMD	95%-CI	Weight
Avoidance of Preoperative Fast									
Tashiro et al. 1991	11	2.56	0.73	11	2.10	0.53	0.69	[-0.17; 1.56]	12.8%
Carli et al. 1997	6	157.00	20.00	6	112.00	9.00	2.68	[0.95; 4.41]	7.4%
Tashiro et al. 1996	22	2.87	0.59	22	2.34	0.53	0.93	[0.30; 1.55]	14.5%
Tashiro et al. 1996b	22	2.78	0.59	22	2.34	0.53	0.77	[0.16; 1.39]	14.6%
Random effects model	61			61			0.95	[0.04; 1.86]	49.4%
Heterogeneity: $I^2 = 33\%$, $\tau^2 = 0.0820$, $p = 0.22$									
Preoperative Fast									
Lattermann et al. 2002	16	79.00	15.91	16	99.00	16.14	-1.22	[-1.98; -0.45]	13.6%
Lattermann et al. 2001	14	54.50	21.39	14	45.00	36.22	0.31	[-0.44; 1.06]	13.7%
Carli et al. 2011	13	111.77	16.81	13	94.85	9.41	1.20	[0.36; 2.05]	13.0%
Carli et al. 1990	6	5.10	0.70	6	4.40	0.60	0.99	[-0.24; 2.22]	10.3%
Random effects model	49			49			0.29	[-1.47; 2.05]	50.6%
Heterogeneity: $I^2 = 85\%$, $\tau^2 = 1.1129$, $p < 0.01$									
Random effects model	**110**			**110**			**0.67**	**[-0.16; 1.50]**	**100.0%**
Heterogeneity: $I^2 = 78\%$, $\tau^2 = 0.6090$, $p < 0.01$									

Figure 5: *Forest plot illustrating relative changes in protein synthesis (A) and protein breakdown (B), before and after surgery, with studies separated by whether patients underwent or avoided preoperative fast. A random-effects, inverse-variance model was used to conduct the meta-analysis.*

Protein breakdown

In four studies [9,41,43,47] measuring protein breakdown patients underwent a preoperative fast, with four studies [11,12,31,42] containing patient cohorts that avoided preoperative fasting or bowel preparation. As before, one study [46] was excluded due to pooled preoperative baseline measures between fasted and non-fasted patients. Avoidance of preoperative fasting resulted in significant increases in protein breakdown (SMD 0.95, 95%CI: 0.04 to 1.86; p = 0.04, Fig. 5b), with fasted patients demonstrating no significant change (SMD 0.29, 95%CI: −1.47 to 2.05, p = 0.76).

Preoperative nutritional management

To further examine the role of preoperative nutrition in the metabolic management of the surgical patient, we examined changes in protein turnover following surgery in patients that received controlled nutritional support opposed to those that didn't, as well as for those articles where this information was unknown.

Protein synthesis

Five studies [6,9,12,42,46] provided early nutritional management in the form of controlled dietary intake (Fig. 6a) commenced 3–7 days before surgery. Three studies [7,8,41] did not provide early nutritional management to patients, with this information being unknown for the remaining four studies [11,[43], [44], [45]]. Lack of early nutritional management resulted in significant declines in protein synthesis rates postoperatively (SMD -1.49, 95%CI: −2.40, −0.59, p = 0.001). Postoperative declines in protein synthesis were not present among studies where patients received early nutritional management (SMD 0.29, 95%CI: −0.53, 1.11, p = 0.50). For studies where preoperative nutritional support information was not available, there was a non-significant effect (SMD -0.85, 95%CI: −3.52, 1.82, p = 0.54) and high heterogeneity ($I^2 = 92\%$).

A: Protein synthesis

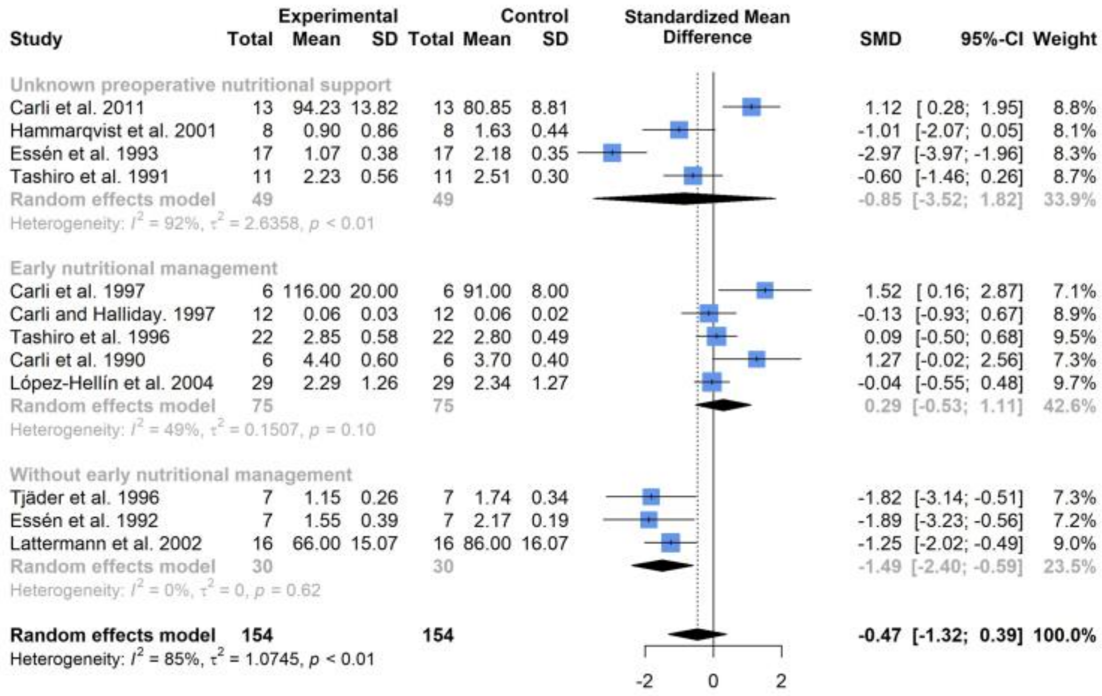

Study	Experimental			Control			SMD	95%-CI	Weight
	Total	Mean	SD	Total	Mean	SD			
Unknown preoperative nutritional support									
Carli et al. 2011	13	94.23	13.82	13	80.85	8.81	1.12	[0.28; 1.95]	8.8%
Hammarqvist et al. 2001	8	0.90	0.86	8	1.63	0.44	-1.01	[-2.07; 0.05]	8.1%
Essén et al. 1993	17	1.07	0.38	17	2.18	0.35	-2.97	[-3.97; -1.96]	8.3%
Tashiro et al. 1991	11	2.23	0.56	11	2.51	0.30	-0.60	[-1.46; 0.26]	8.7%
Random effects model	49			49			-0.85	[-3.52; 1.82]	33.9%
Heterogeneity: $I^2 = 92\%$, $\tau^2 = 2.6358$, $p < 0.01$									
Early nutritional management									
Carli et al. 1997	6	116.00	20.00	6	91.00	8.00	1.52	[0.16; 2.87]	7.1%
Carli and Halliday. 1997	12	0.06	0.03	12	0.06	0.02	-0.13	[-0.93; 0.67]	8.9%
Tashiro et al. 1996	22	2.85	0.58	22	2.80	0.49	0.09	[-0.50; 0.68]	9.5%
Carli et al. 1990	6	4.40	0.60	6	3.70	0.40	1.27	[-0.02; 2.56]	7.3%
López-Hellín et al. 2004	29	2.29	1.26	29	2.34	1.27	-0.04	[-0.55; 0.48]	9.7%
Random effects model	75			75			0.29	[-0.53; 1.11]	42.6%
Heterogeneity: $I^2 = 49\%$, $\tau^2 = 0.1507$, $p = 0.10$									
Without early nutritional management									
Tjäder et al. 1996	7	1.15	0.26	7	1.74	0.34	-1.82	[-3.14; -0.51]	7.3%
Essén et al. 1992	7	1.55	0.39	7	2.17	0.19	-1.89	[-3.23; -0.56]	7.2%
Lattermann et al. 2002	16	66.00	15.07	16	86.00	16.07	-1.25	[-2.02; -0.49]	9.0%
Random effects model	30			30			-1.49	[-2.40; -0.59]	23.5%
Heterogeneity: $I^2 = 0\%$, $\tau^2 = 0$, $p = 0.62$									
Random effects model	**154**			**154**			**-0.47**	**[-1.32; 0.39]**	**100.0%**
Heterogeneity: $I^2 = 85\%$, $\tau^2 = 1.0745$, $p < 0.01$									

B: Protein breakdown

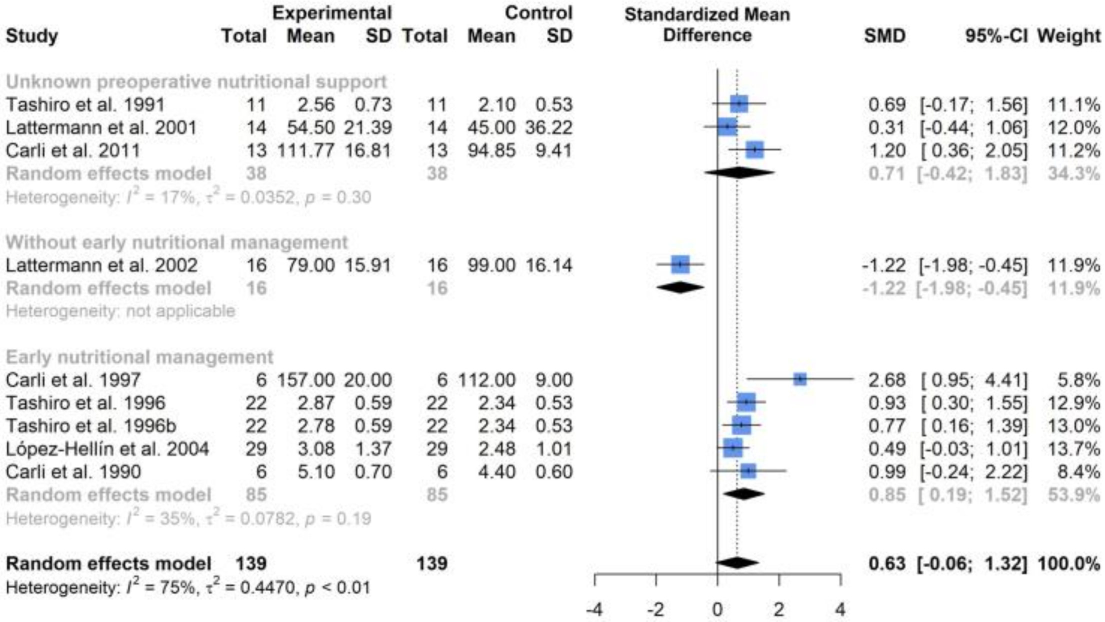

Study	Experimental			Control			SMD	95%-CI	Weight
	Total	Mean	SD	Total	Mean	SD			
Unknown preoperative nutritional support									
Tashiro et al. 1991	11	2.56	0.73	11	2.10	0.53	0.69	[-0.17; 1.56]	11.1%
Lattermann et al. 2001	14	54.50	21.39	14	45.00	36.22	0.31	[-0.44; 1.06]	12.0%
Carli et al. 2011	13	111.77	16.81	13	94.85	9.41	1.20	[0.36; 2.05]	11.2%
Random effects model	38			38			0.71	[-0.42; 1.83]	34.3%
Heterogeneity: $I^2 = 17\%$, $\tau^2 = 0.0352$, $p = 0.30$									
Without early nutritional management									
Lattermann et al. 2002	16	79.00	15.91	16	99.00	16.14	-1.22	[-1.98; -0.45]	11.9%
Random effects model	16			16			-1.22	[-1.98; -0.45]	11.9%
Heterogeneity: not applicable									
Early nutritional management									
Carli et al. 1997	6	157.00	20.00	6	112.00	9.00	2.68	[0.95; 4.41]	5.8%
Tashiro et al. 1996	22	2.87	0.59	22	2.34	0.53	0.93	[0.30; 1.55]	12.9%
Tashiro et al. 1996b	22	2.78	0.59	22	2.34	0.53	0.77	[0.16; 1.39]	13.0%
López-Hellín et al. 2004	29	3.08	1.37	29	2.48	1.01	0.49	[-0.03; 1.01]	13.7%
Carli et al. 1990	6	5.10	0.70	6	4.40	0.60	0.99	[-0.24; 2.22]	8.4%
Random effects model	85			85			0.85	[0.19; 1.52]	53.9%
Heterogeneity: $I^2 = 35\%$, $\tau^2 = 0.0782$, $p = 0.19$									
Random effects model	**139**			**139**			**0.63**	**[-0.06; 1.32]**	**100.0%**
Heterogeneity: $I^2 = 75\%$, $\tau^2 = 0.4470$, $p < 0.01$									

Figure 6: *Forest plot illustrating relative changes in protein synthesis (A) and protein breakdown (B), before and after surgery, with studies separated by whether patients received early nutritional management. A random-effects, inverse-variance model was used to conduct the meta-analysis.*

Protein breakdown

Five studies [9,12,31,42,46] provided early nutritional management through controlled dietary intake (Fig. 6b) commenced 3–7 days before surgery. Only one study [41] could be confirmed to have not provided preoperative nutritional management, with information on preoperative nutrition unknown for three studies

[11,43,47]. Early nutritional management resulted in elevations in (whole-body) protein breakdown (SMD 0.85, 95%CI: 0.19, 1.52, $p = 0.01$). The study without preoperative nutritional management [41] demonstrated significant declines in (whole-body) protein breakdown (SMD -1.22, 95%CI: −1.98, −0.45, $p = 0.002$). Studies where information on preoperative nutritional support was unavailable demonstrated a non-significant effect (SMD 0.71, 95%CI: −0.42, 1.83, $p = 0.22$).

Further subgroup analyses of nutritional support parameters, such as: nutrient composition, preoperative carbohydrate loading and early postoperative resumption of oral feeding, were not possible with the low study numbers contained within this meta-analysis.

Time

Meta-regression of postoperative timepoint sampling (representing the proximity of protein turnover measures to surgery) illustrated a trend for early suppressions in protein metabolism with gradual restoration over time towards baseline values. Protein synthesis demonstrated a non-significant trend ($p = 0.21$, Fig. 7a), while protein breakdown demonstrated a significant trend ($p = 0.01$, Fig. 7b). However, interpretation of these findings is limited by the small study numbers and with respect to protein breakdown measures, potentially impacted by study homogeneity stemming from three data sets by the same author [11,12,45] being grouped closely together within the meta-regression analysis (Fig. 7b).

A: Protein synthesis

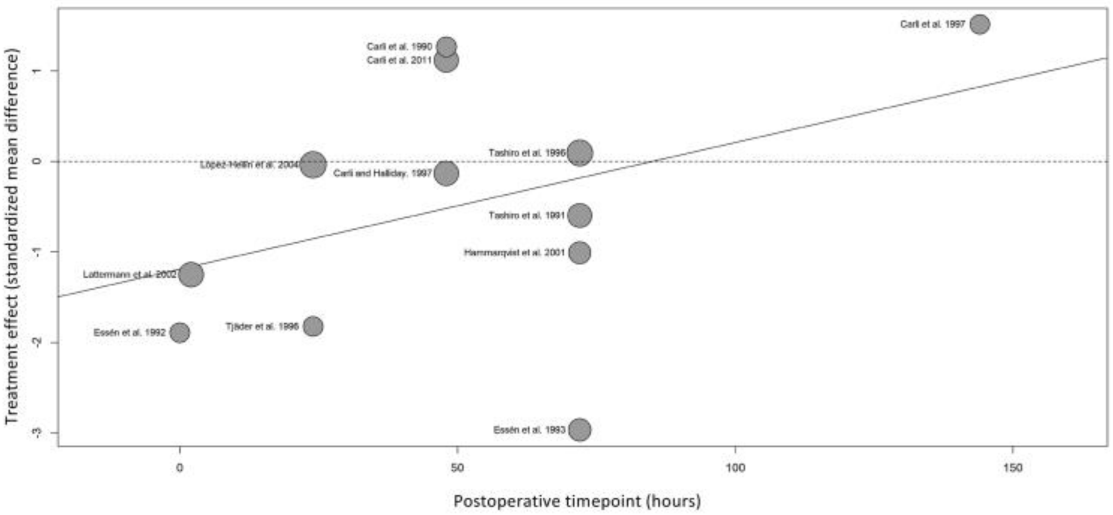

B: Protein breakdown

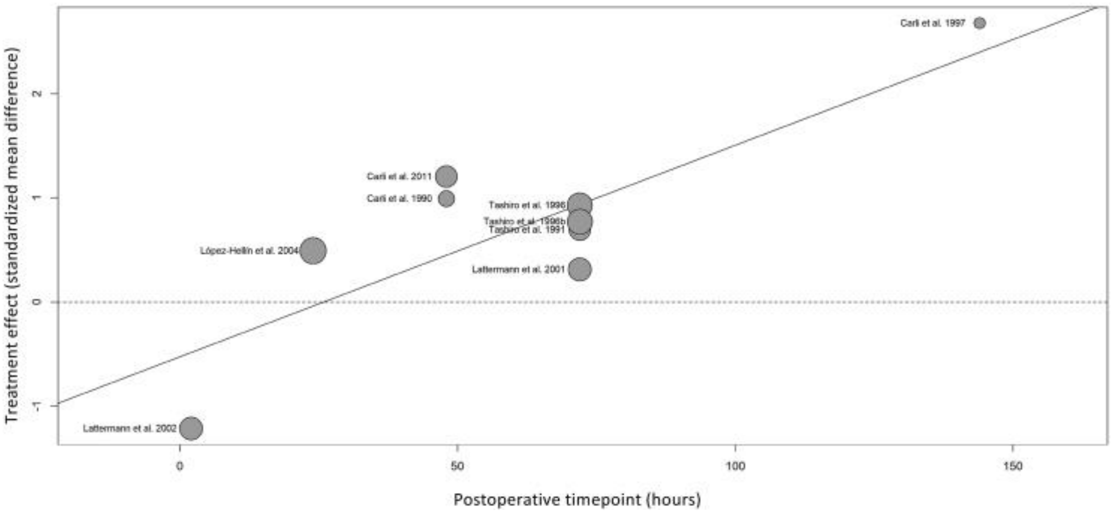

Figure 7: *Bubble plot illustrating meta-regression analysis of postoperative changes in protein synthesis (A) and protein breakdown (B), relative to the timepoint (in hours) of postoperative sampling.*

Anaesthesia, epidural blockade and severity of surgical trauma

There was insufficient reporting of open vs. laparoscopic procedures to enable comparisons between the extent of surgical trauma and measures of protein synthesis/breakdown, with specification of these parameters contained within only two studies [7,45]. Anesthetic regimens differed but there were insufficient study numbers to group by minor modalities (specific drug regimens to induce general anesthesia, Table 1). Only three studies [6,41,47] included a patient cohort where all participants received epidural blockade as part of their anesthetic treatment, with a further two studies [43,44] containing patient cohorts receiving mixed anesthetic treatment with and without epidural administration and five studies [9,11,12,31,46] not providing this information. Therefore, no subgroup analyses were performed on these parameters within this meta-analysis.

2.4 Discussion

What our study found

Assessment via stable isotope techniques demonstrated trends for reductions in protein synthesis and elevations in protein breakdown to occur following abdominal surgery, within the context of varied perioperative care. These were characterized by significant suppressions in skeletal muscle protein synthesis that were not reflected within whole-body measures and significant increases in whole-body end-product but not arterio-venous protein breakdown.

The findings of this meta-analysis suggest that suppressions in postoperative protein synthesis were not contributed by preoperative fasting but are more importantly regulated by whether sufficient caloric and protein intake of patients was met in the days leading up to their operation. Avoidance of preoperative fasting resulted in elevated protein breakdown that was not reflected in patients that underwent preoperative fast, with early nutritional management also resulting in elevated protein breakdown postoperatively and lack of early preoperative diet management resulting in suppressed protein breakdown. Care must be taken in the interpretation of these findings, as only whole-body protein breakdown was measured and based on the findings of this meta-analysis, these measures likely do not accurately reflect the protein kinetics of skeletal muscle. However, it overall appears that sufficient preoperative caloric and protein intake facilitates increased rates of protein turnover postoperatively. Meta-regression provides limited support for postoperative suppressions in protein turnover to be most acute during the immediate postoperative period, and to thereafter increase with time. This may suggest early recommencement of nutritional support to be vital in the immediate postoperative period, although examination of this effect was unfortunately not possible within this meta-analysis.

What is available in the literature

Variation in stable isotope assessment of protein kinetics through techniques measuring distinct metabolic pools has previously been observed in surgical patients undergoing coronary artery bypass grafts [54], who demonstrated significant reductions in muscle protein synthesis (-~36%) but notable increases in plasma fibrinogen (+~177%) and albumin (+~45%) synthesis postoperatively. Discrepancy between these metabolic pools has been suggested to be a result of the different metabolic demands these pools are subject to following surgical trauma [55], wherein amino acids are mobilized from skeletal muscle to necessitate energy and healing demands and liver protein metabolism is accelerated to promote the production of acute phase reactants. Increases in whole-body protein turnover associated with healing-driven hypermetabolism, would be in line with traditional observations correlating early wound healing and elevated urinary nitrogen excretion rates among patients in receipt of good preoperative nutrition [4], where administration of parenteral nutrition during the postoperative period appears to augment hypermetabolism compared to hypocaloric glucose [56], but simultaneously results in improved nitrogen balance [57]. Our findings support these concepts. There is a clear disparity between the postoperative synthetic responses of muscle and whole-body, with muscle alone demonstrating significant reductions postoperatively. Preoperative nutrition aimed at meeting the caloric and protein requirements of patients attenuates reductions in protein synthesis and elevates protein breakdown, with lack of unified magnitude in these responses likely reflective of the inclusion of direct-incorporation methodology within studies measuring protein synthesis. This reaffirms the importance of applying stable isotope techniques specific to the metabolic pool of interest to accurately study protein metabolism.

Strengths and limitations

Only studies utilizing stable isotope tracer methodologies were included in this meta-analysis, with these believed to provide the most comprehensive insight into protein kinetics within the surgical patient [58]. This meta-analysis is strengthened by a pre-test post-test design that enables the accurate determination of relative changes in protein turnover for each patient cohort through measurement of protein turnover in a controlled nutritional state before and after surgery (either postabsorptive or postprandial stable isotope measures). Many previous insights into perioperative catabolism and the investigation of care strategies aimed at modulating the catabolic response to surgery (as measured through stable isotope techniques) have utilized RCT designs centred on postoperative comparisons between cohorts, with many of these studies measuring postabsorptive protein turnover at baseline but postprandial protein turnover postoperatively [59, 60, 61, 62, 63, 64, 65] (Supplementary Table 2). Although this design is suitable in discerning the benefits of care strategies aimed at ameliorating catabolism through between-patient comparisons, they are limited in their ability to discern the mechanistic drivers of these changes during the surgical care period within patients.

However, this exclusion resulted in low study numbers that was unfortunately further contributed by the omission of several eligible articles [10, 48, 49, 50, 51] (Supplementary Table 2) that did not present the continuous data necessary for inclusion in this meta-analysis. Additionally, data from several included papers had to have their means and standard deviations estimated from median and interquartile range [44,45,47]; although this was performed using an established method [35] that has been employed in numerous published meta-analyses. The use of only continuous data to calculate pooled effect sizes does, however, aid in further strengthening the validity of results in the context of a highly heterogenous data set. With reference to the I^2 statistic; for both protein synthesis and protein breakdown, only whole-body [EP] measures under tracer subgrouping had an I^2 statistic <25%, with the majority of subgroups having an I^2 statistic >50%. With low study numbers, it is difficult to discern whether this reduced heterogeneity may be due to the necessary control of nutritional intake to enable accurate stable isotope measures [66] or whether it is influenced by many of these studies being performed by the same research group potentially utilizing standardized procedures [11,12,45]. Overall, heterogeneity for protein synthesis was 85% and 75% for protein breakdown, potentially lower due to the lack of direct-incorporation measures. This high variation must be taken into consideration when evaluating the findings of this meta-analysis, but with such low study numbers this observation is not unexpected, even within a strictly defined meta-analysis design.

Subgroup analyses investigating the impacts of preoperative nutrition on postoperative changes in protein synthesis and breakdown demonstrated preoperative fasting to result in high heterogeneity among study results ($I^2 = 85\%$ for both protein synthesis and breakdown). Less heterogeneity was present among studies where preoperative fasting was avoided ($I^2 = 56\%$ for protein synthesis, $I^2 = 33\%$ for protein breakdown). For studies measuring protein synthesis, early nutritional management presented moderate heterogeneity ($I^2 = 49\%$) and lack of early nutritional management presented low heterogeneity ($I^2 = 0\%$), with unknown nutritional management demonstrating expectantly high heterogeneity ($I^2 = 92\%$). Interpretation of heterogeneity regarding nutritional management for studies measuring protein breakdown is limited due to the presence of only one study that did not receive early nutritional management. Overall, heterogeneity was low to moderate for these results. Following the high heterogeneity present among tracer methodology subgroup analyses, mixed tracer subgrouping by nutritional parameters resulted in relatively low heterogeneity. These observations may support preoperative nutrition to exert effects on the postoperative response of protein turnover, likely through the administration of regimented dietary intake providing adequate caloric and protein intake among patients for their metabolic demands. Unfortunately, varied pre- and postoperative nutritional regimens and varied postoperative nutritional administration prevented examination of these parameters with the low study numbers contained within this meta-analysis.

2.5 Conclusions

Elective abdominal surgery elicits suppressions in skeletal muscle protein synthesis remote to the site of trauma that are not reflected on a whole-body level. Lack of uniform changes across whole-body tracer techniques are likely due to contribution from tissues other than skeletal muscle and complicate the discernment of mechanistic processes driving postoperative skeletal muscle wasting. Future work should focus on tissue-specific stable isotope approaches to comprehensively characterize the protein turnover responses of skeletal muscle, within the context of enhanced recovery after surgery care strategies.

2.6 Supplementary Materials

Supplementary Table 1: PICO statement

Patients	Elective abdominal surgical patients
Intervention	Abdominal operation
Comparison	Pre-postoperative comparison within patient cohorts
Outcomes	Protein turnover measured via stable isotope tracers

Supplementary Table 2: Relevant studies excluded

Article	**Reason for Exclusion**
Lattermann et al. 2007 [59]	Preoperative protein turnover assessed under post-absorptive feeding conditions; postoperative protein turnover assessed under post-prandial feeding conditions
Schricker et al. 2008 [60]	Preoperative protein turnover assessed under post-absorptive feeding conditions; postoperative protein turnover assessed under post-prandial feeding conditions
Lugli et al. 2010 [61]	Preoperative protein turnover assessed under post-absorptive feeding conditions; postoperative protein turnover assessed under post-prandial feeding conditions
Lattermann et al. 2003 [62]	Preoperative protein turnover assessed under post-absorptive feeding conditions; postoperative protein turnover assessed under post-prandial feeding conditions
Schricker et al. 2004 [63]	Preoperative protein turnover assessed under post-absorptive feeding conditions; postoperative protein turnover assessed under post-prandial feeding conditions
Schricker et al. 2005 [64]	Preoperative protein turnover assessed under post-absorptive feeding conditions; postoperative protein turnover assessed under post-prandial feeding conditions
Schricker et al. 2013 [65]	Preoperative protein turnover assessed under post-absorptive feeding conditions; postoperative protein turnover assessed under post-prandial feeding conditions
Tjäder et al. 2004 [33]	Heterogenous surgical population including patients undergoing vascular procedures.
Carli and Halliday. 1996 [10]	Unable to source necessary data from article or author(s)

Carli et al. 1991 [48]	Unable to source necessary data from article or author(s)
Carli et al. 1991b [49]	Unable to source necessary data from article or author(s)
Carli et al. 1997 [50]	Unable to source necessary data from article or author(s)
López Hellín et al. 2008 [51]	Unable to source necessary data from article or author(s)
Carli et al. 1990 [52]	Unable to source necessary data from article or author(s)

2.7 REFERENCES

[1] Weimann A, Braga M, Carli F, Higashiguchi T, Hübner M, Klek S, et al. ESPEN guideline: Clinical nutrition in surgery. Clin Nutr 2017;36:623–50.

[2] Cuthbertson DP. Observations on the disturbance of metabolism produced by injury to the limbs. QJM 1932;1:233–46.

[3] Cuthbertson DP. The metabolic response to injury and other related explorations in the field of protein metabolism: an autobiographical account. Scott Med J 1982;27:158–71.

[4] Moore FD. Metabolic Care of the Surgical Patient. 1959. Philadelphia: W. B. Saunders Co.

[5] Brook MS, Wilkinson DJ, Phillips BE, Perez-Schindler J, Philp A, Smith K, et al. Skeletal muscle homeostasis and plasticity in youth and ageing: impact of nutrition and exercise. Acta Physiol (Oxf) 2016;216:15–41.

[6] Carli F, Halliday D. Continuous epidural blockade arrests the postoperative decrease in muscle protein fractional synthetic rate in surgical patients. Anesthesiology 1997;86:1033–40.

[7] Tjäder I, Essen P, Thörne A, Garlick PJ, Wernerman J, McNurlan MA. Muscle protein synthesis rate decreases 24 hours after abdominal surgery irrespective of total parenteral nutrition. JPEN J Parenter Enteral Nutr 1996;20:135–8.

[8] Essén P, McNurlan MA, Wernerman J, Vinnars E, Garlick PJ. Uncomplicated surgery, but not general anesthesia, decreases muscle protein synthesis. Am J Physiol 1992;262:E253-260.

[9] Carli F, Webster J, Ramachandra V, Pearson M, Read M, Ford GC, et al. Aspects of protein metabolism after elective surgery in patients receiving constant nutritional support. Clin Sci 1990;78:621–8.

[10] Carli F, Halliday D. Modulation of protein metabolism in the surgical patient. Effect of 48-hour continuous epidural block with local anesthetics on leucine kinetics. Reg Anesth 1996;21:430–5.

[11] Tashiro T, Mashima Y, Yamamori H, Horibe K, Nishizawa M, Okui K. Alteration of whole-body protein kinetics according to severity of surgical trauma in patients receiving total parenteral nutrition. JPEN J Parenter Enteral Nutr 1991;15:169–72.

[12] Tashiro T, Yamamori H, Takagi K, Morishima Y, Nakajima N. Effect of severity of stress on whole-body protein kinetics in surgical patients receiving parenteral nutrition. Nutrition 1996;12:763–5.

[13] Tipton KD, Hamilton DL, Gallagher IJ. Assessing the role of muscle protein breakdown in response to nutrition and exercise in humans. Sports Med 2018;48:53–64.

[14] Holm L, O'Rourke B, Ebenstein D, Toth MJ, Bechshoeft R, Holstein-Rathlou N-H, et al. Determination of steady-state protein breakdown rate in vivo by the

disappearance of protein-bound tracer-labeled amino acids: a method applicable in humans. Am J Physiol Endocrinol Metab 2013;304:E895–907.

[15] Holm L, Dideriksen K, Nielsen RH, Doessing S, Bechshoeft RL, Højfeldt G, et al. An exploration of the methods to determine the protein-specific synthesis and breakdown rates in vivo in humans. Physiol Rep 2019;7:e14143.

[16] Varadhan KK, Constantin-Teodosiu D, Constantin D, Greenhaff PL, Lobo DN. Inflammation-mediated muscle metabolic dysregulation local and remote to the site of major abdominal surgery. Clin Nutr 2018;37:2178–85.

[17] Platell C, Hall J. What is the role of mechanical bowel preparation in patients undergoing colorectal surgery? Dis Colon Rectum 1998;41:875–82; discussion 882-883.

[18] Yuill KA, Richardson RA, Davidson HIM, Garden OJ, Parks RW. The administration of an oral carbohydrate-containing fluid prior to major elective upper-gastrointestinal surgery preserves skeletal muscle mass postoperatively--a randomised clinical trial. Clin Nutr 2005;24:32–7.

[19] Gustafsson UO, Scott MJ, Hubner M, Nygren J, Demartines N, Francis N, et al. Guidelines for perioperative care in elective colorectal surgery: Enhanced Recovery After Surgery (ERAS®) Society recommendations: 2018. World J Surg 2019;43:659–95.

[20] El-Sharkawy AM, Daliya P, Lewis-Lloyd C, Adiamah A, Malcolm FL, Boyd-Carson H, et al. Fasting and surgery timing (FaST) audit. Clin Nutr 2021;40:1405–12.

[21] Matthews DE, Motil KJ, Rohrbaugh DK, Burke JF, Young VR, Bier DM. Measurement of leucine metabolism in man from a primed, continuous infusion of L-[1-3C]leucine. Am J Physiol 1980;238:E473-479.

[22] Rennie MJ, Edwards RH, Halliday D, Matthews DE, Wolman SL, Millward DJ. Muscle protein synthesis measured by stable isotope techniques in man: the effects of feeding and fasting. Clin Sci (Lond) 1982;63:519–23.

[23] Ford GC, Cheng KN, Halliday D. Analysis of (1-13C)leucine and (13C)KIC in plasma by capillary gas chromatography/mass spectrometry in protein turnover studies. Biomed Mass Spectrom 1985;12:432–6.

[24] Garlick PJ, Wernerman J, McNurlan MA, Essen P, Lobley GE, Milne E, et al. Measurement of the rate of protein synthesis in muscle of postabsorptive young men by injection of a “flooding dose” of [1-13C]leucine. Clin Sci 1989;77:329–36.

[25] Harrison RA, Lewin MR, Halliday D, Clark CG. Leucine kinetics in surgical patients. I: A study of the effect of surgical “stress.” Br J Surg 1989;76:505–8.

[26] Harrison RA, Lewin MR, Halliday D, Clark CG. Leucine kinetics in surgical patients. II: A study of the effect of malignant disease and tumour burden. Br J Surg 1989;76:509–11.

[27] Wilkinson DJ. Historical and contemporary stable isotope tracer approaches to studying mammalian protein metabolism. Mass Spectrom Rev 2018;37:57–80.

[28] Page MJ, McKenzie JE, Bossuyt PM, Boutron I, Hoffmann TC, Mulrow CD, et al. The PRISMA 2020 statement: an updated guideline for reporting systematic reviews. BMJ 2021;372:n71.

[29] Shea BJ, Reeves BC, Wells G, Thuku M, Hamel C, Moran J, et al. AMSTAR 2: a critical appraisal tool for systematic reviews that include randomised or non-randomised studies of healthcare interventions, or both. BMJ 2017;358:j4008.

[30] Millward DJ, Smith K. The application of stable-isotope tracers to study human musculoskeletal protein turnover: a tale of bag filling and bag enlargement. J Physiol 2019;597:1235–49.

[31] Tashiro T, Yamamori H, Takagi K, Morishima Y, Nakajima N. Increased contribution by myofibrillar protein to whole-body protein breakdown according to severity of surgical stress. Nutrition 1996;12:685–9.

[32] MacLennan PA, Rennie MJ. Effects of ischaemia, blood loss and reperfusion on rat muscle protein synthesis, metabolite concentrations and polyribosome profiles in vivo. Biochem J 1989;260:195–200.

[33] Tjäder I, Essen P, Garlick PJ, McMnurlan MA, Rooyackers O, Wernerman J. Impact of surgical trauma on human skeletal muscle protein synthesis. Clin Sci (Lond) 2004;107:601–7.

[34] Higgins JPT, Thomas J, Chandler J, Cumpston M, Li T, Page MJ, Welch VA (editors). Cochrane Handbook for Systematic Reviews of Interventions version 6.2 (updated February 2021). Cochrane, 2021. Available from www.training.cochrane.org/handbook. (accessed June 7, 2021).

[35] Hozo SP, Djulbegovic B, Hozo I. Estimating the mean and variance from the median, range, and the size of a sample. BMC Med Res Methodol 2005;5:13.

[36] Higgins JPT, Altman DG, Gøtzsche PC, Jüni P, Moher D, Oxman AD, et al. The Cochrane Collaboration's tool for assessing risk of bias in randomised trials. BMJ 2011;343:d5928.

[37] Pustejovsky JE, Rodgers MA. Testing for funnel plot asymmetry of standardized mean differences. Res Synth Methods 2019;10:57–71.

[38] DerSimonian R, Laird N. Meta-analysis in clinical trials. Control Clin Trials 1986;7:177–88.

[39] Knapp G, Hartung J. Improved tests for a random effects meta-regression with a single covariate. Stat Med 2003;22:2693–710.

[40] Higgins JPT, Thompson SG. Quantifying heterogeneity in a meta-analysis. Stat Med 2002;21:1539–58.

[41] Lattermann R, Carli F, Wykes L, Schricker T. Epidural blockade modifies perioperative glucose production without affecting protein catabolism. Anesthesiology 2002;97:374–81.

[42] Carli F, Webster JD, Halliday D. Growth hormone modulates amino acid oxidation in the surgical patient: leucine kinetics during the fasted and fed state using moderate nitrogenous and caloric diet and recombinant human growth hormone. Metab Clin Exp 1997;46:23–8.

[43] Carli F, Ball J, Wykes L, Kubow S. Oral whey protein decreases protein breakdown and increases protein balance in surgical patients. A stable isotope study. Can J Anesth 2011;58:S13.

[44] Hammarqvist F, Sandgren A, Andersson K, Essén P, McNurlan MA, Garlick PJ, et al. Growth hormone together with glutamine-containing total parenteral nutrition maintains muscle glutamine levels and results in a less negative nitrogen balance after surgical trauma. Surgery 2001;129:576–86.

[45] Essén P, McNurlan MA, Sonnenfeld T, Milne E, Vinnars E, Wernerman J, et al. Muscle protein synthesis after operation: effects of intravenous nutrition. Eur J Surg 1993;159:195–200.

[46] López-Hellín J, Baena-Fustegueras JA, Vidal M, Riera SS, García-Arumí E. Perioperative nutrition prevents the early protein losses in patients submitted to gastrointestinal surgery. Clin Nutr 2004;23:1001–8.

[47] Lattermann R, Schricker T, Wachter U, Goertz A, Georgieff M. Intraoperative epidural blockade prevents the increase in protein breakdown after abdominal surgery. Acta Anaesthesiol Scand 2001;45:1140–6.

[48] Carli F, Webster J, Pearson M, Forrest J, Venkatesan S, Wenham D, et al. Postoperative protein metabolism: effect of nursing elderly patients for 24 h after abdominal surgery in a thermoneutral environment. Br J Anaesth 1991;66:292–9.

[49] Carli F, Webster J, Pearson M, Pearson J, Bartlett S, Bannister P, et al. Protein metabolism after abdominal surgery: effect of 24-h extradural block with local anaesthetic. Br J Anaesth 1991;67:729–34.

[50] Carli F, Webster JD, Halliday D. A nitrogen-free hypocaloric diet and recombinant human growth hormone stimulate postoperative protein synthesis: fasted and fed leucine kinetics in the surgical patient. Metabolism 1997;46:796–800.

[51] López Hellín J, Baena-Fustegueras JA, Sabín-Urkía P, Schwartz-Riera S, García-Arumí E. Nutritional modulation of protein metabolism after gastrointestinal surgery. Eur J Clin Nutr 2008;62:254–62.

[52] Carli F, Ramachandra V, Gandy J, Merritt H, Ford GC, Read M, et al. Effect of general anaesthesia on whole body protein turnover in patients undergoing elective surgery. Br J Anaesth 1990;65:373–9.

[53] Yeh DD, Fuentes E, Quraishi SA, Cropano C, Kaafarani H, Lee J, et al. Adequate nutrition may get you home. JPEN J Parenter Enteral Nutr 2016;40:37–44.

[54] Caso G, Vosswinkel JA, Garlick PJ, Barry MK, Bilfinger TV, McNurlan MA. Altered protein metabolism following coronary artery bypass graft (CABG) surgery. Clin Sci (Lond) 2008;114:339–46.

[55] Gillis C, Carli F. Promoting perioperative metabolic and nutritional care. Anesthesiology 2015;123:1455–72.

[56] Pöyhönen MJ, Takala JA, Pitkänen O, Kari A, Alhava E, Alakuijala LA, et al. Urinary excretion of polyamines in patients with surgical and accidental trauma: effect of total parenteral nutrition. Metabolism 1993;42:44–51.

[57] Svanfeldt M, Thorell A, Nygren J, Ljungqvist O. Postoperative parenteral nutrition while proactively minimizing insulin resistance. Nutrition 2006;22:457–64.

[58] Schricker T, Lattermann R. Perioperative catabolism. Can J Anaesth 2015;62:182–93.

[59] Lattermann R, Wykes L, Eberhart L, Carli F, Meterissian S, Schricker T. A randomized controlled trial of the anticatabolic effect of epidural analgesia and hypocaloric glucose. Reg Anesth Pain Med 2007;32:227–32.

[60] Schricker T, Meterissian S, Lattermann R, Adegoke OAJ, Marliss EB, Mazza L, et al. Anticatabolic effects of avoiding preoperative fasting by intravenous hypocaloric nutrition: a randomized clinical trial. Ann Surg 2008;248:1051–9.

[61] Lugli AK, Schricker T, Wykes L, Lattermann R, Carli F. Glucose and protein kinetics in patients undergoing colorectal surgery: perioperative amino acid versus hypocaloric dextrose infusion. Metab Clin Exp 2010;59:1649–55.

[62] Lattermann R, Carli F, Wykes L, Schricker T. Perioperative glucose infusion and the catabolic response to surgery: the effect of epidural block. Anesth Analg 2003;96:555–62.

[63] Schricker T, Meterissian S, Wykes L, Eberhart L, Lattermann R, Carli F. Postoperative protein sparing with epidural analgesia and hypocaloric dextrose. Ann Surg 2004;240:916–21.

[64] Schricker T, Wykes L, Eberhart L, Carli F, Meterissian S. Randomized clinical trial of the anabolic effect of hypocaloric parenteral nutrition after abdominal surgery. Br J Surg 2005;92:947–53.

[65] Schricker T, Wykes L, Meterissian S, Hatzakorzian R, Eberhart L, Carvalho G, et al. The anabolic effect of perioperative nutrition depends on the patient’s catabolic state before surgery. Ann Surg 2013;257:155–9.

[66] Fern EB, Garlick PJ, McNurlan MA, Waterlow JC. The excretion of isotope in urea and ammonia for estimating protein turnover in man with [15N]glycine. Clin Sci (Lond) 1981;61:217–28.

CHAPTER II:

USE OF DEUTERIUM-OXIDE STABLE ISOTOPE TRACER TO STUDY HUMAN METABOLISM

1. INTRODUCTION

1.1 DEUTERIUM-OXIDE STABLE ISOTOPE TRACER

Stable isotopes represent elements that are chemically and functionally identical to their more common isotope counterparts, yet differ in mass due to the addition of 1 or more neutrons within their atomic nucleus. These isotopes occur naturally in very low quantities and contrast with radioactive isotopes, in that their nuclei are stable and non-radioactive. This makes stable isotopes suitable as metabolic tracers for use across a variety of biological and non-biological fields of research, with some of the most commonly employed stable isotope tracers being those of nitrogen (^{15}N), oxygen (^{18}O), carbon (^{13}C) and hydrogen (^{2}H). Following the discovery of deuterium (^{2}H), the stable isotope of hydrogen, by Urey, Brickwedde, & Murphy in 1932[1,2], deuterium became one of the first stable isotopes to be employed as a metabolic tracer in the seminal works of Schoenheimer, Rittenberg, and Ussing, who demonstrated deuterium to incorporate into a variety of metabolic pools[3–5]. While future implementation of stable isotopes in metabolic research slowed following the second world war and the concomitant increase in availability of radioactive isotopes and their associated analytical tools, concerns over their safety in biological research resulted in a resurgence in stable isotope tracers from the 1970s onwards[6].

While early investigations involving stable isotope tracers had demonstrated their utility for specificity towards different metabolic substrates, deuterium-oxide (heavy water) was soon revisited as a tracer capable of enabling numerous metabolic measurements simultaneously[6], due its metabolic incorporation via the body water pool. While this initial renaissance primarily focused on D2O's application to glucose[7] and lipid metabolism[8], attention soon turned to its utilisation for slow-turnover metabolic pools, such as skeletal muscle[9] and cells of the adaptive immune system[10]. This was aided by D2O's ease of oral administration across prolonged periods thanks to its relatively long half-life (~10 days within the body water pool). As D2O equilibrates within the body water pool, it is then transported intracellularly where deuterium is incorporated into a variety of molecules via condensation/hydrolysis reactions *de novo*, which occurs at relatively constant rates[11]. This enables for maintenance of a steady state precursor pool via daily or even weekly top-up doses (although this is generally termed pseudo-steady state dosage). Similar to applications with other stable isotope tracer methodologies, use of deuterium oxide for metabolic measurements generally conforms to a precursor: product model, whereby measurements of metabolic incorporation (substrate turnover) are a function of the availability of the substrate precursor[6]. This circumnavigates the limitations of alternative stable isotope approaches whereby substrate specific isotopes are utilised, whose innate properties may alter cellular and physiological responses (e.g. stable isotope amino acids) or be predicated on the assumption of substrate transport into cellular pools occurring at a constant rate (e.g. amino acid transport)[12]. While the true precursors for many metabolic pools are rarely measured due the difficulty in their repeated or accurate sampling (e.g. aminoacyl-tRNA pool for proteins)[11], deuterium-oxide enables for accessible pseudo-precursor sampling through the ability to measure deuterium enrichment within body water pools such as saliva or urine, which can be measured both non-invasively and have demonstrated direct correlation with deuterium enrichment of the true metabolic precursor pools of interest[13–15]. While this generally requires further considerations in order to accurately model molecular amplification or theoretical labelling sites, use of pseudo-precursor pools aids metabolic measurements where sampling may need to be limited for ethical or logistical constraints (e.g. tissue biopsies of critical care patients or children) or longitudinal studies where deuterium-oxide levels require monitoring over a period of weeks-months.

With the increased interest in systems biology in recent years due to the fast-moving development of -omics based technologies, the application of stable isotopes to measure metabolic processes at a systems-wide level has gained recent attention. Primarily, this has focused on the application of D2O for the labelling of amino acid polypeptides in order to study proteome dynamics[16–19], but also cellular proliferation[10,20,21]. While information on cellular protein turnover is critical to understand proteostasis, this has also proven attractive due to the stochastic nature of proteomics LC-MS data and the combinatorial principles that govern polypeptide synthesis enabling for more simplistic mass spectrometry analysis, at least in principle, compared to other mass spectrometry analyses of metabolites and lipids. Over recent years several software have become available for deuterium-labelled mass isotopic distribution analysis of LC-MS proteomics data[22], where they have been successfully utilised in both pre-clinical and human models[19]. Analysis of this nature is dependent on precise analytical measurements, with isotopic analysis of this nature requiring high-resolution mass spectrometry instrumentation. In humans, for sufficient resolution and analytical precision this necessitates enrichment of deuterium within the body water pool to be approximately 2%, with higher quantities of D2O frequently being utilised in cell culture and animal models[23]. While promising, these techniques are still in a stage of relative infancy compared to more established quantitative protocols.

Since deuterium-oxide was revisited as a metabolic tracer, less attention has been given to the utilisation of this stable isotope tracer towards the study of nucleic acid metabolism (DNA/RNA), especially when compared to the advancements seen in investigations of lipid metabolism over the last ~80 years and the recent interest in deuterium-oxide as a metabolic tracer for the study of protein and metabolite turnover across the past ~10 years[24]. While early investigations into the kinetic analysis of cell proliferation via isotope incorporation began with the use of radioactive tracers that are now deemed unethical for human research, use of deuterium-based stable isotope tracers (D2O and deuterated glucose) are beginning to receive attention for their suitability towards the study of nucleic acid metabolism across a range of physiology and diseases[25–27]. Similar to other metabolic pools already described, use of deuterium-oxide enables for *de novo* incorporation into the (deoxy)ribose moieties of either DNA or RNA, which occurs at high rates during cell proliferation[10]. As ribosomal RNA constitutes approximately 80% of all cellular RNA, deuterium incorporation into ribose moieties can be used to indicate rates of ribosomal synthesis and biogenesis[28], while measurements of deuterium incorporation into the deoxyribose moieties of DNA have provided novel information on the kinetics of cells whose altered rates of cellular proliferation are implicated in a variety of diseases - such as peripheral blood mononuclear B- and T-cells in leukaemia[29] and HIV patients[26]. While pulse-labelling approaches with deuterated glucose have been successfully applied to characterise neutrophil half-lives and labelling kinetics[30], an abundant immune cell type known for its short circulatory life-span, use of deuterium oxide which has a much slower rate of cellular incorporation has proven suitable for prolonged calculation of proliferation in slow-turnover peripheral T-cells[20,26].

1.2 ASSESSING CELL PROLIFERATION THROUGH ^{2}H-LABELLING OF DNA

Initial assessments of isotope incorporation into DNA moieties to measure cell proliferation involved toxic or radioactive analogues that generally were incorporated via salvage pathways[24]. While able to provide early estimates of cell turnover, these measurements were confounded by both artifacts via physiological toxicity impacting cell cycle dynamics and lifespan, as well as difficult to predict non-uniform incorporation via secondary substrate (base or nucleoside) salvage pathways[10]. Alternatively, the *de novo* synthesis pathway predominates cellular contribution to the deoxyribose precursor pool of deoxyribonucleotide-triphosphates (dNTPs), and primarily derives from extracellular glucose flux with input from extracellular nucleoside concentrations or deoxyribose reutilisation following DNA degradation both being negligible. As deuterium-oxide equilibrates with the cellular water pool, it is incorporated at multiple stages of the *de novo* synthesis pathway including glycolysis/gluconeogenesis, the pentose phosphate pathway and ribonucleotide reductase enzyme activity[10]. To avoid the input of base purine/pyrimidine secondary metabolism (from which ^{2}H also becomes incorporated via *de novo* synthesis but is additionally impacted by base salvage) it is recommended that subsequent mass spectrometric analyses specifically target the deoxyribose moiety exclusively, omitting the base portion containing purine deoxyribonucleosides, with analysis of derivatives including the base portion being shown to increase physiological variability and underestimate cellular proliferation rates[31].

At low level body water ^{2}H enrichments (~2%) it is unlikely that deuterium will bind at more than one of the seven possible sites of deoxyribose within slow-turnover cell types, while within rapidly dividing cells it is likely that ^{2}H will bind multiple sites - with these sites providing an amplification factor as a function of body water ^{2}H enrichment[20]. This poses several analytical considerations: firstly, within slow-turnover cells it will be possible to assume that detection at M^{+1} will represent a near complete sum of deuterated deoxyribose derivative compared to base peak M^0, whereas within fast-turnover cell types it will be necessary to assess the isotopic envelope for complete determination of enrichment levels (e.g. M^{+2} and M^{+3}). Secondly, in order to more accurately model the precursor availability of ^{2}H for slow-turnover cell types, a factor reflecting the biological amplification due to the multiple incorporation sites available must be taken into account for modelling slow-turnover cellular proliferation (although as stated above, it is unlikely these will all become labelled). The amplification factor can be calculated from a fast-turnover cell type that is fully enriched to isotopic plateau, from which a fractional replacement rate can be determined and applied to calculate slow-turnover proliferation rates. For example, in a human study assessing naïve T-lymphocyte kinetics[31], granulocytes and monocytes were used for the calculation of fractional replacement rates where they observed an enrichment plateau at 7-10 days of the 8-10 week labelling experiment, with cellular deoxyribose enrichments reaching ~7% at ~2.0% body water deuterium enrichment (amplification factor of ~3.5). This enabled modelling of proliferation rates for slow-turnover naïve T-lymphocytes which demonstrated half-lives ~700 days (fractional replacement rate of ~0.1% per day). This suggests that although D2O may be highly suitable for proliferation measurements in slow-turnover cell types, it is generally still prudent to include a fast-turnover cell type as an internal reference.

While it is possible to perform these analyses with LC-MS, the majority of published reports opt for GC-MS instrumentation[10,32,33], where changes in the ratio of M0 and M^{+1} ions for deoxyribose derivatives are quantified by selected ion-monitoring (SIM). While this has successfully demonstrated analytical precision capable of quantifying changes in deuterium incorporation over time in slow-proliferation cell types[33], a recent report measuring RNA turnover in both proliferating immune cells and skeletal muscle utilised selected reaction monitoring (SRM)[28], which in theory, should provide greater analytical sensitivity. This may be especially relevant to slow-turnover cell types, whose levels of deuterium incorporation will inevitably be lower across time as deuterium is incorporated. Future studies may therefore benefit from implementing SRM to quantify deuterium enrichment in the deoxyribose moieties of hydrolysed DNA via GC-MS, especially in cases where analytical sensitivity at low relative deuterium enrichments is critical.

1.3 KINETIC MEASUREMENTS OF THE CELLULAR PROTEOME WITH DEUTERIUM-OXIDE

While crude or targeted stable isotopic measurements of protein and tissue turnover have proven insightful towards our understanding of protein kinetics across health and disease[6,34], the proteome represents a heterogenous pool of tens of thousands of proteins that exhibit diverse functions. While changes in mRNA expression provide meaningful insights to cellular biology, it has been repeatedly demonstrated that these do not correlate well with protein abundance[35], particularly at cellular level[36]. As such, rates of protein turnover represent an important aspect of proteostasis that is often under-examined. Many pathologies exhibit changes in metabolic rate and cellular remodelling that are either driven or reflect their associated pathologies. Further information on rates of cellular protein turnover across the proteome may inform our ability to diagnose and understand a variety of these conditions, while possibly providing future novel biomarkers based upon protein kinetics.

While early implementation of stable isotopes for kinetic proteome-wide measurements in cell culture and animal models introduced high levels of stable isotopically-labelled amino acids through the diet to enrich peptides/proteins[6], dietary enrichment at these levels is unsuitable for human use. This has necessitated an alternative approach, with D2O representing a suitable replacement metabolic tracer[23]. Across the last decade, investigations into proteome kinetics using D2O have been successfully employed and represent an exciting avenue for future development. Much of this work has been led by the Price[18,37] and Ping[19,38] laboratories, drawing upon previous principles outlined by Hellerstein and Neese[39]. This has centred around analysis of shifts in the mass isotopomer distribution from 'bottom-up' proteomics experiments, which is characterised by reductions on the M0 peptide ion (which alone can be used to calculate half-life/decay rate of the base monoisotopic peak) as well as the appearance and increased intensity of mass isotopic peaks at set intervals related to the M^{+1}, M^{+2}, M^{+3}…for specific peptides detected at MS1 level[22]. Interpretation of these changes as a result of stable isotope introduction depends on comparisons between observed experimental and theoretical mass isotopomer distributions, which can be calculated from the number of exchangeable hydrogens possible within each peptide sequence. As the mass addition from deuterium is known, this enables for prediction of shifts in the mass isotopic distribution over time as deuterium is incorporated. This is dependent on the calculation of accurate peptide mass, which is generally computed through a series of binomial calculations[40]. From this, changes in peptide mass arising from deuterium incorporation can be calculated through combinatorial probability, using theoretical or previously estimated experimental values to model the number of hydrogen atoms available for exchange within a peptide's amino acid sequence[22,37]. As expected, with maintenance of a stable precursor pool, calculations of turnover follow a precursor: product model, with a maximum asymptote value of 1 typically employed during rate calculations[37].

There are several approaches to model turnover rates from stable isotopically-labelled proteomics data. These typically involve either calculating a decay rate of the monoisotopic peak over time as its intensity depletes or comparing shifts across the mass isotopic distribution over time relative to theoretical distributions modelled as a function of deuterium-labelling[22,37,39,41]. Both assess peptide isotopic envelopes at MS1 to quantify these changes in peptides that have typically already been identified via tandem MS and standard database searching. At present, there is no software whose algorithm is capable of accounting for shifts in mass as a result of heavy mass isotopomers and their subsequent fragmentation patterns during database searching. Expectedly, the increased isolation of deuterated precursors for fragmentation and identification via MS2 (DDA) has been associated with decreased rates of peptide and protein identifications during deuterium-labelling experiments[22]. Additionally, data quality controls during secondary analysis of mass isotopic distributions required to meet expected m/z accuracy and peak intensities acts to further decrease the number of peptides (and therefore proteins) taken forth for turnover quantification in proteomics datasets[37]. Together, this has typically resulted in the calculation of turnover rates for only a few hundred proteins or less in published experimental datasets[18,37,42], although greater depth has been reported[19,38]. This emphasises the importance of high-quality proteomics datasets in order to improve rates of protein identification for downstream turnover analysis. While quantitative accuracy is vital within all mass spectrometry applications, this poses a major constraint for the comprehensive analysis of proteome kinetics at present.

There are currently several bioinformatic software capable of analysing deuterium-labelled proteomics datasets, with three of these being openly-available. DeuteRater[37] builds upon the combinatorial principles outlined in Hellerstein and Neese's work on MIDA, and is freely available as both a GUI and Python source code, published on GitHub. d2ome[43] is also a freely available C++ resource on GitHub, while ProTurn[19,38] utilises Java and R programming languages. As expected, these three software model rates of protein turnover through assessments of mass isotopic profiles, where they are capable of combining common database search engines such as Mascot[44], SEQUEST[45] and Andromeda[46], with software specific mass isotopomer detection and quantification algorithms. These workflows generally conform to three stages of analysis: pre-processing, peak detection (of mass isotopic distributions) and fraction new/rate calculations. All three freely-available software accept open file formats; mzid and mzml, with DeuteRater further requiring manual input of a reference file containing all identified sequences from database searches specified at a user-defined limit. All three rate calculation algorithms utilise nonlinear least squares[47] to fit label incorporation, with differences arising from differential calculation between these algorithms not yet being comprehensively investigated. It is likely kinetic proteomic analysis will undergo and benefit from future computational development as more researchers become interested, as has been observed with other proteomics applications in recent years[48–51].

1.4 REFERENCES

1. Urey, H. C., Brickwedde, F. G. & Murphy, G. M. A Hydrogen Isotope of Mass 2. *Phys. Rev.* **39**, 164–165 (1932).

2. Urey, H. C., Brickwedde, F. G. & Murphy, G. M. A Hydrogen Isotope of Mass 2 and its Concentration. *Phys. Rev.* **40**, 1–15 (1932).

3. Schoenheimer, R. & Rittenberg, D. Deuterium as an Indicator in the Study of Intermediary Metabolism. *Science* **82**, 156–157 (1935).

4. Foster, G. L., Keston, A. S., Rittenberg, D. & Schoenheimer, R. DEUTERIUM AS AN INDICATOR IN THE STUDY OF INTERMEDIARY METABOLISM: XII. THE ACTION OF PROTEOLYTIC ENZYMES ON PEPTIDES IN HEAVY WATER. *J. Biol. Chem.* **124**, 159–161 (1938).

5. Rittenberg, D. & Schoenheimer, R. Deuterium as an indicator in the study of intermediary metabolism. 11. Further studies on the biological uptake of deuterium into organic substances, with special reference to fat and cholesterol formation. *J. Biol. Chem.* **121**, 235–253 (1937).

6. Wilkinson, D. J. Historical and contemporary stable isotope tracer approaches to studying mammalian protein metabolism. *Mass Spectrom. Rev.* **37**, 57–80 (2018).

7. Previs, S. F. & Brunengraber, H. Methods for measuring gluconeogenesis in vivo. *Curr. Opin. Clin. Nutr. Metab. Care* **1**, 461–465 (1998).

8. Turner, S. M. *et al.* Measurement of TG synthesis and turnover in vivo by 2H2O incorporation into the glycerol moiety and application of MIDA. *Am. J. Physiol. Endocrinol. Metab.* **285**, E790-803 (2003).

9. Wilkinson, D. J. *et al.* A validation of the application of D2O stable isotope tracer techniques for monitoring day-to-day changes in muscle protein subfraction synthesis in humans. *Am. J. Physiol. - Endocrinol. Metab.* **306**, E571–E579 (2014).

10. Busch, R., Neese, R. A., Awada, M., Hayes, G. M. & Hellerstein, M. K. Measurement of cell proliferation by heavy water labeling. *Nat. Protoc.* **2**, 3045–3057 (2007).

11. Wilkinson, D. J., Brook, M. S. & Smith, K. Principles of stable isotope research – with special reference to protein metabolism. *Clin. Nutr. Open Sci.* **36**, 111–125 (2021).

12. Tipton, K. D., Hamilton, D. L. & Gallagher, I. J. Assessing the Role of Muscle Protein Breakdown in Response to Nutrition and Exercise in Humans. *Sports Med. Auckl. Nz* **48**, 53–64 (2018).

13. Holwerda, A. M. *et al.* Daily resistance-type exercise stimulates muscle protein synthesis in vivo in young men. *J. Appl. Physiol. Bethesda Md 1985* **124**, 66–75 (2018).

14. Moses, A. W. G., Slater, C., Preston, T., Barber, M. D. & Fearon, K. C. H. Reduced total energy expenditure and physical activity in cachectic patients with

pancreatic cancer can be modulated by an energy and protein dense oral supplement enriched with n-3 fatty acids. *Br. J. Cancer* **90**, 996–1002 (2004).

15. MacDonald, A. J. *et al.* Habitual Myofibrillar Protein Synthesis Is Normal in Patients with Upper GI Cancer Cachexia. *Clin. Cancer Res. Off. J. Am. Assoc. Cancer Res.* **21**, 1734–1740 (2015).

16. Holmes, W. E., Angel, T. E., Li, K. W. & Hellerstein, M. K. Chapter Seven - Dynamic Proteomics: In Vivo Proteome-Wide Measurement of Protein Kinetics Using Metabolic Labeling. in *Methods in Enzymology* (ed. Metallo, C. M.) vol. 561 219–276 (Academic Press, 2015).

17. Wang, D. *et al.* Characterization of human plasma proteome dynamics using deuterium oxide. *Proteomics Clin. Appl.* **8**, 610–619 (2014).

18. Price, J. C. *et al.* Measurement of human plasma proteome dynamics with (2)H(2)O and liquid chromatography tandem mass spectrometry. *Anal. Biochem.* **420**, 73–83 (2012).

19. Lam, M. P. Y. *et al.* Protein kinetic signatures of the remodeling heart following isoproterenol stimulation. *J. Clin. Invest.* **124**, 1734–1744 (2014).

20. Ahmed, R. *et al.* CD57+ Memory T Cells Proliferate In Vivo. *Cell Rep.* **33**, 108501 (2020).

21. Lahoz-Beneytez, J. *et al.* Human neutrophil kinetics: modeling of stable isotope labeling data supports short blood neutrophil half-lives. *Blood* **127**, 3431–3438 (2016).

22. Sadygov, R. G. Protein turnover models for LC–MS data of heavy water metabolic labeling. *Brief. Bioinform.* **23**, bbab598 (2022).

23. Miller, B. F. *et al.* CORP: The use of deuterated water for the measurement of protein synthesis. *J. Appl. Physiol.* **128**, 1163–1176 (2020).

24. Brook, M. S., Wilkinson, D. J., Atherton, P. J. & Smith, K. Recent developments in deuterium oxide tracer approaches to measure rates of substrate turnover: implications for protein, lipid, and nucleic acid research. *Curr. Opin. Clin. Nutr. Metab. Care* **20**, 375–381 (2017).

25. Patel, A. A. *et al.* The fate and lifespan of human monocyte subsets in steady state and systemic inflammation. *J. Exp. Med.* **214**, 1913–1923 (2017).

26. Ladell, K. *et al.* Central memory CD8+ T cells have a shorter lifespan and reduced abundance as a function of HIV disease progression. *J. Immunol. Baltim. Md 1950* **180**, 7907–7918 (2008).

27. Tak, T. *et al.* Human CD62Ldim neutrophils identified as a separate subset by proteome profiling and in vivo pulse-chase labeling. *Blood* **129**, 3476–3485 (2017).

28. Brook, M. S. *et al.* A novel D2O tracer method to quantify RNA turnover as a biomarker of de novo ribosomal biogenesis, in vitro, in animal models, and in human skeletal muscle. *Am. J. Physiol. Endocrinol. Metab.* **313**, E681–E689 (2017).

29. Messmer, B. T. *et al.* In vivo measurements document the dynamic cellular kinetics of chronic lymphocytic leukemia B cells. *J. Clin. Invest.* **115**, 755–764 (2005).

30. Koenderman, L., Tesselaar, K. & Vrisekoop, N. Human neutrophil kinetics: a call to revisit old evidence. *Trends Immunol.* **43**, 868–876 (2022).

31. Neese, R. A. *et al.* Measurement in vivo of proliferation rates of slow turnover cells by 2H2O labeling of the deoxyribose moiety of DNA. *Proc. Natl. Acad. Sci. U. S. A.* **99**, 15345–15350 (2002).

32. Mazzarello, A. N., Fitch, M., Hellerstein, M. K. & Chiorazzi, N. Measurement of Leukemic B-Cell Growth Kinetics in Patients with Chronic Lymphocytic Leukemia. in *Chronic Lymphocytic Leukemia: Methods and Protocols* (ed. Malek, S. N.) 129–151 (Springer, 2019). doi:10.1007/978-1-4939-8876-1_11.

33. Voogt, J. N. *et al.* Measurement of very low rates of cell proliferation by heavy water labeling of DNA and gas chromatography/pyrolysis/isotope ratio-mass spectrometric analysis. *Nat. Protoc.* **2**, 3058–3062 (2007).

34. Brook, M. S. & Wilkinson, D. J. Contemporary stable isotope tracer approaches: Insights into skeletal muscle metabolism in health and disease. *Exp. Physiol.* (2020) doi:10.1113/EP087492.

35. Vogel, C. & Marcotte, E. M. Insights into the regulation of protein abundance from proteomic and transcriptomic analyses. *Nat. Rev. Genet.* **13**, 227–232 (2012).

36. Brunner, A. *et al.* Ultra-high sensitivity mass spectrometry quantifies single-cell proteome changes upon perturbation. *Mol. Syst. Biol.* **18**, e10798 (2022).

37. Naylor, B. C. *et al.* DeuteRater: a tool for quantifying peptide isotope precision and kinetic proteomics. *Bioinformatics* **33**, 1514–1520 (2017).

38. Lau, E. *et al.* A large dataset of protein dynamics in the mammalian heart proteome. *Sci. Data* **3**, 160015 (2016).

39. Hellerstein, M. K. & Neese, R. A. Mass isotopomer distribution analysis at eight years: theoretical, analytic, and experimental considerations. *Am. J. Physiol.-Endocrinol. Metab.* **276**, E1146–E1170 (1999).

40. Rockwood, A. L. & Haimi, P. Efficient Calculation of Accurate Masses of Isotopic Peaks. *J. Am. Soc. Mass Spectrom.* **17**, 415–419 (2006).

41. Sadygov, R. G. Partial Isotope Profiles are Sufficient for Protein Turnover Analysis using Closed-form Equations of Mass Isotopomer Dynamics. *Anal. Chem.* **92**, 14747–14753 (2020).

42. Shankaran, M. *et al.* Circulating protein synthesis rates reveal skeletal muscle proteome dynamics. *J. Clin. Invest.* **126**, 288–302.

43. Sadygov, R. G. *et al.* d2ome, Software for in Vivo Protein Turnover Analysis Using Heavy Water Labeling and LC-MS, Reveals Alterations of Hepatic Proteome Dynamics in a Mouse Model of NAFLD. *J. Proteome Res.* **17**, 3740–3748 (2018).

44. Perkins, D. N., Pappin, D. J., Creasy, D. M. & Cottrell, J. S. Probability-based protein identification by searching sequence databases using mass spectrometry data. *Electrophoresis* **20**, 3551–3567 (1999).

45. Eng, J. K., McCormack, A. L. & Yates, J. R. An approach to correlate tandem mass spectral data of peptides with amino acid sequences in a protein database. *J. Am. Soc. Mass Spectrom.* **5**, 976–989 (1994).

46. Cox, J. *et al.* Andromeda: a peptide search engine integrated into the MaxQuant environment. *J. Proteome Res.* **10**, 1794–1805 (2011).

47. Byrd, R. H., Lu, P., Nocedal, J. & Zhu, C. A Limited Memory Algorithm for Bound Constrained Optimization. *SIAM J. Sci. Comput.* **16**, 1190–1208 (1995).

48. Röst, H. L. *et al.* OpenSWATH enables automated, targeted analysis of data-independent acquisition MS data. *Nat. Biotechnol.* **32**, 219–223 (2014).

49. Szyrwiel, L., Sinn, L., Ralser, M. & Demichev, V. Slice-PASEF: fragmenting all ions for maximum sensitivity in proteomics. 2022.10.31.514544 Preprint at https://doi.org/10.1101/2022.10.31.514544 (2022).

50. Demichev, V., Messner, C. B., Vernardis, S. I., Lilley, K. S. & Ralser, M. DIA-NN: Neural networks and interference correction enable deep proteome coverage in high throughput. *Nat. Methods* **17**, 41–44 (2020).

51. Zeng, W.-F. *et al.* AlphaPeptDeep: a modular deep learning framework to predict peptide properties for proteomics. *Nat. Commun.* **13**, 7238 (2022).

2. PROTEOME-WIDE TURNOVER MEASUREMENTS IN DIFFERENTIATING M1- AND M2-LIKE MACROPHAGES *EX VIVO*

ABSTRACT

Background and Aims: Deuterium-oxide (D_2O) stable isotope tracer has recently received attention as a tool to calculate individual protein turnover rates using ‘shotgun’ LC-MS proteomics. This study investigated whether this technique could be applied within a clinically relevant primary cell model of monocytes undergoing differentiation into M1 or M2 macrophages.

Methods: Two healthy blood donors provided 150ml whole blood for monocyte isolation. Eight samples were generated from each blood donor, so that 16 primary monocyte cell cultures were differentiated into macrophages. 5% D_2O was added at days 0 and 4 of a 7-day monocyte differentiation period. Proteome kinetics were measured via LC-MS and quantified using DeuteRater analytical software.

Results: Cells supplemented with 5% D_2O demonstrated similar rates of protein identification and iBAQ compared to matched H_2O controls. Greater than 40% of total identified proteins had rates of turnover quantified within D_2O-labelled cells through shifts in the mass isotopic distribution of individual peptides per protein, following stringent dataset filtering. Turnover rates within differentiating monocytes varied from ~0 to 0.83 day^{-1}, with an average turnover rate of 0.07 day^{-1}.

Conclusions: D_2O presents an effective metabolic tracer capable of enabling simultaneous quantification of protein abundance and turnover during dynamic metabolic processes within a primary cell model of differentiating monocytes.

Keywords: D_2O, protein turnover, proteomics, macrophages, monocytes.

2.1 INTRODUCTION

LC-MS proteomics technologies are advancing at a rapid pace and have recently achieved the sensitivity and throughput required for deep characterisation of a variety of immune cell phenotypes[25]. While great advancements have been made in monitoring alterations in the proteome of single cells, analysis is generally centred around the identification and measurement of protein abundance. Consequently, an important aspect of proteostasis – protein turnover – is often understudied and rarely accounted for. This may represent particular importance to clinical pathologies with known associations to altered cellular proliferation and protein turnover.

Deuterium-oxide (D_2O) represents a safe and versatile stable isotope tracer fit for human consumption at enrichments of 1-10%. Thus far, application of D_2O for measurements of protein turnover via LC-MS technologies have largely been limited to cell culture and pre-clinical models, primarily concerned with proof-of-concept (Chapter II, *section 1.1*).

This study looks to extend this approach to a more complex primary cell model of monocytes undergoing differentiation into macrophages, in the presence and absence of a known immunomodulatory stimulant, the adenosine receptor agonist, NECA[10]. This study aims to address whether D_2O is a suitable metabolic tracer for dynamic measurements of the proteome in a primary cell culture model of clinical relevance.

2.2 METHODS

Monocyte Isolation

150ml peripheral blood was obtained from healthy donors under approval from the University of Nottingham Medical School Ethics Committee (ref 161-1711) in accordance with the Declaration of Helsinki, with all participants providing informed consent. Blood was collected in heparinised 60ml syringes and was layered immediately on Lymphoprep (Stemcell technologies). Blood samples were separated through density centrifugation at 800g for 25min at 21°C on minimum brake. Peripheral blood mononuclear cells (PBMCs) were harvested from the buffy-coat layer and washed twice in endotoxin-free Phosphate Buffer Saline (PBS, Sigma) at 350g for 8min followed by 300g for 5 minutes. Cells were then resuspended in 400µl magnetic-activated cell sorting (MACS) buffer supplemented with PBS, 1% fetal calf serum (FCS) and 2mM EDTA. PBMCs were then incubated for 15 minutes at 4°C with 30µl CD14-antibody magnetic microbeads (Miltenyi). PBMCs were then passed through an LC column with a magnet to retain the CD14+ cells on the column while CD14- cells flowed through. Following three washes with MACS buffer, CD14+ cells were then eluted away from the magnet in 1ml MACS buffer.

Macrophage Cell Culture

CD14+ cells were spun for 5 minutes at 300g before resuspension in culture medium; RPMI 1640 (Hyclone), 10% v/v FCS (Sigma) and NaPy 1% v/v. CD14+ monocytes were then plated in ultra-low attachment 24-well plates (Corning Costar 3473) at a concentration of 10^6 cells per well. For M1-like macrophage differentiation, granulocyte-macrophage colony-stimulating factor (GMCSF, Peprotech) was added at day 0 and day 4 at 10ng/ml with either 5% H2O or 5% D2O in 1ml culture medium, in the presence or absence of 1µM of the adenosine receptor agonist, NECA (Sigma). For M2-like macrophages, macrophage colony-stimulating factor (MCSF, Immunotools) was added at day 0 and day 4 at 10ng/ml with either 5% H2O or 5% D2O in 1ml culture medium, in the presence or absence of 1µM of the adenosine receptor agonist, NECA (Sigma). On day 7, macrophages were washed with PBS twice and scraped in 200µl 100mM ammonium bicarbonate containing 0.1% SDS (pH 8) and transferred into 2ml Eppendorfs (Eppendorf, UK) for storage at -80ºC until further analysis.

Proteomics Analysis

Samples were pelleted via centrifugation at 17,000g for 1 minute, supernatant removed and samples were then processed according to the protocol; *Sample Preparation by Easy Extraction and Digestion* (SPEED) [1]. Briefly, cells were lysed in 100µl pure Trifluoroacetic acid (TFA) then neutralised with 10x 2M Tris-base in double-distilled water (ddH2O). Samples were then immediately reduced and alkylated with the addition of Tris (2-carboxyethyl) phosphine (TCEP) to a final concentration of 10 mM and Iodoacetamide (IAA) to a final concentration of 40mM, and incubated for 5 minutes at 95ºC. Protein concentrations were adjusted to 1µg/µl using a solution of 1x TFA to 10x 2M Tris in ddH2O, and Trypsin was added at a ratio of 1:100 for overnight digestion at 37ºC. Digestion was quenched through addition of TFA to a total concentration of 2% and peptides were desalted using Pierce C18 StageTips (ThermoScientific). Samples were then dried under nitrogen stream using a TurboVap (Biotage) at 40ºC for 30 minutes and stored at -20ºC until mass spectrometry analysis.

For mass spectrometry analyses, samples were resuspended in 95% ddH2O, 5% Acetonitrile (ACN) and 0.1% Formic acid. 1µg peptides were injected for analysis with a Q-Exactive orbitrap mass spectrometer (Thermo Scientific) in line with a Dionex Ultimate 3000 ultra-high pressure nano liquid chromatography system and electrospray ionisation source (Thermo Scientific). A non-linear gradient of solvent B (80% ACN (v/v) in 0.1% FA (v/v)) was applied for a total gradient time of 104 minutes and total run time of 120 minutes. Full MS scans were acquired at a resolution of 60,000 for the mass range 380-1300 m/z, with a precursor isolation window of 2 m/z for MS2 scans at a resolution of 17,500.

Raw data files were provided to the MaxQuant processing software (v. 2.1.3.0) and searched against the human Uniprot databases (UP000005640_9606.fa, UP000005640_9606_additional.fa) using the Andromeda search algorithm[2]. False-discovery rates were controlled at 1% for both peptide spectral matches (PSMs) and proteins. Peptides with a length of 7-50 amino acids were considered, with N-terminal acetylation and methionine oxidation specified as variable modifications and cysteine carbamidomethylation as a fixed modification. Maximum peptide mass was set at 5000 Da and spectra were searched with strict Trypsin specificity (KR not P), allowing up to two missed cleavage sites. Accurate mass identifications were transferred between samples using the ‘match between run’ setting of MaxQuant, with a match window of 0.7 minutes and an alignment window of 20 minutes. Quantitation was performed via intensity-based absolute quantification (iBAQ)[3,4].

MaxQuant search output files were formatted appropriately using Python programming language (v. 3.9.7) for input into the DeuteRater GUI (v. 5). Raw files were additionally converted to mzml format via ProteoWizard (v. 3.0) for peak-picking of the mass isotopic distribution by DeuteRater for peptides identified within the respective MaxQuant output file(s). Within the DeuteRater GUI, deuterium enrichment of the precursor pool was set at 5% for samples supplemented with D2O. The ‘% peptide fraction new’ was calculated via spacing-based measurements of changes in the mass isotopic distribution over time. Turnover rates for identified proteins were then calculated by fitting the ‘fraction new’ to a kinetic rate curve with equation: $1-e^{-rate*time}$, as specified by DeuteRater[5]. These results were further analysed via Python programming language (v. 3.9.7), in conjunction with the Python modules: pandas (v. 2.0.2), matplotlib (v. 3.5.3), seaborn (v. 0.12.2), scipy (v. 1.10.1), scikit-learn (v. 1.1.2) and numpy (1.20.3). PANTHER (release 17.0) was utilised for protein classifications and ontology analysis of associated biological functions.

2.3 RESULTS

Overview

Two healthy participants provided 150ml of blood each for cell culture analyses. Each blood sample enabled the culture of 8 replicate wells resulting in approximately 1 million macrophages per well. Respectively, 4 wells were utilised for the generation of the M1-like macrophage phenotype and 4 wells for the production of the M2-like macrophage phenotype. Each treatment (GMCSF or MCSF supplemented cells) were then divided again into H2O or D2O supplemented cells, with one well from each of these pairs then being further treated with the adenosine receptor agonist, NECA. Cumulatively, this resulted in n=2 for each specific treatment/condition combination within this pilot experiment.

Across the 16 experimental samples, there were ~190,000 peptide spectral matches (PSMs) relating to ~900 protein groups detected in the dataset. Across identified peptides, ~94% contained no missed cleavage sites (cleaved at K or R only, not P) and ~90% of peptides were identified without modifications (including contaminant peptides). Removal of contaminant proteins resulted in a final total of 823 protein groups across samples, which translates to ~700 protein groups detected per sample at 1% FDR. Ontology analyses conducted via PANTHER illustrate the range of protein classes and biological processes identified across samples, which encompass many processes highlighted previously via transcriptional[6] and single-cell proteomic analysis[7] of M1- and M2-like macrophages cultured *ex vivo* and from U-937 cell lines (Figure 1).

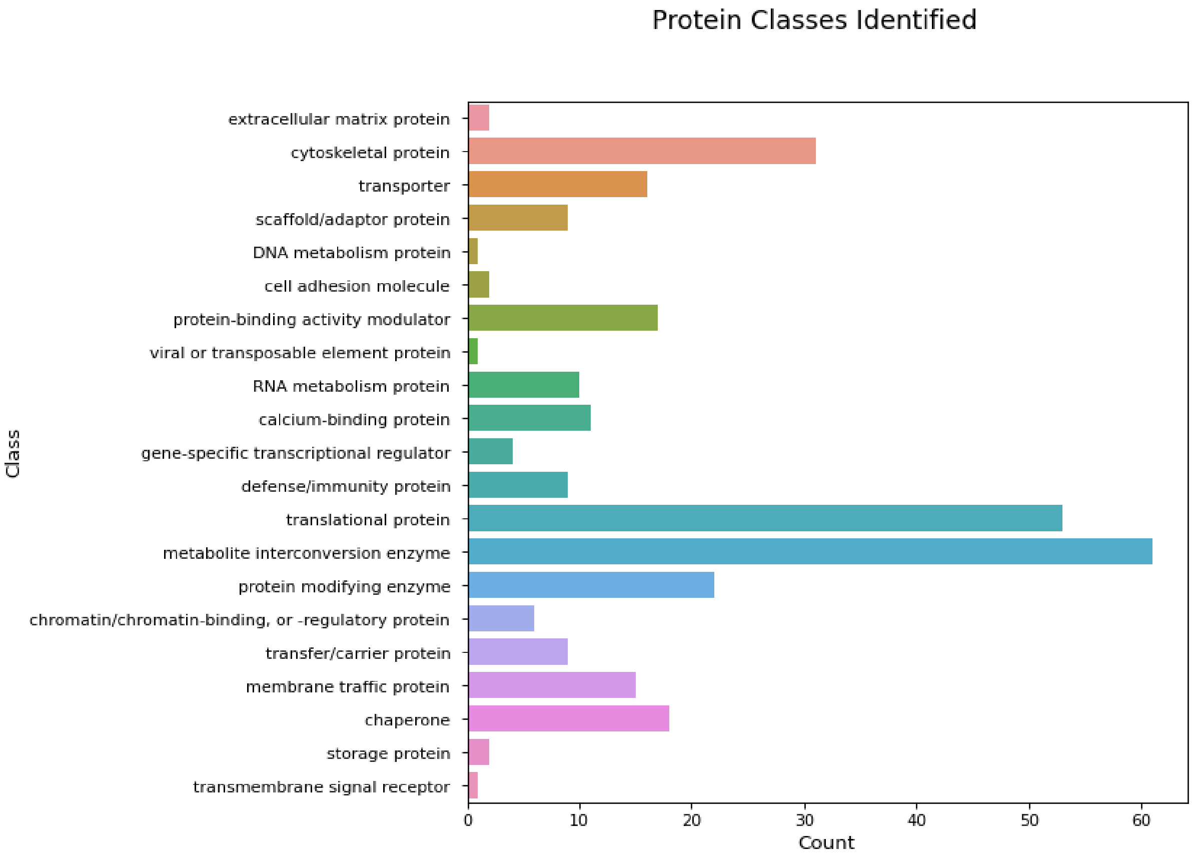

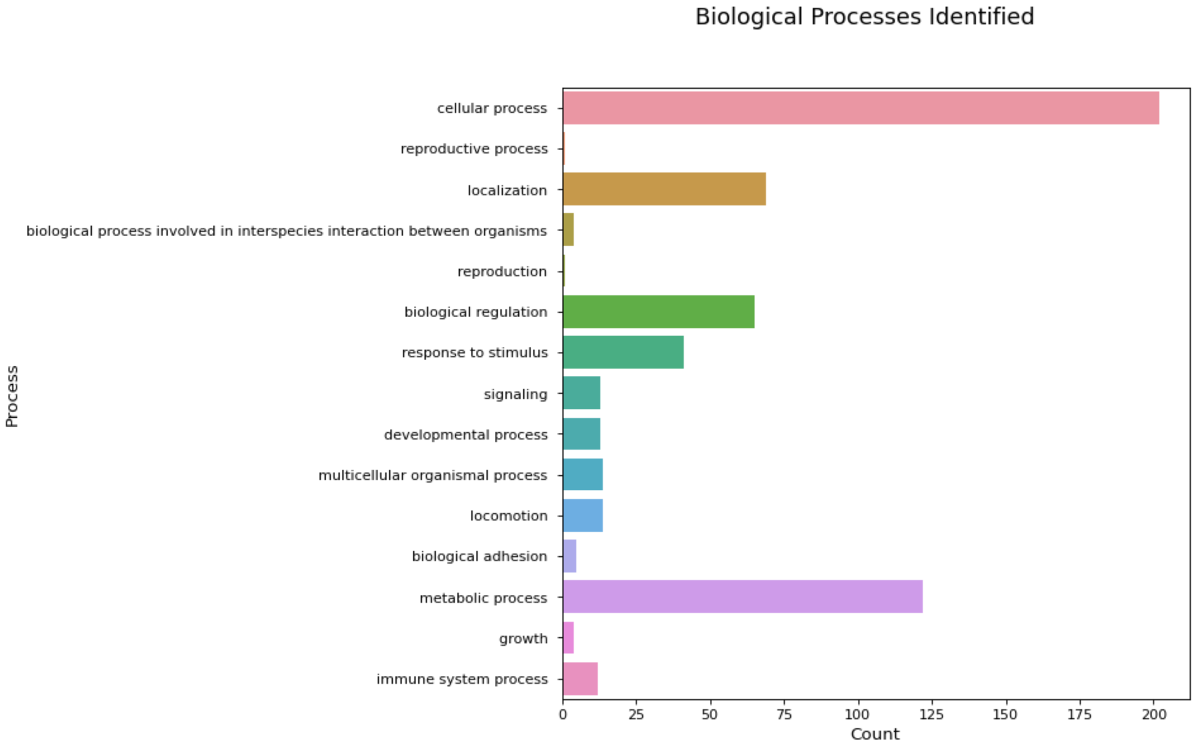

Figure 1: *Protein classes and biological processes associated with identified proteins across samples.*

It has previously been observed that deuterium-labelling coupled with data-dependent acquisition (DDA) results in decreasing rates of peptide and protein identifications over time as deuterium is increasingly incorporated into peptides and proteins *de novo*[8]. To assess whether deuterium-labelling resulted in a decrease in identifications within this dataset, experimental samples supplemented with 5% H2O and 5% D2O were compared for protein group identifications across all treatments.

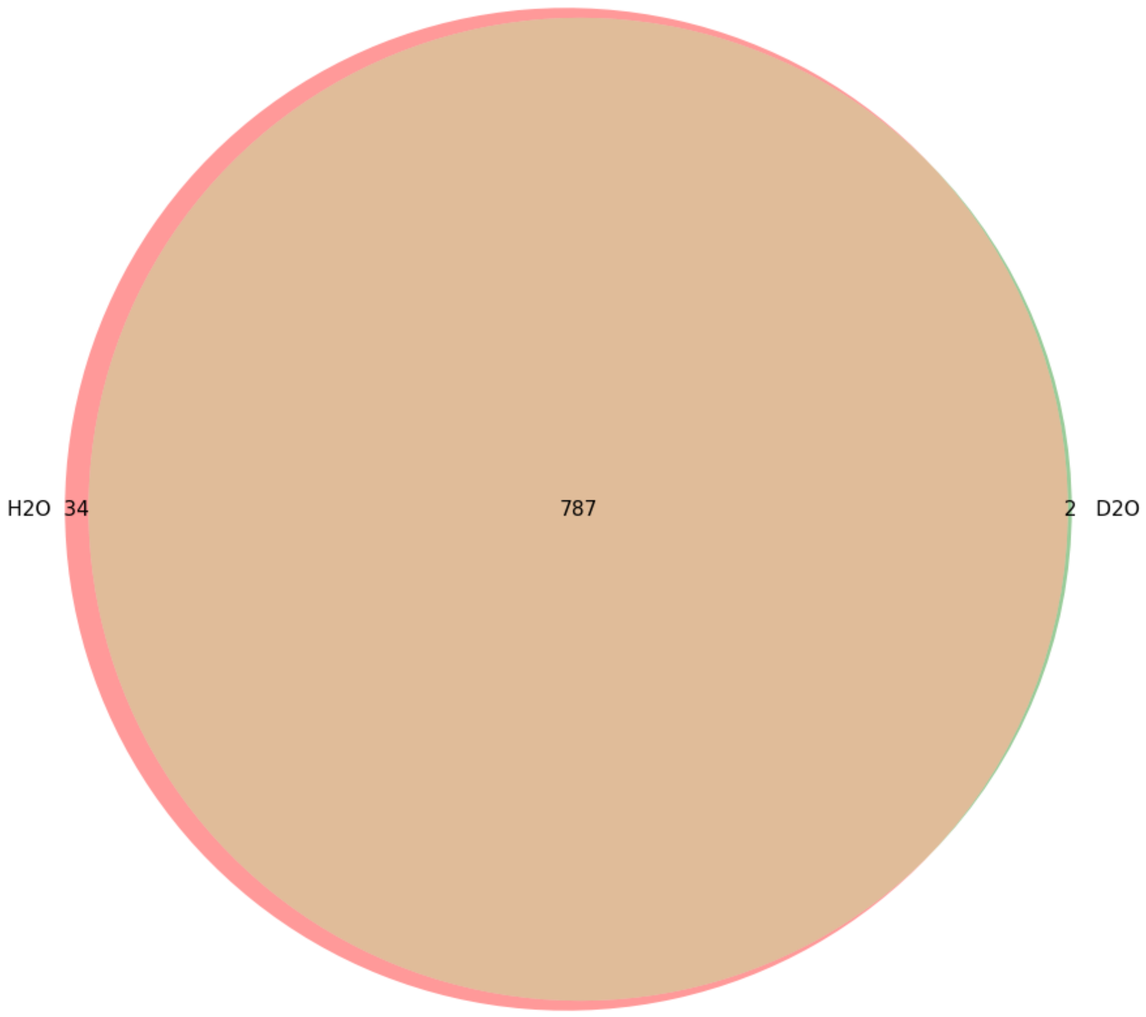

Figure 2: *Venn diagram depicting protein groups identified in samples supplemented with 5% H2O vs 5% D2O.* ***Gold;*** *depicts shared protein groups,* ***orange;*** *protein groups detected only in H2O supplemented samples and* ***green;*** *protein groups detected only in D2O supplemented samples.*

Figure 2 demonstrates a high degree of homology for protein group identifications between H2O and D2O supplemented samples, with 787 of 823 total protein groups shared between both conditions. There are more protein groups uniquely identified in H2O supplemented samples at 34, than the 2 unique protein groups identified in D2O supplemented samples, supporting a minor trend for higher average identifications when averaging the 8 individual H2O treatments vs the 8 individual D2O treatments (713 vs 672 protein groups, respectively). However, cumulatively, as demonstrated in Figure 2 above, this does not represent a tangible shift in rates of protein group identifications. In fact, there was a greater disparity in identification rates between blood donors (617 vs 768 protein groups identified on average per sample) than those samples supplemented with 5% H2O vs 5% D2O, suggesting introduction of deuterium-oxide to result in a lower degree of variation than that provided by interindividual variability.

iBAQ Quantitation

Intensity-based absolute quantitation (iBAQ) was chosen as the method of protein quantification for experimental samples due its utilisation of the entire (detected) mass isotopic cluster, in order to calculate protein abundance relative to the total number of theoretically observable tryptic peptides for a given protein[4]. This method of absolute quantification was deemed suitable for mass spectra containing peptides enriched with deuterium, where it is expected that shifts in the mass isotopic distribution over time as incorporation increases will ultimately lead to numerous peaks of comparable intensities[8].

The impacts of deuterium-labelling on iBAQ intensities relative to paired H2O control samples was first examined to ascertain the influence of deuterium-labelling on protein quantitation accuracy. Figure 3 illustrates log-transformed iBAQ data from H2O and D2O supplemented samples to correlate well across all treatments (GMCSF and MCSF supplementation, as well as NECA treatment). The correlation of these values is in line with other reports of correlations between technical replicates[3], further suggesting that iBAQ is a suitable method of protein quantitation for samples labelled with deuterium for parallel protein turnover experiments.

A

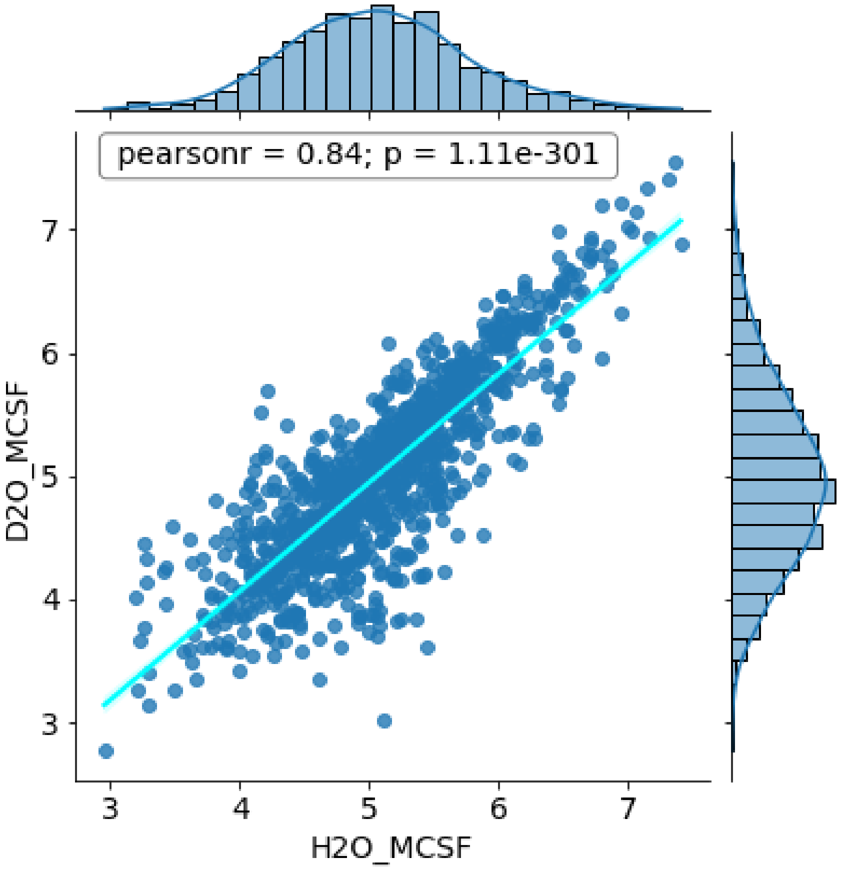

B

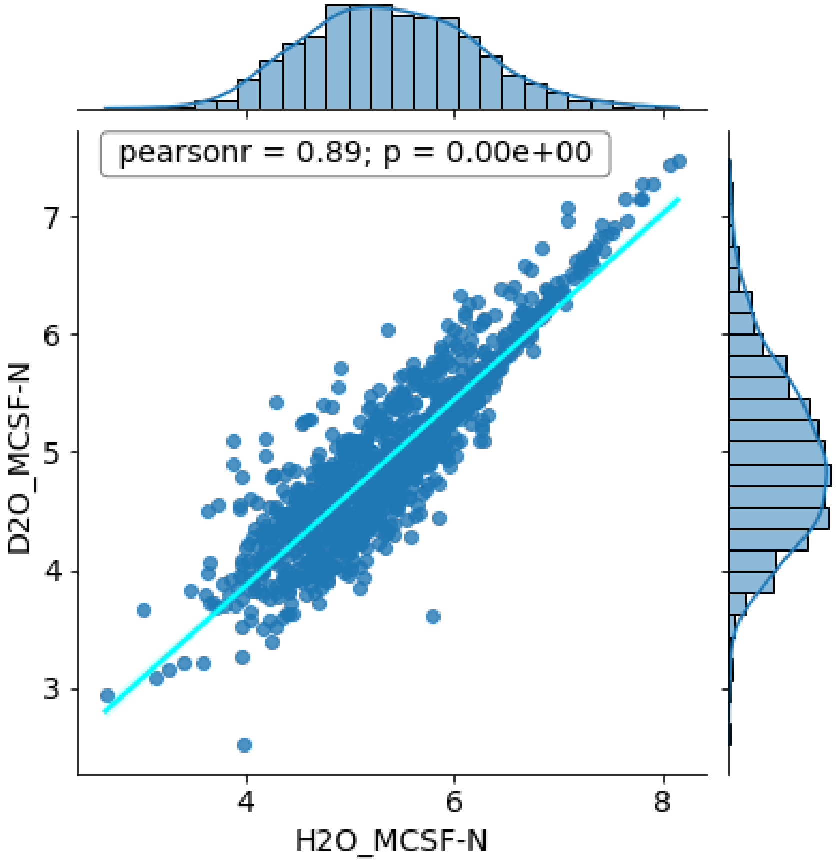
pearsonr = 0.89; p = 0.00e+00
D2O_MCSF-N
H2O_MCSF-N
3
4
5
6
7
4
6
8

C

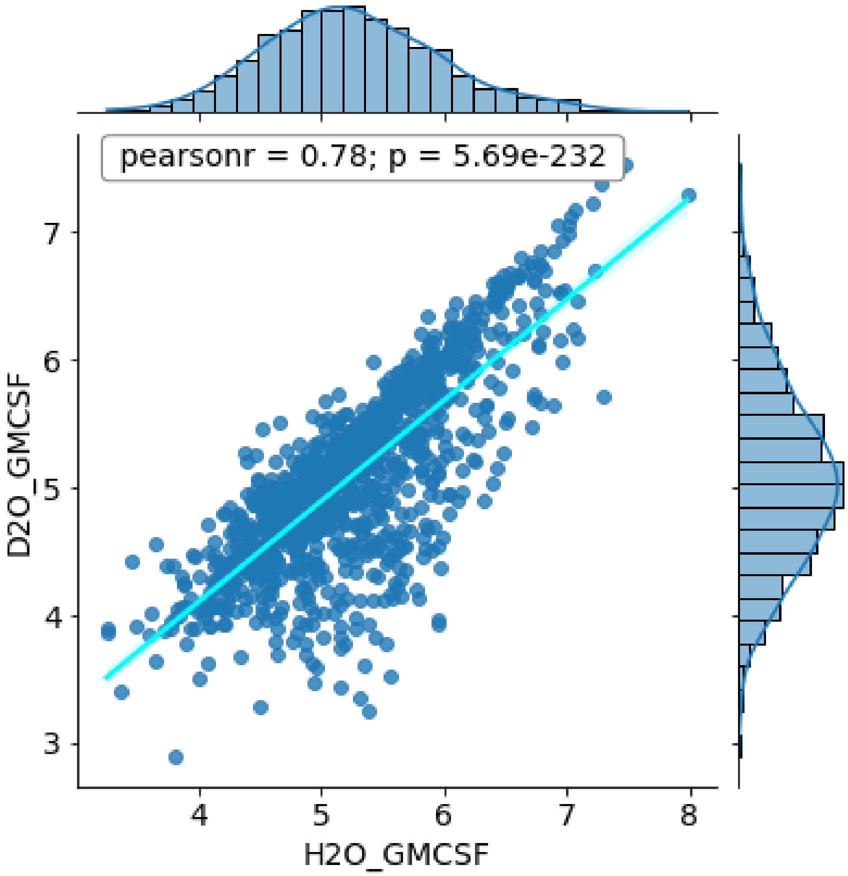
pearsonr = 0.78; p = 5.69e-232
D2O_GMCSF
H2O_GMCSF
3
4
5
6
7
4
5
6
7
8

D

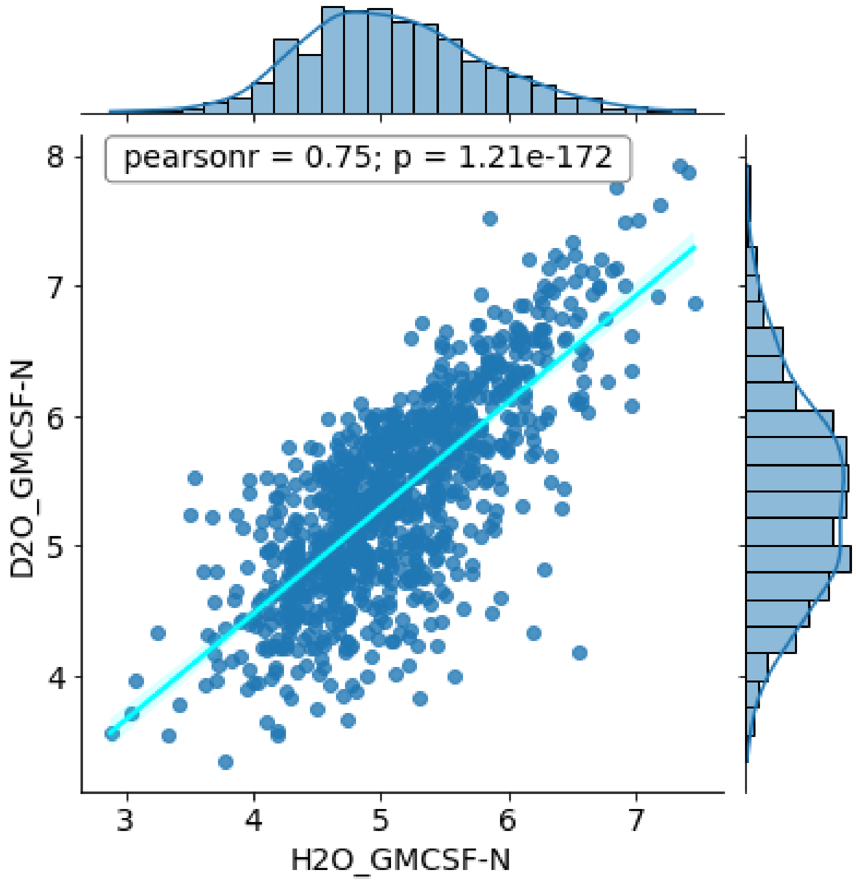

Figure 3: *Jointplots for each cytokine/NECA treatment, containing scatter plots with lines of best-fit, as well as histograms of log-transformed iBAQ data distributions. GMCSF-N and MCSF-N indicate the addition of NECA to the culture media. All treatments demonstrate strong, statistically significant correlations between iBAQ data from H2O and D2O conditions (p<0.05, Pearson correlation coefficient).*

To further assess the impacts of deuterium-labelling from introduction of deuterium-oxide into the macrophage media during differentiation into M1-like (GMCSF) or M2-like (MCSF) phenotypes, principal component analysis (PCA) was performed between H2O vs D2O supplemented samples across all treatments. Figure 4 illustrates that PCA in two-dimensions was unable to effectively separate H2O and D2O conditions across combined cytokine treatments, with further PCA analysis of each separate macrophage subtype (M1-like, GMCSF; M2-like, MCSF) also proving unable to clearly separate H2O vs D2O conditions; albeit with D2O demonstrating tighter clustering relative to H2O and therefore reduced separation along PC2.

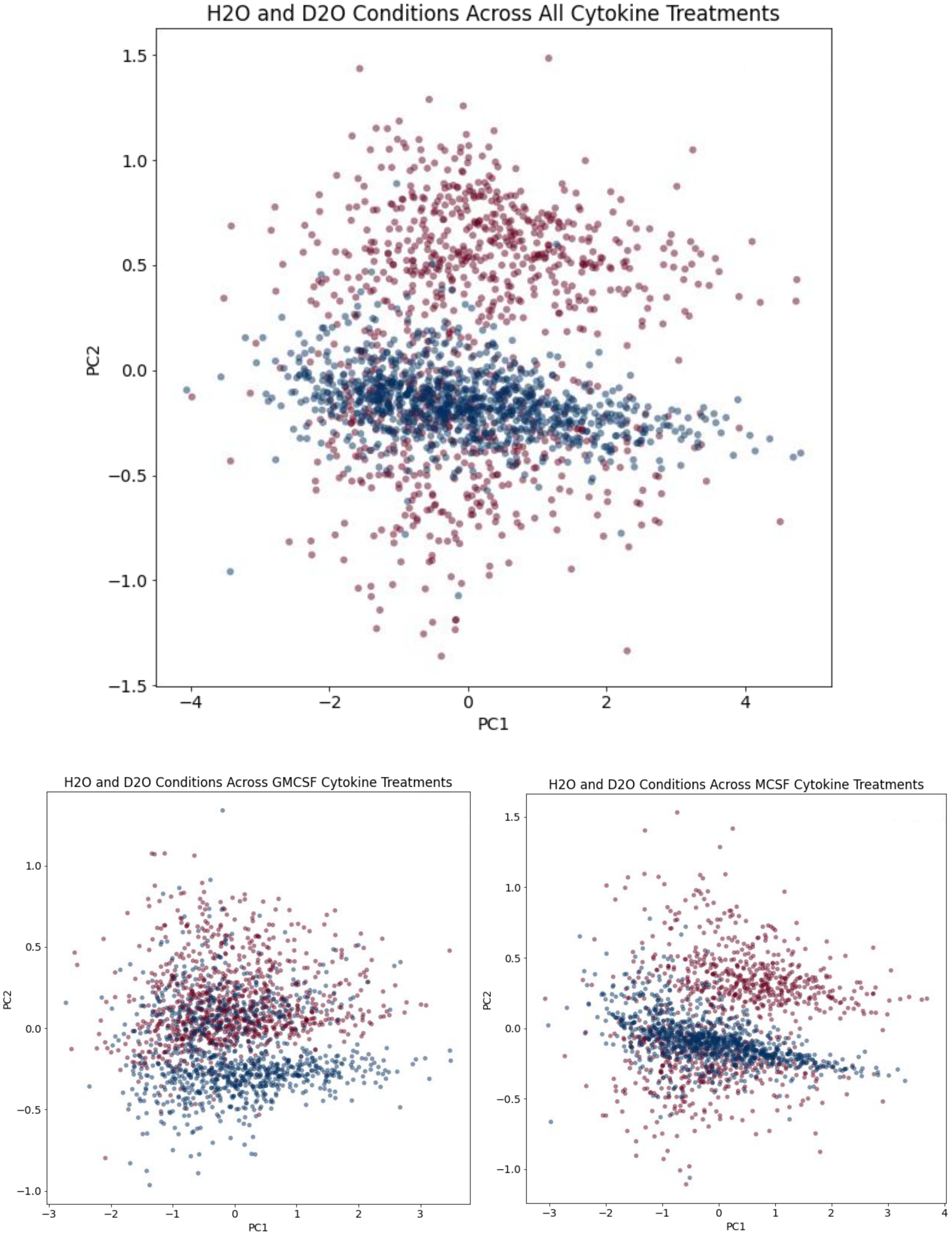

Figure 4: *PCA plots illustrating H2O vs D2O conditions across cytokine treatments (including NECA treatments).* ***Red*** *dots represent H2O supplemented samples and* ***blue*** *dots represent D2O supplemented samples.*

When examining protein identifications (detailed above), it appeared that interindividual variability arising from blood donors (n=2) provided a more significant source of variability within the iBAQ dataset than H2O vs D2O conditions. To further investigate this factor within the iBAQ dataset, PCA analysis was again performed in two-dimensions to ascertain if blood donors could be easily separated with an unsupervised machine learning approach.

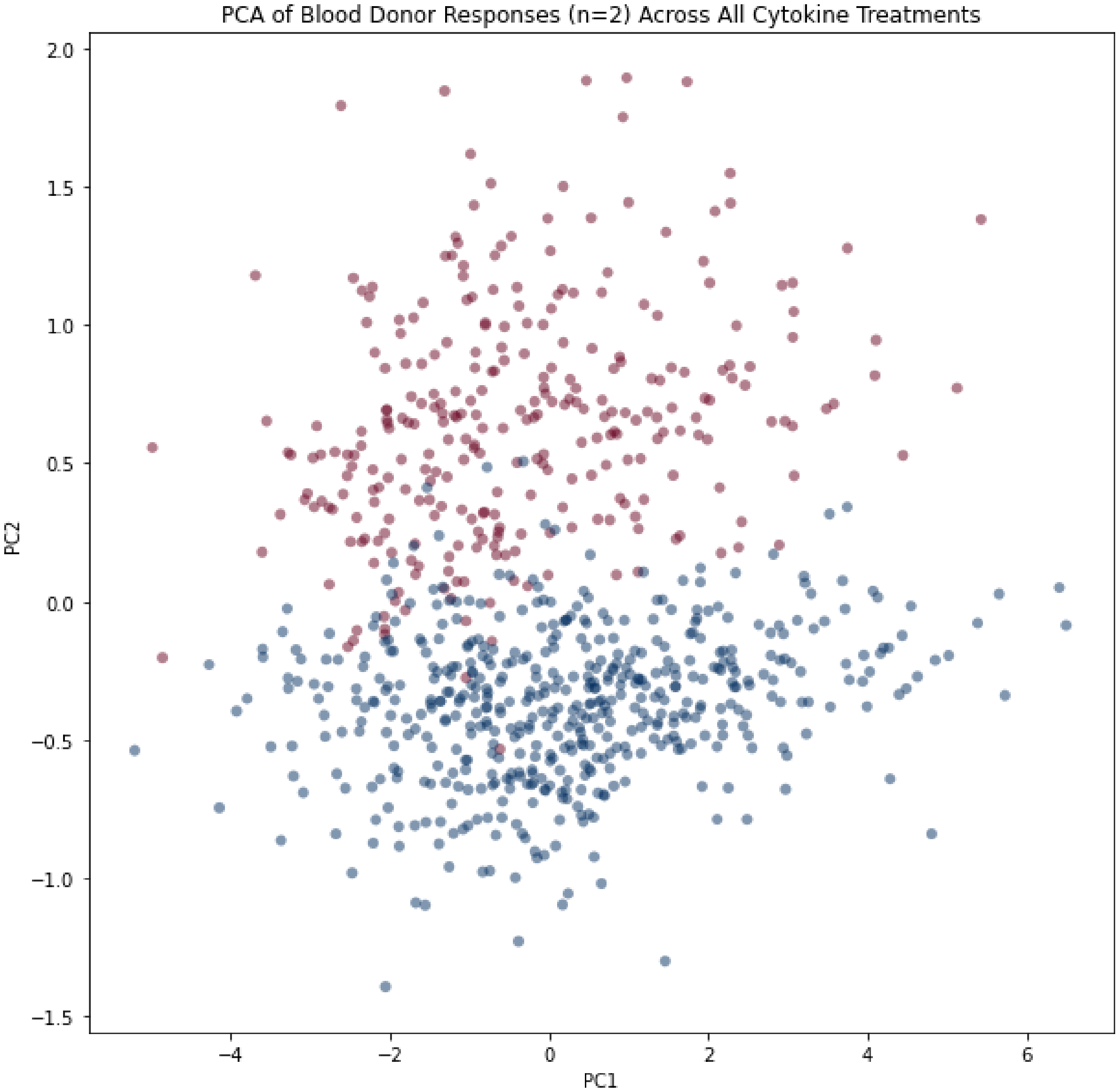

Figure 5: *PCA of interindividual variability arising from blood donors across all treatments.*

Figure 5 illustrates separation of blood donors across PC2, which accounts for ~8.6% of heterogeneity within the PCA model and iBAQ datasets. This supports previous interpretation that interindividual variation in macrophages cultured from different blood donor monocytes is responsible for a significant proportion of heterogeneity within this dataset, although this is not unexpected within such a small experimental sample size[9].

Finally, PCA was performed to ascertain whether macrophage phenotypes (M1, M2) could be separated according to the additional presence of the adenosine receptor agonist, NECA, a known modulator of immunological function[10,11]. Perhaps unsurprisingly, within the context of significant interindividual variability from n=2 blood donors, PCA was unable to separate combined GMCSF and MCSF treatments from their NECA counterparts (Figure 6).

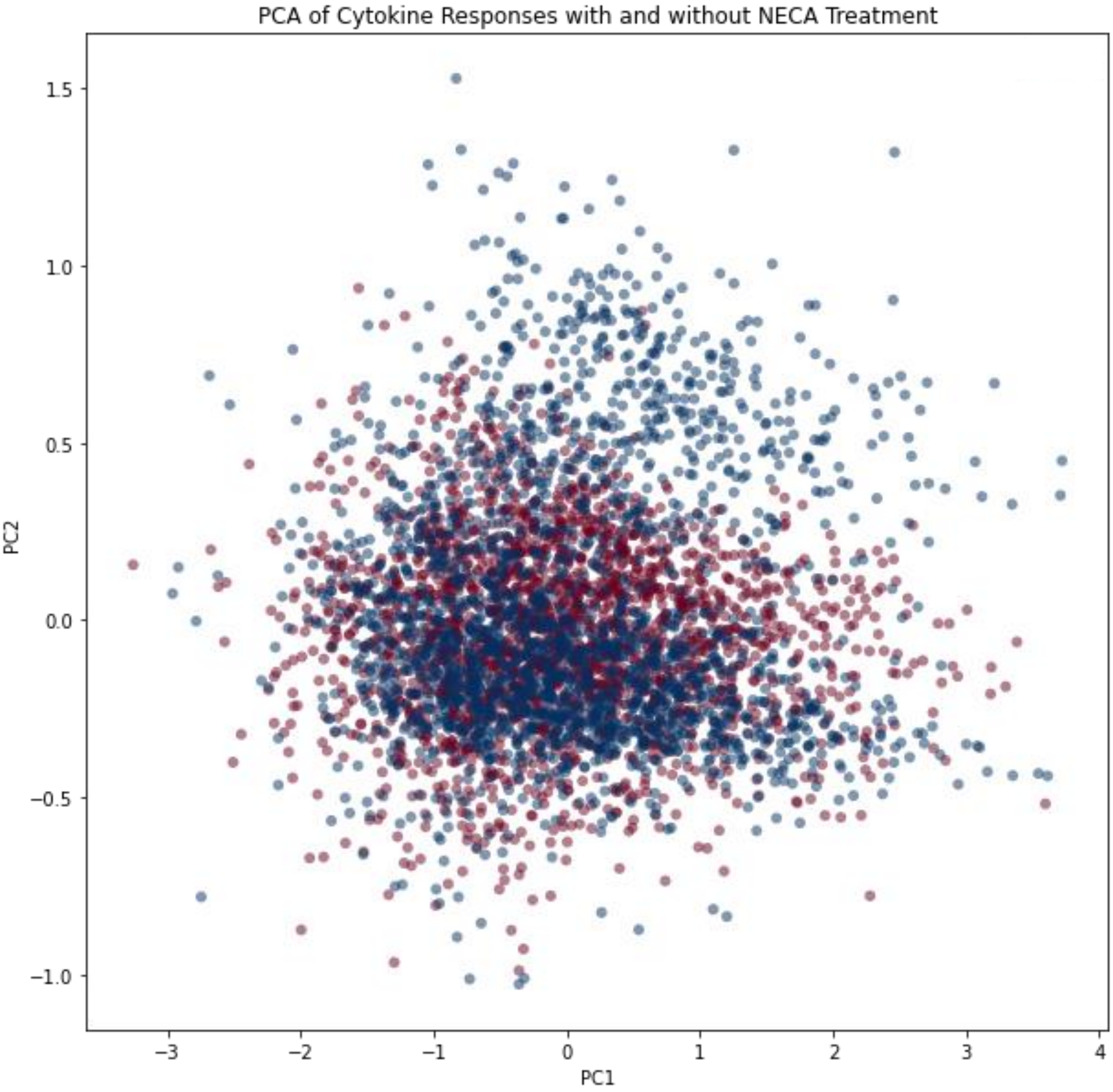

Figure 6: *PCA of M1 and M2 macrophage phenotypes induced by GMCSF and MCSF treatment respectively, without NECA (**red dots**) and with NECA supplementation (**blue dots**).*

In order to assess differences within each macrophage phenotype following NECA treatment, a supervised machine learning approach was adopted. Partial Least Squares Discriminant Analysis (PLS-DA) is a form of partial least squares regression (PLSR) capable of determining whether there are differences between known sample groups, and which features within the dataset best separate these groups (if differences do exist)[12]. For this, iBAQ of proteins shared across sample groups were analysed for each macrophage phenotype (M1, M2) to determine if samples treated by NECA could be separated from their untreated counterparts.

For GMCSF supplemented (M1-like phenotype) macrophage samples, PLS-DA effectively separated NECA treated samples from controls (untreated), with a PLS r^2 value of 0.92 (Figure 7).

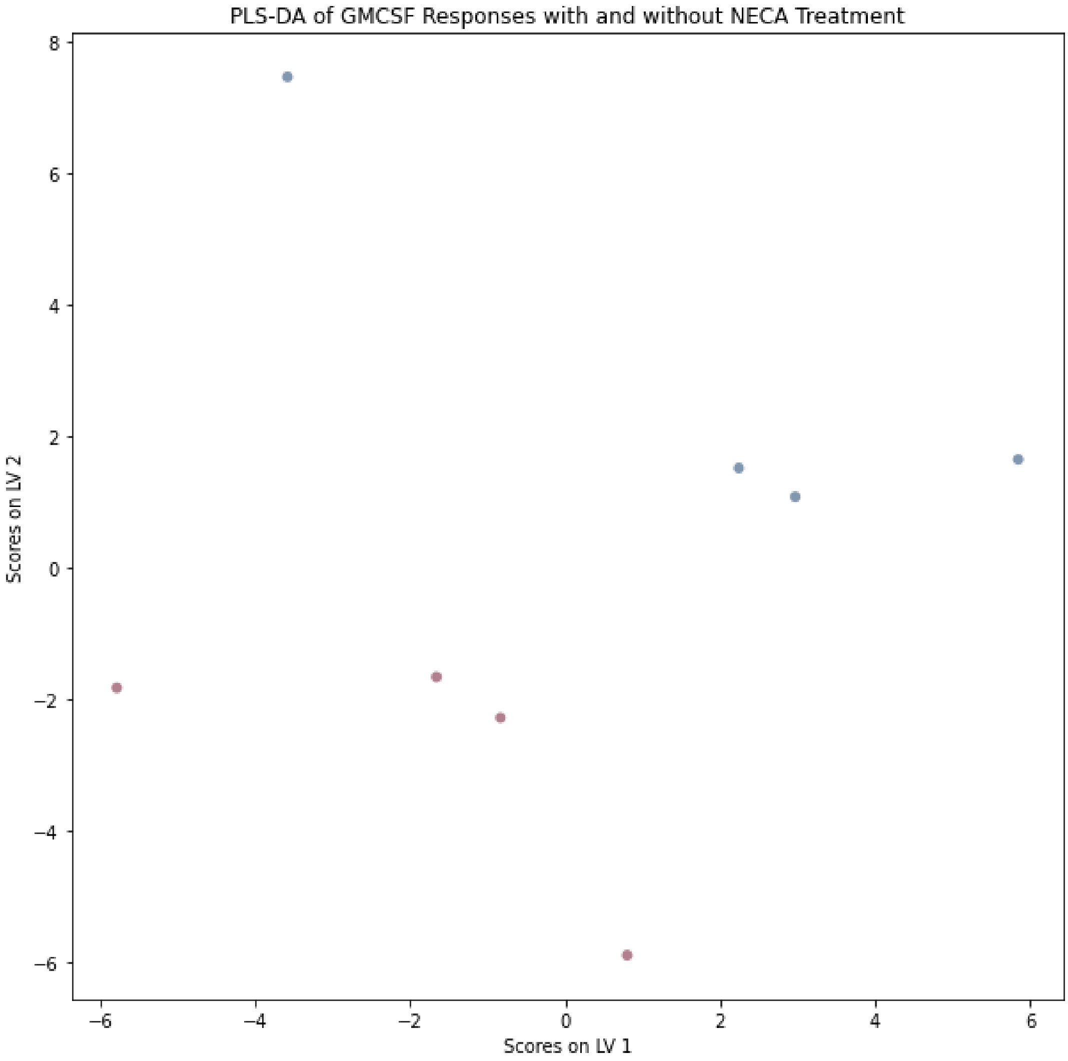

Figure 7: *Partial least squares discriminant analysis of GMCSF supplemented samples with (**blue dots**) and without (**red dots**) NECA treatment, 1µM for 7 days.*

The top 20 features with the greatest coefficients following PLS-DA classification (Figure 7) were extracted and are displayed in Figure 8.

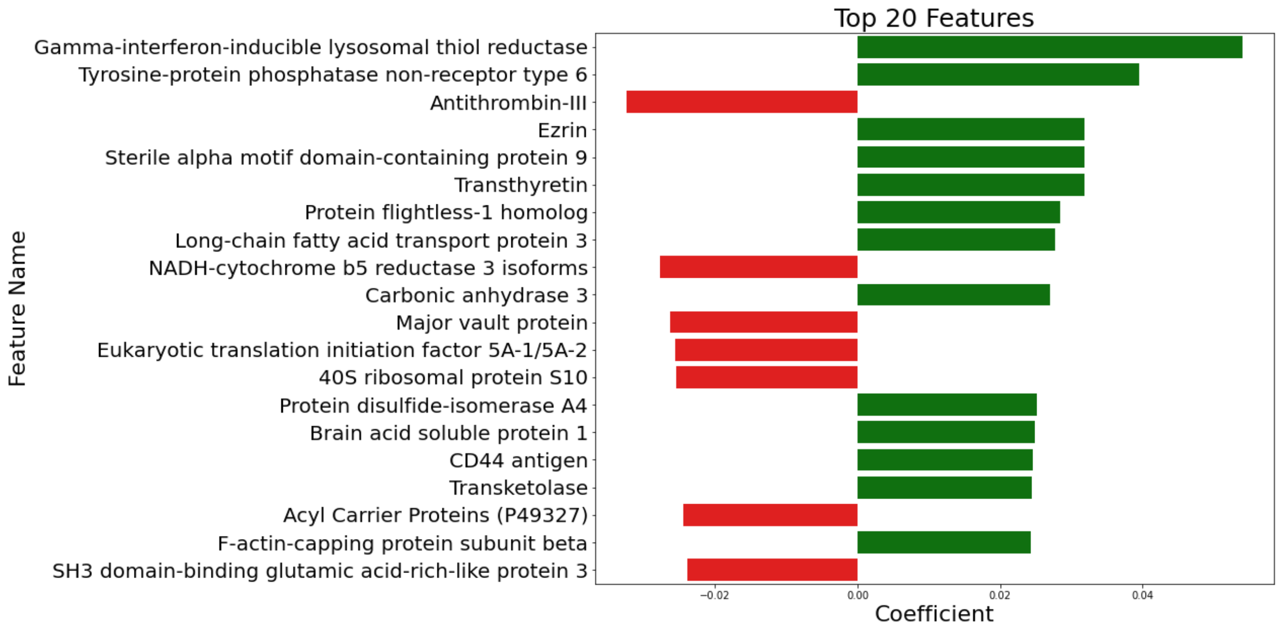

Figure 8: *The 20 features presenting the greatest coefficients following PLS-DA for GMCSF supplemented macrophages, with and without NECA. Positive coefficients are coloured in **green**, negative coefficients in **red**.*

Figure 8 demonstrates both positive and negative coefficients to contribute to separation of M1-like macrophage phenotypes with and without NECA treatment. Classification of these top 20 proteins via PANTHER illustrates these proteins to largely belong to the metabolite interconversion enzyme and translational protein classes (Figure 9).

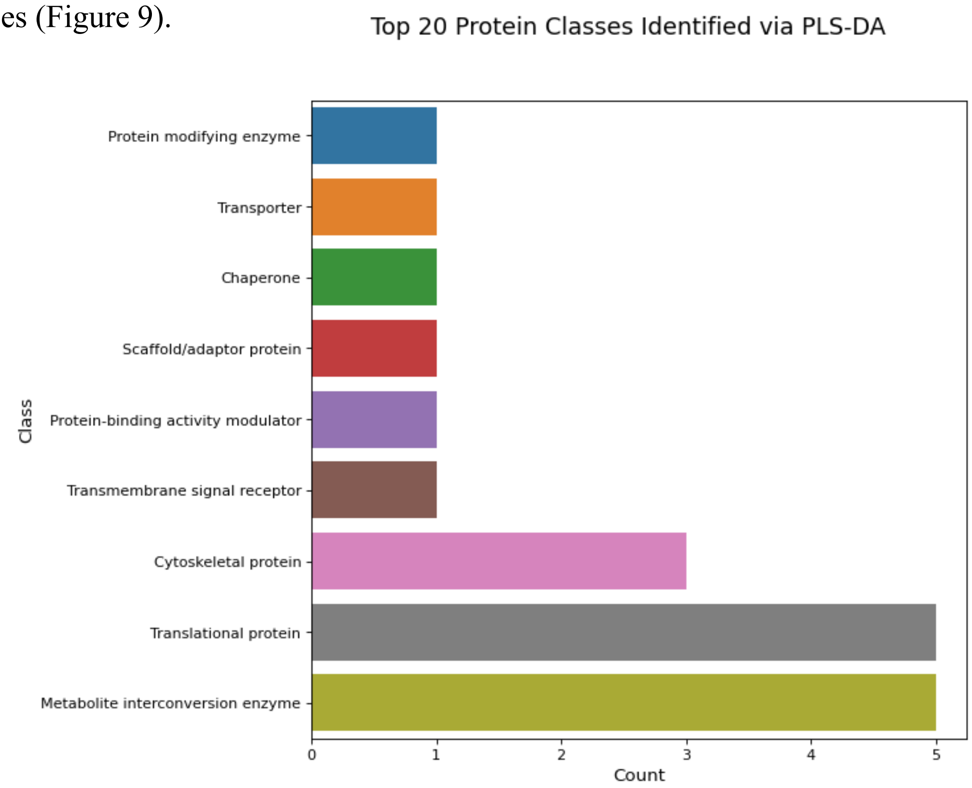

Figure 9: *Protein classification via PANTHER of 20 proteins with the largest coefficients within the PLS-DA model for GMCSF supplemented macrophages.*

Univariate analysis of these 20 proteins in M1-like macrophages cultured with and without NECA were analysed via paired t-test. None of the 20 proteins demonstrated statistically significant differences between NECA and non-NECA treatments ($p>0.05$).

To validate the importance of these features within this model, iBAQ log-transformed data pertaining only to these 20 isolated features, were again subjected to unsupervised PCA analysis for M1-like (GMCSF) macrophages treated with and without NECA.

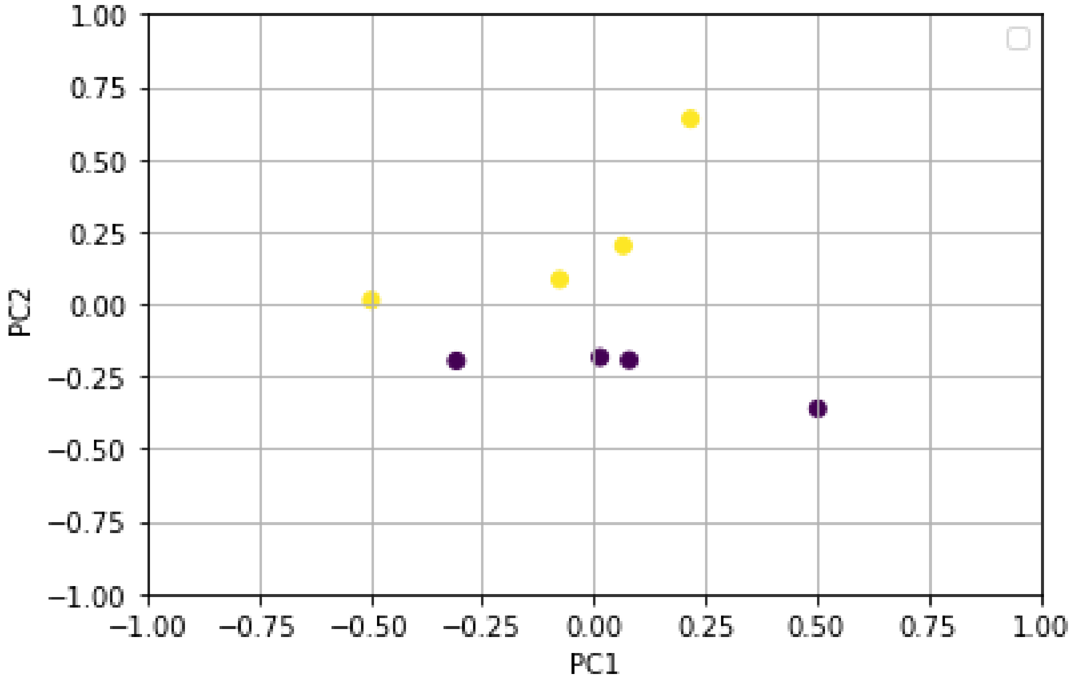

Figure 10: *PCA analysis of the top 20 features identified via PLS-DA for n=8, GMCSF supplemented M1-like macrophages treated with (**yellow dots**) and without (**purple dots**) NECA, 1µM for 7 days.*

Figure 10 illustrates clear separation of M1-like macrophages treated with and without NECA utilising the 20 protein features identified as most important in the supervised machine learning-based classification of these treatment groups via PLS-DA. This supports these features relative importance in differentiating NECA treatment groups, with PC1 being the feature with the highest coefficient identified via PLS-DA (Gamma-interferon-inducible lysosomal thiol reductase) and PC2 representing another protein identified within the top 20 highest coefficients following PLS-DA (SH3 domain-binding glutamic acid-rich-like protein 3).

These analyses were repeated for the separation and classification of M2-like macrophages (MCSF supplemented) for those treated with and without NECA. PLS-DA resulted in the separation of NECA treatment groups, albeit with a reduced model efficacy, presenting a fit with a PLS r^2 value of 0.67 (Figure 11a). This is likely due to an outlier detecting along the latent variable 1 axis, whose subsequent removal resulted in an improved model fit of 0.92 (the same as for M1-like macrophage treatments, Figure 11b). As such this outlier was omitted from further iBAQ analysis.

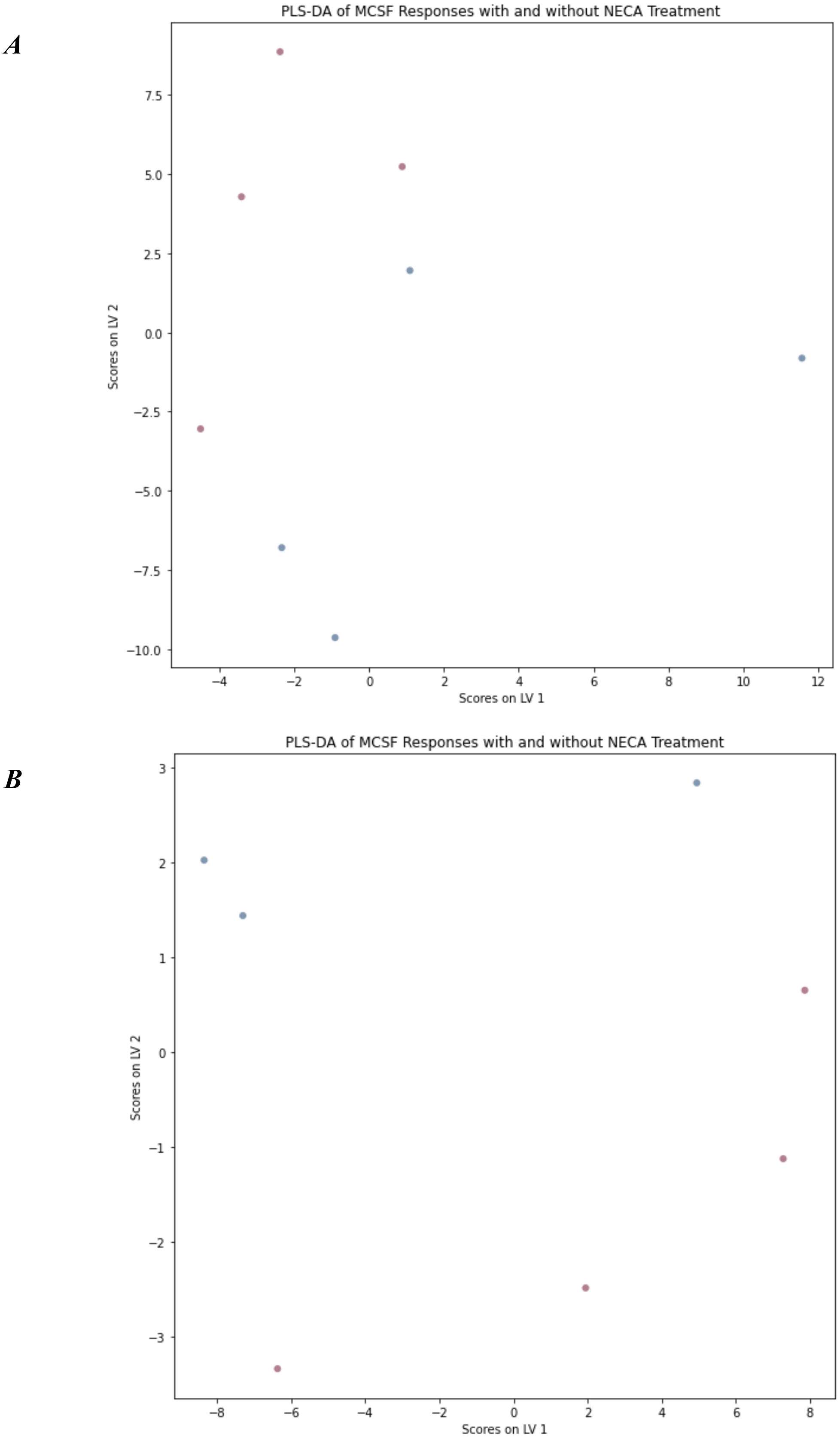

Figure 11: A; *PLS-DA of MCSF supplemented samples with (**blue**) and without (**red**) NECA.* ***B;*** *PLS-DA of MCSF supplemented samples with (**blue**) and without (**red**) NECA following outlier removal.*

The top 20 protein features with the greatest coefficients in the PLS-DA model were then extracted as before and are displayed in Figure 12.

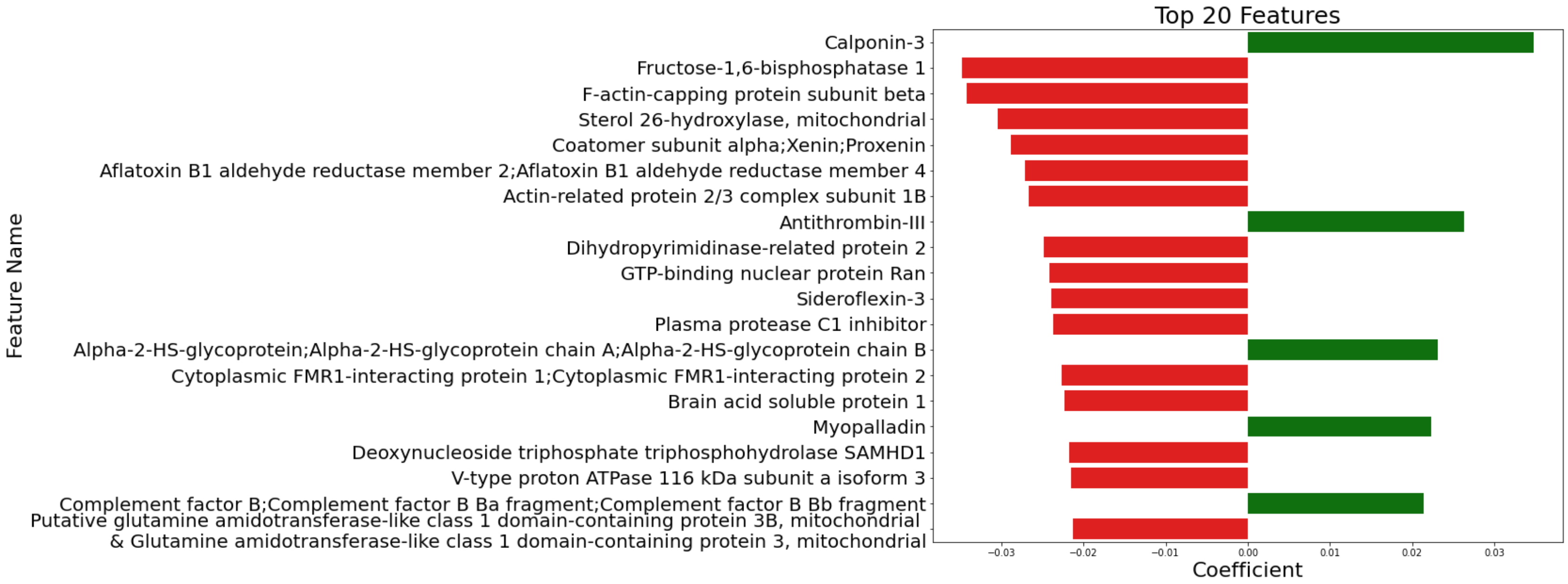

Figure 12: *The 20 protein features with the highest coefficients identified by PLS-DA for M2-like macrophages supplemented with MCSF with and without NECA.*

An interesting observation following PLS-DA to separate M2-like macrophages treated with or without NECA, is that negative coefficients are predominant among the top 20 features with the highest coefficients, which is in contrast to M1-like macrophages where positive coefficients were most prevalent. The top 20 proteins identified via PLS-DA were classified via PANTHER to assess the degree of homology between M1-like vs M2-like macrophage responses to NECA treatment.

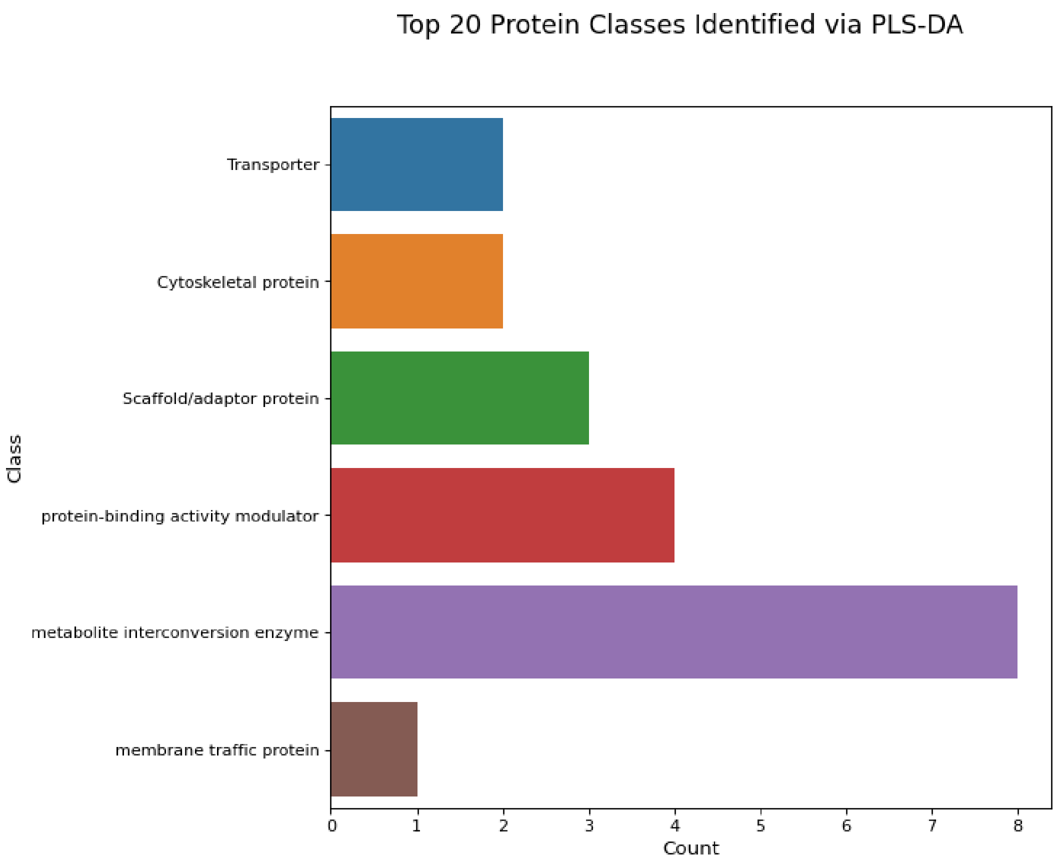

Figure 13: *Protein classification via PANTHER for the top 20 protein features identified via PLS-DA.*

Figure 13 illustrates metabolite interconversion enzyme-related proteins to be among the most important protein features classified within the PLS-DA model, a similar observation to M1-like macrophage NECA classification (Figure 9). However, the translational protein class is not identified as important to the PLS-DA model in M2-like macrophage treatments (as observed with M1-like macrophage classification), with the membrane traffic protein class being uniquely identified in M2-like macrophages, conveying some heterogeneity between protein classes identified as important in separating macrophage phenotypes from their NECA treatment counterparts.

Univariate analysis was performed via paired t-test for the 20 proteins identified as most important in separating NECA treatments within M2-like cultured macrophages. One protein feature was deemed statistically significant between M2-like macrophages that were treated with and without NECA (Aflatoxin B1 aldehyde reductase member 2, p=0.04), with two further protein features nearing statistical significance (Plasma protease C1 inhibitor, p=0.07; Fructose-1,6-bisphosphatase 1, p=0.08). Boxplots displaying the log-transformed iBAQ data for these three protein features are displayed in Figure 14.

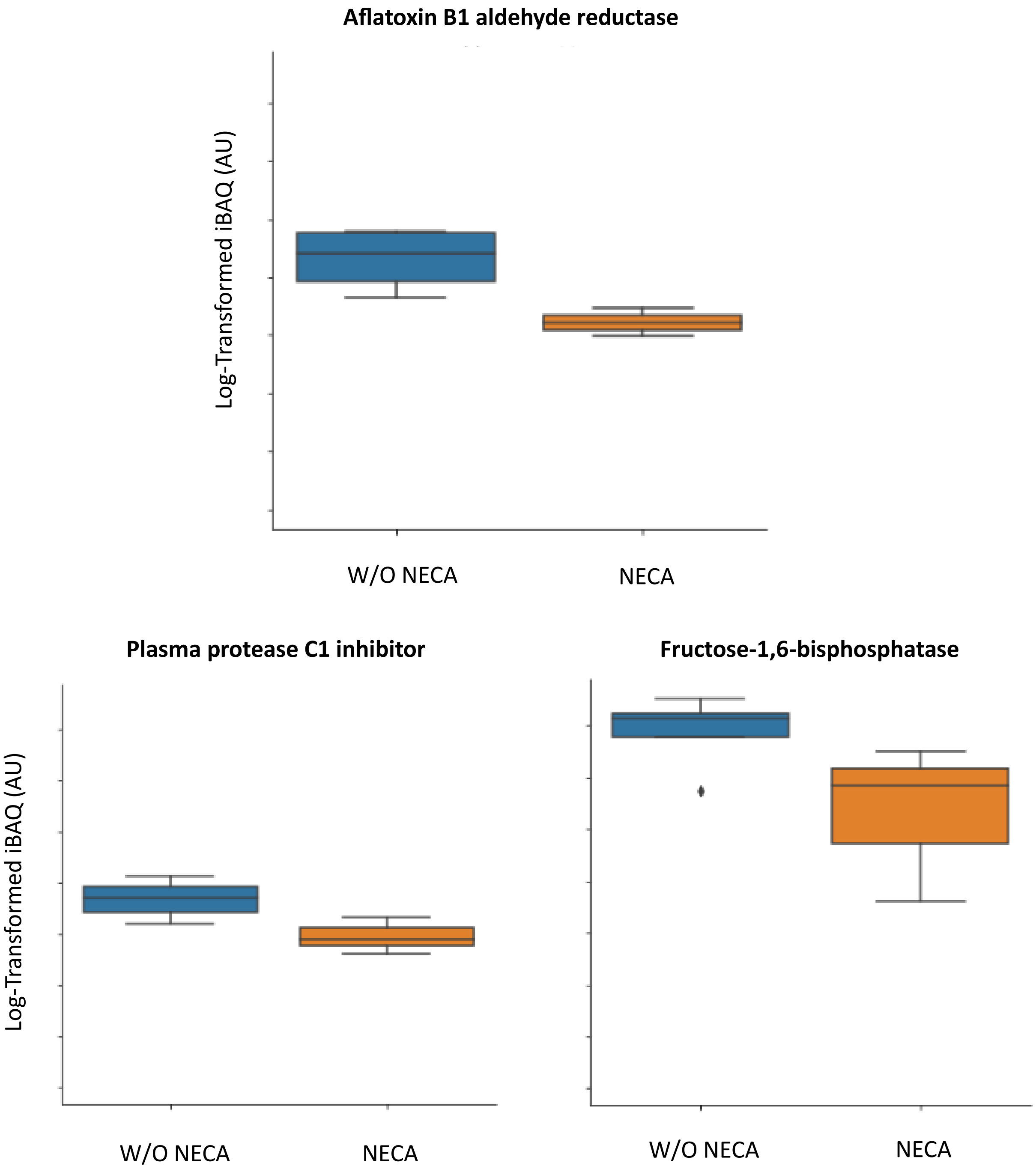

Figure 14: *Box and whisker plots for 3 of the 20 protein features identified as most important via PLS-DA for MCSF/M2-like macrophages treated with and without NECA.*

All of these proteins demonstrate NECA treatment to result in decreased protein abundance relative to the untreated M2-like macrophage phenotype. NECA is known to suppress proinflammatory responses in macrophages[10], with upregulated carbohydrate metabolism and glycolytic flux being hallmarks of classical (M1) macrophage activation[13]. Both Aflatoxin B1 aldehyde reductase and Fructose-1, 6-biphosphatase are implicated in carbohydrate metabolism, with the latter specifically an important regulator of gluconeogenesis[14]. Fructose-1, 6-biphosphatase is allosterically regulated via Fructose-2, 6-biphosphate, which is involved in glycolytic flux and has shown to be upregulated in macrophages following exposure to inflammatory stimuli, such as LPS treatment[13].

Plasma protease C1 inhibitor protein and its alternate isoforms; Epididymis tissue protein Li 173 and Serpin peptidase inhibitor clade G member 1, are all expressed by the SERPING1 gene. This gene has demonstrated the capability to modulate activation of the complement immune system in monocytes, exerting immunosuppressive effects in both HIV+ patients and in monocytes *ex vivo* following treatment with IFN's: α, β and γ[15]. Further, SERPING1 is known to increase vascular permeability through its role as a C1 protease inhibitor, by triggering activation of bradykinin pathways[16]. Macrophage treatment with NECA has previously demonstrated the ability to initiate an "angiogenic switch", that increases angiogenesis growth factors (such as VEGF) as well as vascular permeability[10]. It therefore appears that application of PLS-DA successfully classified treatment groups via proteins whose functions are related to previously reported macrophage responses following NECA treatment.

Measurements of Protein Turnover with Deuterium-Oxide Metabolic Labelling

Data Quality and False-Discovery

DeuteRater identified ~77,000 peptides across the 8 samples supplemented with D2O that contained deuterium incorporation across a minimum peak isotopic envelope of 5, equating to an approximate 9621 peptides per sample. Of the ~77,000 peptides with deuterium incorporation detected across the isotopic envelope, ~25% contained negative values that impacted the calculation of "fraction new" peptides, likely arising as a result of analytical noise from mass spectrometry measurements. These peptides were therefore discarded, leaving ~57,900 peptides with sufficient deuterium incorporation across the isotopic envelope for the calculation of protein turnover rates, for an average of 311 proteins per sample.

As this cell culture experiment contained only one timepoint (cells harvested at day 7), turnover rates could not be fit for each protein as a function of time (as is typically performed in DeuteRater and displayed via graphical output). As a result, rates and coefficient of variation (CV) were calculated manually in Python (v. 3.9.7) across all "neutromer-spacing fraction new" (nsfn) peptides per protein. To calculate rates of protein turnover, median nsfn was calculated from all peptides belonging to a specific protein identifier, and then fit to the rate equation specified in DeuteRater[5]:

$$\mathit{Fraction\ New} = 1 - e^{-rate*time}$$

Average CV for "fraction new" calculations across all samples was 0.5, with 50% of proteins containing a CV of 0.3 or lower and approximately 45% of calculated protein turnover rates presenting a CV of 0.2 or lower. While these CVs are quite high, similar levels have been reported elsewhere in the literature for the quantification of peptide/protein turnover with D2O labelling using DeuteRater[5] and other bioinformatic software[8]. Calculated rates of protein turnover ranged from ~0 (little-no detectable protein synthesis) to 0.83 day^{-1} (high turnover proteins; fixed asymptote value=1), with a mean protein turnover rate of 0.07 day^{-1}.

The “fraction new” output file generated by DeuteRater, which details the amount of turnover for each peptide following deuterium-labelling analysis, was provided to Python (v. 3.9.7) and matched against the MaxQuant database search “evidence” output file containing peptide sequences identified across all samples. This approach was adopted to characterise false-discovery rates for protein turnover when deuterium-labelling analysis was computed from both specific and non-specific peptide sequences, explicitly; a master database containing identified peptides (proteins) from all 8 experimental samples as a reference database of peptide sequences for DeuteRater to search raw mzml data files. Rates of false discovery were then assessed for proteins whose peptides had been quantified for deuterium-labelling.

Database filtering across all 8 samples combined revealed a total FDR of 163 proteins from a total of 2491 calculated protein turnover rates. On average, this equates to an approximate protein turnover FDR of 20 per 311 for each respective sample or ~6.5%. This is approximately double reports of FDR arising from matching-between-runs within label-free quantification experiments[17,18], but far less than reported false matches arising without implementation of the two peptide per protein rule employed for quantitation by MaxQuant’s LFQ algorithm[17]. This suggests that detection of the mass isotopic envelope (feature detection) by DeuteRater and its transfer between samples is relatively stringent at a set deuterium isotopic enrichment, even with the inclusion of protein identifications via single peptides. Turnover rates of falsely-discovered proteins were subsequently removed from the dataset, resulting in a final average of 291 proteins per sample to be taken forward for further analysis.

Protein Turnover vs iBAQ

For each cytokine treatment, the agreement between iBAQ quantitation and turnover rate was investigated across identified proteins, to assess whether there was any relationship between protein abundance and turnover. First, in order to compare iBAQ and turnover datasets, both data were scaled via quantile transformation (scikit-learn v. 1.1.2), which is an effective method to reduce the impacts of outliers and render variables measured at different scales comparable. Proteins identified in both datasets were then visualised via heatmap (Figure 15a-d) and jointplots (Figure 16a-d) to investigate relationships between protein abundance and turnover for each cytokine treatment.

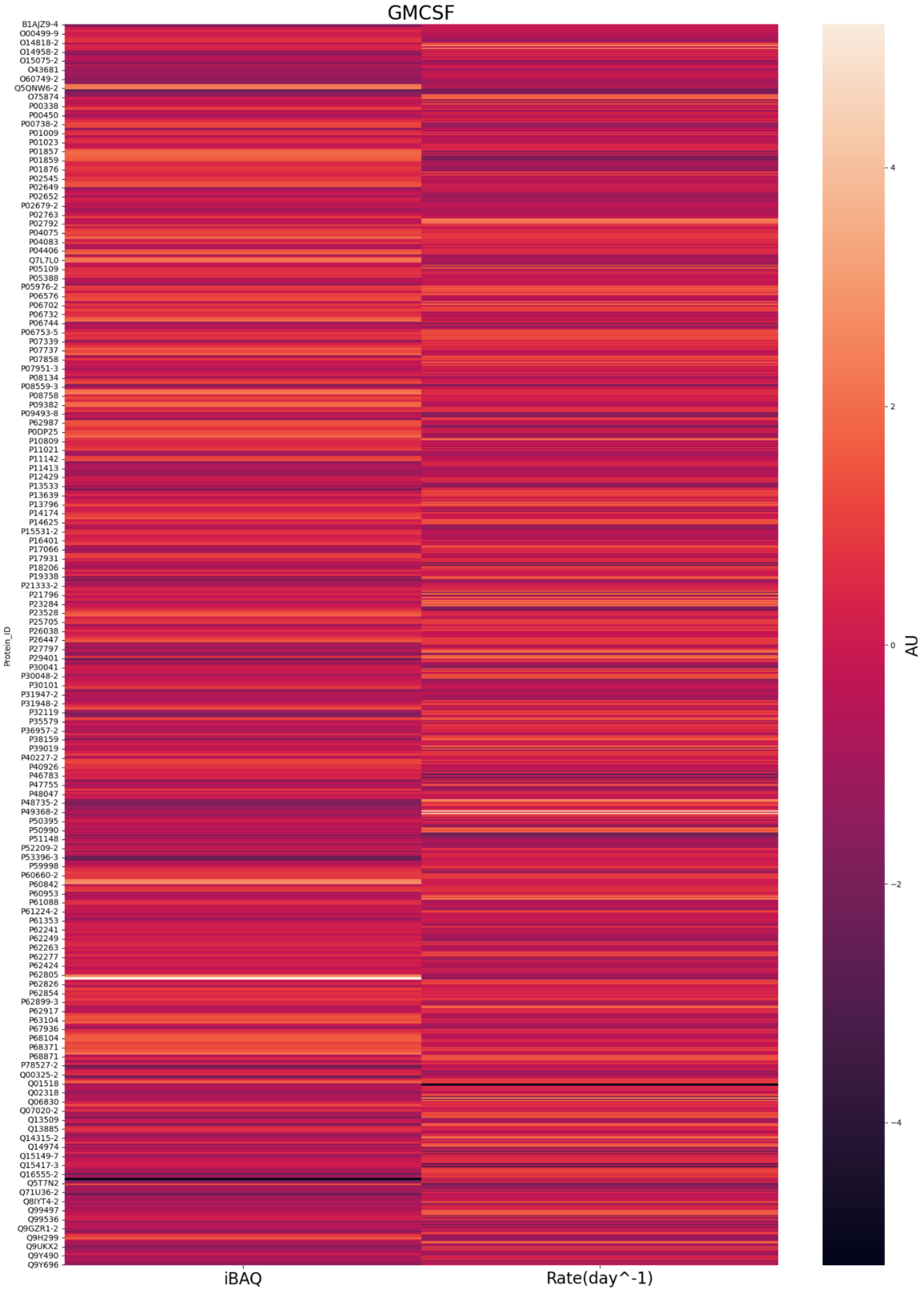
GMCSF
Protein_ID
B1AJZ9-4
O00499-9
O14818-2
O14958-2
O15075-2
O43681
O60749-2
Q5QNW6-2
O75874
P00338
P00450
P00738-2
P01009
P01023
P01857
P01859
P01876
P02545
P02649
P02652
P02679-2
P02763
P02792
P04075
P04083
P04406
Q7L7L0
P05109
P05388
P05976-2
P06576
P06702
P06732
P06744
P06753-5
P07339
P07737
P07858
P07951-3
P08134
P08559-3
P08758
P09382
P09493-8
P62987
P0DP25
P10809
P11021
P11142
P11413
P12429
P13533
P13639
P13796
P14174
P14625
P15531-2
P16401
P17066
P17931
P18206
P19338
P21333-2
P21796
P23284
P23528
P25705
P26038
P26447
P27797
P29401
P30041
P30048-2
P30101
P31947-2
P31948-2
P32119
P35579
P36957-2
P38159
P39019
P40227-2
P40926
P46783
P47755
P48047
P48735-2
P49368-2
P50395
P50990
P51148
P52209-2
P53396-3
P59998
P60660-2
P60842
P60953
P61088
P61224-2
P61353
P62241
P62249
P62263
P62277
P62424
P62805
P62826
P62854
P62899-3
P62917
P63104
P67936
P68104
P68371
P68871
P78527-2
Q00325-2
Q01518
Q02318
Q06830
Q07020-2
Q13509
Q13885
Q14315-2
Q14974
Q15149-7
Q15417-3
Q16555-2
Q5T7N2
Q71U36-2
Q8IYT4-2
Q99497
Q99536
Q9GZR1-2
Q9H299
Q9UKX2
Q9Y490
Q9Y696
iBAQ
Rate(day^-1)
4
2
0
−2
−4
AU

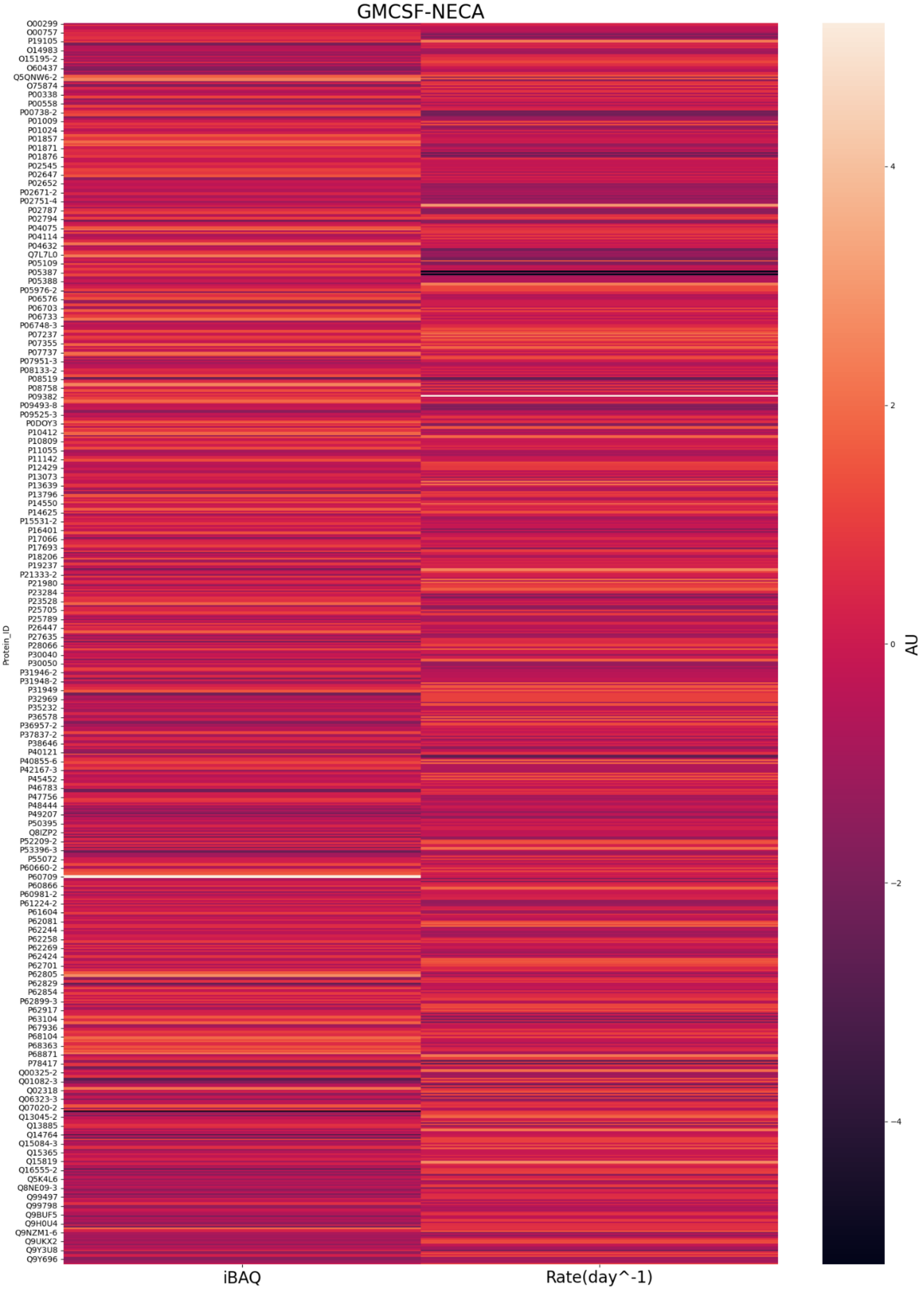
GMCSF-NECA
Protein_ID
O00299
O00757
P19105
O14983
O15195-2
O60437
Q5QNW6-2
O75874
P00338
P00558
P00738-2
P01009
P01024
P01857
P01871
P01876
P02545
P02647
P02652
P02671-2
P02751-4
P02787
P02794
P04075
P04114
P04632
Q7L7L0
P05109
P05387
P05388
P05976-2
P06576
P06703
P06733
P06748-3
P07237
P07355
P07737
P07951-3
P08133-2
P08519
P08758
P09382
P09493-8
P09525-3
P0DOY3
P10412
P10809
P11055
P11142
P12429
P13073
P13639
P13796
P14550
P14625
P15531-2
P16401
P17066
P17693
P18206
P19237
P21333-2
P21980
P23284
P23528
P25705
P25789
P26447
P27635
P28066
P30040
P30050
P31946-2
P31948-2
P31949
P32969
P35232
P36578
P36957-2
P37837-2
P38646
P40121
P40855-6
P42167-3
P45452
P46783
P47756
P48444
P49207
P50395
Q8IZP2
P52209-2
P53396-3
P55072
P60660-2
P60709
P60866
P60981-2
P61224-2
P61604
P62081
P62244
P62258
P62269
P62424
P62701
P62805
P62829
P62854
P62899-3
P62917
P63104
P67936
P68104
P68363
P68871
P78417
Q00325-2
Q01082-3
Q02318
Q06323-3
Q07020-2
Q13045-2
Q13885
Q14764
Q15084-3
Q15365
Q15819
Q16555-2
Q5K4L6
Q8NE09-3
Q99497
Q99798
Q9BUF5
Q9H0U4
Q9NZM1-6
Q9UKX2
Q9Y3U8
Q9Y696
iBAQ
Rate(day^-1)
4
2
0
−2
−4
AU

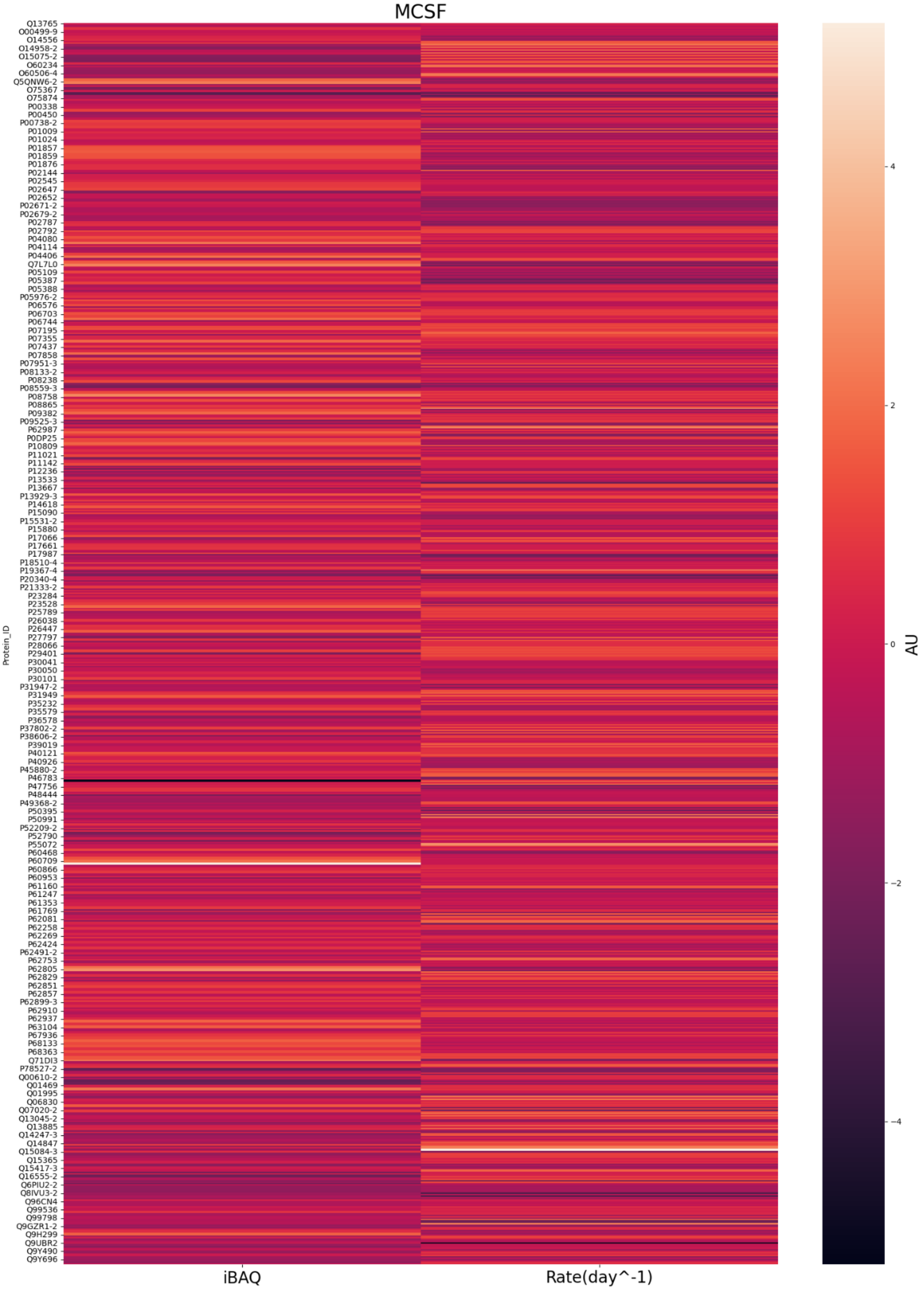
MCSF

Q13765
O00499-9
O14556
O14958-2
O15075-2
O60234
O60506-4
Q5QNW6-2
O75367
O75874
P00338
P00450
P00738-2
P01009
P01024
P01857
P01859
P01876
P02144
P02545
P02647
P02652
P02671-2
P02679-2
P02787
P02792
P04080
P04114
P04406
Q7L7L0
P05109
P05387
P05388
P05976-2
P06576
P06703
P06744
P07195
P07355
P07437
P07858
P07951-3
P08133-2
P08238
P08559-3
P08758
P08865
P09382
P09525-3
P62987
P0DP25
P10809
P11021
P11142
P12236
P13533
P13667
P13929-3
P14618
P15090
P15531-2
P15880
P17066
P17661
P17987
P18510-4
P19367-4
P20340-4
P21333-2
P23284
P23528
P25789
P26038
P26447
P27797
P28066
P29401
P30041
P30050
P30101
P31947-2
P31949
P35232
P35579
P36578
P37802-2
P38606-2
P39019
P40121
P40926
P45880-2
P46783
P47756
P48444
P49368-2
P50395
P50991
P52209-2
P52790
P55072
P60468
P60709
P60866
P60953
P61160
P61247
P61353
P61769
P62081
P62258
P62269
P62424
P62491-2
P62753
P62805
P62829
P62851
P62857
P62899-3
P62910
P62937
P63104
P67936
P68133
P68363
Q71DI3
P78527-2
Q00610-2
Q01469
Q01995
Q06830
Q07020-2
Q13045-2
Q13885
Q14247-3
Q14847
Q15084-3
Q15365
Q15417-3
Q16555-2
Q6PIU2-2
Q8IVU3-2
Q96CN4
Q99536
Q99798
Q9GZR1-2
Q9H299
Q9UBR2
Q9Y490
Q9Y696
Protein_ID
iBAQ
Rate(day^-1)
4
2
0
−2
−4
AU

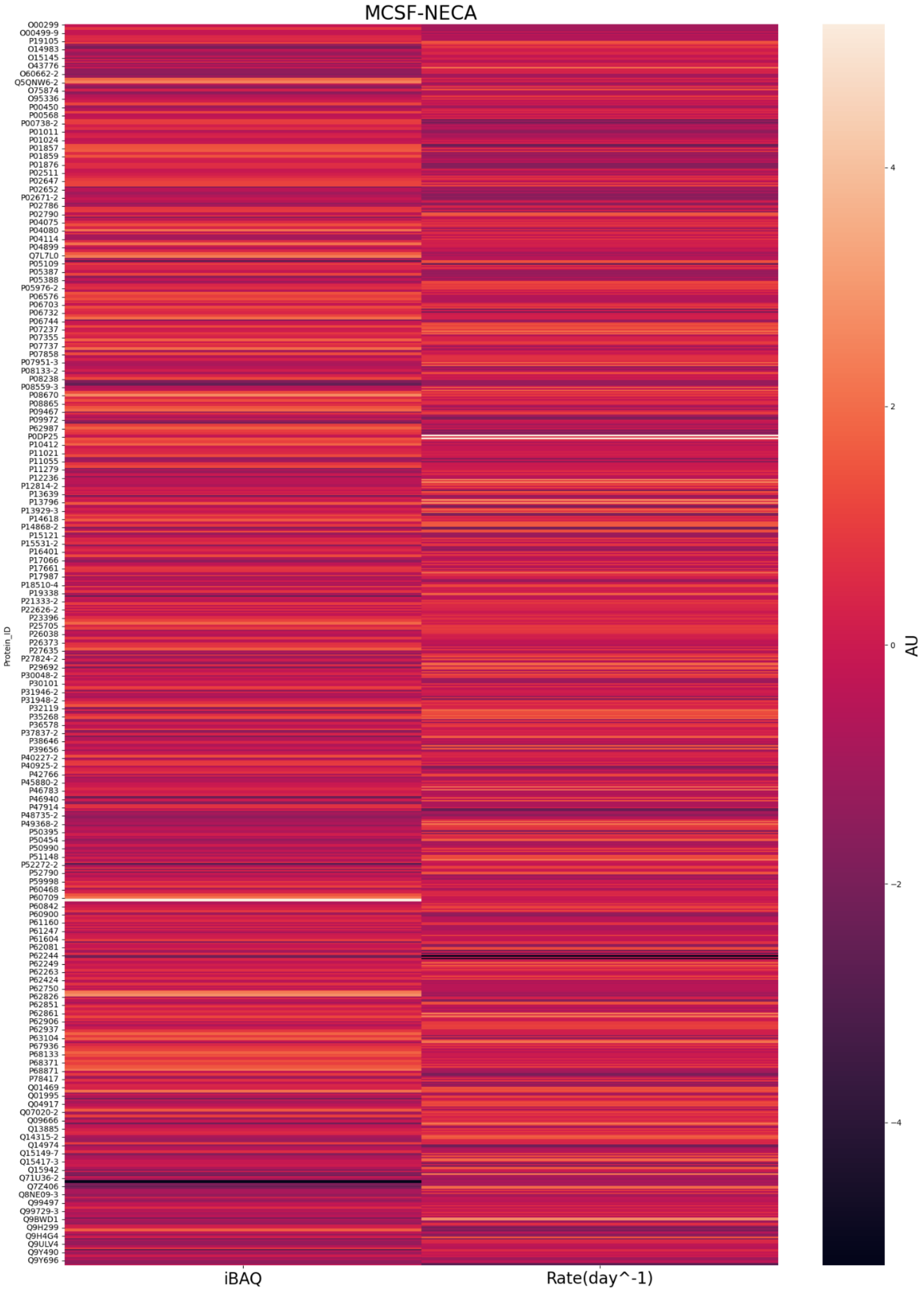

Figure 15: *Heatmaps depicting iBAQ vs turnover rate (day^{-1}) for proteins identified in treatments:* ***A;*** *GMCSF,* ***B;*** *GMCSF-NECA,* ***C;*** *MCSF,* ***D;*** *MCSF-NECA.*

A

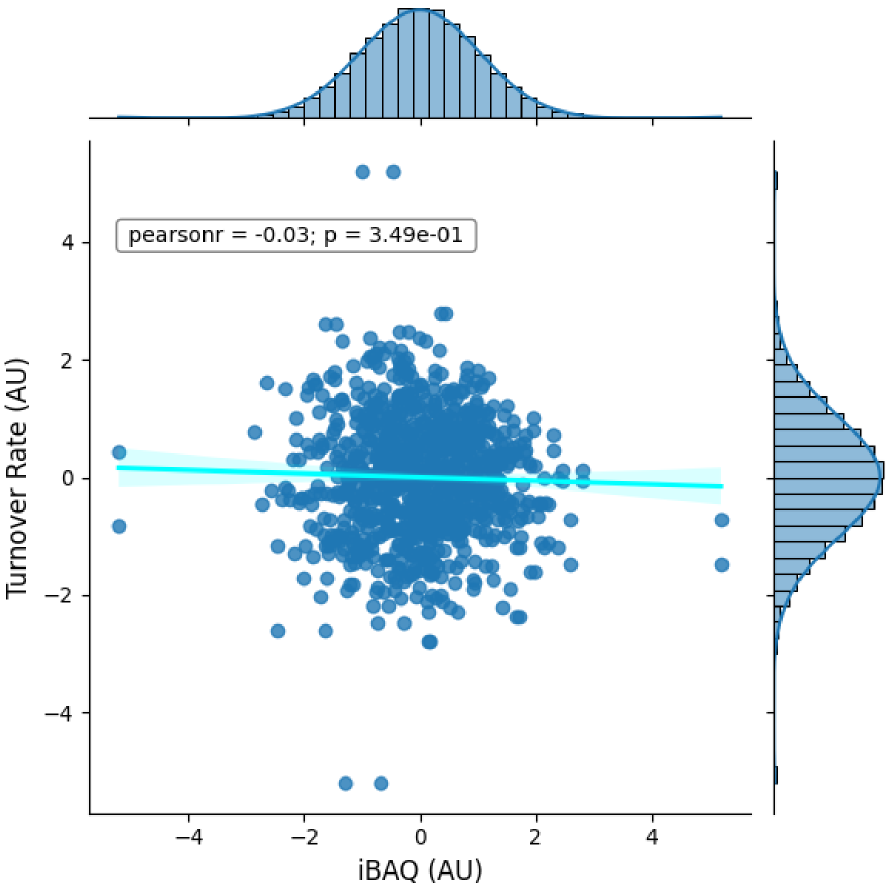
pearsonr = -0.03; p = 3.49e-01
Turnover Rate (AU)
iBAQ (AU)
4
2
0
−2
−4
−4
−2
0
2
4

B

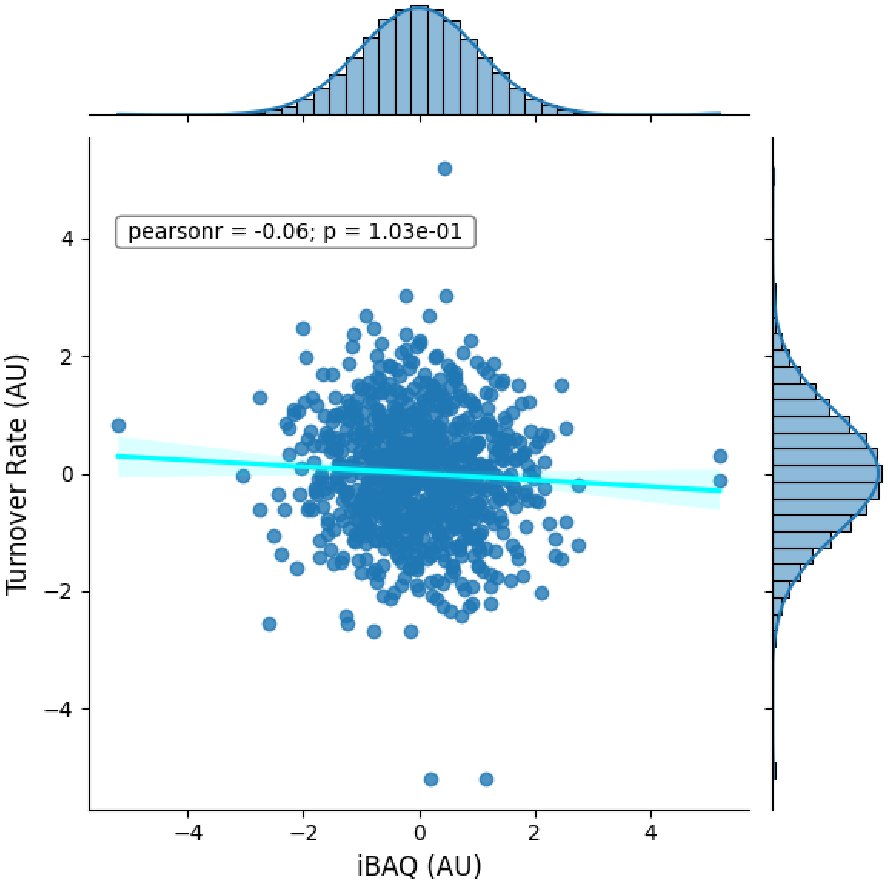
pearsonr = -0.06; p = 1.03e-01
Turnover Rate (AU)
iBAQ (AU)
4
2
0
−2
−4
−4
−2
0
2
4

C

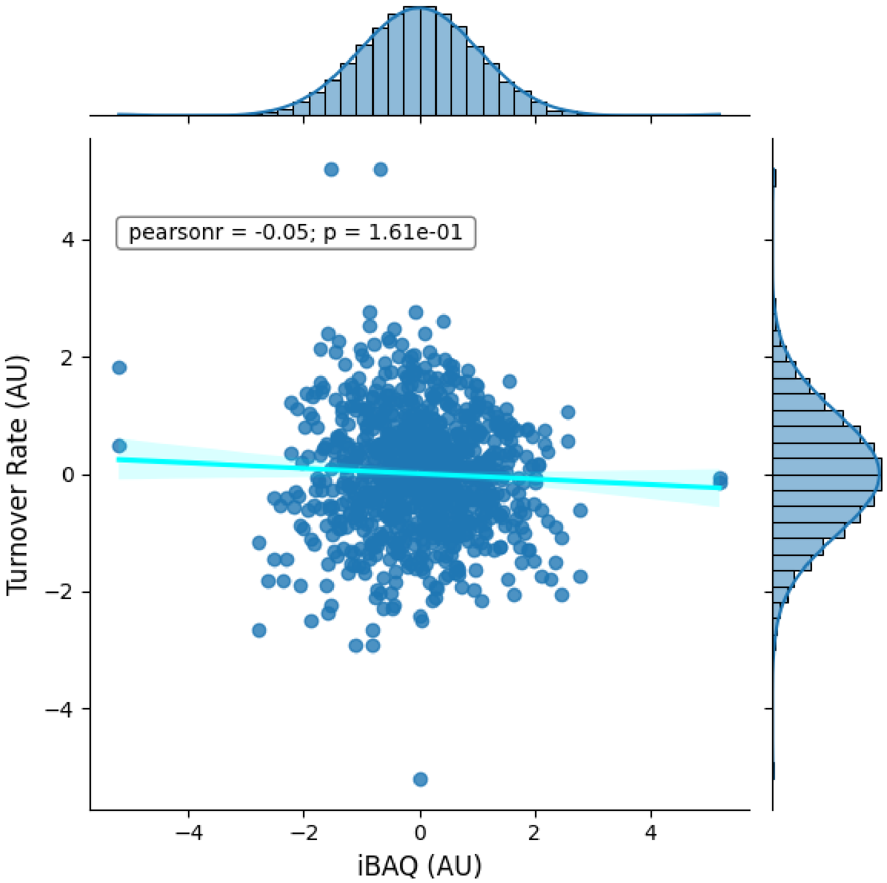
pearsonr = -0.05; p = 1.61e-01
Turnover Rate (AU)
4
2
0
−2
−4
−4
−2
0
2
4
iBAQ (AU)

D

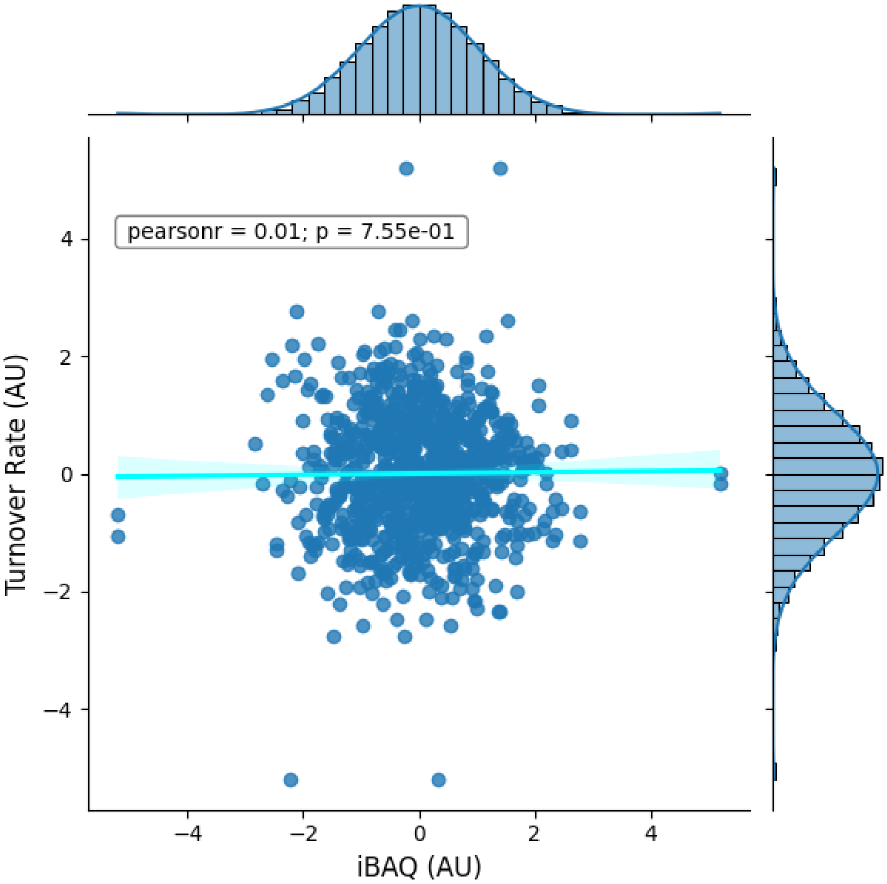
pearsonr = 0.01; p = 7.55e-01
Turnover Rate (AU)
4
2
0
−2
−4
−4
−2
0
2
4
iBAQ (AU)

Figure 16: *Jointplots depicting scatter plots with lines of best-fit, as well as histograms, of iBAQ and turnover rates for proteins identified in treatments:* ***A;*** *GMCSF,* ***B;*** *GMCSF-NECA,* ***C;*** *MCSF,* ***D;*** *MCSF-NECA.*

Figure 15 illustrates a largely complementary relationship between protein abundance (iBAQ) and protein turnover (rate day^{-1}) for each cytokine treatment, with a relatively low proportion of proteins demonstrating similar heatmap values for both abundance and turnover within each respective treatment. This would suggest that turnover measurements are providing an additional level of information on proteome regulation relative to measures of abundance. Figure 16 illustrates that three of four treatments present a negative correlation between protein abundance and turnover, albeit with none of the treatment correlations reaching statistical significance ($p>0.05$). This however, may suggest a slight trend for reduced protein turnover in proteins of high abundance, as has been previously reported in deuterium-labelling experiments[19,20].

This relationship may be influenced by the propensity for DDA to select high abundance precursors for MS2 fragmentation and subsequent peptide sequencing, with a consequent bias towards the identification of high abundant peptides (and proteins) within the dataset. Simultaneously, as DDA with narrow window isolation (as employed in this experiment at 2 m/z) is unlikely to select and successfully sequence M0 base monoisotopic peaks in highly deuterated (turned-over) peptides, it is further plausible that DDA proteomics analysis within a relatively long deuterium-labelling protocol (such as the one-week protocol employed within this experiment) may preferentially identify and quantify peptides of low deuterium enrichment for rate calculations. This would not be surprising, given that various other D2O-labelling experiments have reported proteins whose turnover rates are saturated and therefore unable to be accurately quantified due to their respectively high rates of protein turnover and deuterium-labelling[5,21]. An average quantified protein turnover rate of 0.07 day^{-1} within this dataset would further support this theory and would therefore pose as one potential mechanistic explanation for the relationship between protein abundance and turnover observed within this dataset. Depending on the experimental design and the intended target proteins deemed to be of highest importance, the duration of D2O labelling should therefore be carefully considered during experimental planning.

Another potential explanation for the observed negative trend in Figure 16 may be that the potential increases in deuterium-labelling in fact assist feature detection and subsequent iBAQ quantitation of the isotopic envelope (cluster), especially in low abundant peptides (proteins) presenting reduced signal: noise within the MS1 spectra. Similarly, as low abundant peptides may be nearing the limits of analytical detection, quantifying shifts in their mass isotopic distributions becomes more challenging as signal intensity decreases, and it is possible that during data processing the removal of “fraction new” peptides impacted by negative values arising from analytical noise disproportionately affects low abundant peptides of low deuterium enrichment. This would therefore produce a relative increase in low abundant peptides with greater deuterium incorporation (higher turnover), capable of passing stringency filters and may further present an explanation for the minor negative correlation observed within the dataset. Regardless, dataset filtering should also be considered as an important downstream parameter for the quantification of protein turnover in datasets where abundance is being investigated in parallel.

Within -omics datasets it is also common for biologically relevant proteins to be obscured through relatively lower levels of expression compared to those proteins (often of high abundance) whose core functions are less responsive to cellular or environmental stress[22]. It is therefore further possible that the observed leftward shift in (lower) relative protein abundance to higher rates of cellular protein turnover is merely a reflection of the relative expression levels of proteins that may be more responsive to each cytokine and adenosine receptor agonist (NECA) treatment. Furthermore, with DDA proteomics datasets prone to preferential detection of high abundance proteins, it is plausible complete turnover of this cellular protein pool will follow a longer time course, assuming that across experimental conditions the majority of proteins will present little-no change in their regulation[22,23].

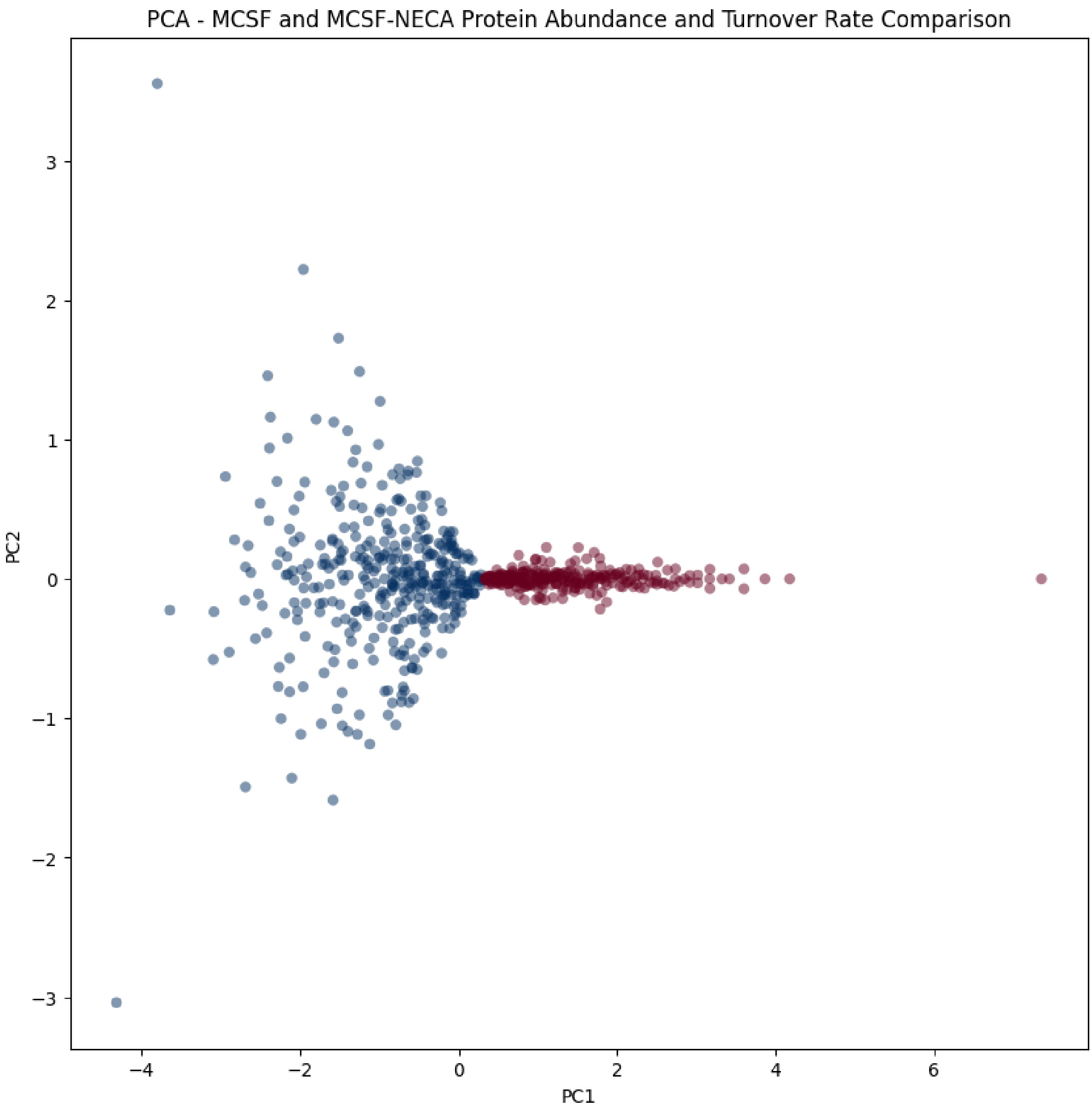

Figure 17: *Principal component analysis of M1-like and M2-like macrophages protein turnover and abundance (iBAQ) data.* ***Red*** *dots indicate iBAQ data and* ***blue*** *dots indicate turnover data.*

Principal component analysis clearly separates protein turnover from abundance datasets (Figure 17) for both macrophage phenotypes. In both cases, two proteins (Chloride intracellular channel protein 1; Myc box-dependent-interacting protein 1) belonging to the localisation protein class (PANTHER ontological classification) represent the most important features for PCA.

Protein Turnover Analysis: M1- and M2-like Macrophage Responses to NECA

To assess the utility of deuterium-labelling derived protein turnover measurements to separate culture treatments, principal component analysis was performed on M1-like (GMCSF supplemented) and M2-like (MCSF supplemented) macrophages in response to NECA treatment. Principal component analysis was unable to separate M1-like macrophages from those that received NECA, although minor separation was apparent along PC1, with an alternate unsupervised clustering technique, feature agglomeration, also unable to clearly separate NECA treatments (Figure 18a and b, respectively).

A

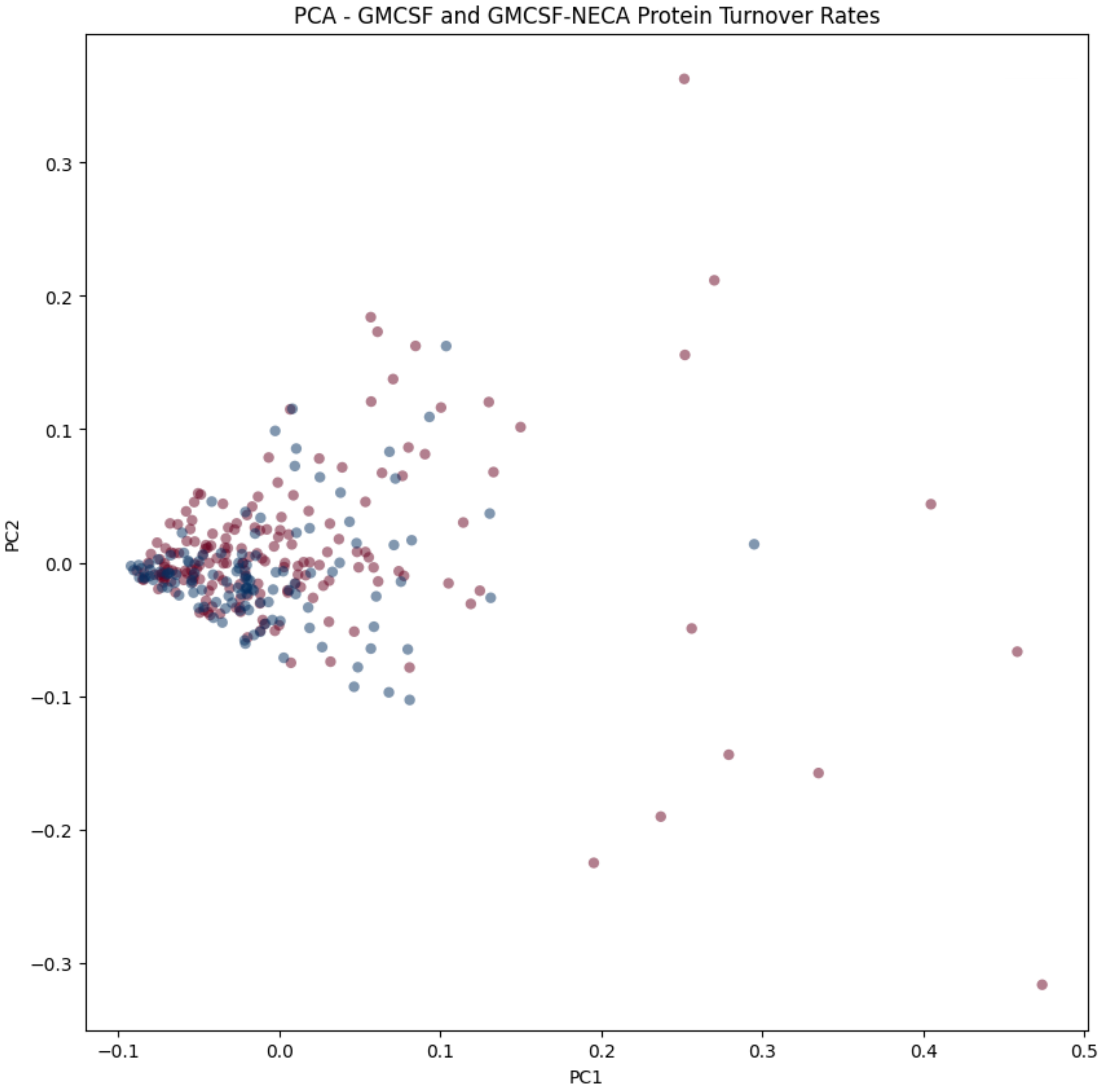

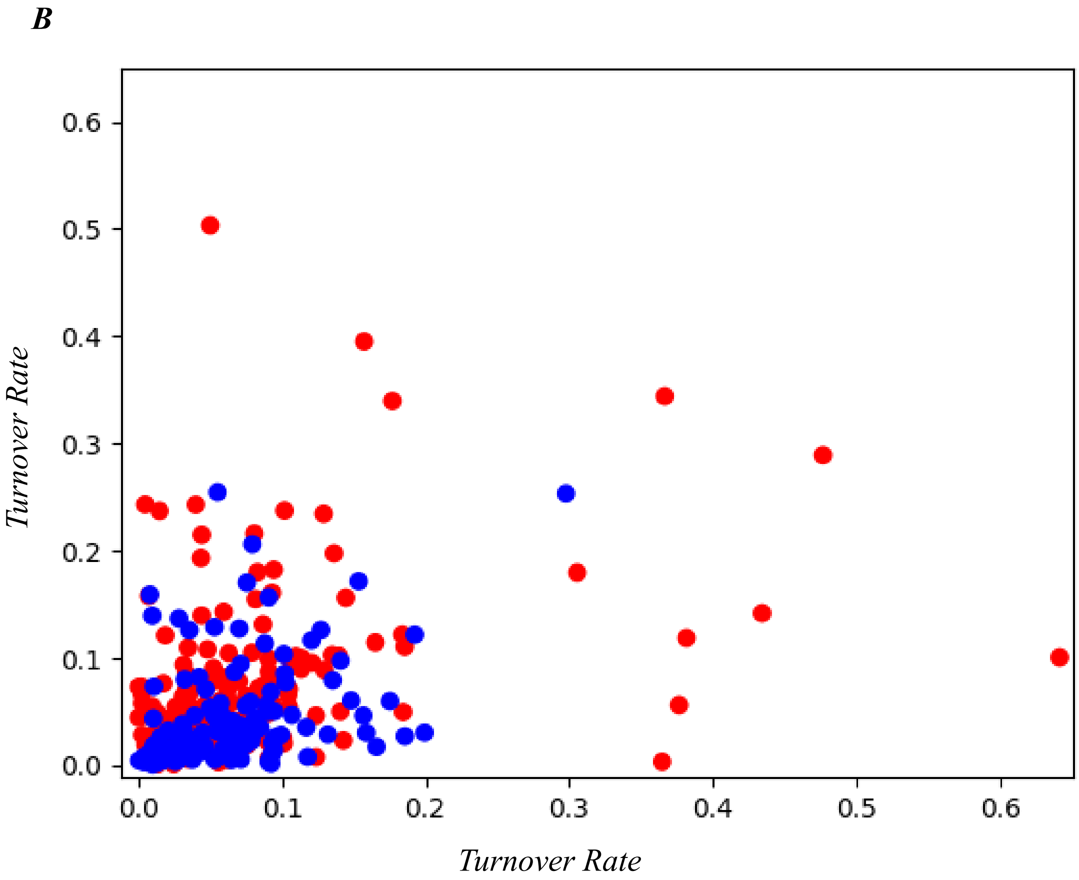

***Figure 18:** A; Principal component analysis of protein turnover rates in GMCSF and GMCSF-NECA treated macrophages. **B;** Feature agglomeration of GMCSF and GMCSF-NECA treated macrophages protein turnover rates. **Red** dots represent GMCSF-treated (M1-like) macrophage protein turnover rates, **blue** dots represent GMCSF-NECA treated (M2-like) macrophage protein turnover rates.*

While unsupervised machine learning techniques were unable to clearly separate GMCSF supplemented samples treated with and without NECA, this was similarly observed previously for protein abundance (iBAQ) analysis (Figure 6). Unfortunately, due to the low sample size (n=2) PLS-DA is not suitable to separate NECA treatments as previously performed for the iBAQ datasets (Figure 7). For further visual comparison of GMCSF and GMCSF-NECA protein turnover rates, heatmaps and jointplots were produced (Figure 19a and b).

A

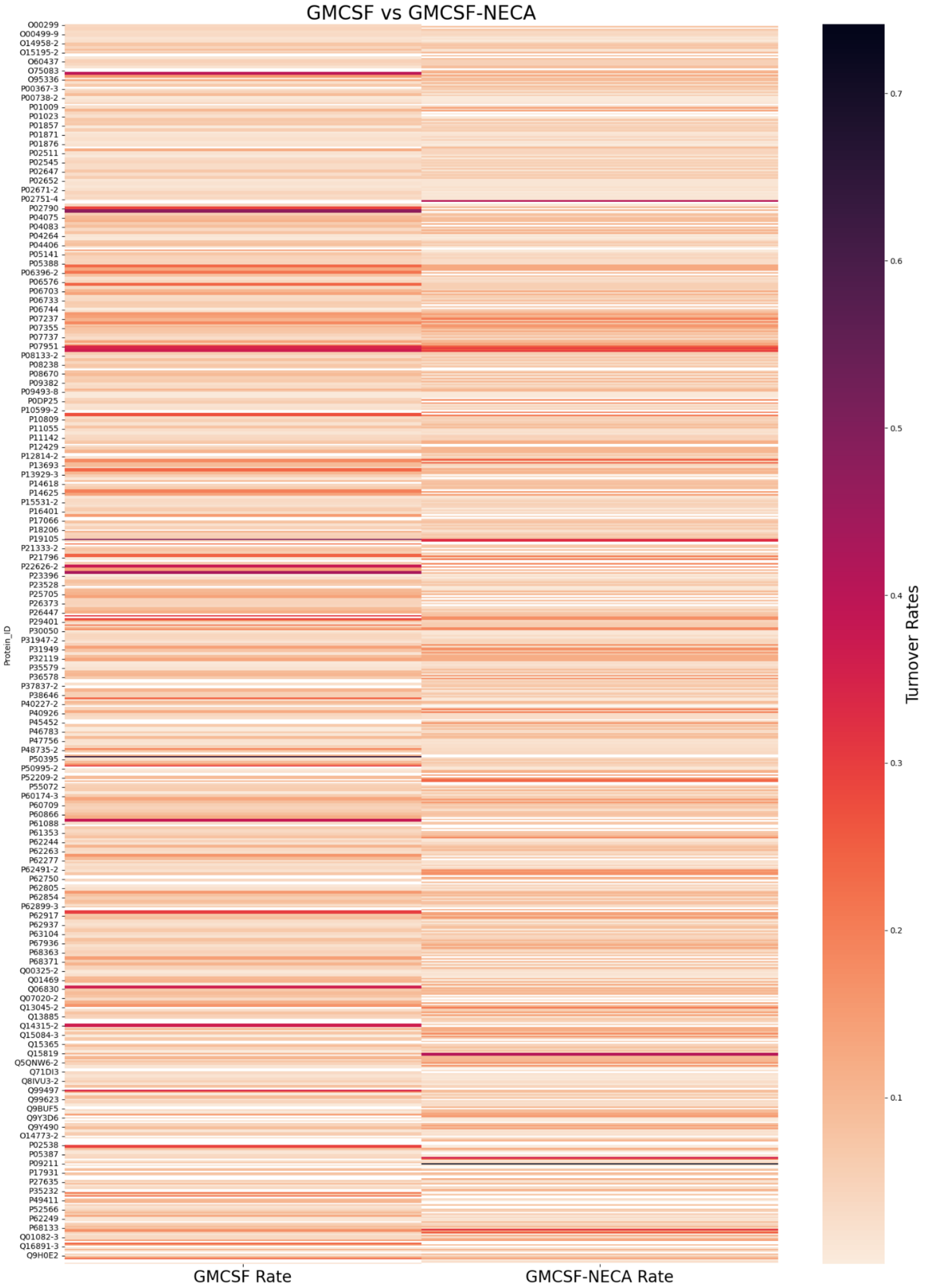
GMCSF vs GMCSF-NECA
Protein_ID
O00299
O00499-9
O14958-2
O15195-2
O60437
O75083
O95336
P00367-3
P00738-2
P01009
P01023
P01857
P01871
P01876
P02511
P02545
P02647
P02652
P02671-2
P02751-4
P02790
P04075
P04083
P04264
P04406
P05141
P05388
P06396-2
P06576
P06703
P06733
P06744
P07237
P07355
P07737
P07951
P08133-2
P08238
P08670
P09382
P09493-8
P0DP25
P10599-2
P10809
P11055
P11142
P12429
P12814-2
P13693
P13929-3
P14618
P14625
P15531-2
P16401
P17066
P18206
P19105
P21333-2
P21796
P22626-2
P23396
P23528
P25705
P26373
P26447
P29401
P30050
P31947-2
P31949
P32119
P35579
P36578
P37837-2
P38646
P40227-2
P40926
P45452
P46783
P47756
P48735-2
P50395
P50995-2
P52209-2
P55072
P60174-3
P60709
P60866
P61088
P61353
P62244
P62263
P62277
P62491-2
P62750
P62805
P62854
P62899-3
P62917
P62937
P63104
P67936
P68363
P68371
Q00325-2
Q01469
Q06830
Q07020-2
Q13045-2
Q13885
Q14315-2
Q15084-3
Q15365
Q15819
Q5QNW6-2
Q71DI3
Q8IVU3-2
Q99497
Q99623
Q9BUF5
Q9Y3D6
Q9Y490
O14773-2
P02538
P05387
P09211
P17931
P27635
P35232
P49411
P52566
P62249
P68133
Q01082-3
Q16891-3
Q9H0E2
GMCSF Rate
GMCSF-NECA Rate
Turnover Rates
0.7
0.6
0.5
0.4
0.3
0.2
0.1

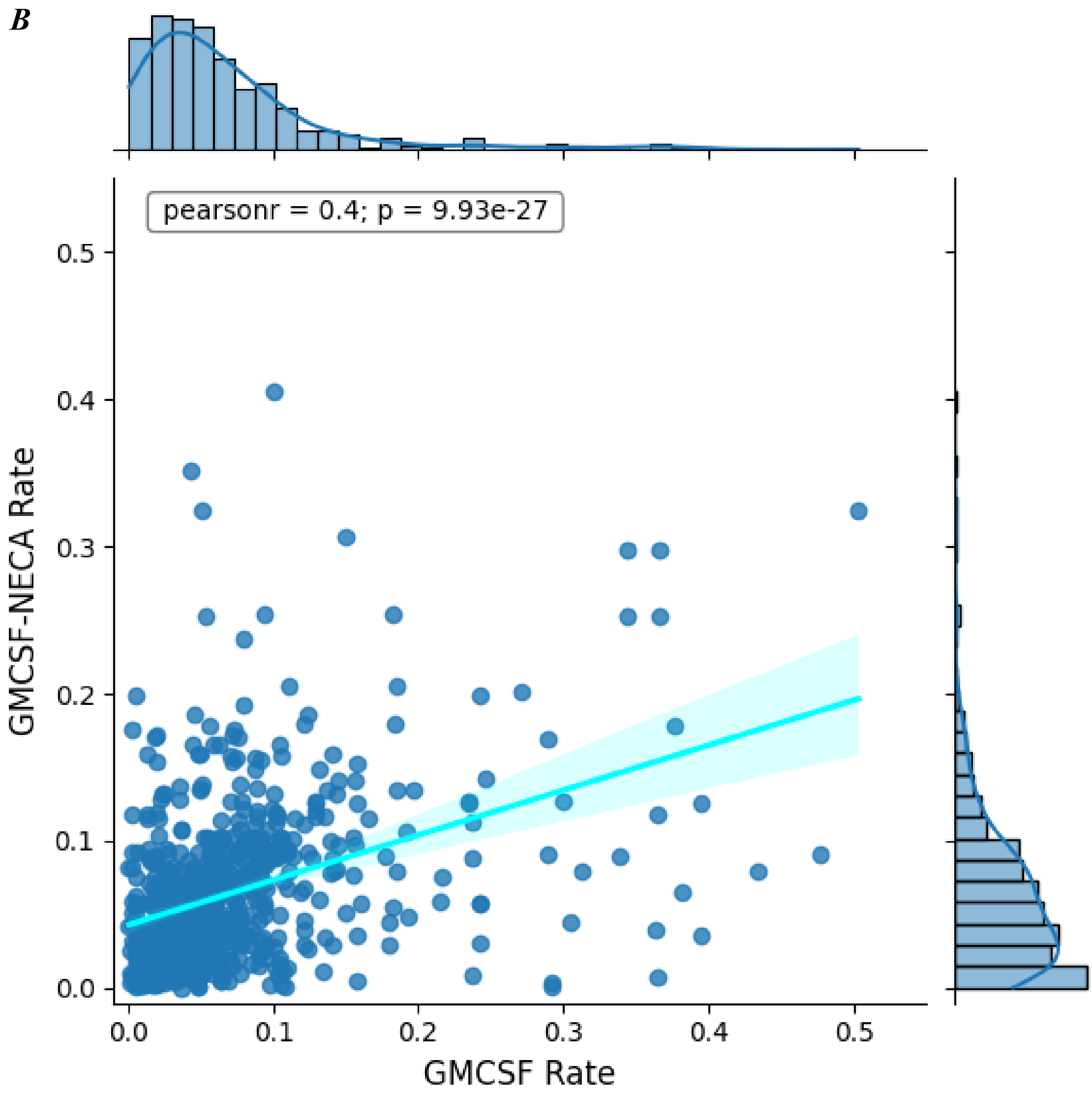

Figure 19: *A; Heatmap depicting GMCSF and GMCSF-NECA treated macrophage protein turnover rates.* ***B;*** *Jointplot combining scatter plot with line of best-fit and histograms for GMCSF and GMCSF-NECA protein turnover rates.*

Figure 19a illustrates predominantly similar rates for protein turnover in GMCSF and GMCSF-NECA treated macrophages across proteins identified in both treatments, however, some clear differences are present. In this untransformed data comparison, the extent of proteins that possess low rates of turnover (<0.1 rate day^{-1}) is apparent, and is represented by the leftward skew of turnover distributions illustrated in Figure 19b histograms. GMCSF and GMCSF-NECA demonstrate correlated and statistically significant protein turnover rates, however, this again is likely influenced by the relative proportion of protein turnover rates clustered in the bottom left of the scatter plot (Figure 19b). To further investigate differences between treatments, 20 proteins with the highest rates of turnover for both GMCSF and GMCSF-NECA supplemented macrophages were examined. Figure 20 illustrates protein classes with the highest turnover rates for GMCSF and GMCSF-NECA treated macrophages.

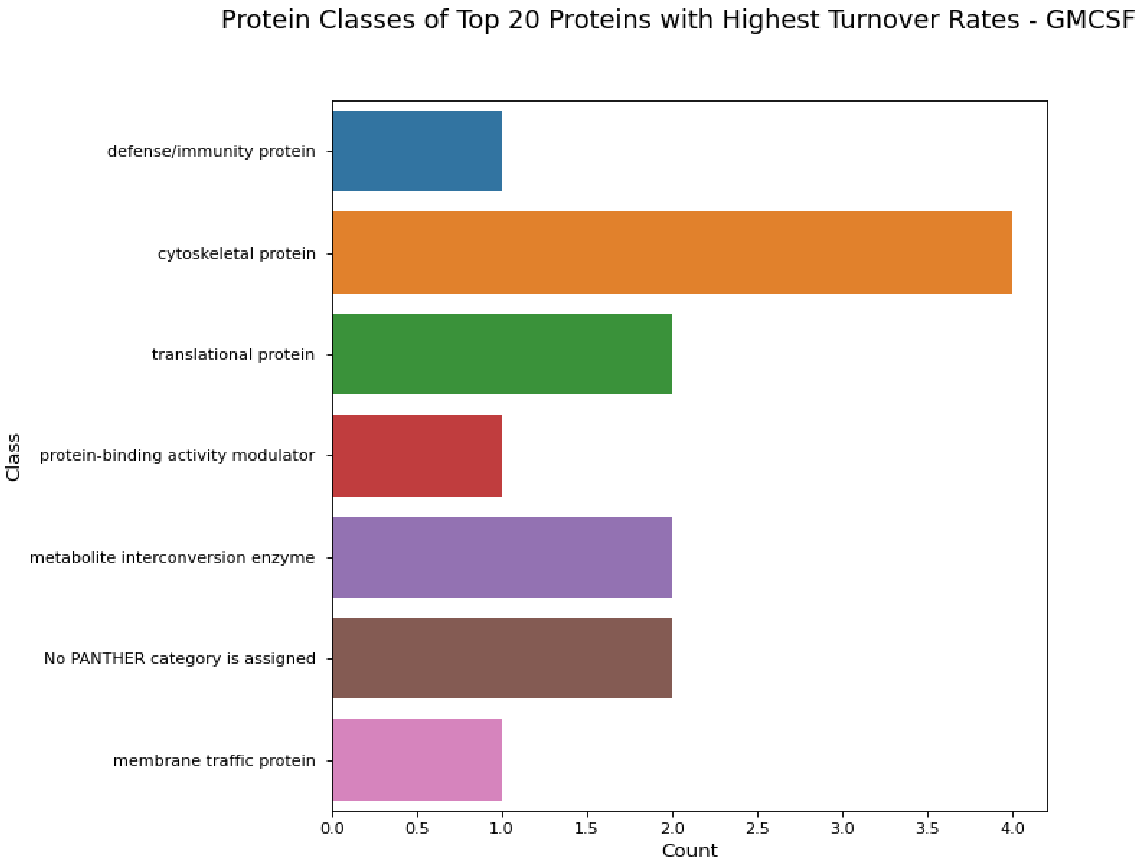

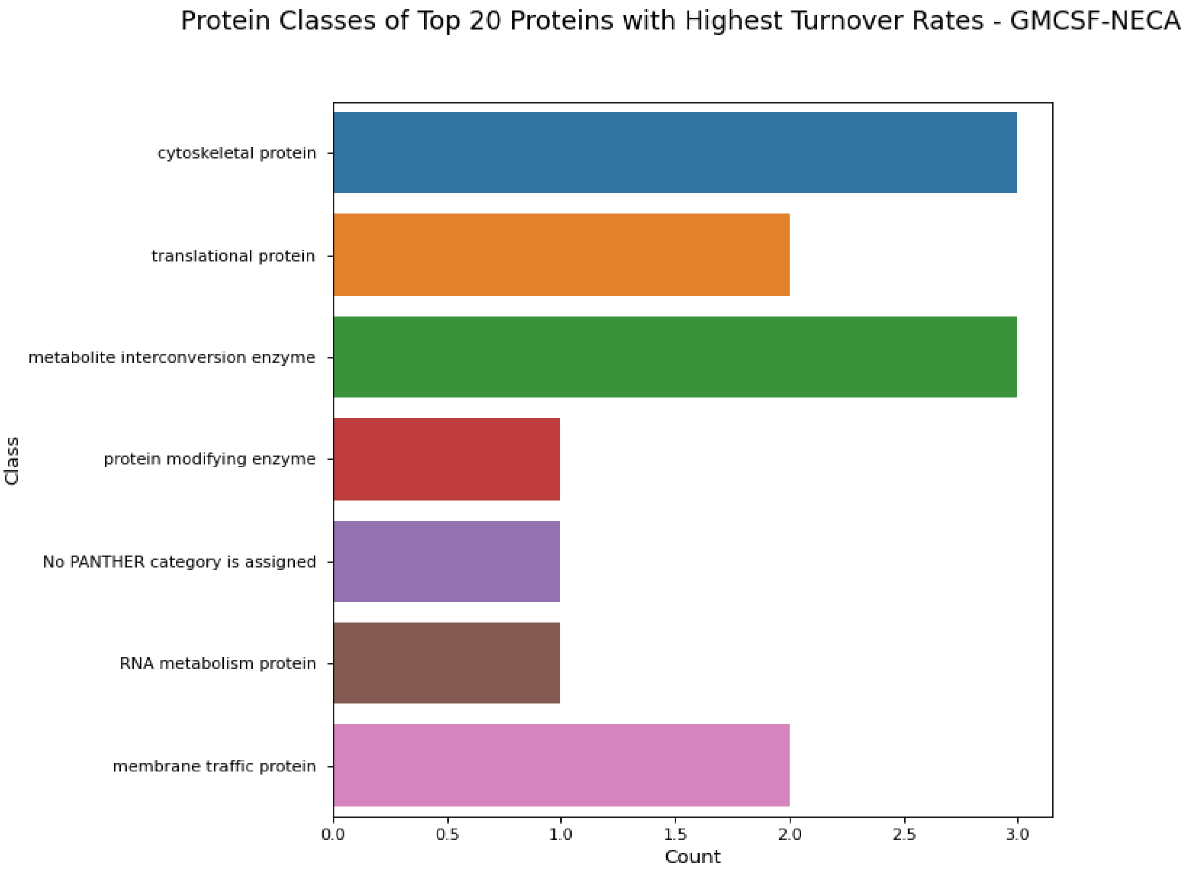

Figure 20: *Protein classes associated with 20 proteins of highest turnover for GMCSF and GMCSF-NECA macrophages.*

Ontological analysis of the 20 proteins with the highest turnover rates revealed minor changes, with the RNA metabolism and protein modifying enzyme classes unique to GMCSF-NECA treatment and the defence/immunity protein class unique to GMCSF treated macrophages. With low sample sizes, further multivariate exploratory analysis of differences in protein turnover rates is limited, but lack of the defence/immunity protein class would align with NECA's anti-inflammatory effect on macrophages.

Analyses investigating differences in protein turnover rates were repeated for M2-like macrophages (MCSF) treated with and without NECA (MCSF/MCSF-NECA). Similar responses to GMCSF treated macrophages were observed for all analyses into the effects of NECA supplementation (Figures 21-24).

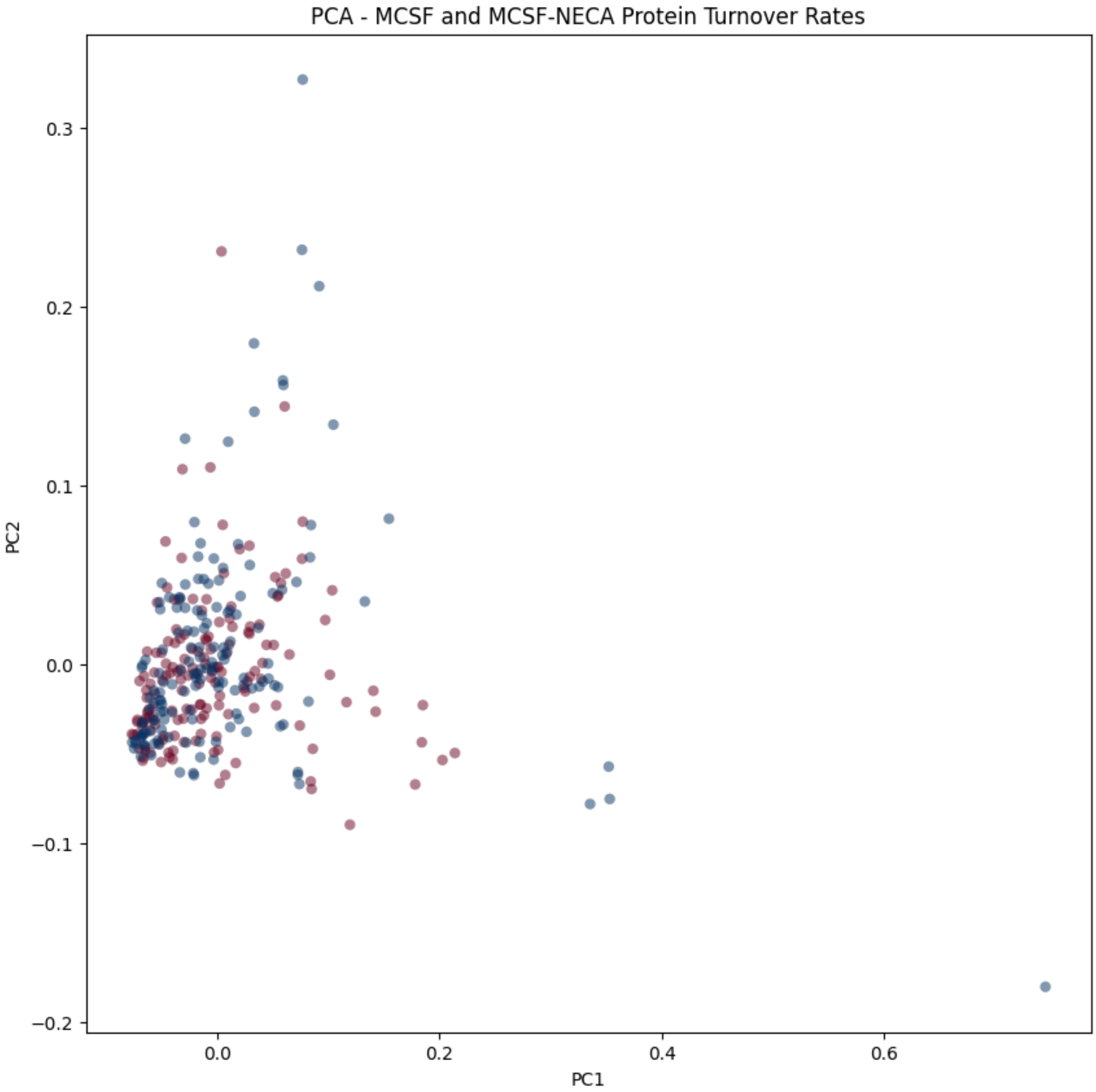

Figure 21: *Principal component analysis of protein turnover rates in MCSF and MCSF-NECA treated macrophages.* ***Red*** *dots represent MCSF treatment and* ***blue*** *dots represent MCSF-NECA treatment.*

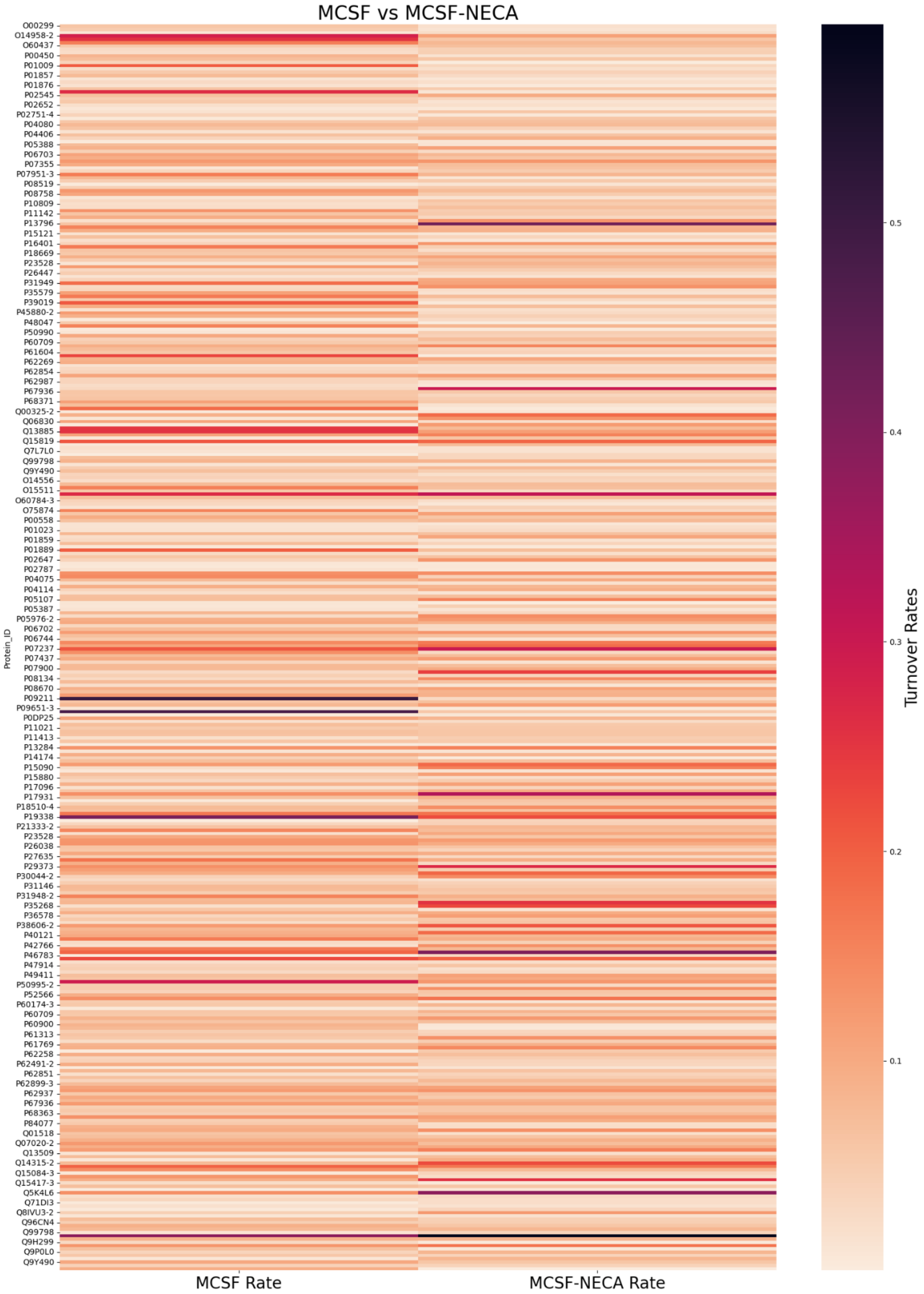

Figure 22: *Heatmap depicting MCSF and MCSF-NECA treated macrophage protein turnover rates.*

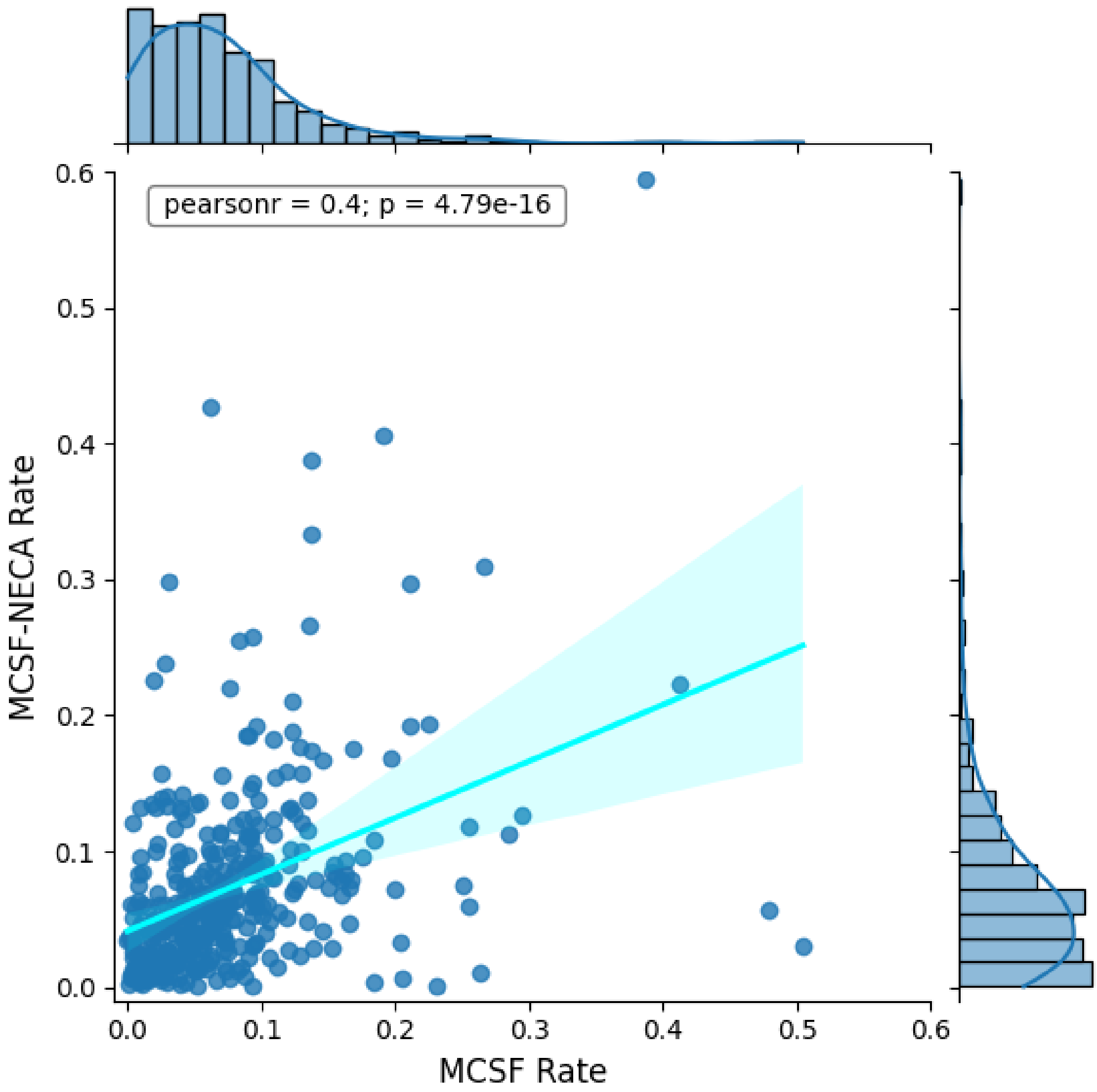

Figure 23: *Jointplot combining scatter plot with line of best-fit and histograms for MCSF and MCSF-NECA protein turnover rates.*

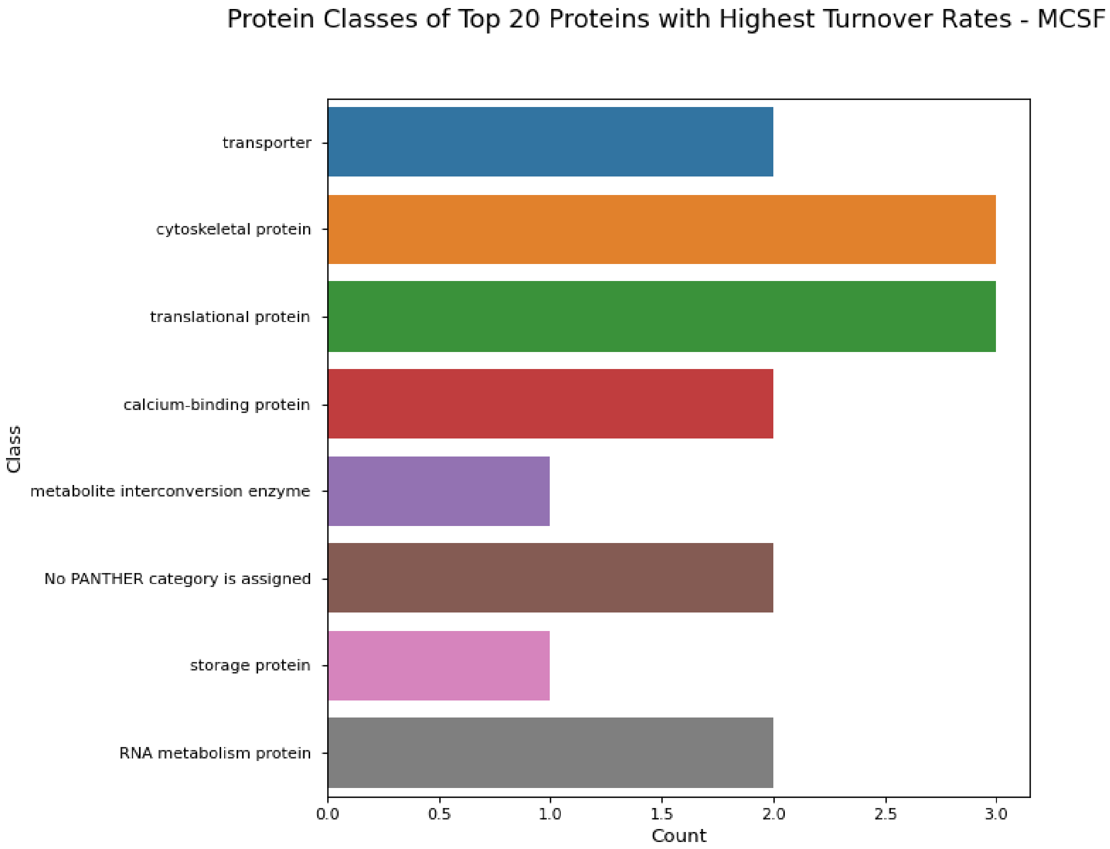

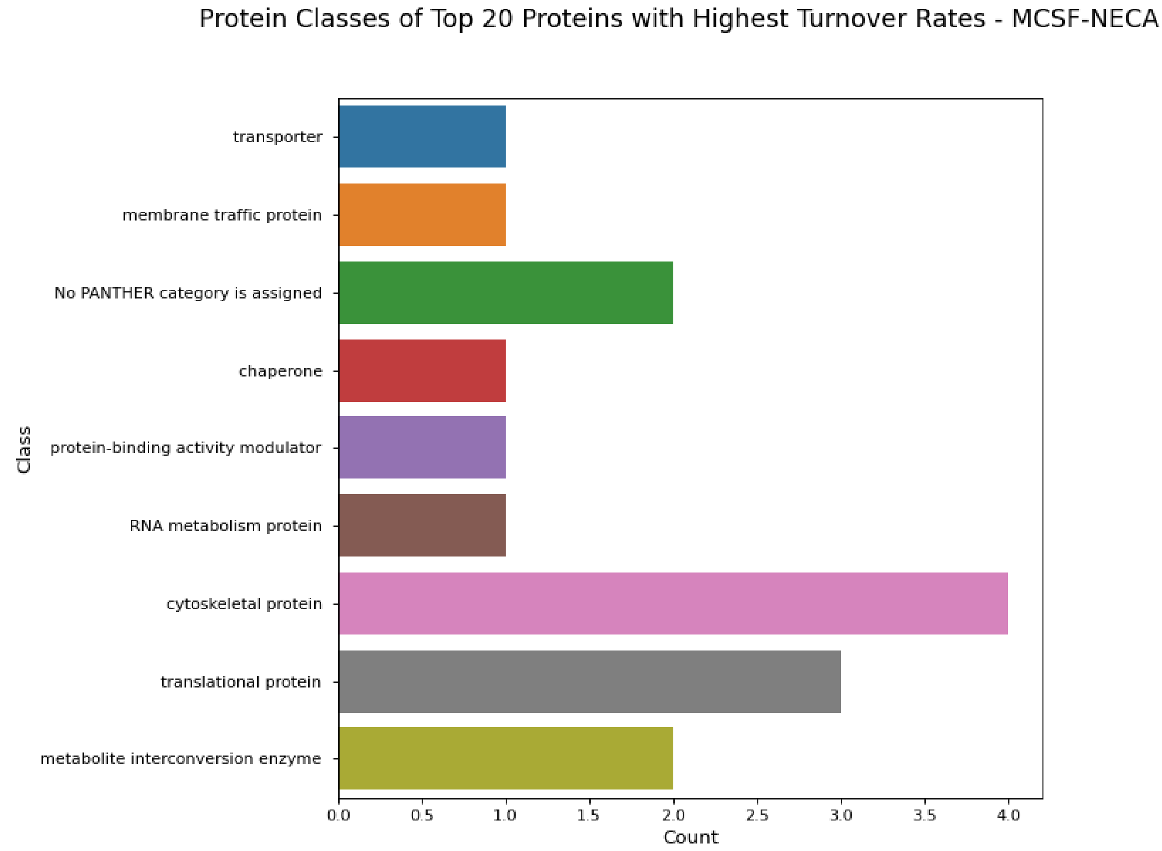

Figure 24: *Protein classes associated with 20 proteins of highest turnover for MCSF and MCSF-NECA macrophages.*

2.4 DISCUSSION

Application of deuterium-oxide (D2O) to an *ex vivo* cell culture model of differentiating M1- and M2-like macrophages enabled for quantitative analysis of proteome-wide turnover through an effective and minimalist metabolic stable isotope labelling approach. Application of a relatively stringent mass isotopic envelope (5 peptide isotopic peaks meeting m/z spacing criterion) enabled for an average quantification of >40% of total detected proteins per sample within this pilot experiment. Use of 5% D2O further allowed for the parallel quantitation of protein abundance via iBAQ[4], without notable effects on quantitative precision, presenting similar results from paired (5%) H2O and D2O treatments to those previously reported in the literature for technical replicates[3]. Furthermore, deuterium-labelling appeared to have a minimal effect on rates of protein identification compared to H2O-supplemented controls, contrasting with previous reports of reduced rates of peptide and protein identifications following a deuterium-labelling protocol[8].

Deuterium metabolic labelling of proteins covered a range of turnover rates in identified peptides/proteins, which in this dataset averaged 0.07 day^{-1}. This supports D2O as an effective metabolic tracer for temporal investigations into protein metabolism over periods of days-months. While 5% D2O was maintained in macrophages across the period of 7 days with the aim to capture changes between differentiating M1- and M2-macrophage phenotypes with and without the adenosine receptor agonist, NECA, it is possible that peptides (proteins) of higher turnover were not detected after 7 days due to large shifts in the mass isotopic distribution preventing identification of these peptides (proteins) at this timepoint. Shorter metabolic measurements with D2O may therefore enable assessment of protein dynamics in fast-turnover proteins where the monoisotopic precursor peak is unlikely to be selected by DDA for sequencing at high deuterium enrichments. Consideration should therefore be taken during experimental planning to ascertain the importance of fast- vs slow-turnover proteins. D2O poses as a versatile metabolic stable isotope tracer for use in cell culture studies interested in investigating temporal protein dynamics, an often overlooked aspect of proteome regulation in quantitative workflows[24].

While hindered by the low sample size of this pilot study, multivariate analysis was still able to clearly separate protein abundance and turnover measurements (Figure 17), driven by proteins of shared ontology according to PANTHER classification. Visualisation of iBAQ and turnover values for shared proteins across macrophage treatments demonstrated a minor trend for negative correlation between turnover rate and abundance (Figure 16a-c), suggesting a possible relationship between high turnover rates and low abundance in this dataset. A similar observation has previously been observed in a technical report on proteome kinetics with D2O that utilised an alternative method of protein quantitation[19], although the authors failed to comment on potential reasons for this observation. This seemingly complementary relationship merits further investigation in future experiments, with deuterium-labelling protocols proving insightful when applied to other pre-clinical models that combine protein kinetics with iBAQ quantitation[21].

iBAQ data alone enabled for separation of both M1- and M2-like macrophages with and without NECA treatment, even within the context of low sample sizes (n=4, respectively). This demonstrates the ability of protein abundance measures applied in parallel with D2O-labelling to successfully separate macrophage responses to a known anti-inflammatory stimulus[10]. In future, the combined analysis of iBAQ quantitation and protein kinetic analysis may pose a powerful tool in deciphering proteome regulation. While promising, there is still a paucity of studies applying D2O-labelling techniques to human and clinical models. Future work should therefore aim to utilise the versatility of deuterium-oxide as a metabolic tracer to further investigate the role of protein turnover in health and disease through integrated proteomics analysis.

2.5 REFERENCES

1. Doellinger, J., Schneider, A., Hoeller, M. & Lasch, P. Sample Preparation by Easy Extraction and Digestion (SPEED) - A Universal, Rapid, and Detergent-free Protocol for Proteomics Based on Acid Extraction. *Mol. Cell. Proteomics MCP* **19**, 209–222 (2020).
2. Cox, J. *et al.* Andromeda: a peptide search engine integrated into the MaxQuant environment. *J. Proteome Res.* **10**, 1794–1805 (2011).
3. Krey, J. F. *et al.* Mass spectrometry quantitation of proteins from small pools of developing auditory and vestibular cells. *Sci. Data* **5**, 180128 (2018).
4. Schwanhäusser, B. *et al.* Global quantification of mammalian gene expression control. *Nature* **473**, 337–342 (2011).
5. Naylor, B. C. *et al.* DeuteRater: a tool for quantifying peptide isotope precision and kinetic proteomics. *Bioinformatics* **33**, 1514–1520 (2017).
6. Martinez, F. O., Gordon, S., Locati, M. & Mantovani, A. Transcriptional Profiling of the Human Monocyte-to-Macrophage Differentiation and Polarization: New Molecules and Patterns of Gene Expression1. *J. Immunol.* **177**, 7303–7311 (2006).
7. Specht, H. *et al.* Single-cell proteomic and transcriptomic analysis of macrophage heterogeneity using SCoPE2. *Genome Biol.* **22**, 50 (2021).
8. Sadygov, R. G. Protein turnover models for LC–MS data of heavy water metabolic labeling. *Brief. Bioinform.* **23**, bbab598 (2022).
9. Buscher, K. *et al.* Natural variation of macrophage activation as disease-relevant phenotype predictive of inflammation and cancer survival. *Nat. Commun.* **8**, 16041 (2017).

10. Haskó, G. & Pacher, P. Regulation of macrophage function by adenosine. *Arterioscler. Thromb. Vasc. Biol.* **32**, 865–869 (2012).
11. Csóka, B. *et al.* Adenosine promotes alternative macrophage activation via A2A and A2B receptors. *FASEB J. Off. Publ. Fed. Am. Soc. Exp. Biol.* **26**, 376–386 (2012).
12. Ruiz-Perez, D., Guan, H., Madhivanan, P., Mathee, K. & Narasimhan, G. So you think you can PLS-DA? *BMC Bioinformatics* **21**, 2 (2020).
13. Ruiz-García, A. *et al.* Cooperation of Adenosine with Macrophage Toll-4 Receptor Agonists Leads to Increased Glycolytic Flux through the Enhanced Expression of PFKFB3 Gene. *J. Biol. Chem.* **286**, 19247–19258 (2011).
14. Timson, D. J. Fructose 1,6-bisphosphatase: getting the message across. *Biosci. Rep.* **39**, BSR20190124 (2019).
15. Sanfilippo, C. *et al.* SERPING1 mRNA overexpression in monocytes from HIV+ patients. *Inflamm. Res. Off. J. Eur. Histamine Res. Soc. Al* **66**, 1107–1116 (2017).
16. Valerieva, A. & Longhurst, H. J. Treatment of hereditary angioedema-single or multiple pathways to the rescue. *Front. Allergy* **3**, 952233 (2022).
17. Lim, M. Y., Paulo, J. A. & Gygi, S. P. Evaluating False Transfer Rates from the Match-between-Runs Algorithm with a Two-Proteome Model. *J. Proteome Res.* **18**, 4020–4026 (2019).
18. Yu, F., Haynes, S. E. & Nesvizhskii, A. I. IonQuant Enables Accurate and Sensitive Label-Free Quantification With FDR-Controlled Match-Between-Runs. *Mol. Cell. Proteomics MCP* **20**, 100077 (2021).
19. Lau, E. *et al.* A large dataset of protein dynamics in the mammalian heart proteome. *Sci. Data* **3**, 160015 (2016).

20. Kim, T.-Y. *et al.* Metabolic Labeling Reveals Proteome Dynamics of Mouse Mitochondria. *Mol. Cell. Proteomics MCP* **11**, 1586–1594 (2012).

21. Lam, M. P. Y. *et al.* Protein kinetic signatures of the remodeling heart following isoproterenol stimulation. *J. Clin. Invest.* **124**, 1734–1744 (2014).

22. Brunner, A. *et al.* Ultra-high sensitivity mass spectrometry quantifies single-cell proteome changes upon perturbation. *Mol. Syst. Biol.* **18**, e10798 (2022).

23. Cox, J. *et al.* Accurate Proteome-wide Label-free Quantification by Delayed Normalization and Maximal Peptide Ratio Extraction, Termed MaxLFQ. *Mol. Cell. Proteomics MCP* **13**, 2513–2526 (2014).

24. Holmes, W. E., Angel, T. E., Li, K. W. & Hellerstein, M. K. Chapter Seven - Dynamic Proteomics: In Vivo Proteome-Wide Measurement of Protein Kinetics Using Metabolic Labeling. in *Methods in Enzymology* (ed. Metallo, C. M.) vol. 561 219–276 (Academic Press, 2015).

25. Rieckmann, J. C. et al. Social network architecture of human immune cells unveiled by quantitative proteomics. Nature Immunology 18, 583–593 (2017).

3. INVESTIGATIONS INTO CELLULAR PROLIFERATION AND PROTEIN TURNOVER IN HUMAN IMMUNE CELL POPULATIONS USING DEUTERIUM-OXIDE *IN VIVO*: A PILOT STUDY

ABSTRACT

Background and Aims: Application of deuterium-oxide (D_2O) metabolic tracer for 'shotgun' measurements of proteome kinetics via LC-MS have primarily employed cell culture and pre-clinical models. This study aimed to assess proteome kinetics in peripheral immune cell populations isolated from the blood of healthy participants dosed with D_2O.

Methods: Six healthy participants were dosed with D_2O to reach a deuterium body water enrichment of ~1.5%, which was maintained across a six-week period. Deuterium body water enrichment was determined from saliva samples at each study visit. Venous blood was drawn via venepuncture at eight timepoints and cell populations were isolated via MACs/FACs. Cell populations were then analysed by mass spectrometry to determine rates of cellular proliferation and proteome kinetics.

Results: Deuterium body water enrichment plateaued at 1.64 ± 0.16% across study participants. Monocytes and effector memory T-cells demonstrated average cellular turnover rates of 7%/day and 0.48%/day, respectively. Approximately 90% of identified proteins in effector memory T-cells were quantified for turnover across the study time-course, with participant body water deuterium enrichments of 1-1.2% proving optimal for proteome kinetic analysis. Only ~6% of total identified monocyte proteins rates of turnover were successfully quantified.

Conclusions: Deuterium body water enrichment of 1-1.2% is sufficient to enable mass spectrometry-based measurements of cellular proliferation and proteome kinetics in peripheral immune cell populations. Future work should address constraints in modelling turnover that arise from input of fast cellular proliferation rates which consequently reduce proteome coverage. Optimal time point sampling is therefore imperative during proteome kinetic experiments in proliferating cell types.

Keywords: D_2O, monocytes, effector-memory T-cells, turnover, proliferation.

3.1 INTRODUCTION

Previous applications of deuterium-oxide (D_2O) metabolic tracer for ‘shotgun’ measurements of proteome kinetics via LC-MS have primarily utilised cell culture and pre-clinical models. While informative, there is a current paucity of studies utilising D_2O as a metabolic tracer for proteome-wide kinetic measurements *in vivo* (Chapter II, *section 1*). Furthermore, this has, to the author’s knowledge, yet to be employed in proliferating immune cell types isolated from human peripheral blood.

This study therefore aims to simultaneously assess cellular proliferation and proteome kinetics in peripheral immune cell populations isolated from the blood of healthy participants dosed with D_2O across a six-week period. To fully address the utility of this technique, a fast-proliferation cell type of the innate immune system, monocytes, as well as a more slowly proliferating cell type, effector memory T-cells, have been selected for kinetic analysis.

This study aims to not only provide proof-of-concept for the analysis of proteome kinetics in proliferating cell types of the immune system, but to also investigate parameters intrinsic to performing D_2O labelling studies in humans - such as the ability to effectively estimate and maintain deuterium body water enrichment at a defined constant, the effects of participant characteristics on D_2O loading (BMI, sex), and importantly to determine the analytical constraints and capabilities of these analyses. This will inform future studies interested in utilising D_2O as a metabolic tracer for *in vivo* analysis of human proteome kinetics.

3.2 METHODS

Study Participants

Eight healthy adult participants (five males and three females; Table 1) were recruited to the study, with none presenting a history of autoimmune disease. This study was approved by the University of Nottingham Medical School Ethics Committee in accordance with the Declaration of Helsinki and all participants provided informed consent and completed a general health questionnaire prior to enrolment. This study was performed following the second UK COVID-19 lockdown and as such, recruitment was constrained to staff and students at the University of Nottingham. Unfortunately, due to the ongoing prevalence of COVID-19 and UK government restrictions, several participants missed one or more study timepoints due to self-isolation or COVID-19 infection during the six-week study protocol (detailed in Table 1). Following recovery and a negative COVID-19 test result, participants were allowed to resume their involvement in the pilot study.

Participants were asked to maintain their current levels of exercise and to not alter their diet across the duration of the study. The morning of each study day, participants were asked to refrain from drinking for at least 30 minutes and to not consume food for at least two hours prior to their visit. Estimates of body water content were based on participant body mass and activity level, with estimates ranging from 55-65% body mass[1].

Deuterium Enrichment

Deuterium-oxide (D_2O, 70% atom, IsoWater Corporation) was administered to participants during an initial 'ramp' phase spread across 1-2 days aimed at achieving a deuterium enrichment of approximately 1-2% total body water, calculated relative to total body mass (600-1050ml 70% D_2O administered). Assuming body water turnover of approximately 6% per day[2], daily 'top-up' doses of D_2O were administered throughout the remainder of the six-week study period to maintain isotopic plateau (40-100ml of 70% D_2O administered per day).

Rapid increases in deuterium body water enrichment during the ramp phase has been known to result in nausea and dizziness, attributed to temporary shifts in water density that affect the vestibular system of the inner ear[3]. These are transient at low deuterium enrichments (1-2% total body water) and once deuterium levels equilibrate with the body water pool, have no known side effects. One of the eight study participants experienced acute nausea during the early stages of the loading protocol (~halfway through the ramp phase) which resulted in vomiting. This study participant was therefore immediately withdrawn from the study and monitored by a physician, during which they experienced no further side effects. One study participant withdrew from the study following the ramp phase of their own personal volition, with the baseline samples from these two participants stored under the Human Tissues Act (2005) and subsequently utilised for development of proteomics sample preparation protocols (*section 3.2*). All six remaining study participants completed the six-week loading protocol without issue. Participant characteristics from the study are described in Table 1.

To monitor deuterium enrichment in body water throughout the study protocol, saliva samples were collected from participants at each study visit. Once collected, saliva was immediately separated by centrifugation (10 minutes at 13,000 rpm) and the supernatant stored at -80ºC until analysis. The deuterium enrichment of saliva samples was analysed via base-catalysed isotopic exchange of hydrogen (deuterium) atoms with acetone[4]. Briefly, 100µL from each sample was incubated with 2µL of 10M NaOH and 1µL of acetone for approximately 15h at room temperature. Following incubation, acetone was extracted through the addition of 200µL n-heptane and 1µL of the extracted n-heptane phase was injected into a Trace 1310 gas-chromatograph (Thermo Scientific) linked to a ISQ single-quadrupole mass spectrometer (Thermo Scientific) for isotope analysis. Samples were run alongside a standard curve of known D_2O enrichment to enable calculation of body water enrichment, through monitoring changes in the ratio of the 59:58 m/z ions of acetone.

Blood Sampling and Immune Cell Isolation

At each study visit, 20ml blood was drawn via venepuncture into green lithium heparin BD vacutainers (Becton, Dickinson and Company, USA). Blood was collected at baseline (immediately prior to commencement of D_2O dosing) and then at days 2, 7, 14, 21, 28, 35 and 42 of the six-week study. At the end of each study visit, participants consumed their daily maintenance dose under supervision and were provided with a sufficient volume of D_2O to enable self-administration until the next study visit.

To isolate peripheral blood mononuclear cells (PBMCs), blood was immediately layered on 15ml histopaque (Sigma) at room temperature. Density centrifugation was performed at 800g for 25 minutes at 21°C on minimum brake to acquire layered blood samples. PBMCs were then harvested from the buffy-coat layer, washed twice in endotoxin-free Phosphate Buffer Saline (PBS, Sigma) at 350g for 8 minutes, followed by 300g for 5 minutes to eliminate any remaining red blood cells. PBMCs were resuspended in Magnetic-activated cell sorting (MACS) buffer, PBS, 1% FCS and EDTA 2mM. PMBCs were then incubated for 15 minutes at 4°C with CD14 antibody coated magnetic microbeads (Miltenyi). Using an MS column (Miltenyi) attached to a magnet, PBMCs were passed through the column allowing for the CD14- cells to flow through. Following 3 washes with MACS buffer, CD14+ cells were eluted in 1ml MACS buffer away from the magnet.

CD14- cells were spun down and resuspended in MACS buffer according to PBMC yield; 40µl per 10^7 PBMCs. Pan T-cell Biotin-Antibody cocktail was then added at a volume of 10µl per 10^7 PBMCs. Cells were vortexed and incubated at 4°C for 5 minutes. Next, 20µl of Pan T-cell Microbead cocktail was added per 10^7 PBMCs and mixed by vortex. Following 10 minutes incubation at 4°C, cells were passed through an LS column (Miltenyi) attached to a magnet. After 3 washes with MACS buffer, flow-through containing pan T-cell mix was collected.

Every T-cell sample was then distributed into four tubes for sorting of CD3+CD45RO+CCR7+ vs CD3+CD45RO+CCR7-. Two of the tubes served as Fluorescence Minus One (FMO) samples where cells were incubated with CD3 antibody, plus either CD45RO antibody and CCR7 isotype control or CD45RO isotype control and CCR7 antibody. One sample would contain unstained cells in order to distinguish the CD3+ cells. Using the FMO samples and a SONY cell sorter (SH800S), CD3+CD45RO+CCR7+ cells could be distinguished from CD3+CD45RO+CCR7-. Briefly, the FMO sample containing a mix of T-cells was run through the SONY SH800S sorter on ordinary flow cytometry mode. Projecting a dot plot display of Forward vs Side Scatter, T-cells were gated excluding debris and possible dead cells. Next, forward side-scatter area vs forward side-scatter height graphs were used in order to exclude doublets or falsely oversized cells. Single cells were then plotted as Side Scatter vs Fluorescence Intensity. Using the FMO controls and the unstained sample, a gate separating the two populations of interest was set before running the analytical samples. Each sample was then sorted into two tubes containing CD3+CD45RO+CCR7+ and CD3+CD45RO+CCR7- cells, respectively.

10µl of each sample was used to confirm correct labelling of the sorted cells with a MACSQuant 10 flow cytometer and sorted samples were then pelleted by centrifugation 300g 5 minutes and all of the supernatant was removed by pipetting and discarded. Cells were sorted at an average efficiency of 94%.

All sorted cell populations were finally spun at 300g for 5 minutes to obtain a cell pellet for mass spectrometry analyses. Samples were divided equally and washed three times with phosphate buffered saline (PBS) via centrifugation at 300g for 5 minutes and PBS removed from cell pellets. Cells were then stored at -80°C until processing for mass spectrometry analyses. Information on sorted cell numbers for each immune population at their respective participant timepoints are detailed in Table 2.

Measurement of Deuterium Incorporation into Nucleic Acids

Immune cells were thawed on ice and 200µL extraction buffer (0.1M Tris·HCl, pH 8, 0.01M EDTA, pH 8, and 1M NaCl) was used to lyse cell pellets via pipetting. Equal volume phenol: chloroform: isoamyl alcohol (pH 8) was added to samples, inverted 15 times and centrifuged for 10 minutes at 13,000rpm, 4ºC. Following centrifugation, the upper aqueous layer was removed to a clean Eppendorf. Nucleic acids were precipitated through addition of equal volume isopropanol, inverted 15 times and centrifuged at 13,000rpm for 20 minutes at 4ºC. Isopropanol was removed and pellets were washed with addition of 100µL 70% ethanol and centrifugation at 13,000rpm for 5 minutes (4ºC). This wash step was repeated twice. Pellets were allowed to air-dry at room temperature before resuspension with 22µl molecular biology grade water and samples stored at -80°C until further analysis.

Samples were thawed and nucleic acids hydrolysed via addition of 5µl of 375mM sodium acetate (pH 4.8) and 750µM $ZnSO_4$ containing 0.5 units of nuclease S1 and 0.25 units of potato acid phosphatase at 37°C overnight. Hydrolysates were then reacted with 10µl of O-(2,3,4,5,6-Pentafluorobenzyl) hydroxylamine hydrochloride (2% wt/vol) and 7.5µl of acetic acid at 100°C for 30 min. Samples were then cooled at room temperature prior to the addition of 100µl acetic anhydride followed by 10µl of 1-methylimidazole. Reactions were transferred to boiling tubes after approximately 20 minutes and quenched by the addition of 2ml of double-distilled water. Newly formed derivates were extracted via addition of 500µl of dichloromethane (DCM), following vortex and phase separation. By prewetting the tip with DCM, the lower layer was removed to a clean boiling tube and this step was repeated to ensure all formed derivatives were successfully transferred. Derivatives were dried under nitrogen stream at room temperature (~25ºC), resuspended in 40µl ethyl acetate and transferred to fresh autosampler vials for GC-MS/MS analysis.

For CD14+ monocytes, 0.5µl of sample was injected into a Trace 1310 Gas Chromatograph connected to a TSQ 8000 triple quadrupole GC-MS/MS (Thermo Scientific). For CCR7- T-cells with lower cell counts and respective nucleic acid yields, 2µL sample was injected. All samples were injected on splitless mode with an inlet temperature of 280°C, with GC ramp conditions: 120°C for 1 min, ramp to 280°C at 10°C/min, and hold for 3 min. Selected reaction monitoring (SRM) was performed at m/z 395: 112 and 396: 113, representing the M0 and M^{+1} ions of deoxyribose, following a collision-induced dissociation energy of 15. Shifts in the ratio of the mass isotopic product ion peaks were monitored over time, and along with body water deuterium enrichment values determined from saliva, enabled calculation of cellular turnover rates as follows:

Changes in deuterium enrichment were calculated as:

$$M^{+1}/(M + M^{+1})$$

with the mole percent excess (MPE) expressed as difference from unlabelled D_2O free samples.

Fractional turnover were calculated as:

$$F\% = (r\text{-}MPE)/[(p\text{-}MPE \times af)] \times 100$$

where *r-MPE* is the excess enrichment of bound deoxyribose, *p-MPE* is the mean precursor enrichment over the time period, *af* is the amplification factor of the precursor enrichment due to the multiple binding sites of deoxyribose, multiplied by 100 to convert fractional turnover into a percentage.

Fractional replacement rates (*k*) were then calculated as:

$$-\ln[1-f]/t$$

where *f* refers to the fraction of new cells (fractional turnover) and *t* represents the time between measurements.

For mass spectrometry analyses, all samples were run in triplicate alongside standard curves of deoxyribose at known standard concentrations. Average values for each triplicate measurement were taken forward for further analysis, for all samples. All cellular proliferation data are displayed as mean ± standard deviation, unless otherwise stated. Statistical significance is defined as $p<0.05$.

Participant	Age	Sex	Height (cm)	Weight (kg)	BMI	Ramp Phase D_2O Volume (ml)	Daily Maintenance D_2O Volume (ml)	Target D_2O Enrichment (%)
1	25	Male	187.5	67.5	19.2	950	100	1.5
2	26	Male	176.5	75	24.1	1050	100	1.5
3	28	Female	169	57.2	20	800	NA	1.5
4	28	Female	166	71.3	25.9	1000	NA	1.5
5	54	Male	172	64	21.6	800	50	1.5
6	23	Male	180	64	19.75	800	50	1.5
7	40	Female	163	64.1	24.1	600	40	1.2
8	31	Male	177	78.8	25.2	800	50	1

Table 1: *Study participant characteristics and deuterium-oxide (D_2O, 70% atom) doses administered to each participant over the ramp and maintenance phase of the 6-week study protocol. No daily maintenance D_2O volumes are presented for participants 3 and 4 (NA), as participant 3 withdrew from the study due to personal reasons and participant 4 was withdrawn from the study due to acute nausea during the ramp phase that resulted in vomiting.*

Proteomics Sample Preparation

Immune cells were lysed by the addition of 50-100µl trifluoroacetic acid (TFA), gently vortexed and incubated on ice for approximately 8 minutes. Samples were then gently vortexed for 2 seconds and immediately neutralised via addition of neutralisation buffer (2M Tris Base in double-distilled H_2O) at 10 times the volume of TFA. Neutralisation was left to occur at room temperature for 10 minutes. Reduction/alkylation buffer (100 mM Tris (2-carboxyethyl) phosphine (TCEP), 400 mM Iodoacetamide (IAA) in double-distilled H_2O) was added at 1.1 times volume of TFA and samples were immediately incubated in the dark at 95ºC for 5 minutes. Samples were then cooled on ice for approximately 30 minutes prior to determination of protein quantification at 280nm using a NanoDrop Lite Spectrophotometer (Thermo Scientific). Samples were then stored at -80ºC until further processing.

100µg of protein was aliquoted into fresh Protein LoBind Eppendorfs (Thermo Scientific) and diluted 1:5 with double-distilled H_2O. Trypsin was added to protein samples at a ratio of 1:100, and samples were incubated overnight for approximately 19 hours at 37ºC. Tryptic digests were quenched via the addition of TFA to 2% total volume. Sample peptides were transferred to chromatography vials and dried under liquid nitrogen stream at 40ºC for 30 minutes. Samples were then stored at -80ºC until nanoLC-MS/MS analysis.

Samples were thawed at room temperature for 15 minutes before resuspension in 50µl 95% Acetonitrile (ACN), 5% double-distilled H_2O with 0.1% formic acid (FA). Peptide concentrations were estimated by nanodrop measurements at 280nm and samples adjusted to approximately 1 µg/µl peptide concentrations. 2µl from each sample was pooled for quality control measurements (QCs) and all analytical batches included standards, sample specific QCs and blank instrument measurements to monitor instrument performance and repeatability throughout the run.

For CD14+ monocyte samples, 2µg of peptides were analysed via a LTQ Orbitrap XL (Thermo Scientific) mass spectrometer in line with an EASY-nLC 1000 ultra-high pressure liquid chromatography system and EASY-Spray nano electro spray ionisation (nESI) source (Thermo Scientific). Peptides were loaded onto a pre-column (C18 Pepmap100 5mm x 5um), prior to separation on a 50cm analytical column (C18, 5um, 50cm, 100 Aº Easy nano spray column #ES903, Thermo Scientific) at a flow rate of 250nl/min. A non-linear gradient of solvent B (80% ACN (v/v) in 0.1% FA (v/v)) was applied for a total gradient time of 104 minutes and total run time of 131 minutes. Data were acquired in data-dependent acquisition (DDA) mode. Full MS scans were acquired at 60,000 resolution m/z 200 measured using Orbitrap mass analyser, with a mass range 400-1600 m/z. The top 12 precursor ions were selected with an isolation window of 2 m/z units for fragmentation via CID at a normalised collision energy of 35. MS2 spectra were acquired at a resolution of 17,500 m/z 200 with the Orbitrap mass analyser and a dynamic exclusion duration of 180 seconds.

For CCR7- samples, 5µg of peptides were analysed via a Q-Exactive Focus orbitrap mass spectrometer (Thermo Scientific) in line with an EASY-nLC 1000 ultra-high pressure liquid chromatography system and EASY-Spray nano electro spray ionisation (nESI) source (Thermo Scientific). After equilibrating the column at 98%

solvent A (0.1% FA in water) and 2% solvent B (0.1% FA in 80% ACN) samples were loaded onto a μ-precolumn (C18 Pepmap100 5mm x 5um) and eluted using a linear gradient from 2-40% solvent B over 120mins. Following this solvent B was increase to 98% over 1min, held at 98% for 10mins and returned to 2% for equilibration over 18mins. Flow rate was set at 250nl/min. The QE was operated in DDA and positive ionisation mode. Full MS scans were acquired at 70,000 resolution for a mass range of 400 -1600 m/z, with AGC 1e6 and a maximum IT of 120ms. The top 12 most abundant precursor ions were selected with an isolation window of 2 m/z units for HCD fragmentation at a normalised collision energy of 25%. MS2 spectra were acquired at 17,500 resolution, with AGC 1e5 and 60ms maximum IT.

Mass Spectrometry Data Analysis

Raw data files were input to the MaxQuant processing software (v. 2.1.3.0) and searched against the human Uniprot databases (UP000005640_9606.fa, UP000005640_9606_additional.fa) using the Andromeda search algorithm[30]. False-discovery rates were controlled at 1% for both peptide spectral matches (PSMs) and proteins. Peptides with a length of 7-50 amino acids were considered, with N-terminal acetylation and methionine oxidation specified as variable modifications and cysteine carbamidomethylation as a fixed modification. Maximum peptide mass was set at 5000 Da and spectra were searched with strict Trypsin specificity (KR not P), allowing up to two missed cleavage sites. Accurate mass identifications were transferred between samples using the ‘match between run’ setting of MaxQuant, with a match window of 0.7 minutes and an alignment window of 20 minutes. Quantitation was performed via intensity-based absolute quantification (iBAQ)[31].

MaxQuant search output files were formatted appropriately using Python programming language (v. 3.9.7) for input into the DeuteRater GUI (v. 5). Raw files were additionally converted to mzml format via ProteoWizard (v. 3.0) for peak-picking of the mass isotopic distribution by DeuteRater for peptides identified within the respective MaxQuant output file(s). Deuterium enrichment of the body water (precursor) pool for each participant timepoint were provided to the DeuteRater GUI. The ‘% peptide fraction new’ was calculated via spacing-based measurements of changes in the mass isotopic distribution over time. Turnover rates for identified proteins were then calculated by fitting the ‘fraction new’ to a kinetic rate curve with equation: $1-e^{-(rate+proliferation)*time}$, as specified by DeuteRater[32]. These results were formatted for further analysis via Python programming language (v. 3.9.7), in conjunction with the Python modules: pandas (v. 2.0.2), matplotlib (v. 3.5.3), seaborn (v. 0.12.2), scipy (v. 1.10.1), scikit-learn (v. 1.1.2) and numpy (1.20.3). PANTHER (release 17.0) was utilised for protein classifications and ontology analysis of associated biological functions.

3.3 RESULTS

Deuterium Enrichment in the Body Water Pool

Rapid increases in levels of deuterium within the body water pool during the ‘ramp’ phase were measured in two study participants (Participants 5 and 6) across the first ~8 hours of D_2O loading. Figure 1 demonstrates both participants followed relatively linear increases in body water deuterium enrichment (P5: R^2 0.91; P6: R^2 0.99) across the initial period of D_2O loading towards a body water enrichment of >1.5%. Participant 6 consumed all D_2O doses allocated for the ramp-phase within the ~8-hour period to reach a peak body water deuterium enrichment of 1.77%, whereas Participant 5 consumed 75% of D_2O doses for the ramp-phase during the ~8-hour period, and as such, reached a lower body water deuterium enrichment of 1.56% (Figure 1). This may explain a less linear increase in deuterium enrichment during the first ~8 hours of D_2O loading (R^2 0.91, Figure 1). Participant 5 consumed the remaining D_2O doses for the ramp-phase over the following two days.

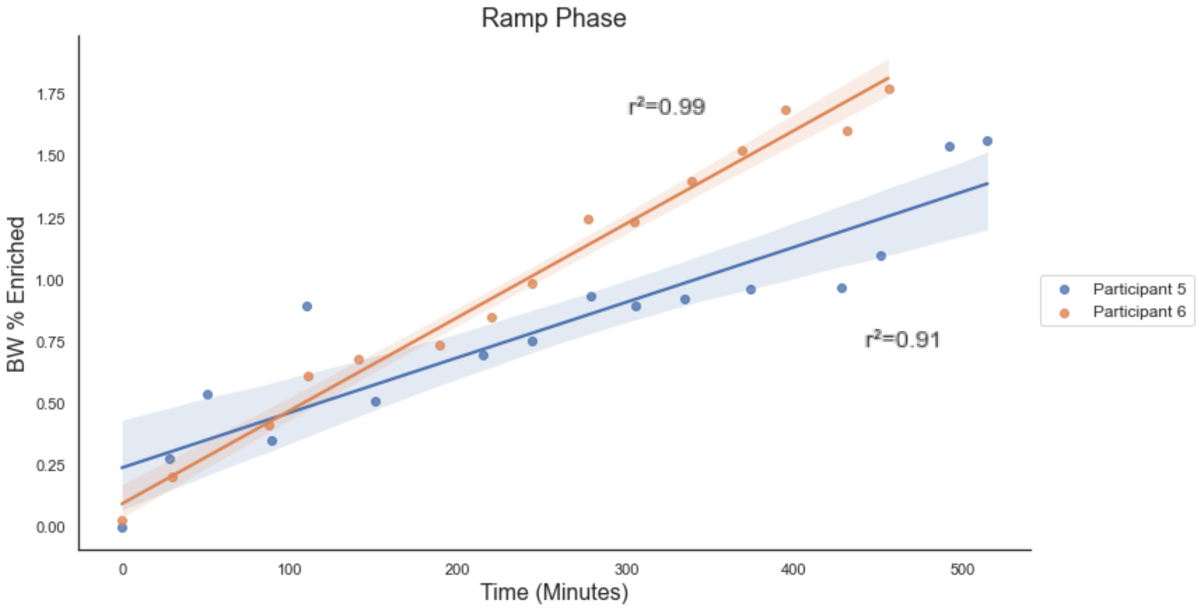

Figure 1: *Body water deuterium enrichments in Participants 5 and 6 over the first approximate 8-hours of the deuterium loading protocol (‘ramp’ phase).* ***R^2*** *represents the Pearson correlation coefficient and shading represents the 95% confidence intervals for each participant’s deuterium time courses, respectively.*

As D_2O is known to take 2-5 hours to equilibrate within the body water pool[33], it is likely that these values at the end of the initial ~8-hour loading period are slight overestimations of the values of deuterium present within total body water. Figure 2 demonstrates that once deuterium had equilibrated within the body water pool, Participants 5 and 6 plateaued at the expected deuterium body water enrichments of 1.53% ± 0.17% and 1.51% ± 0.09% respectively, over the duration of the 6-week study protocol.

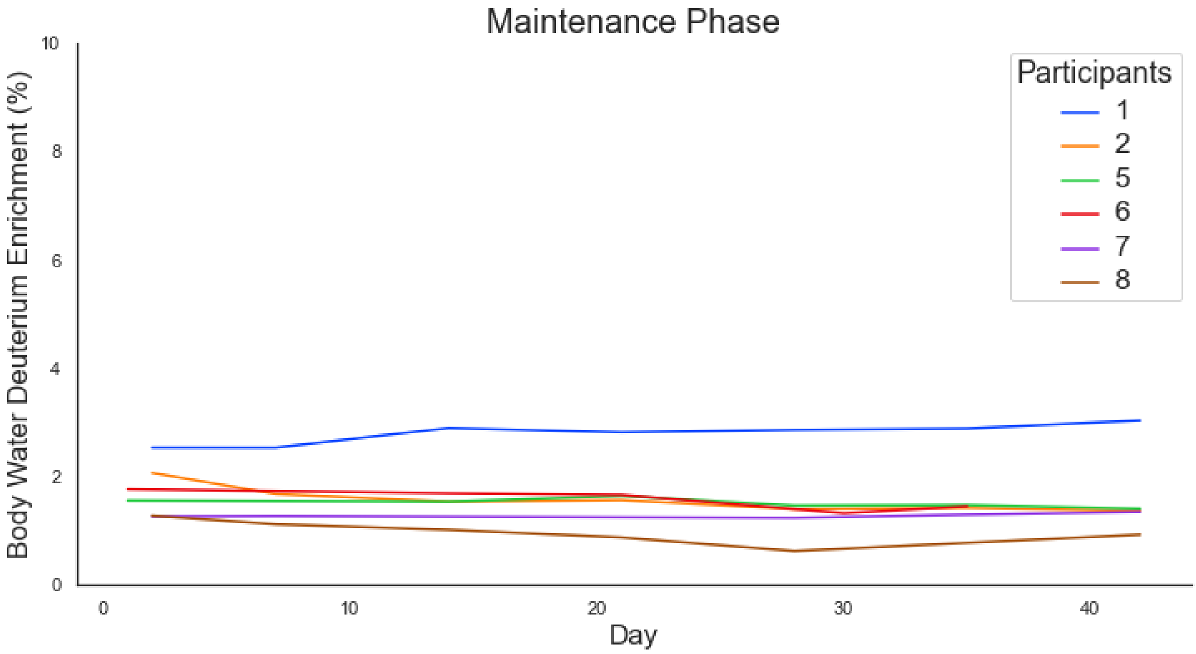

Figure 2: *Deuterium enrichment of the body water pool for each participant across the six-week study period.*

Over the six-week study protocol, average deuterium enrichment in body water was 1.64 ± 0.16% across all study participants. The first four study participants were dosed with D_2O with the aim of reaching a body water enrichment of approximately 1.5%. This was successfully achieved in three study participants (Participant 2: 1.58 ± 0.24%; Participant 5: 1.53% ± 0.17%; Participant 6: 1.51% ± 0.09%; Figure 2). Participant 1, however, reached an average body water deuterium enrichment of 2.8 ± 0.19%. As enrichment in this participant is stable across the 6-weeks, it is likely that this is due to an erroneous estimation of total body water content and not the rate of body water turnover. Participant 1 presented a BMI of ~19 which borders on underweight classification (<18.5). This, paired with a low level of physical activity, likely resulted in an overestimation of body water content as a result of reduced skeletal muscle mass relative to that typically expected at this participant's body mass (kg).

Participants 7 and 8 consumed D_2O with the aim of reaching lower deuterium enrichments of 1.2 and 1% body water respectively. This was to provide a range of deuterium enrichments within this pilot study for downstream mass spectrometry analyses of cellular labelling. Participants 7 and 8 demonstrated respective deuterium body water enrichments of 1.29 ± 0.04% and 0.95 ± 0.22% (Figure 2). This demonstrates that the majority of study participants reached the approximate deuterium enrichments intended, with methods for calculating D_2O doses appearing suitable in both male and female participants during free-living conditions. Participant 1, however, illustrates that these calculations may need to further consider BMI and the ramifications of body composition on total body water estimates, with lower dosages likely being suitable for inactive participants with low skeletal muscle mass. However, with a coefficient of variation of 0.1 across six study participants encompassing an approximate three-fold range in body water deuterium enrichments, methods for the calculation of body water turnover appear robust for future implementation, with the observed variation in body water turnover rates comparable to other reported estimates[2]. Finally, to further validate these calculations, a saliva sample was collected from Participant 7 two-weeks after the final D_2O dose in order to assess the decay rate of deuterium from the body water pool.

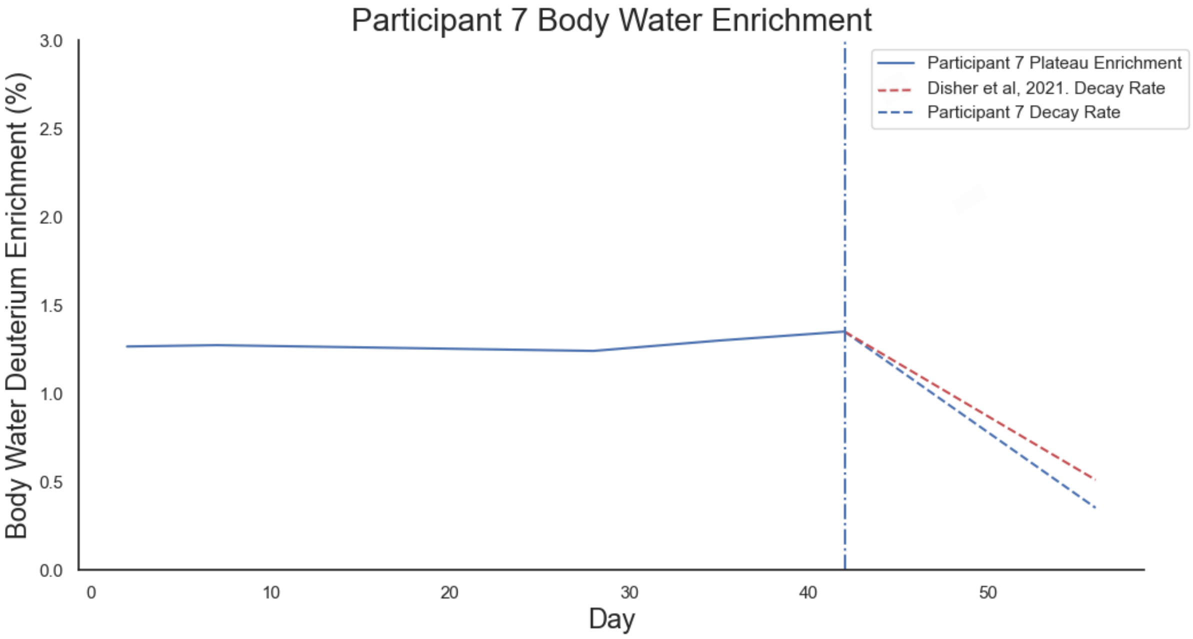

Figure 3: *Body water deuterium enrichment across the 6-week maintenance phase and subsequent decay of deuterium from the body water pool of Participant 7 following two weeks without* D_2O.

Figure 3 displays Participant 7's body water deuterium enrichment during the maintenance phase and the subsequent decay rate of deuterium from the body water pool across two weeks following the final D_2O dose. For this study, a body water decay rate of 6% was utilised for maintenance dose calculations, based on previous estimates from Disher et al, 2021[2]. Figure 3 demonstrates Participant 7 to have a slightly higher decay rate than this literature average, with a daily deuterium body water decay rate of 7%. However, this rate is well within the limits reported by Disher et al, 2021, and implementation of a 6% decay rate still enabled for stable maintenance of deuterium enrichment in the body water pool of Participant 7, who presented a standard deviation of 0.04% across the 6-week plateau phase. This data therefore supports previous estimations of body water turnover in active individuals from which future body water deuterium decay rate and maintenance dose calculations can be based.

Deuterium-Labelling of DNA to Determine Cellular Proliferation Rates

Monocytes (CD14+) and effector memory T-cells (CD14- CD3+ CD45RO+ CCR7-) were subjected to mass spectrometry analysis to quantify incorporation of deuterium into the deoxyribose moieties of DNA, in order to calculate rates of cellular proliferation through changes in the deuterium enrichment of these cell type's DNA over the time course of deuterium-labelling. Monocytes were selected as a fast-turnover cell population that are expected to have fully turned-over within the blood compartment after approximately 2 weeks[18,34,35]. Effector memory T-cells were selected as a model cell type for slow-turnover immune populations associated with the adaptive immune system, whose changes in proliferation and function are associated with a variety of immunological disorders[17,35,36].

Selective reaction monitoring (SRM) was performed via GC-MS/MS for unlabelled (M0) and labelled (M^{+1}) products of deoxyribose. Changes in the isotopic ratio were then normalised to body water deuterium enrichment and an amplification factor, calculated from body water and DNA deuterium enrichments (present as a result from the multiple potential hydrogen/deuterium exchange sites of deoxyribose). This enabled the calculation of fractional turnover rates for both monocytes and effector memory T-cells, displayed in Figure 4.

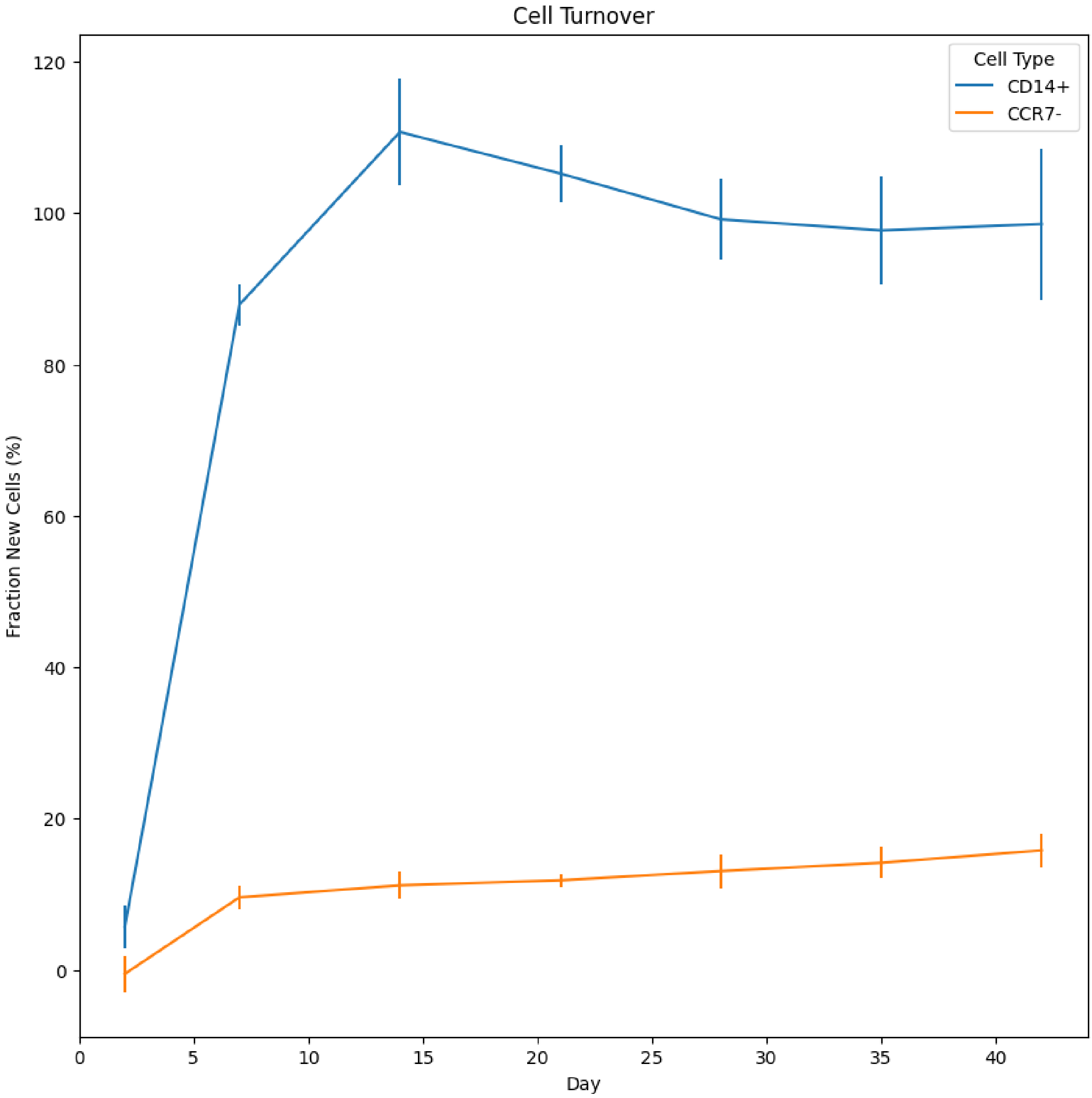

Figure 4: *Fraction of newly divided cells in monocytes (CD14+) and effector memory T-cells (CCR7-) populations across the 6-week D_2O loading time course. Error bars represent standard error of the mean.*

Fractional turnover illustrates monocytes to have fully turned over in the blood compartment by day 14, in line with previous estimations from other D_2O labelling experiments in humans[18,34,35]. At days 14 and 21 it appears that fraction new cells exceeded the expected plateau of 100% newly divided cells. This may be explained by two primary factors. Firstly, data were normalised to an average amplification factor that may not reflect interindividual or intraindividual variability across time as a result of differential amplification from the multiple potential deuterium exchange sites in deoxyribose. Secondly, three of six study participants were believed to have contracted COVID-19 between days 2-14, which may have very likely impacted both monocyte kinetics and the size of the blood monocyte pool (although no increase in monocyte cell numbers following MACs were noted at these timepoints, *section 3.23*). This, however, would additionally explain the increased fraction of newly divided effector memory T-cells between days 2-7 observed in Figure 4. Average fractional turnover in monocytes was 7%/day, which is in line with previous estimations of monocyte turnover from D_2O labelling in humans (at 6%/day)[34]. Effector memory T-cells demonstrated an average turnover of 0.48%/day.

The fractional replacement rate constant (*k*) for each cell type was additionally calculated according to Neese et al, 2002[34]. Figure 5a illustrates *k* rates for both cell types, with Figure 5b illustrating replacement *k* rates for effector memory T-cells only.

A

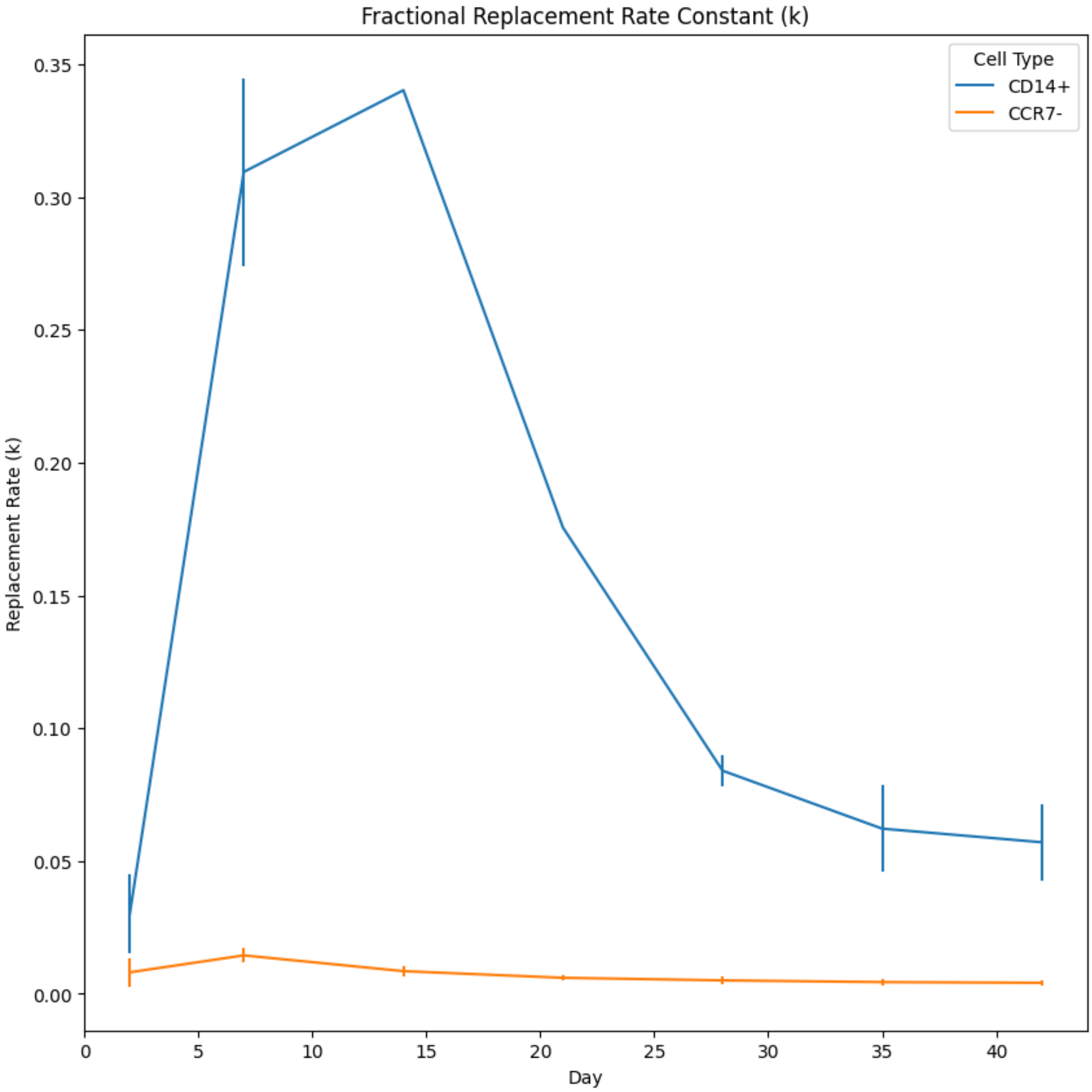

Figure 5A: *Fractional replacement rate constants (k) for monocytes (CD14+) and effector memory T-cells (CCR7-) across D_2O loading.*

B

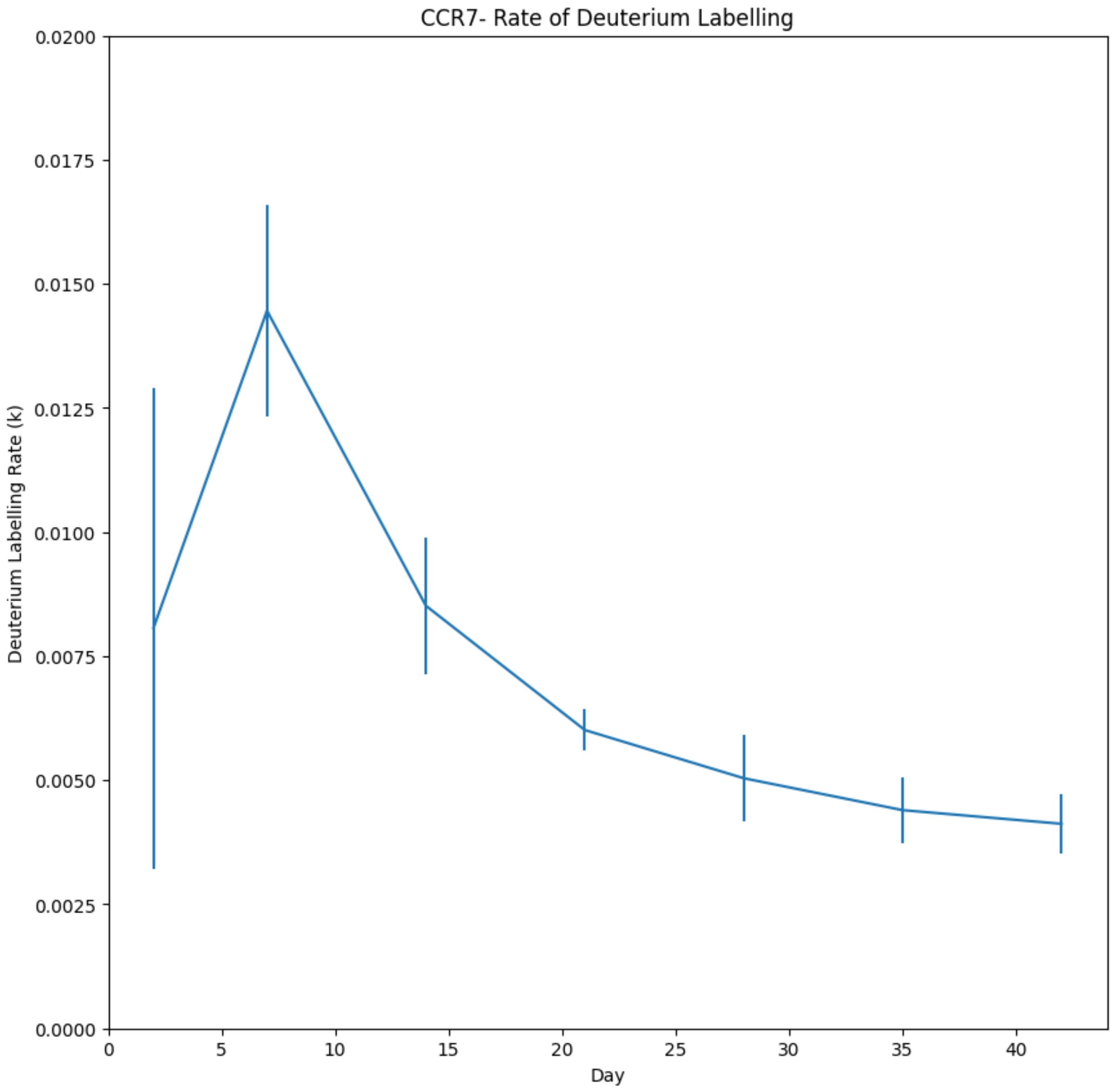

Figure 5B: *Fractional replacement rate constant (k) for effector memory T-cells (CCR7-) with adjusted y-axis scale. Error bars represent standard error of the mean.*

Figure 5a and 5b illustrate *k* rates to increase sharply from day 2-7 of D_2O loading, with a subsequent decrease from day 14 to 21, after which rates plateau. This is an expected observation for monocytes, whose fractional turnover would be expected to be highest until ~14 days, after which it would be expected that cells are fully turned over and consequently the rate of deuterium-labelling will fall sharply to plateau. The sharp increase in monocyte *k* rate from day 2-7 is also expected and likely explained by the post-mitotic release of monocytes from bone marrow into the peripheral blood taking approximately 1.6 days, with similar increases in monocyte fractional deuterium-labelling previously being reported in humans using deuterated glucose[18]. The fractional replacement rate of effector memory T-cells also demonstrates an early increase followed by stabilisation to plateau at ~21 days onwards. While less expected for this slower turnover immune cell population, initial expansion followed by reductions in relative deuterium-labelling have been observed in other deuterium-labelling experiments[37], especially where infection elicits a rapid expansion of the active cellular pool then subsequent decline due to increased cell death. To the author's knowledge, deuterium-labelling kinetics for effector memory T-cells isolated via expression of these specific cell-surface markers (CD14- CD3+ CD45RO+ CCR7-) has not previously been reported in humans, and as such this data represents the first deuterium-labelling kinetic dataset of its kind. Broader comparisons between the average fractional turnover of effector memory T-cells within this dataset (Figure 4, average 0.48%/day) and those available within the current literature[35], demonstrate turnover to be within the range of that expected in humans at steady-state (~0.33%/day) and increased rates as a result of active immune disease (~1.33, active HIV-1/AIDs infection). Again, it is possible that the proliferation rates of this dataset may be impacted by COVID-19 infection in three of the six participants within this pilot study, which would explain the increased *k* rates and fractional turnover between days 2-21 across this active infection window (Figures 4 and 5b).

To determine whether COVID-19 infection is impacting calculation of fractional cellular turnover in this dataset, the three participants that were believed to have contracted COVID-19 (two tested positive and one self-isolated due to proximity to one of the COVID-19 infected study participants) were compared against the other three participants of the pilot study (Figure 6a and 6b).

A

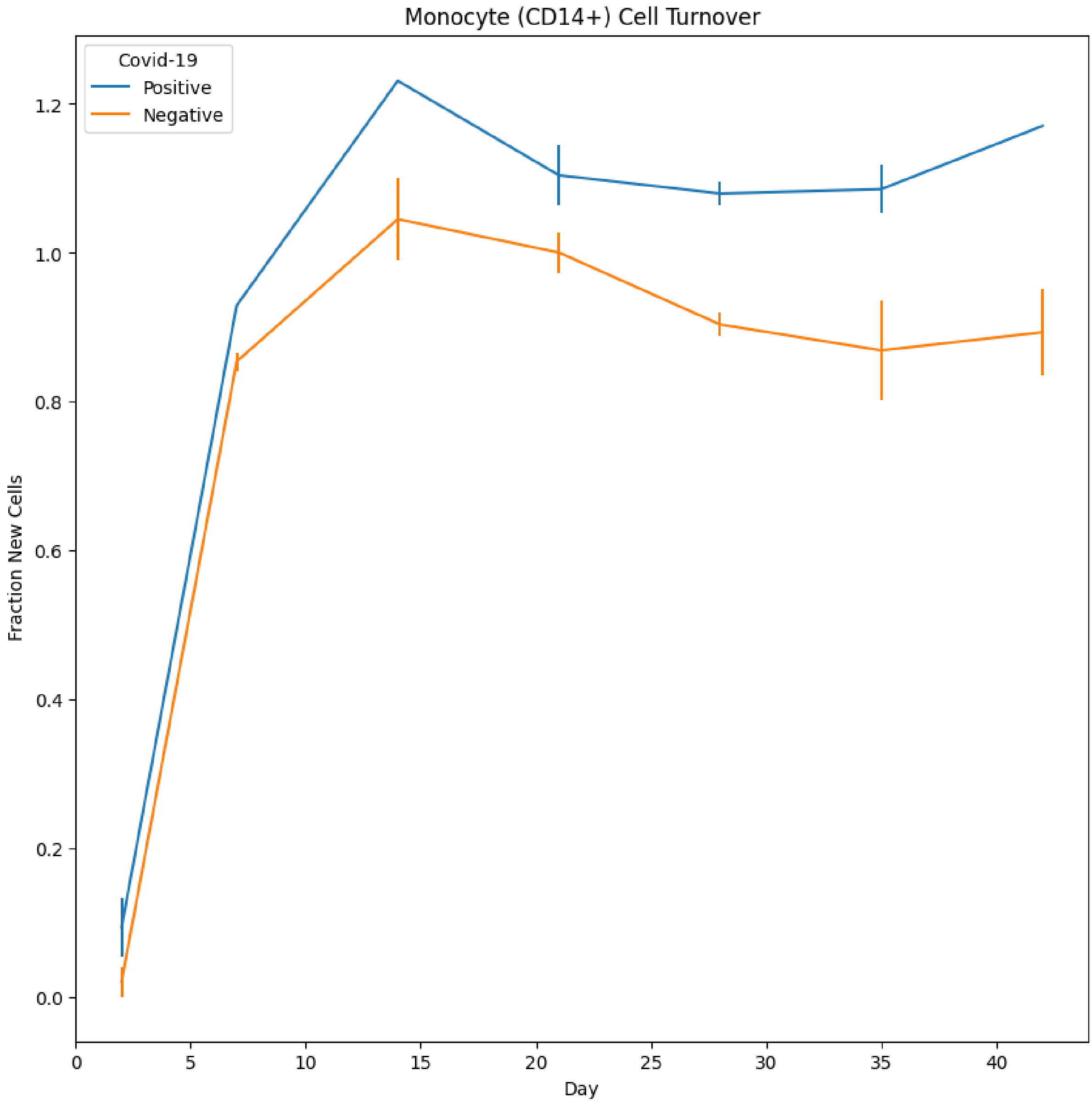

Figure 6A: *Fractional turnover of monocytes (CD14+) in COVID-19 positive (n=3) and negative (n=3) participants over time (days).*

B

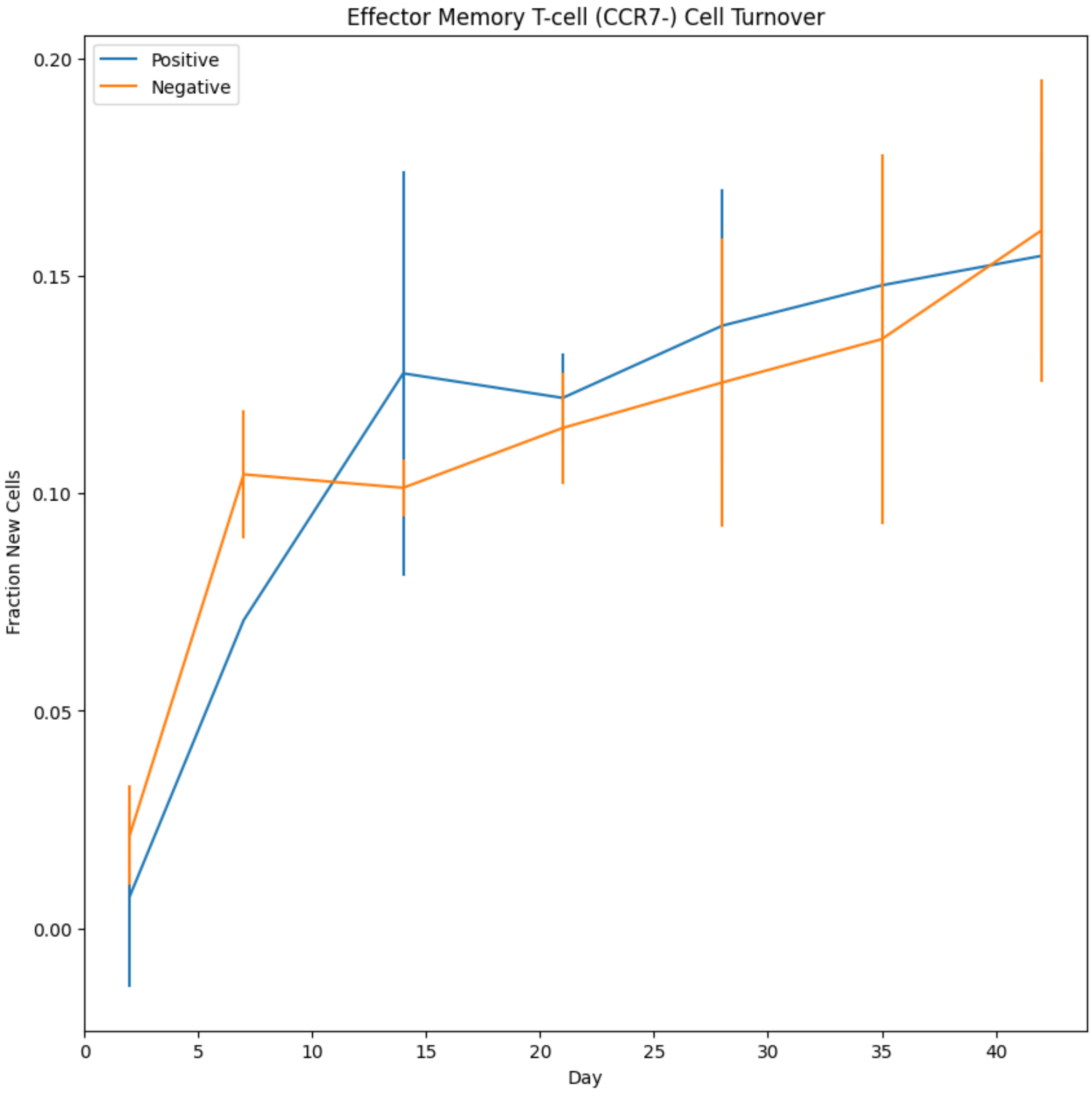

Figure 6B: *Fractional turnover of effector memory T-cells (CCR7-) in COVID-19 positive (n=3) and negative (n=3) participants over time (days). Error bars represent standard error of the mean.*

Figure 6a demonstrates a clear increase in the fractional turnover of monocytes in participants infected with COVID-19 compared to those uninfected, which surpasses the theoretical maximum fractional turnover of 1 (100%). COVID-19 negative participant fractional monocyte turnover increases to the expected maximum of 1 at day 14, in line with previous estimates[18,34,35], albeit with a subsequent plateau slightly below the expected value of 1 from thereon. Figure 6a supports the hypothesis that the previously observed increase in the fraction of new monocytes past the expected fractional plateau of 1 (100% turned over cells, Figure 4) is likely driven by increases in the size of the monocyte pool in participants following COVID-19 infection, with participants who were COVID-19 negative not surpassing the % fraction new cell threshold of 100% at any timepoint. Differences between COVID-19 positive and negative participants during the study duration are less apparent in effector memory T-cell fractional turnover (Figure 6b), with average values across timepoints between groups generally within one standard error of each other's mean.

In Vivo Proteome Kinetics in Human Monocytes

Due to the fast proliferation rates of monocytes, only data from days 2, 7, 14 and 21 were included for calculating turnover rates in proteins identified by LC-MS/MS analysis. Across these timepoints, 348 proteins were detected across a diverse range of ontologies (Figure 7a and 7b).

A

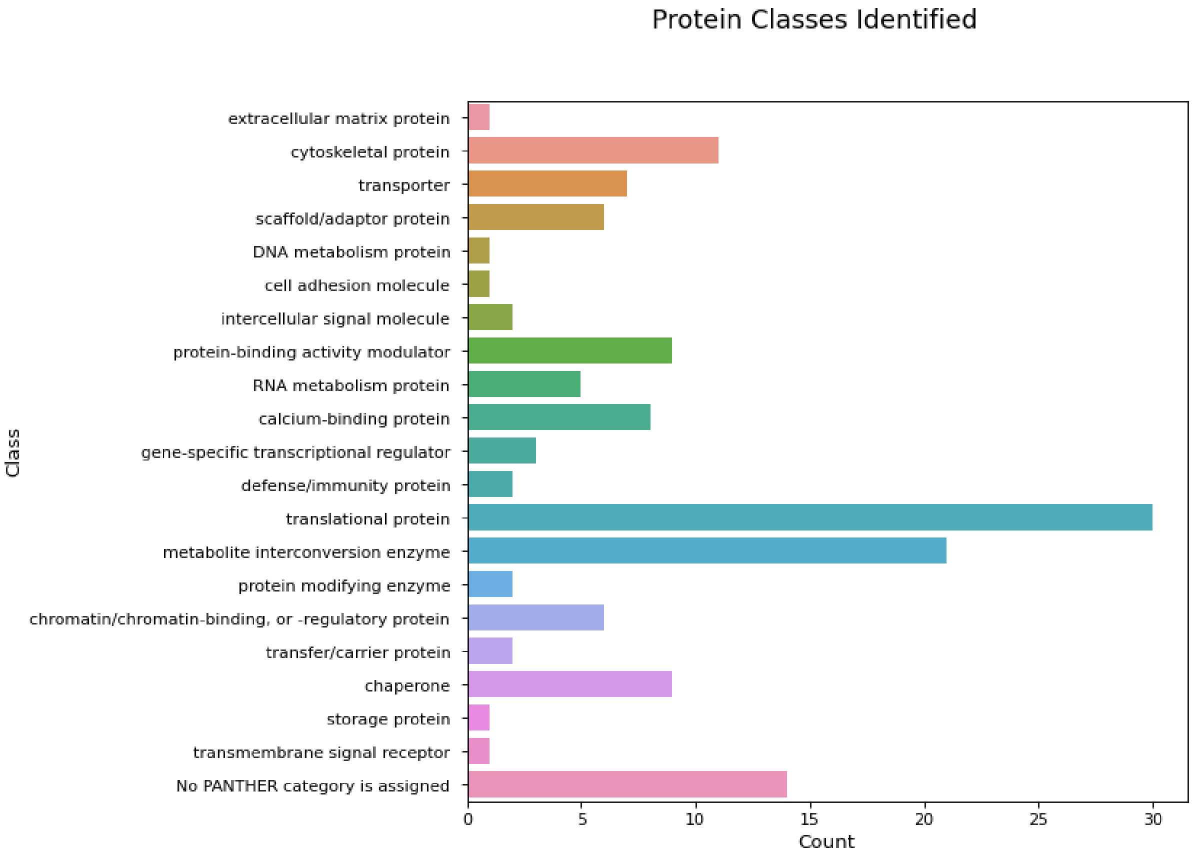

Figure 7A: *Protein classes identified by PANTHER in human monocytes proteomics dataset during the first 3-weeks of D_2O loading.*

B

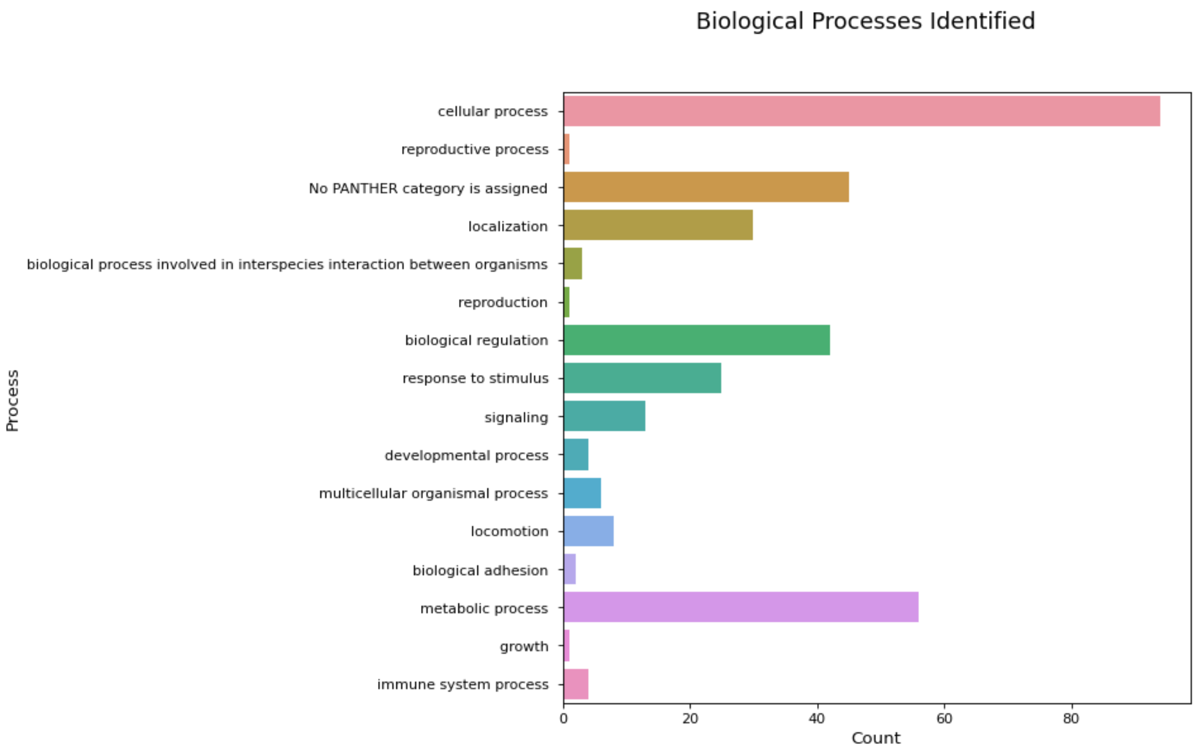

Figure 7B: *Biological processes identified by PANTHER in human monocytes proteomics dataset during the first 3-weeks of* D_2O *loading.*

Deuterium incorporation was then quantified across a minimum peak isotopic envelope of 5, resulting in ~2400 peptide sequences, equating to approximately 270 peptides per sample. The coefficient of variation (CV) among these measurements per peptide was relatively low (CV 0.18) and median values were taken forward from each peptide per protein for turnover rate calculations. Isotopic envelopes that contained negative values which may impact turnover rates were removed and the neutromer-spacing “fraction new” values for proteins were fit to the rate equation specified by DeuteRater:

$$Fraction\ New = 1-e^{-(rate+proliferation)*time}$$

which accounts for the input of cell proliferation in order to accurately model protein turnover.

This resulted in the successful calculation of turnover rates for 20 proteins identified within the dataset, with an average turnover rate among these proteins of $0.44/day^{-1}$. While these quantified proteins represent a low proportion of the total proteins identified (~6%), it may be that within these fast-turnover cells deuterium incorporation arising from cell proliferation predominates that incorporated into cellular peptides (proteins) over time. This, in addition to the previously demonstrated interindividual variability as a result of COVID-19 (Figure 6a) and use of an average proliferation rate calculated across timepoints and participants (Figure 5a), appears to present difficulties in modelling protein turnover within monocytes. Indeed, of the 20 proteins quantified, many are proteins associated with core cellular functions (e.g. actin-beta, histones) that are typically present in high abundance, whose turnover rates demonstrate relatively uniform increases over time (Figure 8). To further investigate the reliability of these measurements, changes in the mass isotopic distribution of actin-beta peptides were investigated (Figure 9a-c) to ascertain whether changes in isotopic peak intensities met theoretical and experimental expectations from previous deuterium-labelling experiments[14,32].

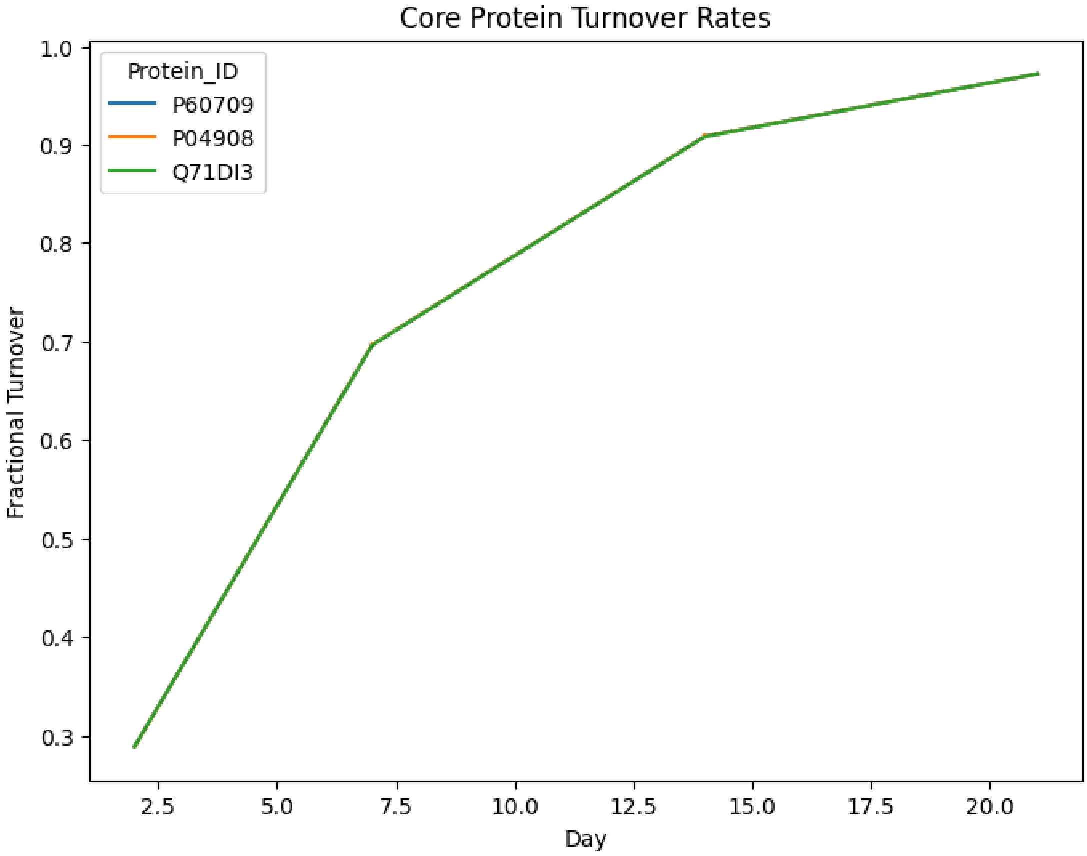

Figure 8: *Fractional turnover of proteins; actin-beta (P60709), Histone H2A type 1 (P04908) and Histone H3.2 (Q71DI3). Error bars represent standard error of the mean.*

A

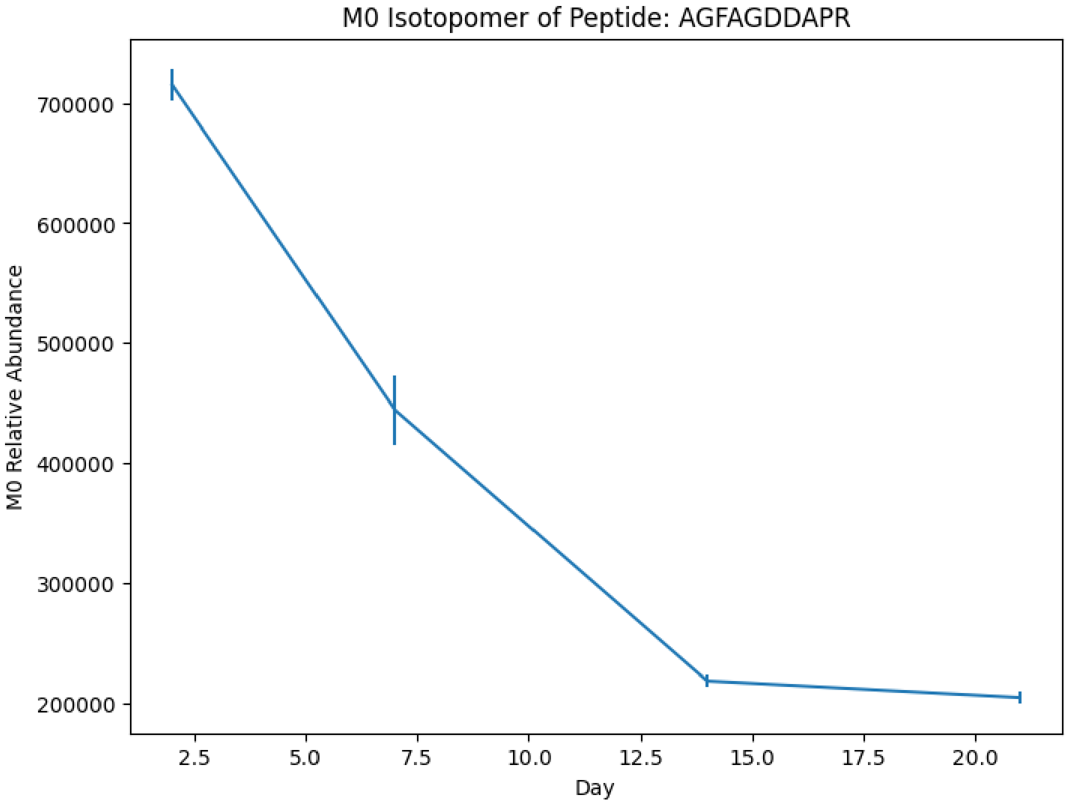
M0 Isotopomer of Peptide: AGFAGDDAPR
M0 Relative Abundance
700000
600000
500000
400000
300000
200000
2.5
5.0
7.5
10.0
12.5
15.0
17.5
20.0
Day

B

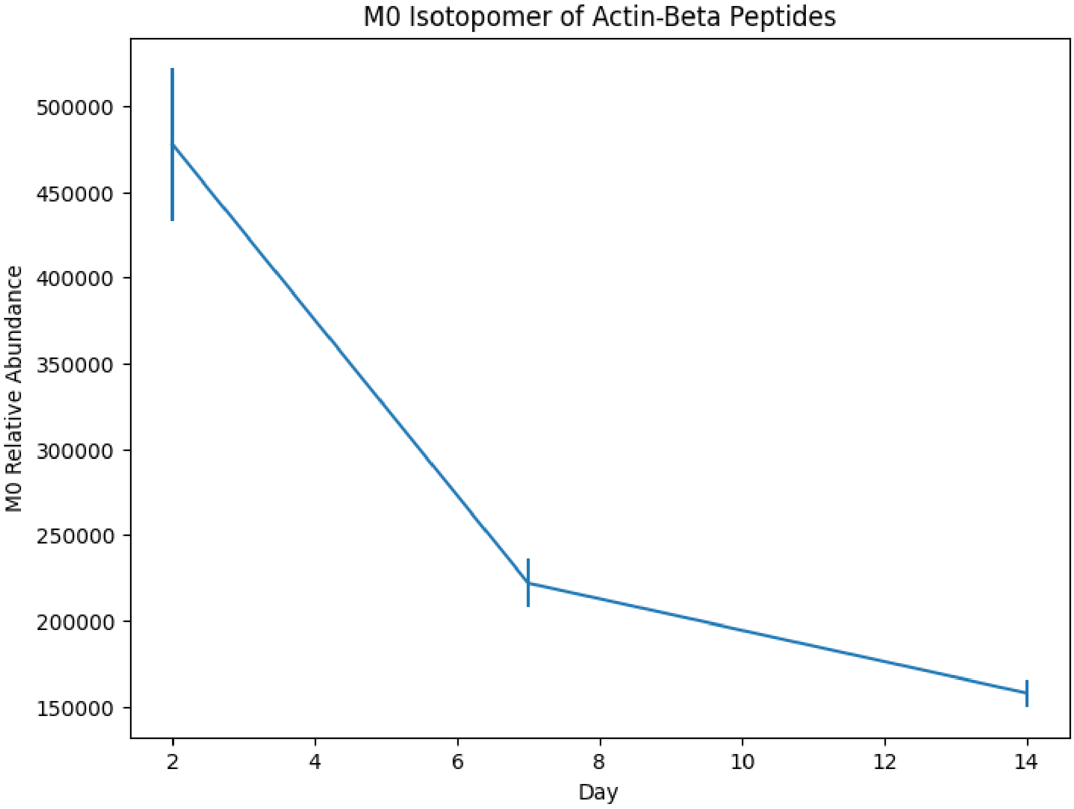
M0 Isotopomer of Actin-Beta Peptides
M0 Relative Abundance
500000
450000
400000
350000
300000
250000
200000
150000
2
4
6
8
10
12
14
Day

C

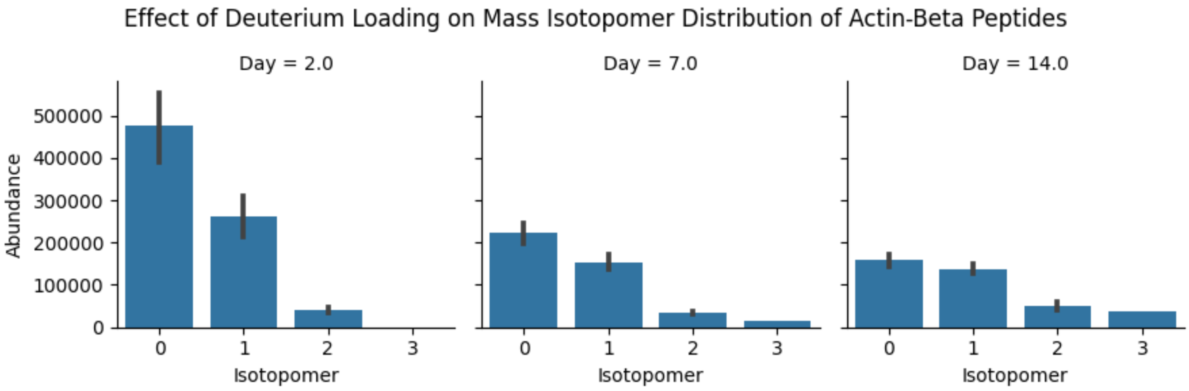

Figure 9: *Decay rate of monoisotopic peak (M0) of actin-beta peptide, AGFAGDDAPR (**A**) and all detected actin-beta peptides; AGFAGDDAPR, DLTDYLMK, GYSFTTTAER, DSYVGDEAQSK, SYELPDGQVITIGNER (**B**). Error bars represent standard error of the mean. **C;** shifts in peak abundance of the mass isotopic distribution of M0-3 for all actin-beta peptides.*

Figure 9 demonstrates decay of the monoisotopic peak abundance of actin-beta peptide from days 2-14 and then to plateau from days 14-21, both of which support the fractional protein turnover of core proteins (actin-beta, histone H2A type-1 and H3.2) depicted in Figure 8. Decay of the monoisotopic peak of a peptide as deuterium-labelling increases is an expected observation in protein turnover LC-MS studies utilising D_2O[14]. Shifts in abundance from the unlabelled monoisotopic peak towards M^+ isoforms is further confirmed for actin-beta peptides in Figure 9c, with stark relative increases in the M^{+3} isotopomer observed in conjunction with the decrease of the monoisotopic peak abundance. Interestingly, a similar decrease in iBAQ abundance for actin-beta protein was observed over the time-course of deuterium-labelling (Figure 10a) from days 2-14.

To investigate this further, iBAQ abundance was assessed across days 2-21 in all proteins quantified for measures of turnover via deuterium-labelling. Figure 10b clearly demonstrates stable iBAQ quantification during the period of 2-7 days of deuterium-labelling, but a severe decrease of approximately three-fold from days 7-14 which plateaus from days 14-21. This suggests that in a fast-turnover immune cell population such as monocytes, that once cells have largely been replaced, deuterium-labelling of this extent within cells (and therefore proteins) prevents the accurate quantitation of the cellular proteome via iBAQ, assuming that in this dataset expression of these proteins remains relatively stable across time[31,38].

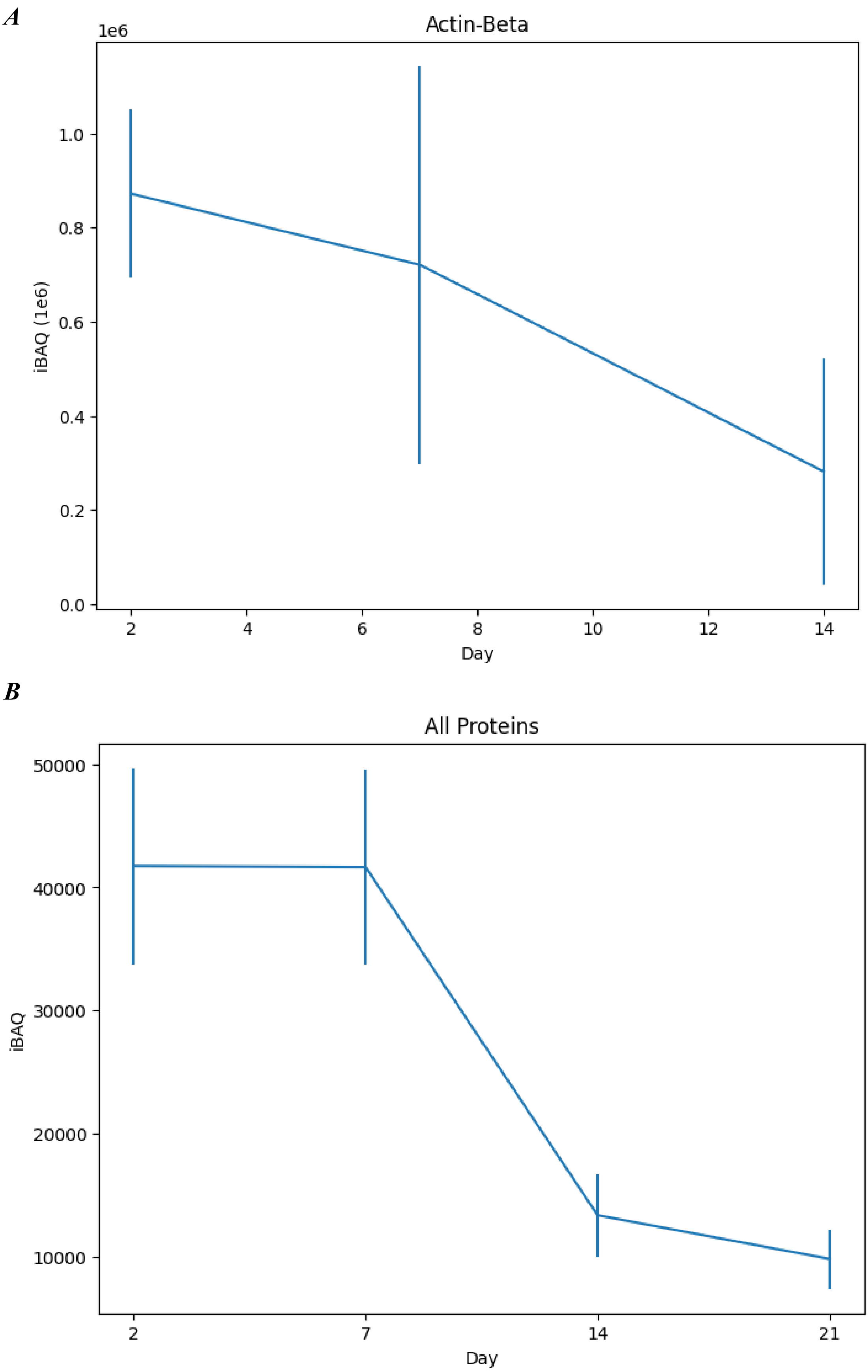

Figure 10: A; *iBAQ quantitation of actin-beta in human monocytes over the first two weeks of* D_2O *loading.* ***B;*** *iBAQ quantitation of all proteins with calculated turnover rates via deuterium-labelling. Error bars represent standard error of the mean.*

To confirm the relationship between iBAQ quantitation and deuterium-labelling over time, CVs were calculated from extracted ion current (XIC, MaxQuant) peptide intensity values for proteins across study participants. Figure 11 demonstrates the duration of deuterium-labelling does not have a notable effect on (raw) calculated protein intensity CVs from peptides.

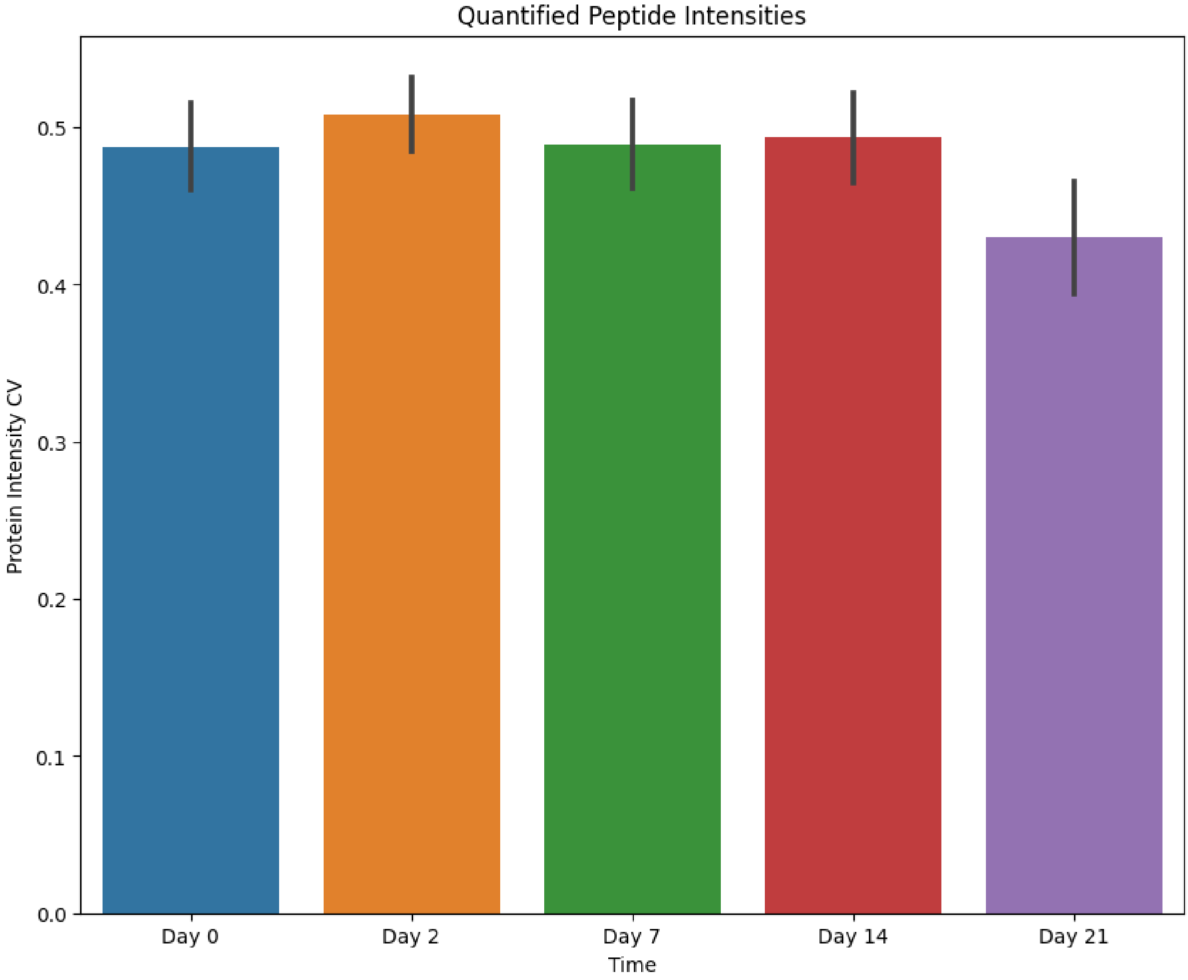

Figure 11: *Coefficients of variation for extracted ion current peptide intensities quantified across the first three weeks of D_2O loading in human monocytes, in vivo. Error bars represent standard error of the mean.*

Figure 11 supports that the decrease in iBAQ quantitation observed with deuterium-labelling in Figure 10 is not related to reduced confidence in LC-MS measurements as a result of the *in vivo* human D_2O loading protocol. As Figure 9c has previously confirmed the expected shifts in the mass isotopic distribution of peptides within this dataset over time, the relationship between the number of isotopic peaks used to calculate peptide intensity was next investigated.

Figure 12a displays the number of isotopic peaks utilised for abundance quantification in identified peptides across the deuterium-labelling time-course.

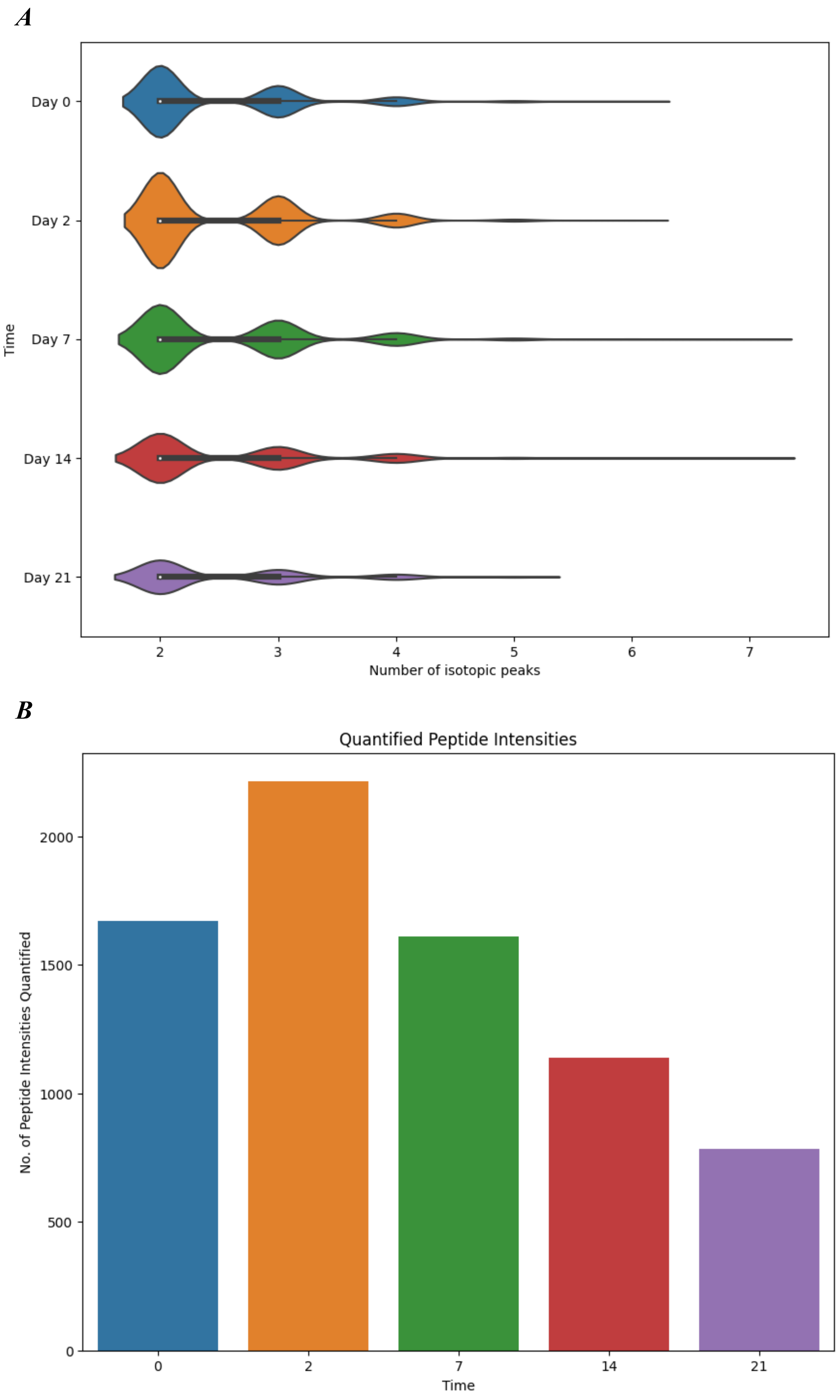

***Figure 12:** A; Violin plots of quantified peptide isotopic distributions/envelopes relative to the number of isotopic peaks detected by MaxQuant, **B;** The number of quantified peptides at each time point of the D_2O loading pilot study.*

Figure 12a demonstrates an increase in the number of mass isotopic peaks quantified across peptides as deuterium-labelling increases from days 0 and 2 to days 7 and 14, with day 21 then demonstrating a decrease in the number of mass isotopic peaks quantified. While this has demonstrated no impact on quantitative precision (Figure 11) there is a clear impact for deuterium-labelling on the number of peptides whose abundance can be quantified. Figure 12b suggests a transitory point of cellular deuterium-labelling at days 7-14, where the number of quantifiable peptides thereafter drastically decreases, which is reflected in the reduced density of the mass isotopic distribution that is still detected at M0-M^{+3} compared to other time points (Figure 12a). This suggests detection of the mass isotopic distribution itself to be the limiting factor impacting peptide quantitation, which appears to decrease as deuterium-labelling shifts the mass isotopic distribution past ~70% fractional turnover (Figure 8), after which it is likely only those proteins of high abundance (or low turnover) are still sufficiently detected in the mass spectrum for protein quantitation. This is confirmed by an observed relationship between peptide extracted ion current (XIC) intensity and number of mass isotopomers quantified (Figure 13), where there is a rightward shift in the intensity and number of mass isotopic peaks over the period of *in vivo* deuterium-labelling.

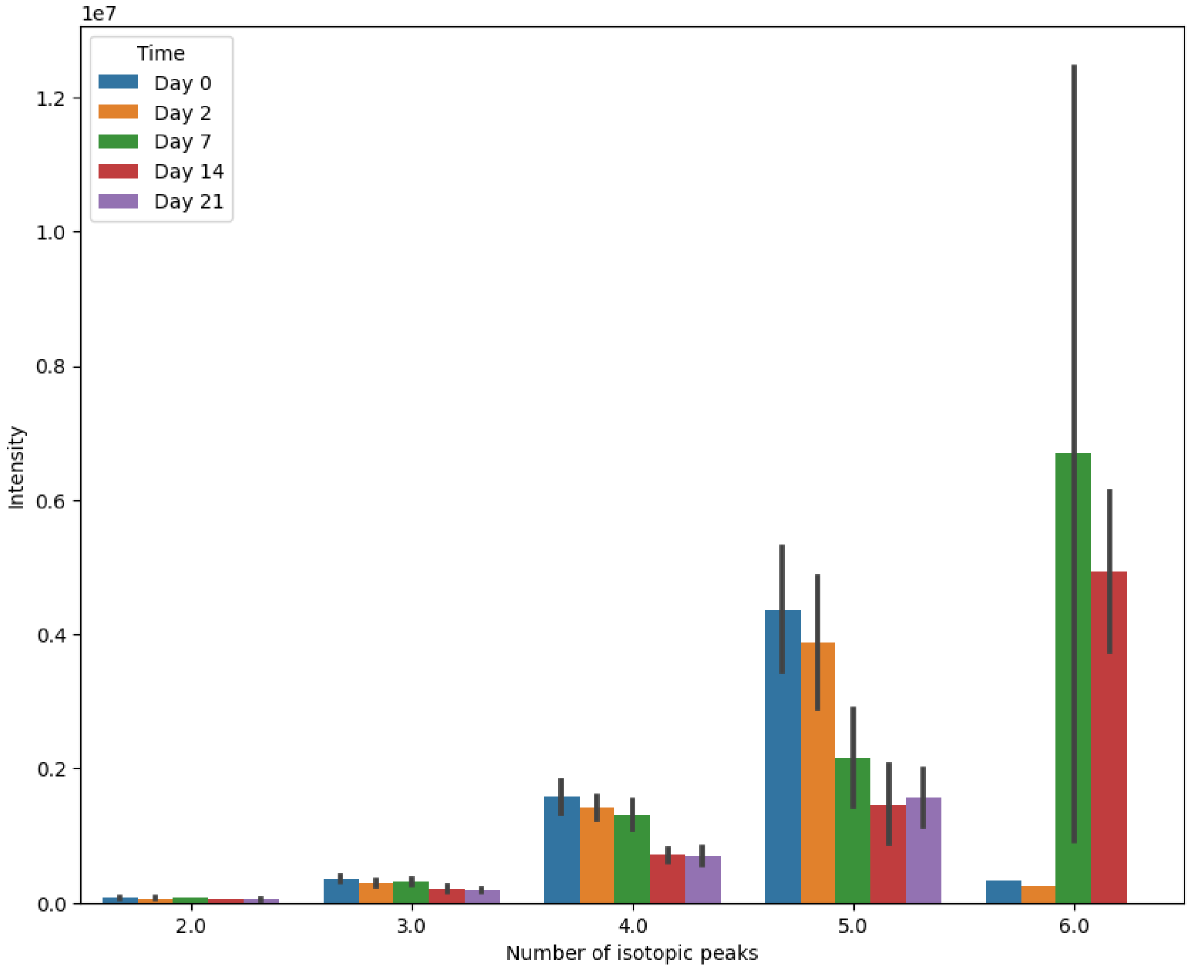

Figure 13: *Extracted ion current intensities of peptides quantified across a mass isotopic distribution of 2-6 mass isotopomers. Bars represent time points. Error bars represent standard error of the mean.* ***Note:*** *only 1 peptide is detected with 6 mass isotopic peaks at days 0 and 2.*

In Vivo Proteome Kinetics in Human Effector Memory T-cells

As effector memory T-cells have demonstrated slower proliferation rates than monocytes (Figure 4), an additional late study time point of Day 42 was included for turnover analyses. This resulted in the total identification of 249 distinct proteins across a range of ontologies (Figure 14a and 14b), with a notable detection of proteins related to translational processes (Figure 14a), similar to that previously detected in monocytes (Figure 7a).

A

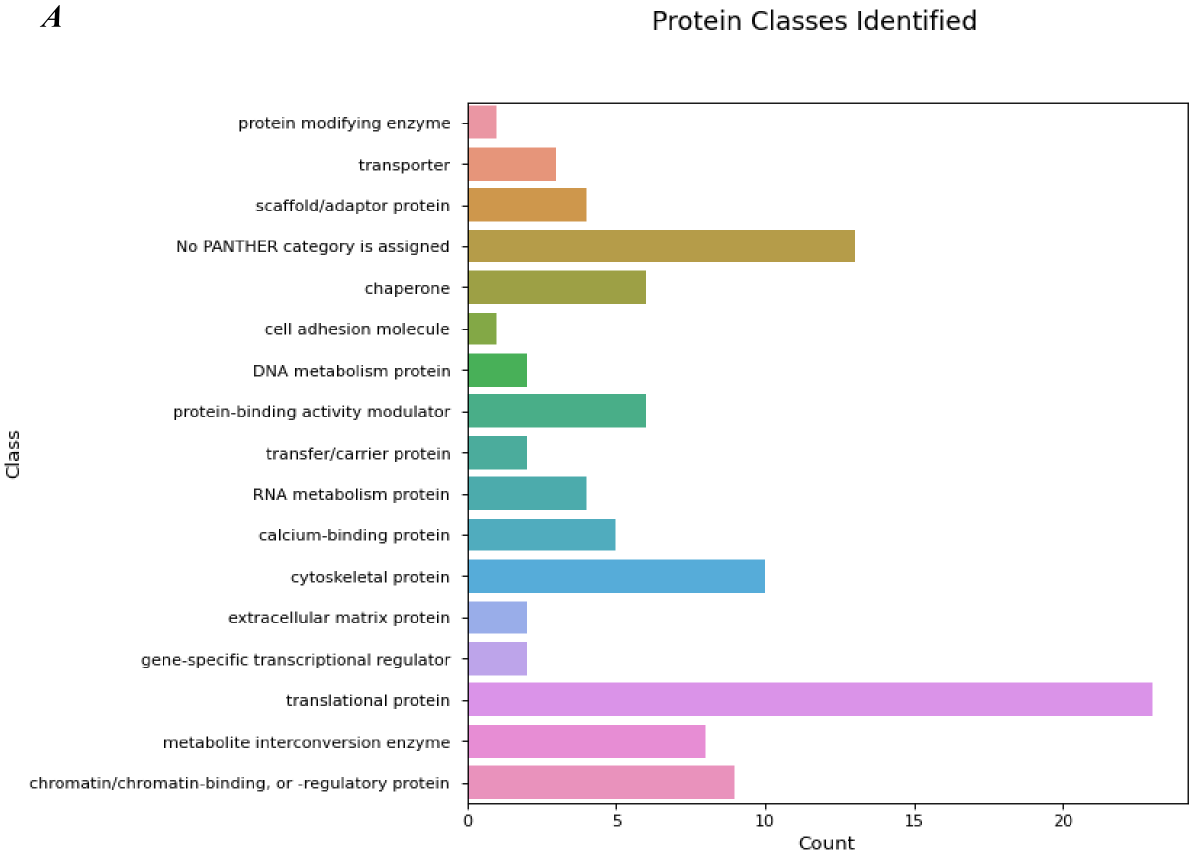

Figure 14A: *Protein classes identified by PANTHER in effector memory T-cells across D_2O loading in humans.*

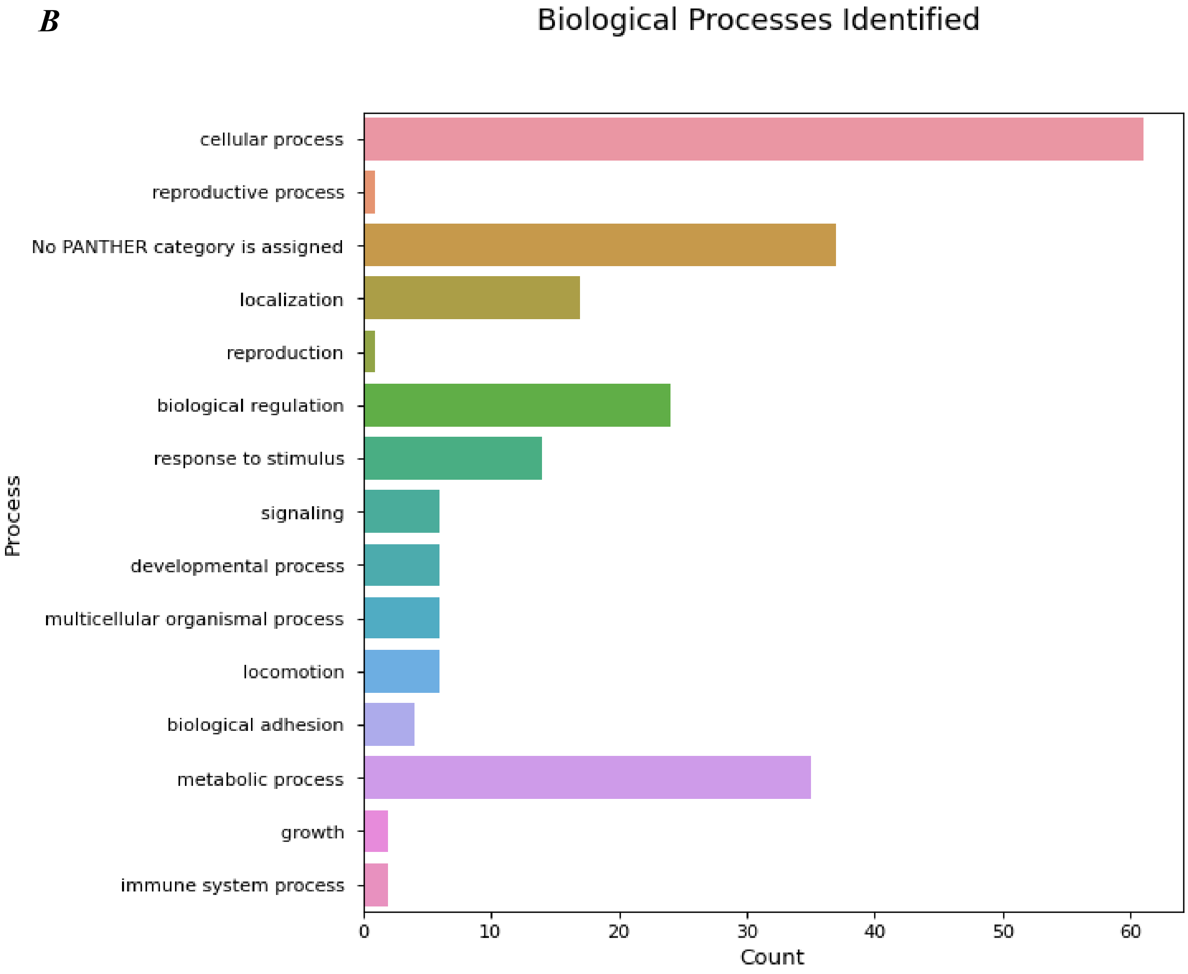

Figure 14B: *Biological processes identified by PANTHER in effector memory T-cells across D_2O loading in humans.*

Assessing deuterium incorporation across a minimum peak isotopic envelope of 5, resulted in the detection of 138,652 deuterium-labelled peptides across all samples, translating to ~4620 peptides per participant across the study time course. Removal of negative values within the isotopic envelope that may impact turnover rate calculations, resulted in 110,553 peptides suitable for quantification within the dataset, relating to 234 proteins and an average of 127 proteins detected per participant. The coefficient of variation (CV) among these measurements per peptide was at an acceptable level (CV 0.28), with median values then calculated from all peptides per protein in order to calculate protein turnover.

When modelling protein turnover rates, factoring in the input of "fraction new" cells (as described in section: *In Vivo Proteome Kinetics in Human Monocytes*), this resulted in turnover rates for 224 proteins, with these calculations requiring the detection of proteins at a minimum of two study time points in at least one participant. This accounts for approximately 90% of the total proteins identified within this dataset (249 proteins). This appears to follow an inverse relationship to monocytes, whose proteins are most easily quantified at early time points due to their fast cellular turnover, whereas protein turnover is more easily quantified at later time points in effector memory T-cells (Figure 15).

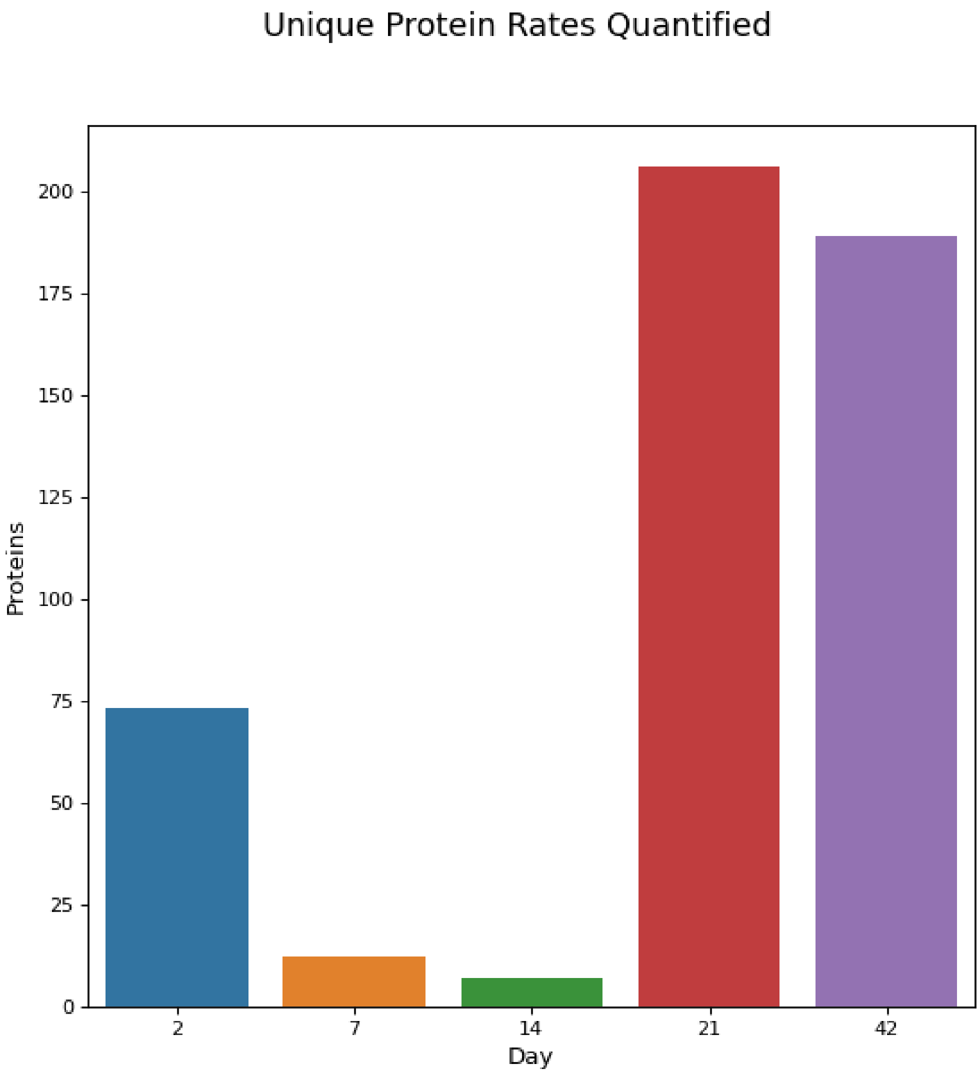

Figure 15: *Counts of unique proteins modelled via deuterium-labelling turnover measurements at sampled study time points.*

As with monocytes, this is likely explained by the input from fraction new cells within the turnover rate model, whereby there appears to be optimal sampling windows for protein turnover measurements relative to cellular proliferation. This is clearly demonstrated for effector memory T-cells in Figure 16, whereby average “fraction new” protein exceeds that of “fraction new” cells at days 21 and 42 of D_2O loading.

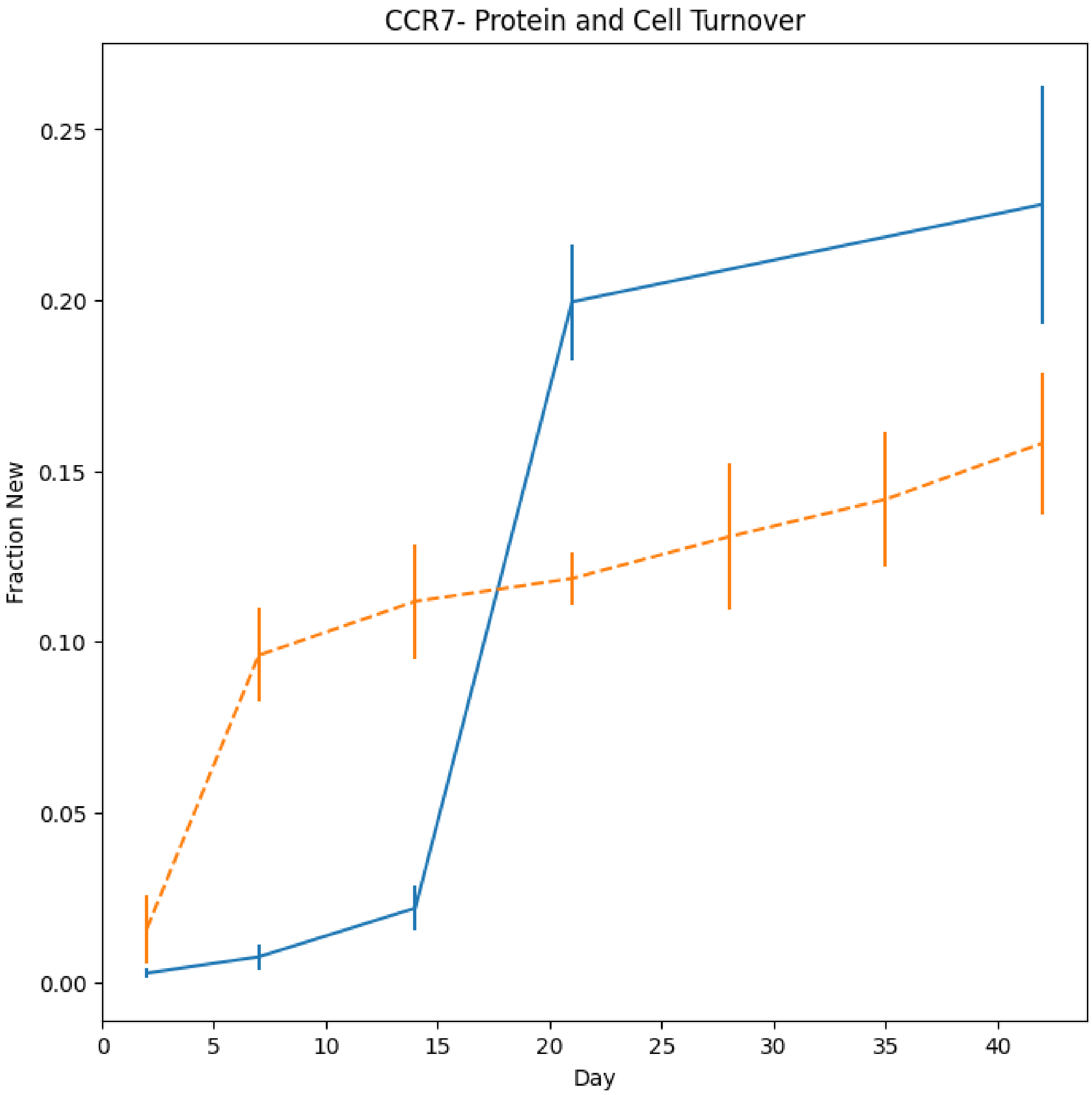

Figure 16: *Fraction new cells (**orange**, dashed line) and fraction new protein (**blue**, solid line) across D_2O loading. Error bars represent standard error of the mean.*

This is largely attributed to a high proportion of protein turnover rates being within two decimal places of cellular turnover, suggesting that many proteins turn over as a result of cellular proliferation, with a smaller subset of proteins presenting rates greater than cell proliferation. 163 proteins demonstrate rates above cell proliferation, however, only 83 of these are above cell proliferation in all instances (across participants). Visualising these proteins fractional turnover in Figure 17a clearly illustrates the input of cellular proliferation on protein turnover modelling, with only 3 proteins detected at day 2, none at days 7 and 14 (no error bars present), with 65 and 13 detected at days 21 and 42, respectively. As at day 42, fractional turnover is starting to exceed 50%, it is likely the decrease in turnover rates at this time point is impacted by reduced peptide identifications and quantitation of the isotopic envelope, as previously illustrated in monocytes (Figures 8 and 12).

A

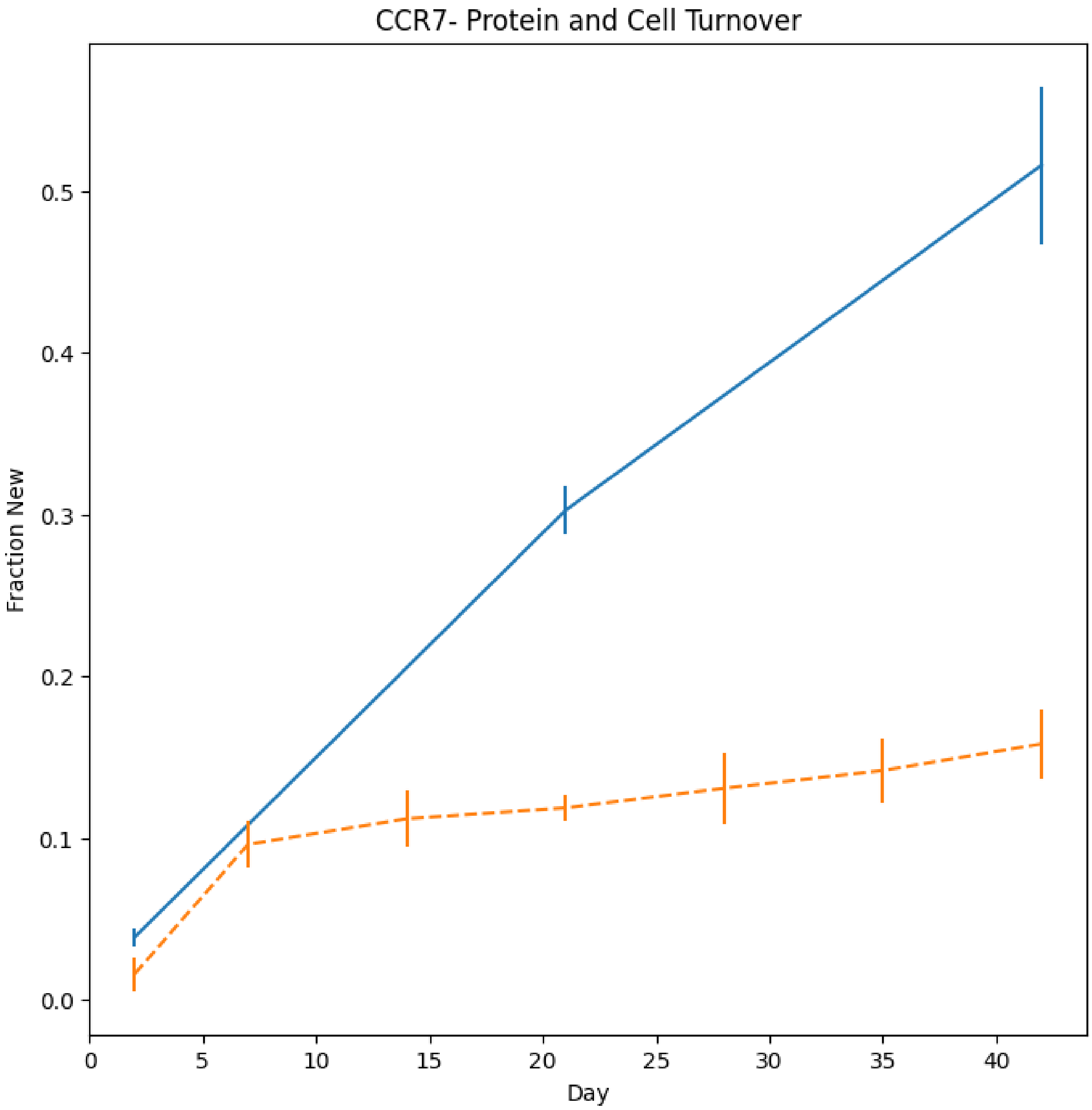

Figure 17A: *Fraction new protein and cells in effector memory (CCR7-) T-cells.* ***Orange****, dashed line illustrates fraction new cells,* ***blue****, solid line indicates fraction new protein, with error bars representing standard error of the mean.*

B

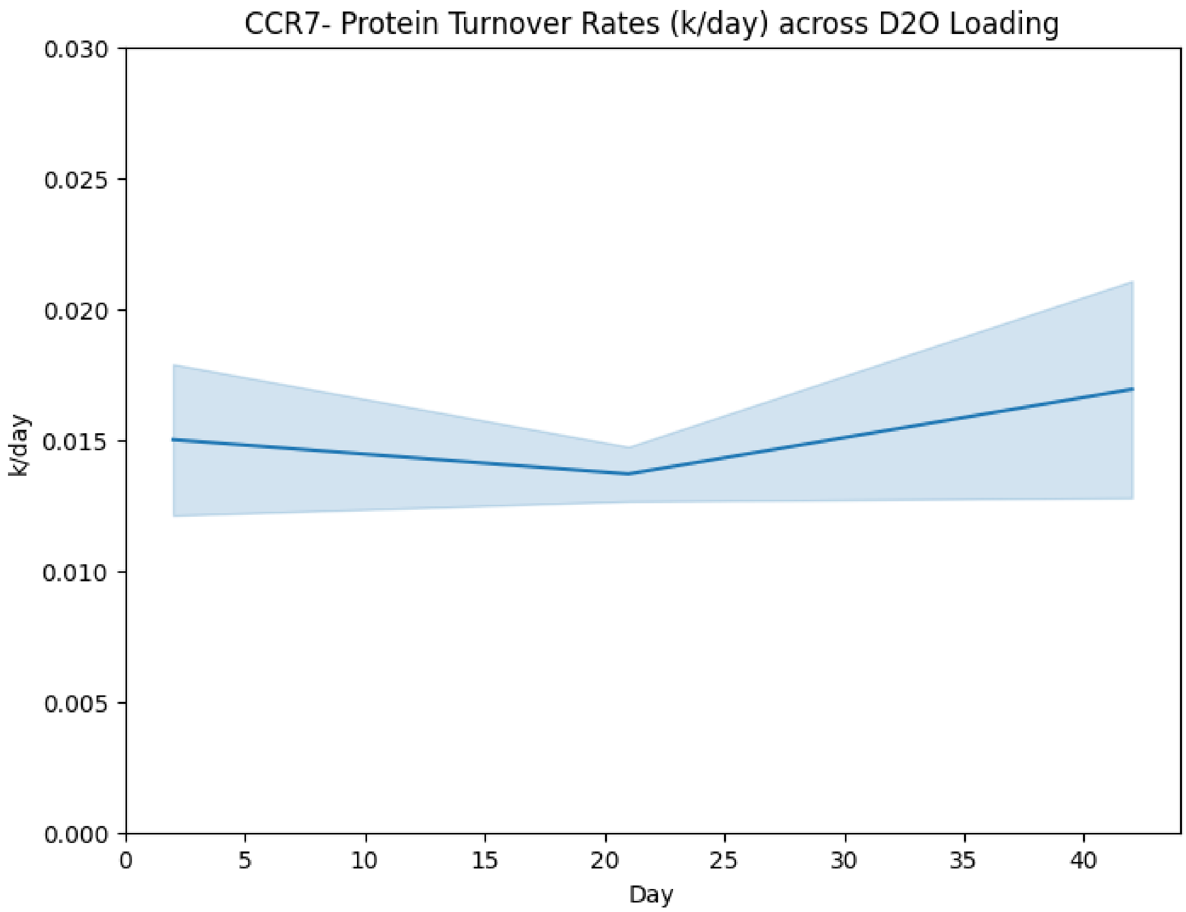

Figure 17B: *Relatively stable protein turnover (k/day) for rates greater than cell proliferation in effector memory (CCR7-) T-cells at time points 2, 21 and 42 days* D_2O *loading. Shaded area represents standard error of the mean.*

To assess differences between proteins whose turnover diverged from deuterium-labelling via cellular renewal, ontology analyses were conducted of protein classes and associated biological pathways (Figure 18a and 18b). Figure 18a protein class ontology demonstrates clear differences in proteins whose turnover reflect or exceed cellular proliferation. Of note, is that the translational protein class that was present in high abundance in previous ontology analysis of this proteomics dataset (Figure 14a) is preferentially detected in the high protein turnover grouping, being >20% of overall proteins. Also of note, are significant increases in metabolite interconversion enzyme and cytoskeletal protein classes, with an increase in unassigned proteins. Drastic decreases in the presence of protein classes are also evident in high vs equal-to-proliferation protein turnover groups, including the transporter, DNA metabolism and gene-specific transcriptional regulator protein classes. Pathway analysis (Figure 18b) reveals distinct changes in a variety of biological pathways, with increases in: cytoskeletal regulation by Rho GTPase, nicotinic acetylcholine receptor signalling and glycolysis; and significant decreases in cadherin and VEGF signalling.

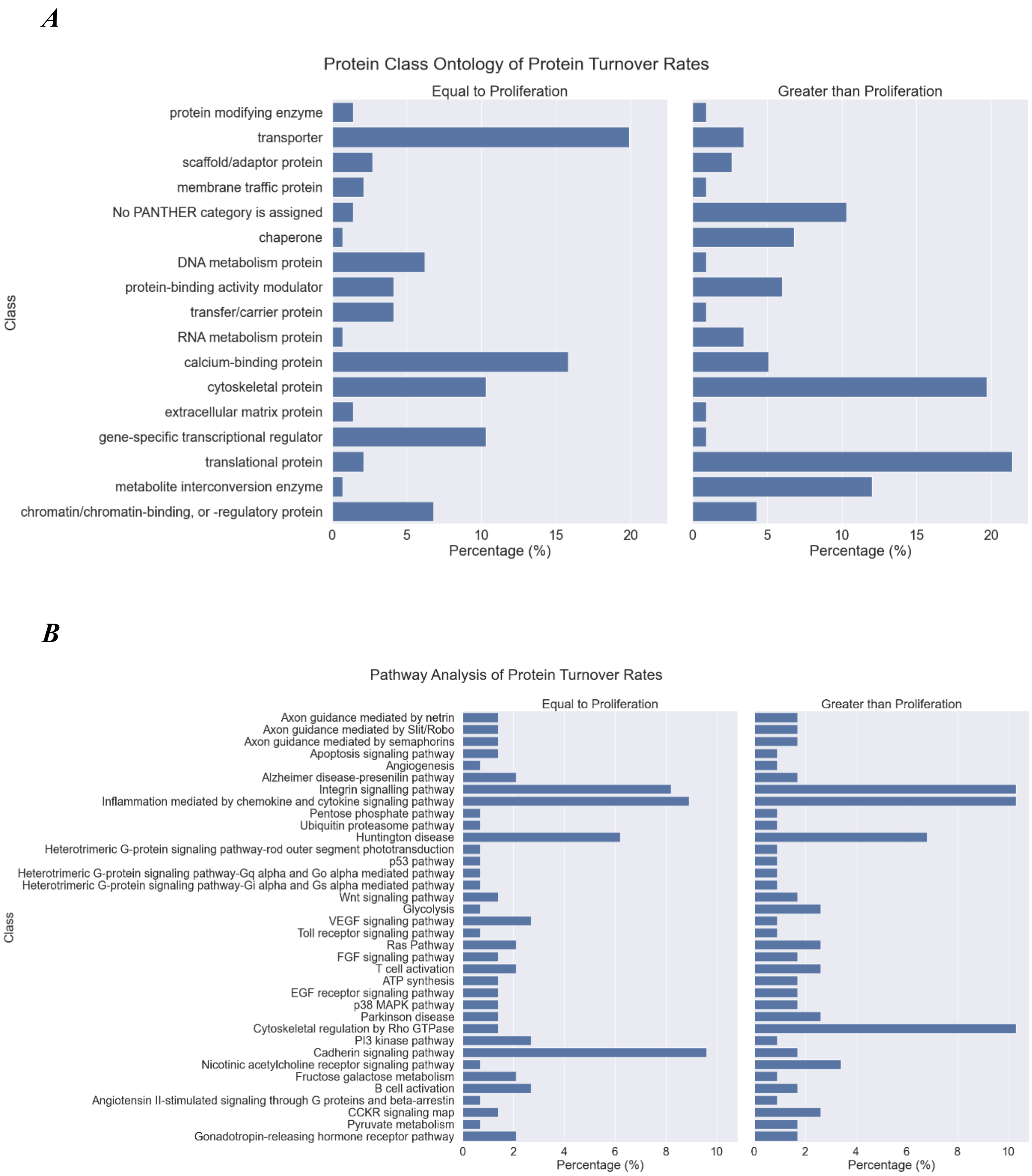

Figure 18: *Protein classes (**A**) and biological pathways (**B**) identified by PANTHER in effector memory T-cells, whose protein turnover approximates (equals) or exceeds (is greater than) cell proliferation rates.*

To assess the impact of deuterium-labelling on protein quantitation in effector memory T-cells, changes in abundance of the mass isotopic distribution was assessed at day 2 and 21 of D_2O loading (Figure 19a). Figure 19 demonstrates both a relative rightward shift in the mass isotopic distribution over time, as well as a significant reduction in abundance of the monoisotopic peak. Figure 19b shows quantified peptide abundance (XIC) to plateau from day 21-42, however, a significant reduction in peptides identified is observed from day 21 to day 42 (370 to 34 peptides), supporting previous interpretation that reduced peptide sampling occurs after day 21 in this dataset as a result of deuterium-labelling above 50% fractional turnover.

A

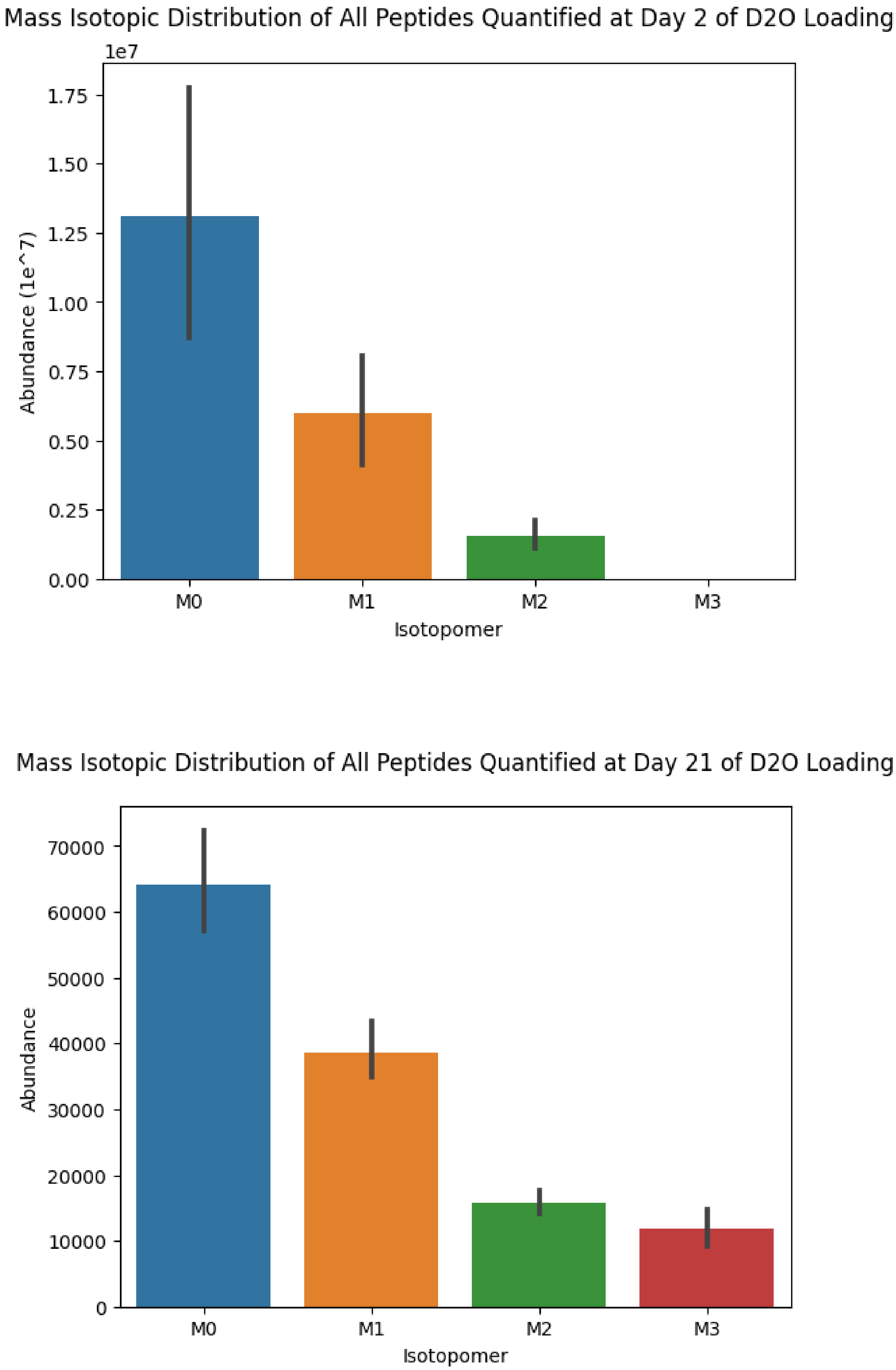

Figure 19A: *Mass isotopic distribution intensities of peptides quantified for protein turnover in effector memory T-cells, at days 2 and 21 of D_2O loading.*

B

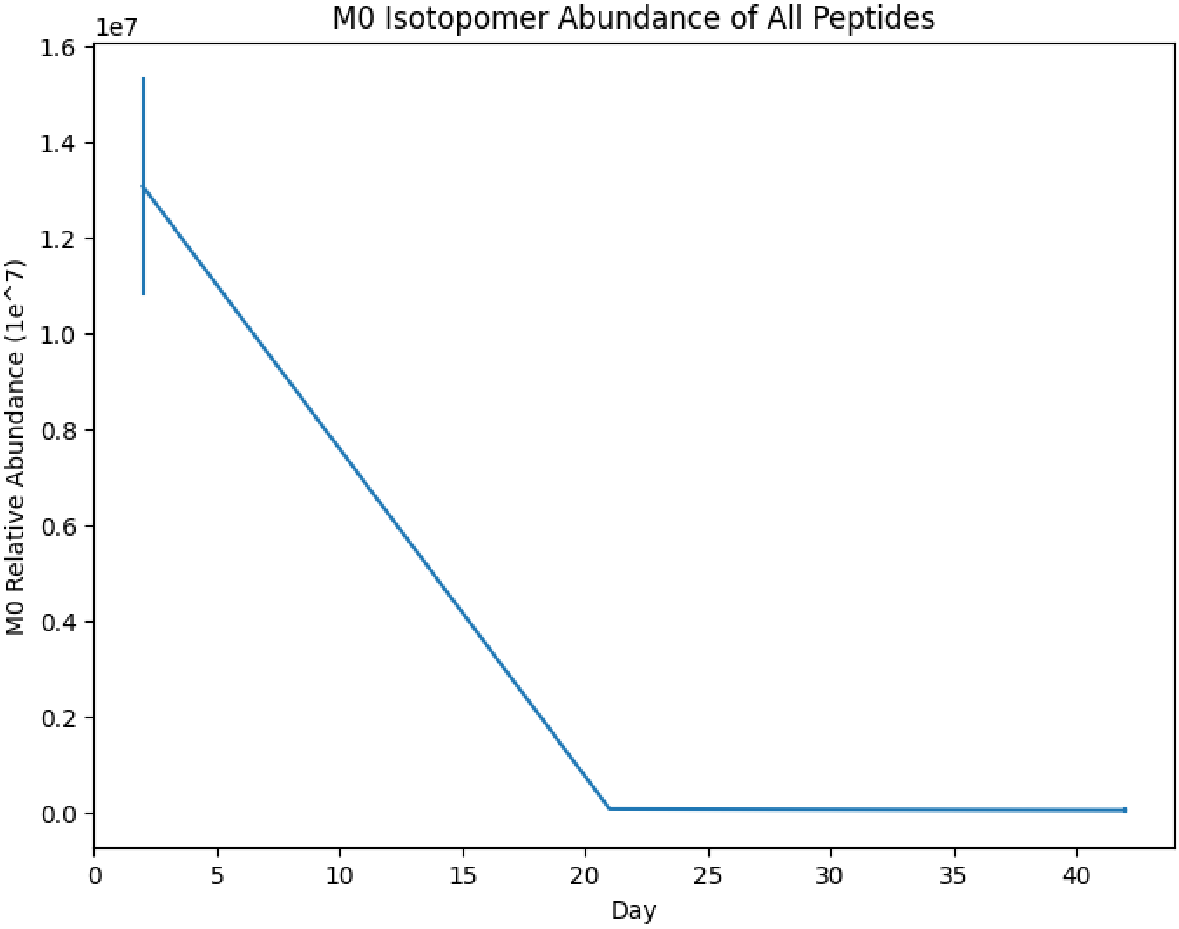

Figure 19B: *Changes in the monoisotopic peak abundance of all peptides quantified for protein turnover in effector memory T-cells at days 2, 21 and 42 of* D_2O *loading. Error bars represent standard error of the mean at all time points.*

To investigate the relationship between iBAQ protein abundance and turnover (*k* rate) measurements, data were log-transformed and visualised via jointplot. Figure 20 demonstrates a slight negative correlation between protein turnover (*k* rate) and iBAQ quantitation, similar to that previously reported in cultured *ex vivo* human monocytes (*chapter II, section 2.2*) and the available literature[39,40]. As previously alluded to in *chapter II, section 2.3*, it is possible that this is a result of a real biological relationship or can be attributed to biases in peptide sampling and quantitation concomitant with DDA LC-MS/MS analysis.

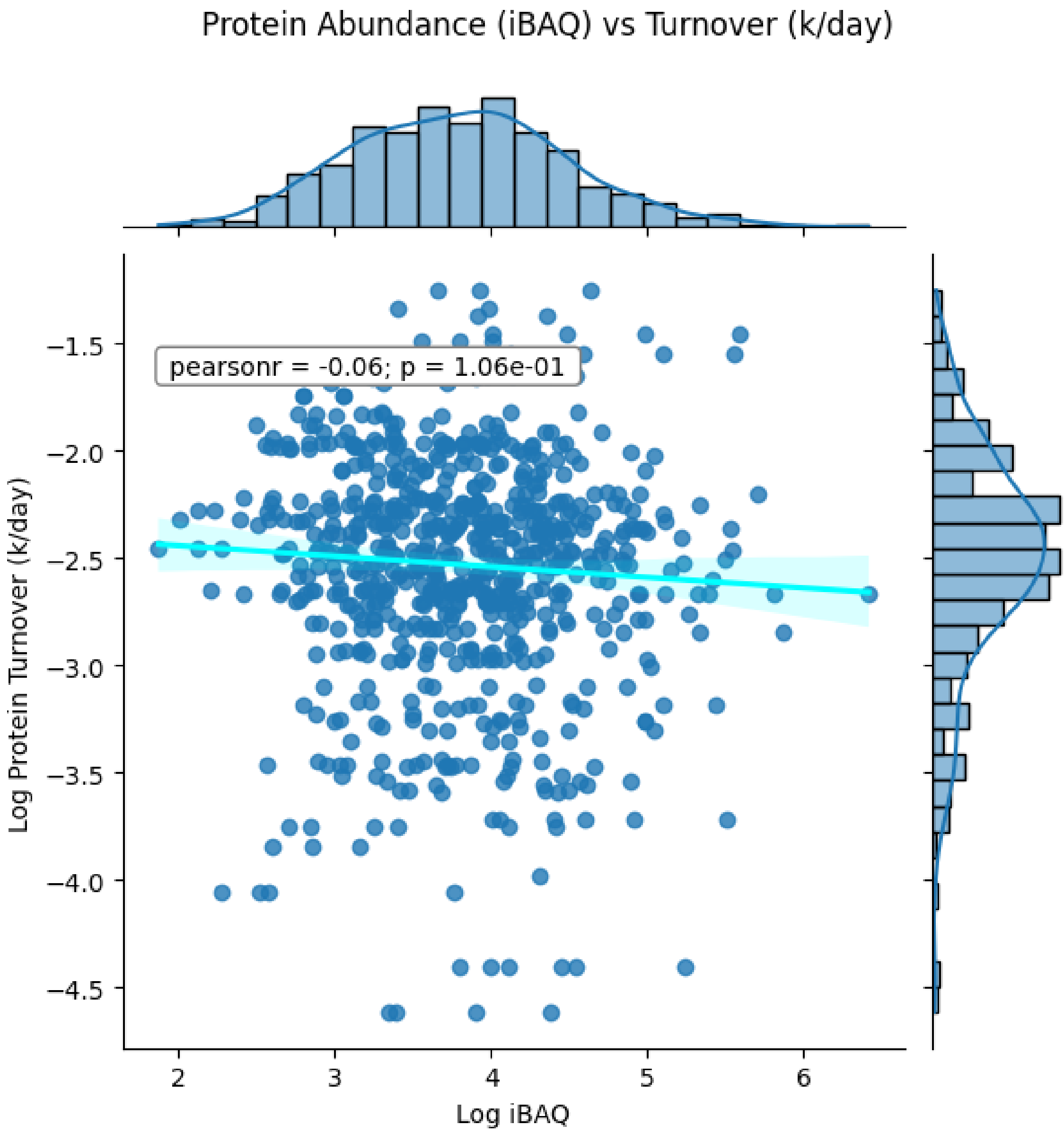

Figure 20: *Jointplot depicting scatter plot with line of best fit for log-transformed protein abundance (iBAQ) vs protein turnover (k rate), and histograms of data distributions for each dataset, respectively.*

Of final interest, was to investigate whether the temporal limitations in peptide identification and consequent quantitation were related to the body water deuterium enrichments of participants, which spanned an approximate three-fold range (Figure 2). While all identified proteins in the dataset were detected at each time point in at least one participant, Figure 21 demonstrates a clear reduction in unique proteins quantified by iBAQ (Figure 21a) and for protein turnover (Figure 21b) in participants loaded to higher body water deuterium enrichments. Figure 21a illustrates deuterium enrichments of 1-1.2% body water to present significant improvements in number of proteins quantified via iBAQ, compared to those participants with deuterium body water enrichments >1.5%. Interestingly, an increase in average plateau enrichment from ~1.5% to ~2.8% did not have as significant an impact on iBAQ quantitation (Figure 21a) as increases from 1-1.2% to ~1.5%. Of further interest, there appears to be a greater improvement in the number of proteins quantified for turnover measurements than for iBAQ with lower body water deuterium enrichments of 1-1.2% (Figure 21b). This demonstrates lower body water deuterium enrichments to have beneficial effects for both deuterium-labelling measures of protein turnover and iBAQ quantitation, with the added experimental benefit of reduced dose volumes concurrent with decreased cost, time and potential side-effects within participants during D_2O loading. A trend for higher deuterium enrichments (~2.8) to aid iBAQ and turnover quantitation at earlier time points (days 2-14), followed by a shift towards lower deuterium enrichments (~1.5%) to aid quantitation at later time points (days 21-42) supports previous interpretations of deuterium-labelling to alter detection of the mass isotopic distribution over time (*chapter II, section 2.3 and 3.3*). No differences were observed between COVID-19 positive and negative participants across the study duration.

A

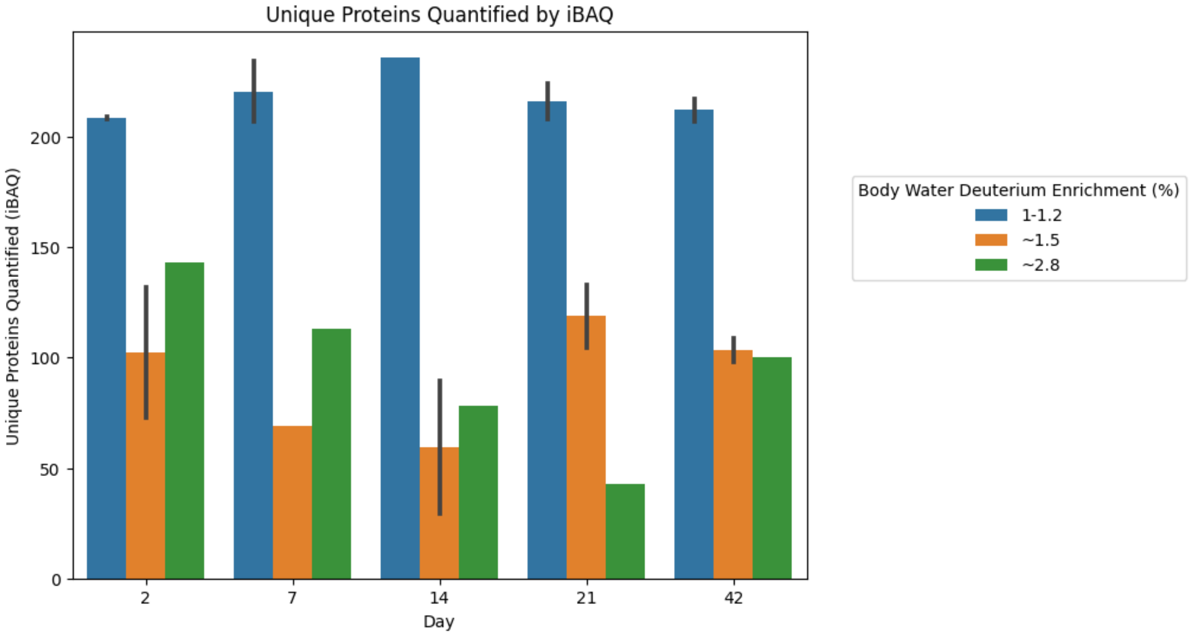

Figure 21A: *Unique proteins quantified for iBAQ per body water deuterium enrichment range and time point (day). Error bars represent standard error of the mean. Due to COVID-19 self-isolation, ~1.5% body water deuterium enrichment has only one participant timepoint at day 7 and 1-1.2% has only one participant timepoint at day 14. Only one participant was loaded to ~2.8% body water deuterium enrichment for the study duration (Participant 1).*

B

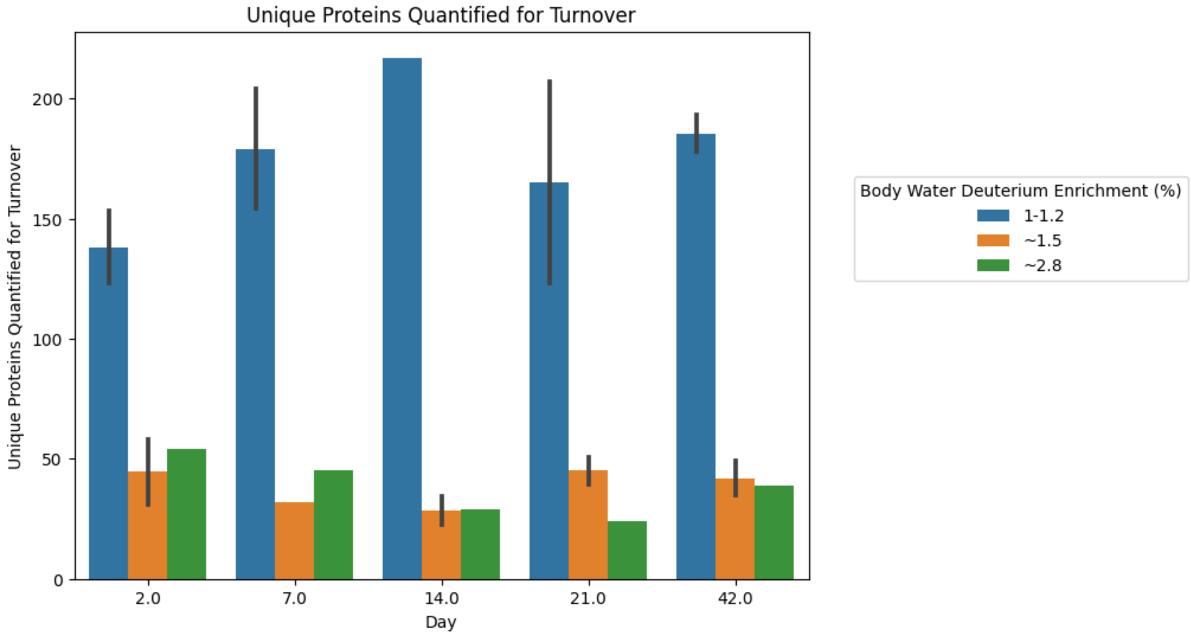

Figure 21B: *Unique proteins quantified for turnover per body water deuterium enrichment range and time point (day). Error bars represent standard error of the mean. Due to COVID-19 self-isolation, ~1.5% body water deuterium enrichment has only one participant timepoint at day 7 and 1-1.2% has only one participant timepoint at day 14. Only one participant was loaded to ~2.8% body water deuterium enrichment for the study duration (Participant 1).*

3.4 DISCUSSION

This pilot study's findings demonstrate that deuterium-oxide (D_2O) can be safely administered to both male and female participants, in order to accurately enrich and maintain deuterium concentrations within the body water pool for metabolic measurements of cellular proliferation and protein turnover in immune cell populations. This enabled the determination of cellular proliferation in both fast (monocyte) and slow (effector memory T-cell) immune populations, with sufficient sensitivity to detect differences both acutely and temporally within these processes following infection with COVID-19 (Figure 6a). Differences between rates of cellular proliferation, however, present greater challenges towards successful modelling of protein turnover in these cell populations, with greater difficulties apparent when quantifying proteome kinetics in fast-turnover (monocyte) vs slow-turnover (effector memory T-cell) populations. Both datasets convey the importance of optimal time point sampling, with early sampling recommended for monocytes (<7 days) and later sampling appearing optimal for protein turnover quantification in effector memory T-cells (~21 days; Figures 15 and 17). For future studies, this suggests that consideration of optimal time point sampling is vital to experimental planning, but also demonstrates that alterations in protein turnover rate modelling may be required in order to improve proteome coverage throughout deuterium-loading time courses (Figures 16 and 17a), in particular with regards to addressing limitations in the use of standardised and/or linear constants to account for input from the dynamic processes of cellular turnover, that may not fully account for interindividual variability.

Assessment of changes in the mass isotopic distribution with deuterium-labelling abided by previous theoretical and experimental observations[14,32], in both monocytes and effector memory T-cells (Figures 9 and 19). Interestingly, the effects of deuterium-labelling on quantitative precision for both abundance and turnover appear to be a reflection of the detection of the mass isotopic distribution (i.e. peptide identification) opposed to any alterations in quantitative accuracy resulting from variation in the numbers or intensity of mass isotopomers used for quantification (Figure 11). Of further interest, is that this observation has a greater impact on proteome depth for turnover measurements with deuterium-labelling than on iBAQ quantitation (Figure 21), both of which suggest a lower body water deuterium enrichment of 1-1.2% to be superior to ≥1.5%. This proves beneficial for future studies that may consequently benefit from reduced costs due to decreased deuterium-oxide volumes and a reduced likelihood of any potential side-effects (such as nausea) that are known to occur as a result of D_2O dosing[3].

Relatively stringent dataset filtering during protein turnover quantification in this study still enabled for the quantification of turnover rates in ~90% of all identified proteins in slow-turnover effector memory T-cells, albeit a much lower range of ~6% was achieved in fast-turnover monocytes. It is likely interindividual variability in cellular proliferation rates as a result of COVID-19 (Figure 6a) and body water deuterium enrichments (Figure 21b) largely impacted this pilot study's ability to quantify turnover rates of these immune populations proteomes. However, knowledge of the inputs and relative importance of these factors may prove invaluable for future studies looking to implement similar stable isotope labelling techniques to assess proteome-wide protein turnover measurements. While the range and depth of these datasets is largely impacted by limitations in peptide (and therefore protein) identifications with deuterium-labelling, quantitative accuracy was at acceptable levels for protein turnover measurements (average CVs: monocytes 0.18, effector memory T-cells 0.28). The capability to simultaneously quantify protein abundance via iBAQ in parallel to protein turnover during deuterium-labelling experiments with D_2O loading has previously been illustrated in *chapter II, section 2.2*, along with one published study[41], albeit this study only presented iBAQ data as a complement to turnover rates in rats, and not humans. This pilot study is therefore the first (to the author's knowledge) to provide *in vivo* iBAQ data in tandem with paired protein kinetics through deuterium-labelling from D_2O in humans. Comparisons between paired protein turnover and abundance measurements demonstrated a minor negative correlation as previously reported in the literature[39,40], in *chapter II, section 2.2*, and in both monocytes (not shown) and effector memory T-cells (Figure 20) within this dataset. While a mechanistic explanation has previously been alluded to in *chapter II, section 2.2*, this dataset further displays an interesting effect in Figure 10b, whereby at high fractional cellular turnover (≥70%) iBAQ quantitation of all monocyte proteins quantified for turnover decreases drastically after day 7 to plateau at days 14-21. Figure 12 suggests this may be due to shifts in the mass isotopic distribution at high levels of deuterium-labelling subsequently reducing peptide sampling through a decreased ability to identify the monoisotopic peak (required for peptide identification), with the additional requirement for higher numbers of mass isotopic peaks to be included in XIC (and therefore iBAQ) quantitation in order to provide accurate abundance measurements (Figure 13). Insufficient detection of a mass isotopic envelope of 6 or greater (Figure 13) may be why there is a significant decline and probable underestimation of iBAQ protein abundances at later time points during D_2O loading, which is supported in Figure 12a where a mass isotopic envelope of only 2-5 mass isotopomers is quantifying highly deuterated peptide species. Due to the slower proliferation rate of effector memory T-cells, this behaviour is not detected following 6-weeks of *in vivo* deuterium-labelling in this cell type (Figure 21a).

3.5 CONCLUSIONS

The work of chapter II presents deuterium-oxide as a versatile and effective stable isotope tracer for application to cellular proliferation and proteome kinetic analyses in humans, within both *ex vivo* and *in vivo* experiments. Ease of administration enables deuterium-oxide to be utilised without the requirement for extensive prior clinical experience within human studies, and is extremely well-suited to free-living investigations where maintenance of deuterium enrichment in the body water pool can be achieved through participant self-administration across a period of days-months. Stable maintenance of body water deuterium enrichment in human participants within this study was easily achieved across a three-fold range, without prior knowledge of individual body water kinetics, although caution is advised for participants whose BMI may be near underweight or obese classification, especially when in conjunction with relative inactivity. In human studies, where it is desirable to administer as little D_2O as possible, it appears deuterium enrichment of 1-1.2% body water is sufficient for both cellular proliferation and proteome kinetic analyses. Future work should look to address constraints in protein turnover modelling arising from inputs of cellular proliferation, that may consequently reduce proteome depth or quantitative accuracy, particularly in proteins of low turnover or cell types with fast cellular renewal.

Implementation of these techniques in tandem with more established quantitative methods, such as iBAQ, will benefit experiments interested in deciphering proteome regulation across a diverse range of cell types, while drawing much needed attention to the often overlooked aspect of proteome regulation that is, protein turnover. It is likely for these stable isotope techniques to reach the proteome depth required for comprehensive characterisation of cellular proteome kinetics, that implementation of more up-to-date instrumentation and acquisition strategies is required, with great potential for improved bioinformatic approaches incorporating deuterium-labelled peptide-specific search algorithms and quantitation being desirable in order to improve confidence within these measurements. With many diseases characterised by alterations in cellular and proteome turnover, these techniques pose exciting avenues for mass spectrometrists and biologists alike, which may present an important step to further understanding a plethora of human pathologies.

3.6 APPENDIX

Optimising Proteomics Sample Preparation

Proteome Coverage of Unlabelled Immune Cell Populations

3.61 Methods

Prior to the commencement of this study, it was important to test the efficacy of our current proteomics protocols for single-cell immune populations. 35ml of whole blood was obtained from one healthy participant following informed consent under ethical approval from the University of Nottingham, from which blood sample PBMCs were isolated via Histopaque gradient. Briefly, 35ml whole blood was carefully layered onto 15ml Histopaque (Sigma). The sample was centrifuged at 800g for 25 minutes at 21ºC. The PBMC layer was removed with a 10ml glass pipette and transferred to a fresh 50ml tube, and PBS added to a total volume of 50ml. The sample was then centrifuged at 1400rpm for 8 minutes at room temperature and supernatant discarded. Cells were washed twice with PBS by centrifugation at 300g for 5 minutes.

PBMCs were counted using a cell counter and MACS buffer containing CD14+ beads was added at a volume based on manufacturer's recommendations (Miltenyi). The sample was mixed and incubated at 4ºC for 15 minutes before addition of 20ml cold MACS buffer, and washed via centrifugation at 1000rpm for 5 minutes. Supernatant was discarded and the cell pellet resuspended in 500µl MACS buffer. An MS column (Miltenyi) was equilibrated with 500µl MACS buffer before addition of the sample. The column was washed three times with 500µl MACS buffer and the CD14- flow-through collected for downstream FACs. The CD14+ fraction was subsequently eluted from the column by passing through 1ml MACS buffer away from the magnet.

The CD14- cell flow-through was collected and resuspended in MACS buffer according to PBMC yield, as detailed previously (*section 3.2*). 50µl of sample was removed for use as a control, and the remaining sample was stained with antibodies; CD3-PE, CD4-APC, CD8-PE-Vio 770 (Miltenyi) and CD14 APC-eFluor 780 (eBioscience), in order to sort CD4+ and CD8+ T-cell populations with a Beckman Coulter Astrios EQ. Isolated cells were pelleted via centrifugation at 300g for 5 minutes and supernatant removed, then washed three times with phosphate buffered saline (PBS) by centrifugation at 300g for 5 minutes. PBS was carefully removed from cell pellets and these were then stored at -80°C until processing for mass spectrometry analysis.

Immune cell populations CD14+ monocytes, CD14- CD4+ T-cells and CD14- CD8+ T-cells, were lysed by addition of 100µl 100mM ammonium bicarbonate containing 0.1% SDS (pH 8). 2.1µl of 500mM Dithiothreitol (DTT) in 50mM ammonium bicarbonate was added to the samples (final sample concentration of ~10mM DTT), which were then incubated at 50ºC for 45 minutes. Samples were cooled for 10 minutes on ice before addition of 11.5µl 500mM Iodoacetamide (IAA) in 50mM ammonium bicarbonate (final IAA sample concentration of ~50mM) and incubation in the dark at room temperature for 20 minutes. 460µl ice-cold acetone was then added to samples which were incubated overnight at -20ºC to precipitate proteins. The following day, samples were centrifuged at 17,000g for 20 minutes at 4ºC. Acetone was carefully removed and the resulting protein pellets washed with 50µl ice-cold acetone and centrifugation at 17,000g for 5 minutes. Acetone was removed and protein pellets air-dried prior to resuspension in 100µl 50mM ammonium bicarbonate. 1µg of MS Grade Trypsin (Pierce, Thermo Scientific) was added to samples which were incubated at 37ºC overnight. 2.5µl of 10% formic acid was added the following morning to quench protein digestion and samples were transferred to glass LC-MS vials and dried under nitrogen stream for 30 minutes at 40ºC. Samples were resuspended in 100µl 95% double-distilled H_2O and 5% acetonitrile with 0.1% formic acid. 1µg peptides were injected for analysis with a Q-Exactive orbitrap mass spectrometer (Thermo Scientific) in line with a Dionex Ultimate 3000 ultra-high pressure nano liquid chromatography system and electrospray ionisation source (Thermo Scientific). A non-linear gradient of solvent B (80% ACN (v/v) in 0.1% FA (v/v)) was applied for a total gradient time of 104 minutes and total run time of 120 minutes. Full MS scans were acquired at a resolution of 60,000 for the mass range 380-1300 m/z, with a precursor isolation window of 2 m/z for MS2 scans at a resolution of 17,500.

Data were analysed with Proteome Discoverer software (v. 2.4) utilising the SEQUEST and INFERYS modules. Raw data files were searched against the UniProt Homo Sapiens databases (UP000005640_9606.fa, UP000005640_9606_additional.fa) and a vendor-specific contaminant file. Peptides of amino acid length 7-30 were searched for with cysteine carbamidomethylation set as a static modification and methionine oxidation set as a dynamic modification, allowing up to two missed cleavage sites. Peptide and protein identifications were controlled at a false-discovery rate (FDR) of 1%. Output files were read into Python programming language (v. 3.9.7) for analysis and plotting through use of the modules: Pandas (v. 1.4.4), SciPy (v. 1.9.1), Matplotlib (v. 3.5.3) and Seaborn (v. 0.11.2). PANTHER (release 17.0) was utilised for protein classifications and gene ontology analysis of biological function.

3.62 Results

At 1% FDR, 6215 peptides were identified in CD14+ monocytes, relating to 1436 proteins and 1056 protein groups. In CD4+ T-cells, 4214 peptides were identified, relating to 1013 proteins and 713 protein groups. And in CD8+ T-cells, 2436 peptides were identified, relating to 790 proteins and 459 protein groups. Across all cell types there were 1306 protein groups identified, with 329 protein groups shared among cell types, 522 protein groups detected uniquely in monocytes, 136 uniquely in CD4+ T-cells and 55 proteins unique to CD8+ T-cells (Figure 1).

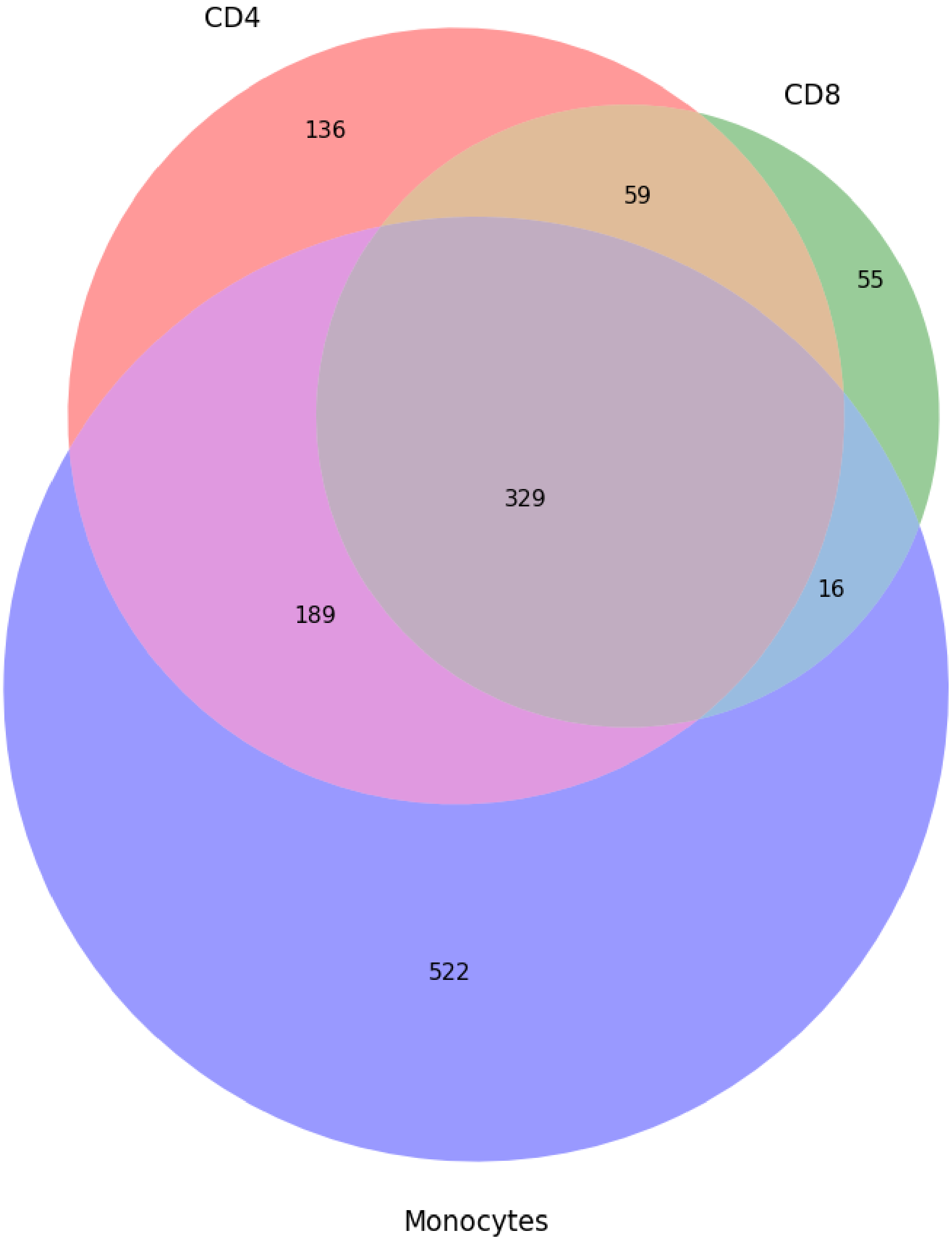

Figure 1: Venn-diagram displaying shared and unique protein groups across immune cell types; CD14+, CD14- CD4+, CD14- CD8+, isolated via MACs and FACs. This graph was generated using the module matplotlib_venn.

Figure 1 illustrates differences in protein group identifications relative to cell type, with ~50% of identified protein groups in monocytes not detected in the other two T-cell populations. A similar level of separation is present between CD4+ T-cells and CD8+ T-cells, with ~45% of protein groups unique to CD4+ cells. There is slightly less separation between CD8+ T-cells and CD14+ monocytes, with only around 33% of CD8+ protein groups not detected in CD14+ monocytes, however, this may be related to the reduced number of protein group identifications in CD8+ cells and not differences in homology *per se*. The number of unique protein identifications for monocytes are approximate to those demonstrated elsewhere in a study evaluating protein homology between immune cell types isolated from patient bone marrow, albeit with the caveat of differences in sample numbers and cell types assessed[5].

To further examine the proteomes of these three cell types, ontology analysis of protein groups identified from each cell type were input to PANTHER in order to identify the range and abundance of protein classes present (Figure 1A). Across all cell types, the most prevalent protein classes were: metabolite interconversion enzyme, cytoskeletal protein, RNA metabolism protein and translational protein classes (Figure 1B). For both CD4+ and monocyte cells, the predominant protein class was, metabolite interconversion enzyme, which currently relates to 192 genes known to be implicated in enzymatic activity of various metabolites (*accessed 31/05/2023*, Figure 1A). For the CD8+ cell type, the extracellular matrix protein class was the most prevalent.

The relevance of these protein classes was confirmed via gene ontology analysis of the identified cell proteome's biological functions, which again illustrated metabolite interconversion enzyme activity, cytoskeletal proteins, RNA metabolism proteins and extracellular matrix proteins to be among the most enriched groupings (Figure 2).

A

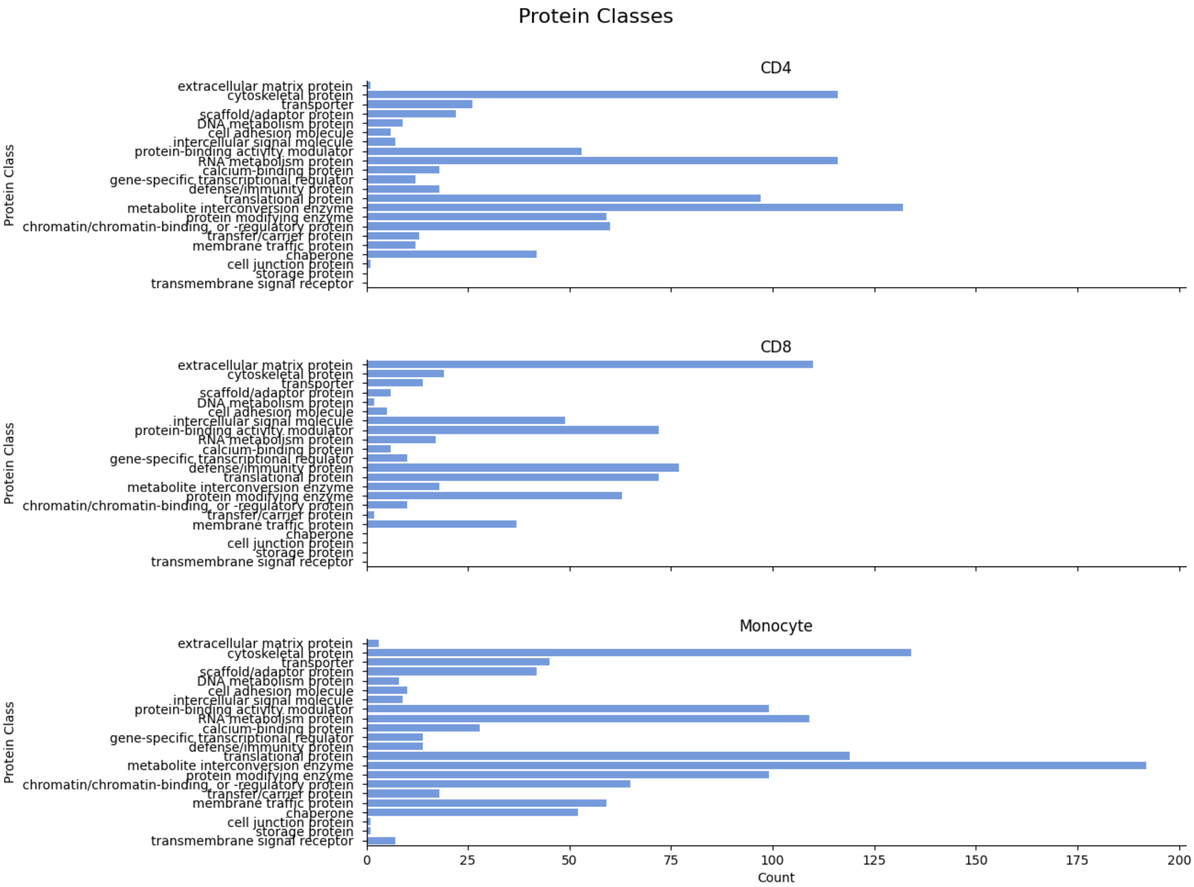

Figure 1A: Protein classes identified for each immune cell type using PANTHER.

B

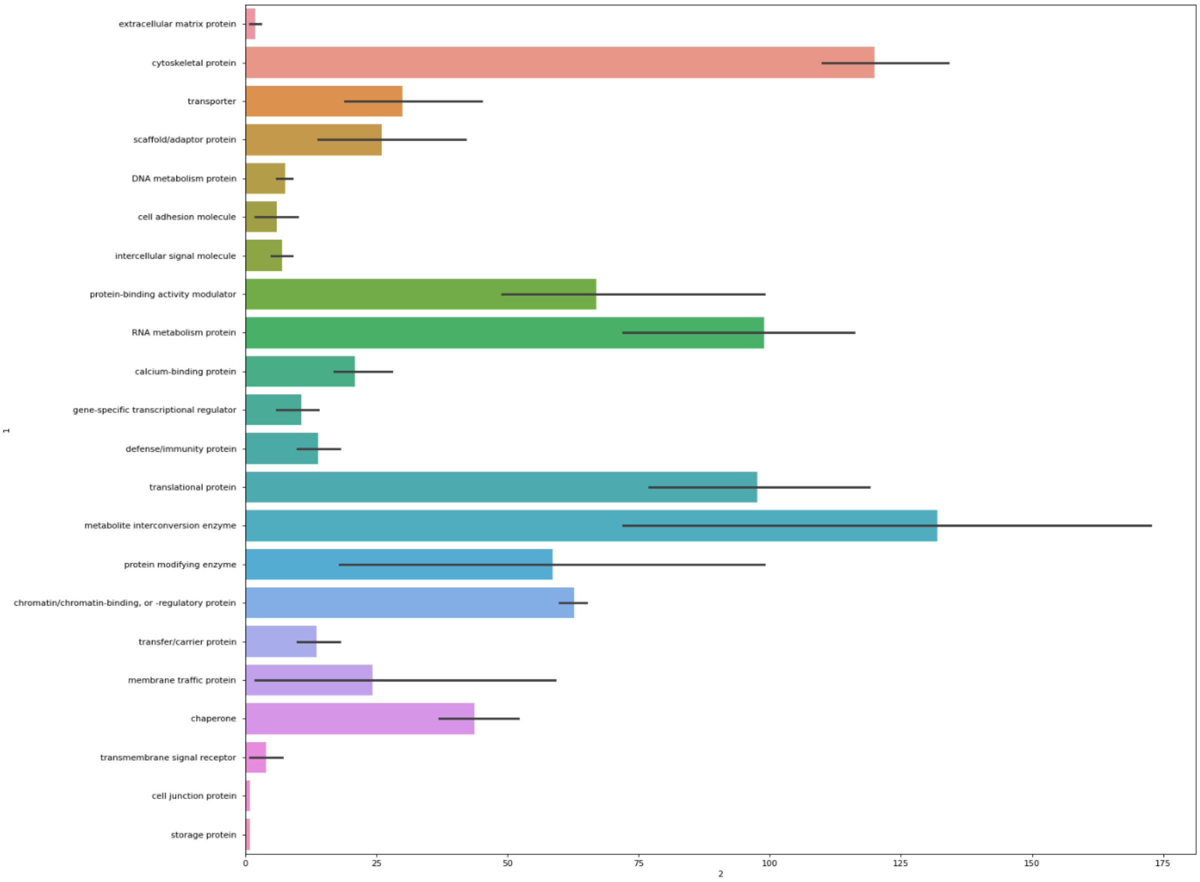

Figure 1B: Protein class identifications across all immune cell types with PANTHER, error bars represent 95% confidence intervals.

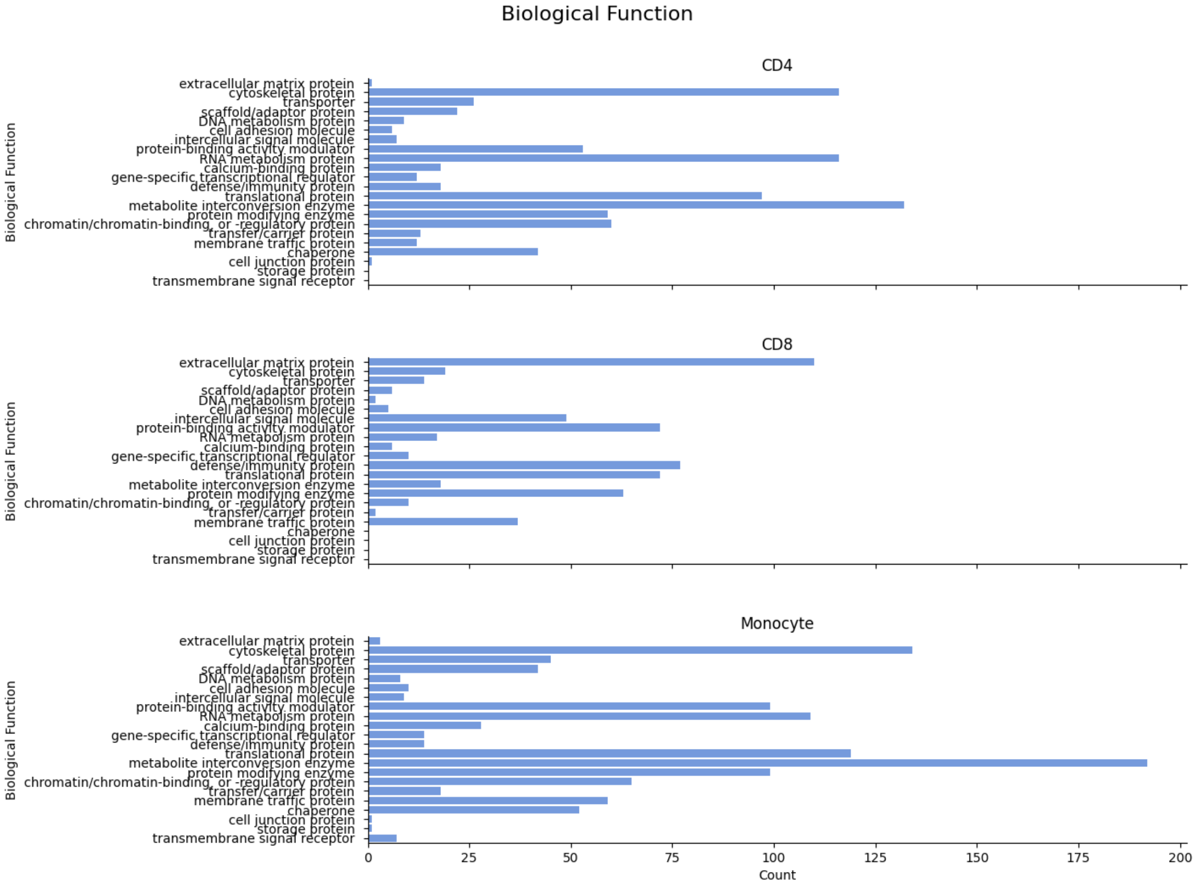

Figure 2: Gene ontology analysis via PANTHER for biological functions related to identified protein groups across all three immune cell types.

3.63 Future Steps

While these results are initially satisfactory and similar in proteomic depth to protein identification rates reported elsewhere through single-injection shotgun proteomic analysis using similar instrumentation[6,7], to gain more detailed insight into biological processes and the regulation of the human proteome, isolation of distinct cellular populations is important in order to comprehensively characterise biological responses.

For this pilot study, central memory (CD14- CD3+ CD45RO+ CCR7+) and effector memory (CD14- CD3+ CD45RO+ CCR7-) T-cell populations were chosen[8,9], as they represent cell types whose functions are implicated in a variety of immunological diseases[10–12]. While these cell types are still sufficiently abundant in the periphery for their successful isolation from whole blood via FACs[10,11], due to the need to also assess cellular proliferation in order to calculate accurate measurements of protein turnover with *in vivo* deuterium-oxide stable isotope labelling, sorted immune cells will consequently need split for downstream analysis. This will therefore substantially reduce cell numbers for mass spectrometry analysis. Label-free proteomic analysis of low abundant immune cells has proven challenging with commercial mass spectrometers >10 years old, such as the Q-Exactive instrument (Thermo Scientific)[6]. While recent advances in sample preparation and instrument optimisation have successfully enabled mass spectrometry-based proteomics down to true single-cell resolution using orbitrap mass spectrometers[13], it has additionally been observed that stable isotope labelling with deuterium-oxide reduces peptide and protein identifications via data-dependent acquisition schemes[14]. This is due to shifts in the mass isotopic distribution of deuterium-labelled peptides over time resulting in increased spectral complexity and reduced sampling of the M0 (unlabelled peptide) precursor for sequencing via tandem MS, thus reducing spectral matching and peptide identification with current analytical software[14,15]. Together, it is unclear to what extent these factors will impact proteomics analysis within this current proteomics workflow.

To assess this, several samples of deuterium-labelled CD14- CD3+ CD45RO+ CCR7+ cells were analysed from one study participant (Participant 5, Table 1) according to the proteomics protocol detailed in section *3.21 Methods*. Application of this proteomics protocol resulted in an average protein identification rate of ~90 proteins, confirming the requirement for optimisation of this proteomics protocol prior to further analysis. As similar T-cell populations have exhibited relatively slow rates of cellular proliferation[16,17], CD14+ cells were retained within this pilot study to enable comparison with a fast-turnover cell population[18], for measures of cellular proliferation and protein turnover. All cell counts are detailed in Table 2.

Participant	**Timepoint (Day)**	**CD14+ (Total cells sorted)**	**CD14+ Proteomics Cells (Approx.)**	**CD3+CD45RO+CCR7- (Total cells sorted)**	**CCR7- Proteomics Cells (Approx.)**	**CD3+CD45RO+CCR7+ (Total cells sorted)**	**CCR7+ Proteomics Cells (Approx.)**	**Unsorted CD14- Cell Count**
1	0	4216500	2108250	*NS*	*NS*	*NS*	*NS*	4940000
1	2	5475000	2737500	221522	110761	441794	220897	
1	7	9087500	4543750	233279	116640	801863	400932	
1	14	7125000	3562500	101270	50635	370366	185183	
1	21	1700000	850000	119903	59952	453383	226692	
1	28	1350000	675000	183171	91586	638115	319058	
1	35	985000	492500	326264	163132	802291	401146	
1	42	925000	462500	141901	70951	286032	143016	
2	0	2047500	1023750	*NS*	*NS*	*NS*	*NS*	1625000
2	2	2700000	1350000	137247	68624	19362	9681 *	
2	7	1657500	828750	135548	67774	34056	17028 *	
2	14	3005000	1502500	160803	80402	70630	35315 *	
2	21	1300000	650000	175672	87836	106890	53445	
2	28	730000	365000	79429	39715 *	50652	25326 *	
2	35	875000	437500	500144	250072	821550	410775	
2	42	355000	177500	146525	73263	62507	31254 *	
3	0	750000	375000	72540	36270 *	100119	50060	
4	0	2400000	1200000	141115	70558	462057	231029	
5	0	970000	485000	209900	104950	138454	69227	
5	2	684000	342000	191958	95979	117048	58524	
5	7	*NI*	*NI*	*NI*	*NI*	*NI*	*NI*	
5	14	760000	380000	167632	83816	275540	137770	
5	21	1560000	780000	227315	113658	224990	112495	

5	28	1770000	885000	490063	245032	750010	375005	
5	35	1990000	995000	503838	251919	1210910	605455	
5	42	2220000	1110000	581272	290636	1621105	810553	
6	0	1585000	792500	13914	6957 *	6139	3070 *	
6	2	1600000	800000	113619	56810	99273	49637 *	
6	7	*NC*	*NC*	*NC*	*NC*	*NC*	*NC*	
6	14	1215000	607500	150526	75263	528208	264104	
6	21	1125000	562500	142528	71264	210418	105209	
6	30	1785000	892500	183459	91730	925283	462642	
6	35	3300000	1650000	362233	181117	1722597	861299	
6	42	*NA*	*NA*	*NA*	*NA*	*NA*	*NA*	
7	0	2580000	1290000	405043	202522	837950	418975	
7	2	3060000	1530000	556707	278354	1698447	849224	
7	7	2800000	1400000	502315	251158	1455829	727915	
7	14	*NC*	*NC*	*NC*	*NC*	*NC*	*NC*	
7	21	2200000	1100000	457625	228813	1855944	927972	
7	30	930000	465000	*NS*	*NS*	*NS*	*NS*	3900000
7	35	1550000	775000	762771	381386	2060087	1030044	
7	42	4450000	2225000	705728	352864	2973549	1486775	
8	0	5650000	2825000	*ND*	*ND*	*ND*	*ND*	
8	2	7400000	3700000	399099	199550	447046	223523	
8	7	3830000	1915000	1411041	705521	963066	481533	
8	14	7950000	3975000	1661165	830583	1644741	822371	
8	21	6550000	3275000	1036882	518441	980176	490088	
8	30	170000	85000	*NS*	*NS*	*NS*	*NS*	3240000
8	35	4500000	2250000	1083732	541866	1030187	515094	
8	42	2500000	1250000	856428	428214	1011718	505859	

Table 2*: Cell counts from isolated cells via MACs (CD14+/-) and FACs (CD14- CD3+ CD45RO+ CCR7+/-).* ***NC****; no sample collection due to COVID-19 infection.* ***NI;*** *No sample collected due to self-isolation following contact with COVID-19 infected, Participant 6.* ***NA****; no sample available due to participant absence.* ***NS****; no sample sorted via FACs due to technical difficulties.* ***ND;*** *No data available for FACs cell counts. Samples indicated with asterisk (*) are deemed low abundance at <50,000 cells.*

3.64 Optimising Protein Extraction

An initial observation with this method of proteomics sample preparation was a low protein yield during protein extraction, with an average concentration of 0.52µg/µl in 100µl (total protein content: 52µg) extraction buffer across cell types (CD14+, 0.9µg/µl; CCR7+, 0.52µg/µl; CCR7-, 0.14µg/µl; Participant 5, Table 2). This not only reduces the quantity of protein for tryptic digestion and LC-MS/MS analysis, but also means that subsequent precipitation steps to remove SDS detergent may result in a more profound loss of sample relative to total protein content. While this proteomics protocol incorporates an element of single-pot processing to reduce sample loss via adsorption to pipette and vial surfaces, digested peptide samples are required to be transferred to LC-MS vials for drying and resuspension prior to analysis, which again can reduce sample yield. Together, it seems important to first optimise protein extractions to provide the greatest amount of material for further processing and analysis. All samples used for purposes of development were collected under this study's ethics (detailed in *section 3.2*).

To minimise introduction of detergent (SDS) which is non-compatible with MS analysis[19–22], the current protocol utilises 0.1% SDS and 100mM ammonium bicarbonate (ABC) to lyse cells with the aid of mechanical lysis (pipetting). To further solubilise proteins for extraction, DTT is added for the reduction of disulphide bonds under denaturing conditions (incubation at 50ºC for 45 minutes). As other current protocols for the analysis of low cell numbers have utilised Tris (2-carboxyethyl) phosphine (TCEP)) as a reducing agent opposed to DTT[23,24], the choice of reducing agent on protein concentrations was first assessed.

Use of TCEP (at equal concentration to DTT; 10mM) for sample preparation of CCR7+ cells (Participant 4, Table 2) resulted in an improvement in peptide yield of 50% and 59% at concentrations of 0.04 and 100µg/µl protein respectively (Figure 3), using the protocol outlined in section *3.21 Methods*. Such a drastic improvement in end peptide yield is surprising and use of TCEP poses other benefits, as a less toxic reagent that is not known to chemically inhibit the activity of any commonly employed alkylating reagent for proteomics sample preparation[25].

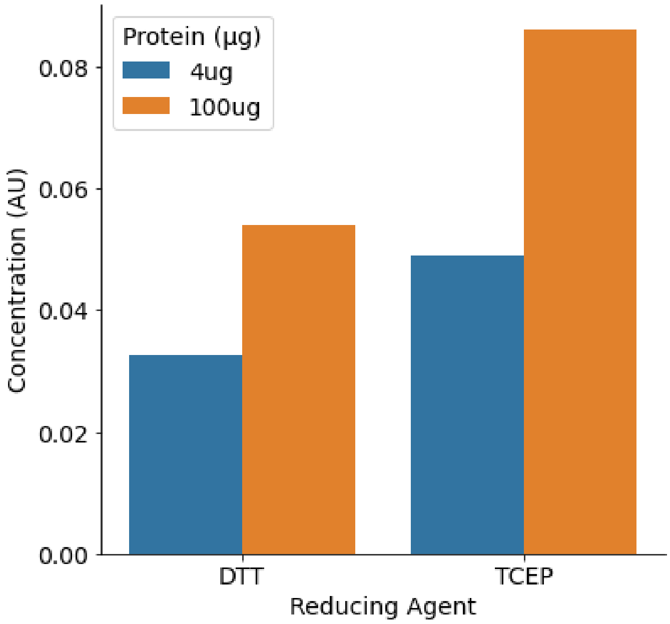

Figure 3: *Comparison of reducing agents, DTT and TCEP, on peptide concentrations (technical replicate samples from one participant). Concentrations are expressed as arbitrary units (AU).*

Within this protocol, improvements in sample yield were assessed at the peptide level, as loss of protein from acetone precipitation (during detergent clean-up) may impact respective concentrations and so protein was standardised following acetone precipitation prior to reduction and alkylation steps.

Sample protein concentration was quantified immediately after lysis and then following subsequent acetone precipitation. Surprisingly, protein concentrations were improved when assessed following sample clean-up with acetone by approximately 5-fold. This suggests that even the low level of SDS present within the extraction buffer (100mM ammonium bicarbonate, 0.1% SDS) is impacting protein quantification accuracy, as well as any standardisation across samples thereafter. While the downstream use of TCEP demonstrates a clear benefit in end peptide concentrations, it is unclear whether this is through improved protein yield or digestion efficiency, and this information is unlikely to be elucidated when applying this protocol due to the necessity for sample clean-up steps via acetone precipitation.

To assess the effects of TCEP as a reducing agent at the protein level, the proteomics sample preparation method, SPEED[26] was adopted (as detailed in *Chapter II, Section 2.1*). As this method of sample preparation has noted improved protein yields within a protocol that assesses protein concentrations following reduction of proteins with TCEP (albeit through measurements of turbidity at a different wavelength, 360nm), the apparent benefit of TCEP for proteomics sample preparation was confirmed according to SPEED's protocol, with the exception that IAA was retained as the alkylating reagent (opposed to CAA) in order to enable a comparison with the above protocol (Figure 3).

Following reduction with TCEP and alkylation with IAA, SPEED demonstrated a significant protein concentration of 7.1µg/µl in 1.21ml from CCR7+ cells (Participant 3, Table 2; Figure 4). Irrespective of potential losses following acetone precipitation, this protein concentration is far greater than any previously achieved with the protocol outlined in *section 3.21*, while additionally avoiding the use of MS-incompatible detergent, SDS and additional sample clean-up. For this reason, SPEED was taken forward for further development of proteomics sample processing.

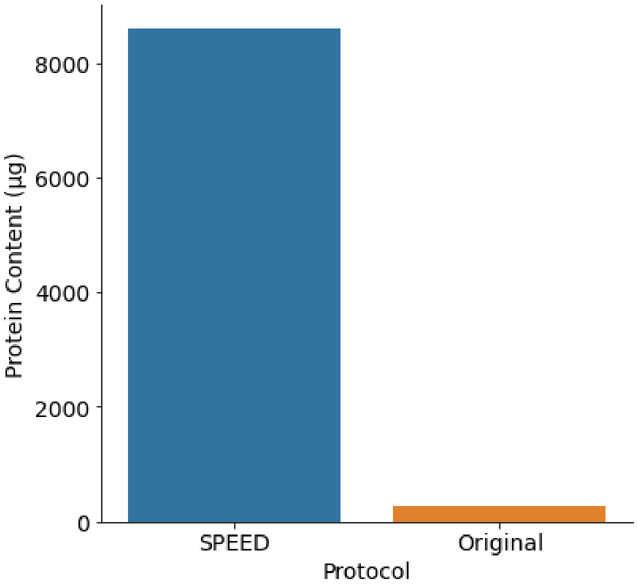

Figure 4: *Averaged comparisons of protein extractions following sample preparation with SPEED vs methods detailed in section* ***3.21*** *(technical replicates, n=3 per protocol). Concentration is expressed as protein content to account for differences in sample volumes. SPEED demonstrates ~33-fold increase in protein content, which extends to ~150-fold when data is normalised to cell numbers (not shown).*

Following confirmation of the benefits of TCEP reducing agent for protein extraction and processing, the impact of alkylating reagents on protein yield was next assessed. SPEED utilises chloroacetamide (CAA) opposed to the Iodoacetamide (IAA) implemented previously (Figure 4). To assess which alkylating agent was the most suitable, one sample (CD14+, Participant 3) was lysed according to SPEED's acidification approach, neutralised and then separated into six aliquots of lysate. Comparison of protein yield following reduction with TCEP and alkylation with IAA or CAA was performed in triplicate to assess the impacts of alkylating reagent on end protein yield (prior to tryptic digest). Figure 5 illustrates that IAA alkylation enabled an average 12-fold increase in protein concentration compared to CAA. These results are somewhat surprising, as there is no available data in the literature to suggest an interactive effect between TCEP and CAA that would inhibit either's activity. Of further interest, protein concentrations were also determined before reduction and alkylation; following cell lysis with trifluoroacetic acid and neutralisation with 2M tris base. It appears that reduction and alkylation with TCEP/IAA increased protein concentrations by ~12-fold but no change in protein concentrations occurred with TCEP/CAA. This may further support the potential for an interactional effect of TCEP reducing agent with CAA alkylating reagent, that does not occur with IAA (Figure 5). To confirm these observations, the experiment was repeated using replicates of the CCR7- cell type (Participant 3 and 4; n=4), which demonstrated the same response to alkylating reagents.

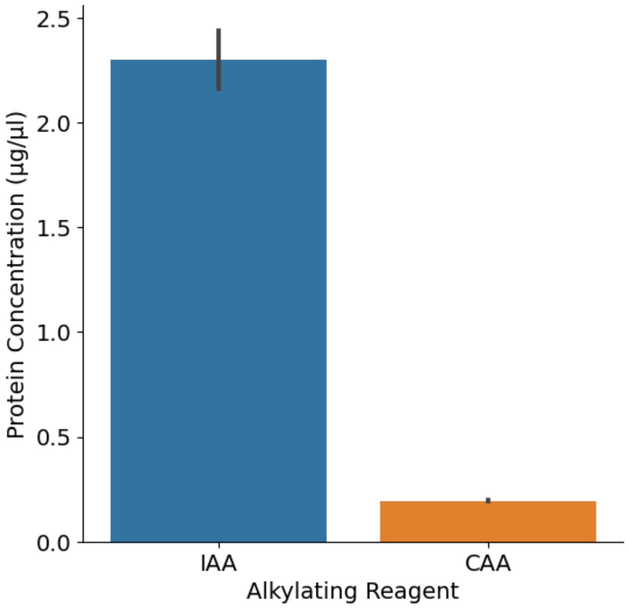

Figure 5: *Bar plot displaying effects of alkylating reagents; Iodoacetamide (IAA) and Chloroacetamide (CAA), on protein concentrations with SPEED sample preparation. Error bars represent standard deviation.*

Nanodrop spectrophotometers determine protein concentration through the absorbance of light from the aromatic amino residues: cysteine, tryptophan and tyrosine. As reducing agents target the disulphide bonds between cysteine residues within proteins, it is possible that protein concentrations appear amplified following reduction of these bonds and alkylation of these sites to prevent bond reformation, increasing absorbance at the wavelength 280nm (Nanodrop Lite Spectrophotometer, User Guide 2012, Thermo Scientific). Readings of protein concentration may therefore be related to increased absorbance and not protein concentration *per se*. However, the results of Figure 3 illustrated that improvements during reduction/alkylation translated to downstream increased estimates at the peptide level. As reduction and alkylation with SPEED occur under denaturing conditions (5 minutes at 95ºC) it is possible that the efficacy of these reactions is also subject to temperature[25]. Overall, these observed improvements in protein and peptide concentrations, as determined by a NanoDrop Lite Spectrophotometer (Thermo Scientific), seem indicative of improved proteomics processing within this protocol and illustrate SPEED's acidification-based approach for proteomics sample preparation to provide the greatest protein yield from the isolated immune cell populations contained within this study.

SPEED's protocol[26] relies on utilisation of the exothermic reaction of neutralisation to further optimise reduction and alkylation efficiency and protein solubilisation through denaturation. As experience applying this protocol for sample development progressed, further changes in protein extraction and processing were implemented. It was observed that increasing cell incubation time with TFA from 2-3 minutes to approximately 8 minutes, followed by extending denaturation via exothermic neutralisation with 2M Tris from immediate to 10 minutes prior to the subsequent reduction/alkylation (TCEP, IAA) of samples, further improved protein concentrations to an average of 10µg/µl in CD14+ cells, 9.3µg/µl in CCR7- cells and 8.4µg/µl in CCR7+ cells.

As these developments in sample processing were largely to facilitate reduced cell numbers and protein yields, the capacity for this protocol to extract and process protein from the least abundant samples of this study (indicated by * in Table 2) was tested. All parameters of sample handling and processing were as before, except that reduced volumes were utilised relative to a TFA lysis volume of 50µl, opposed to 100µl. The newly optimised application of SPEED for protein extraction and sample processing not only enabled sufficient protein yield from as low as ~3000 CD14- CD3+ CD45RO+ CCR7+ T-cells (Participant 6, timepoint 1), relative to cell numbers it operated more efficiently than with samples of higher cell counts (Figure 6). This successfully enabled a more than sufficient level of protein to be extracted from all low abundant samples collected under this study.

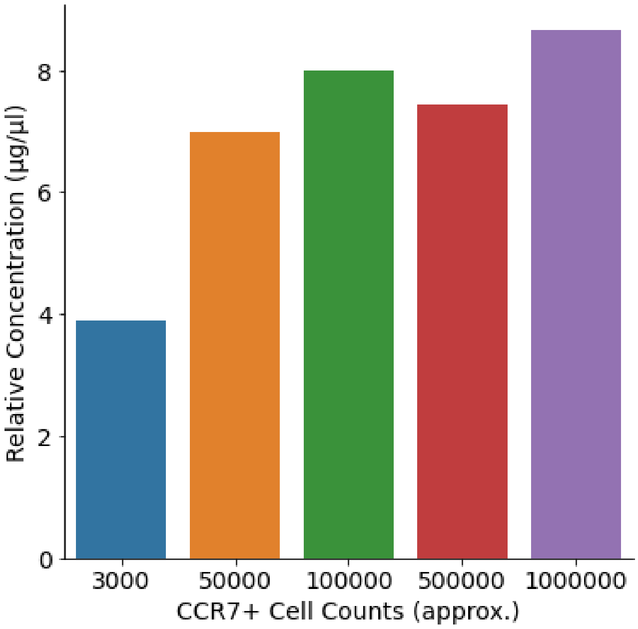

Figure 6: *Relative protein concentrations across low-high cell numbers for CCR7+ cell type. Samples used in analysis: participant 2, day 21; participant 6, day 0 and 21; participant 7, day 21; participant 8, day 42.*

It had previously been noted that application of this protocol to CD14+ monocytes, with cell counts ranging from 100,000s-1,000,000+, exhibited similar or occasionally decreased protein concentrations than either T-cell population with cell counts of 10,000s-100,000s. As SPEED utilises TFA for cell lysis, not only due to its ability to disrupt the cellular membrane to lyse cells, but also as it constitutes an excellent solvent for the solubilisation of cellular proteins, within the range of 40,000-1,000,000+ cells the same volume of TFA has been utilised for processing (100µl). It is therefore possible that the lysis and solubilisation of cellular protein is saturated at this volume in higher abundance samples, which from this pilot study appears to be at ~100,000 cells irrespective of cell type (Figure 6, other cell data not displayed). There was no further investigation to optimise the protein extraction of higher abundance samples, however, as protein concentrations were already well-sufficient for downstream processing.

3.65 Data Quality: Tryptic Digestion and Modifications

Previous implementation of proteomics sample preparation with SPEED in *section 2.2*, demonstrated a tryptic digest efficiency of ~93.7% in cultured macrophages (i.e. no missed cleavages with strict specificity; cleaved at K and R residues, not P), which represents an improvement over SPEED's publication[26] that exhibited ~77% of identified peptides to have no missed cleavage sites (albeit when applied across different cell types; HeLa, *E.Coli*, *B.Cereus* cells and mouse lung tissue). As SPEED recommends the dilution of samples prior to tryptic digest in order to reduce the molarity of salts, omitting further introduction of Tris salt during standardisation of protein samples prior to digestion (as performed in the SPEED protocol) was tested to investigate whether this had a positive effect on digestion efficiency. By additionally implementing a nano electrospray ionisation source, which demonstrates a higher tolerability to non-volatile salts such as Tris[27,28], it could be hypothesised that the reduction of Tris salt may negate the requirement for offline desalting via C18 columns (e.g. with C18 StageTips, Thermo Scientific), reducing sample handling and associated peptide losses.

In order for this to be feasible, all samples had to exhibit relatively homogenous protein extraction yields to maintain relative concentrations of enzyme and protein, which will invariably differ across samples even if the ratio of enzyme: protein (1: 100µg) is kept constant. By not standardising each sample aliquot of protein with Tris-trifluoroacetate solution (aka. sample dilution buffer; SPEED protocol[26]) prior to dilution with double-distilled water for tryptic digest, across samples (incl. all cell types) this would result in a relative protein concentration of ~1-2µg/µl during tryptic digestion. As previous implementation of this protocol (*section 2.2*) involved digestion by Trypsin at a concentration of 1µg/µl, it was important to additionally assess whether the consequent variability in protein and enzyme dilutions across samples impacted digestion reactions. By increasing protein yields through protocol optimisation (demonstrated above), direct sample dilution enabled for a reduction in sample processing volumes to <100µl (on average 60-65µl volumes). As tryptic digestion occurs under Michaelis-Menten kinetics[29], this alteration will increase substrate availability and may therefore result in improved digestion efficiency.

To test this, 0.5/2/5µg peptides from CCR7- samples (Participant 8, timepoint 4) were injected into a LTQ Orbitrap XL (Thermo Scientific) mass spectrometer in line with an EASY-nLC 1000 ultra-high pressure liquid chromatography system and EASY-Spray nano electro spray ionisation (nESI) source (Thermo Scientific). Peptides were loaded onto a pre-column (C18 Pepmap100 5mm x 5um), prior to separation on a 50cm analytical column (C18, 5um, 50cm, 100 A^0 Easy nano spray column #ES903, Thermo Scientific) at a flow rate of 250nl/min. A non-linear gradient of solvent B (80% ACN (v/v) in 0.1% FA (v/v)) was applied for a total gradient time of 69 minutes and total run time of 96 minutes. Data were acquired in data-dependent acquisition (DDA) mode. Full MS scans were acquired at 60,000 resolution m/z 200 measured using an orbitrap mass analyser, within a mass range of 400-1600 m/z. The top 12 precursor ions were selected with an isolation window of 2 m/z units for fragmentation via CID at a normalised collision energy of 35. MS2 spectra were acquired at a resolution of 17,500 m/z 200 with the Orbitrap mass analyser and a dynamic exclusion duration of 180 seconds.

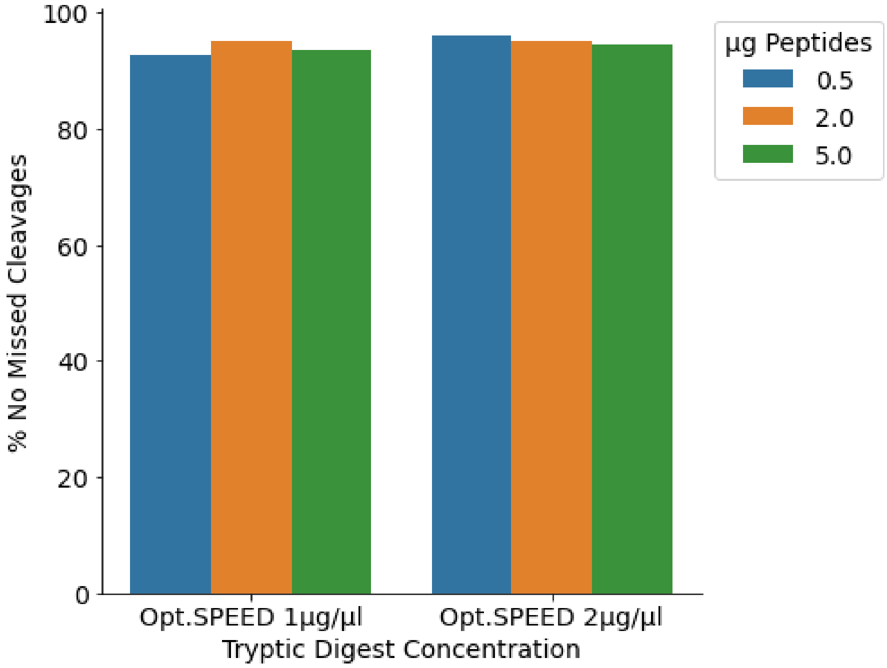

Figure 7: *Tryptic digest efficiency of CCR7- cell type across two protein concentrations and loading conditions for mass spectrometry analysis (Participant 8, timepoint 4).*

Figure 7 demonstrates an average tryptic digestion efficiency of 93.9% (1µg/µl) and 95.3% (2µg/µl) identified peptides with no missed cleavage sites, maintaining an improvement over rates demonstrated in SPEED's publication[26], with a minor increase over previous application with cultured macrophages (*section 2.2*). Importantly, there was no difference between digests conducted under the protein concentrations ~1µg/µl vs ~2µg/µl over triplicate sample injections at three different peptide amounts (Figure 7, paired t-test $p>0.05$). This enabled MS analysis without offline desalting (as performed in SPEED and *section 2.2)*, while reducing sample processing volumes to maximise sample recovery.

The effects of sample preparation on rates of peptides identified through modifications (Methionine oxidation, protein N-terminal acetylation and combinations/multiple sites) were also assessed (Figure 8). Mass spectrometry analysis demonstrated modified peptides to constitute <6% of total identified peptides (combined across both protein concentrations; 1µg/µl and 2µg/µl), an improvement over both the modification rates published with SPEED[26] (which presented an average of ~80% unmodified peptides relative to total) and those previously observed in *section 2.2*. This demonstrates that protocol optimisation of sample processing provides direct benefits for data quality, specifically tryptic digest activity and reduced rates of modified peptides. Furthermore, this data demonstrates sample concentrations of up to 2µg/µl protein to not impact these results (paired t-test, $p>0.05$).

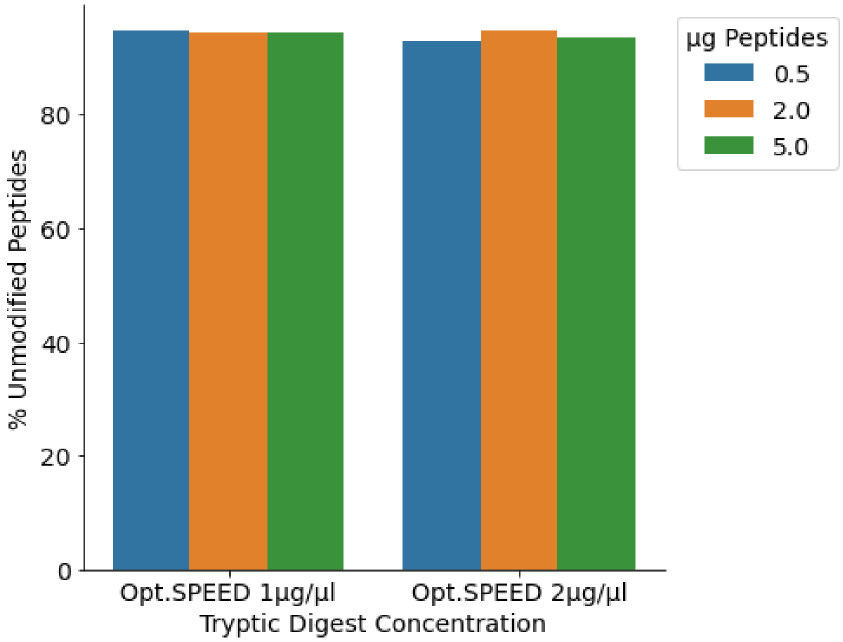

Figure 8: *Triplicate measurements across peptide loads (0.5, 2 and 5 µg) for peptides identified via modifications encompassing Acetylation of the protein N-terminal or Methionine oxidation, for CCR7- samples digested under 1 or 2µg/µl protein concentrations. Paired t-test demonstrated no statistical significance between treatments.*

Finally, it was assessed whether together these alterations to proteomics sample preparation translated to improved identification rates for peptides and proteins, a problem previously identified in *section 3.23*. Identification rates from these samples are depicted in Figure 9.

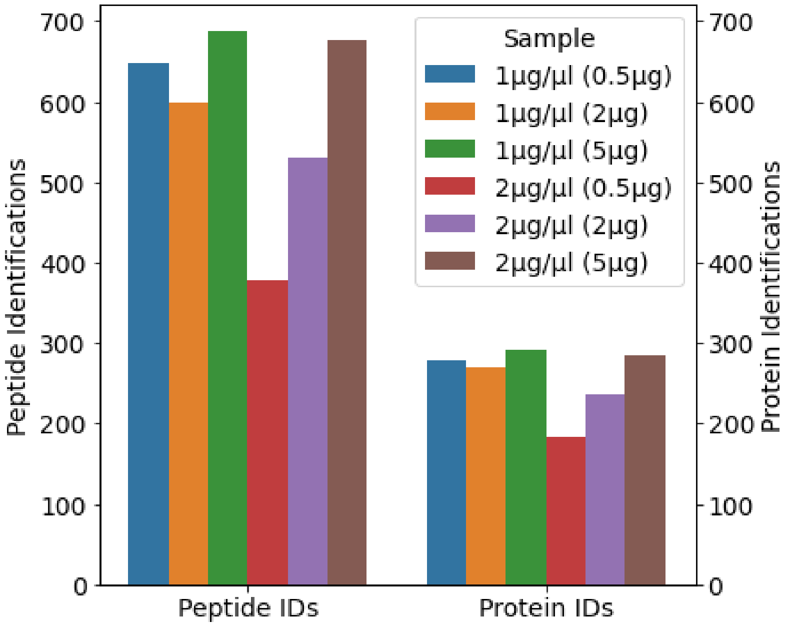

Figure 9: *Peptide and protein identifications from CCR7- sample digested at two different protein concentrations and triplicate measurements at three peptide quantities.*

Figure 9 demonstrates identifications up to approximately 700 peptides and 300 proteins with mass spectrometry analysis. Protein identifications are approximately three times greater than those achieved previously in a similar cell type (CCR7+)

within this thesis using alternate methods (*section 3.23*). Analysis of 5µg peptide quantities provided the greatest rates of peptide and protein identifications, with little difference observed between 1µg/µl and 2µg/µl protein digests at this peptide load. However, there were increased peptide and protein identifications at the lower peptide quantities of 0.5 and 2µg for 100µg protein digests. While there was no indication of this disparity at the level of data quality (% fully cleaved peptides), there is a clear pattern for improved peptide and protein identifications at the lower peptide loads of 0.5 and 2µg (Figure 9, however, neither peptide nor protein identification rates between treatments reached statistical significance: paired t-test, $p>0.2$; albeit this is likely influenced by high data variability from identifications across loading conditions further reducing statistical power with only triplicate measurements).

This data was generated from a CCR7- sample of Participant 8 collected at day 14 of the deuterium-loading protocol (Table 2). As such, it would be expected that peptides (and therefore proteins) identified at this stage will be enriched with deuterium. Applying a shorter analytical gradient of 96 minutes than previously (*section 3.21)* and based on identification rates in FACs cell types published elsewhere[6], these peptide and protein identifications are acceptable for downstream analysis of deuterium-incorporation to model protein turnover within this pilot study. From these results, 100µg protein digests and 5µg peptide loads were selected as optimal for proteomics analysis within the remainder of the study.

3.7 REFERENCES

1. Watson, P. E., Watson, I. D. & Batt, R. D. Total body water volumes for adult males and females estimated from simple anthropometric measurements. *Am. J. Clin. Nutr.* **33**, 27–39 (1980).
2. Disher, A. E., Stewart, K. L., Bach, A. J. E. & Stewart, I. B. Contribution of Dietary Composition on Water Turnover Rates in Active and Sedentary Men. *Nutrients* **13**, 2124 (2021).
3. Money, K. E. & Myles, W. S. Heavy water nystagmus and effects of alcohol. *Nature* **247**, 404–405 (1974).
4. Yang, D. *et al.* Assay of Low Deuterium Enrichment of Water by Isotopic Exchange with [U-13C3]Acetone and Gas Chromatography–Mass Spectrometry. *Anal. Biochem.* **258**, 315–321 (1998).
5. Hennrich, M. L. *et al.* Cell-specific proteome analyses of human bone marrow reveal molecular features of age-dependent functional decline. *Nat. Commun.* **9**, 4004 (2018).
6. Maes, E., Cools, N., Willems, H. & Baggerman, G. FACS-Based Proteomics Enables Profiling of Proteins in Rare Cell Populations. *Int. J. Mol. Sci.* **21**, E6557 (2020).
7. Rørvig, S., Østergaard, O., Heegaard, N. H. H. & Borregaard, N. Proteome profiling of human neutrophil granule subsets, secretory vesicles, and cell membrane: correlation with transcriptome profiling of neutrophil precursors. *J. Leukoc. Biol.* **94**, 711–721 (2013).
8. Sallusto, F., Lenig, D., Förster, R., Lipp, M. & Lanzavecchia, A. Two subsets of memory T lymphocytes with distinct homing potentials and effector functions. *Nature* **401**, 708–712 (1999).

9. Jameson, S. C. & Masopust, D. Understanding Subset Diversity in T Cell Memory. *Immunity* **48**, 214–226 (2018).

10. Wang, Y. *et al.* A novel mechanism linking memory stem cells with innate immunity in protection against HIV-1 infection. *Sci. Rep.* **7**, 1057 (2017).

11. Moaaz, M., Youssry, S., Baess, A., Abed, A. & Moaaz, M. Immune signature of CCR7+ central memory T cells associates with disease severity and Immunoglobulin E in bronchial asthma. *Eur. Ann. Allergy Clin. Immunol.* **53**, 115–127 (2021).

12. Kwiecień, I. *et al.* Effector Memory T Cells and CD45RO+ Regulatory T Cells in Metastatic vs. Non-Metastatic Lymph Nodes in Lung Cancer Patients. *Front. Immunol.* **13**, (2022).

13. Kelly, R. T. Single-cell Proteomics: Progress and Prospects. *Mol. Cell. Proteomics MCP* **19**, 1739–1748 (2020).

14. Sadygov, R. G. Protein turnover models for LC–MS data of heavy water metabolic labeling. *Brief. Bioinform.* **23**, bbab598 (2022).

15. Deberneh, H. M. & Sadygov, R. G. Software Tool for Visualization and Validation of Protein Turnover Rates Using Heavy Water Metabolic Labeling and LC-MS. *Int. J. Mol. Sci.* **23**, 14620 (2022).

16. Ahmed, R. *et al.* CD57+ Memory T Cells Proliferate In Vivo. *Cell Rep.* **33**, 108501 (2020).

17. Ladell, K. *et al.* Central memory CD8+ T cells have a shorter lifespan and reduced abundance as a function of HIV disease progression. *J. Immunol. Baltim. Md 1950* **180**, 7907–7918 (2008).

18. Patel, A. A. *et al.* The fate and lifespan of human monocyte subsets in steady state and systemic inflammation. *J. Exp. Med.* **214**, 1913–1923 (2017).

19. Loo, R. R., Dales, N. & Andrews, P. C. Surfactant effects on protein structure examined by electrospray ionization mass spectrometry. *Protein Sci. Publ. Protein Soc.* **3**, 1975–1983 (1994).

20. Loo, R. R., Dales, N. & Andrews, P. C. The effect of detergents on proteins analyzed by electrospray ionization. *Methods Mol. Biol. Clifton NJ* **61**, 141–160 (1996).

21. Rundlett, K. L. & Armstrong, D. W. Mechanism of signal suppression by anionic surfactants in capillary electrophoresis-electrospray ionization mass spectrometry. *Anal. Chem.* **68**, 3493–3497 (1996).

22. Danko, K., Lukasheva, E., Zhukov, V. A., Zgoda, V. & Frolov, A. Detergent-Assisted Protein Digestion—On the Way to Avoid the Key Bottleneck of Shotgun Bottom-Up Proteomics. *Int. J. Mol. Sci.* **23**, 13903 (2022).

23. Schoof, E. M. *et al.* Quantitative single-cell proteomics as a tool to characterize cellular hierarchies. *Nat. Commun.* **12**, 3341 (2021).

24. Phlairaharn, T. *et al.* High Sensitivity Limited Material Proteomics Empowered by Data-Independent Acquisition on Linear Ion Traps. *J. Proteome Res.* **21**, 2815–2826 (2022).

25. Evans, C. A. Reducing Complexity? Cysteine Reduction and S-Alkylation in Proteomic Workflows: Practical Considerations. *Methods Mol. Biol. Clifton NJ* **1977**, 83–97 (2019).

26. Doellinger, J., Schneider, A., Hoeller, M. & Lasch, P. Sample Preparation by Easy Extraction and Digestion (SPEED) - A Universal, Rapid, and Detergent-free Protocol for Proteomics Based on Acid Extraction. *Mol. Cell. Proteomics MCP* **19**, 209–222 (2020).

27. Juraschek, R., Dülcks, T. & Karas, M. Nanoelectrospray--more than just a minimized-flow electrospray ionization source. *J. Am. Soc. Mass Spectrom.* **10**, 300–308 (1999).

28. Wilm, M. Principles of Electrospray Ionization. *Mol. Cell. Proteomics MCP* **10**, M111.009407 (2011).

29. Michaelis, L., Menten, M. L., Johnson, K. A. & Goody, R. S. The original Michaelis constant: translation of the 1913 Michaelis-Menten paper. *Biochemistry* **50**, 8264–8269 (2011).

30. Cox, J. *et al.* Andromeda: a peptide search engine integrated into the MaxQuant environment. *J. Proteome Res.* **10**, 1794–1805 (2011).

31. Cox, J. *et al.* Accurate Proteome-wide Label-free Quantification by Delayed Normalization and Maximal Peptide Ratio Extraction, Termed MaxLFQ. *Mol. Cell. Proteomics MCP* **13**, 2513–2526 (2014).

32. Naylor, B. C. *et al.* DeuteRater: a tool for quantifying peptide isotope precision and kinetic proteomics. *Bioinformatics* **33**, 1514–1520 (2017).

33. Davidsson, L. Introduction to Body Composition Assessment Using the Deuterium Dilution Technique with Analysis of Saliva Samples by Fourier Transform Infrared Spectrometry: IAEA Human Health Series No. 12. *Introd. Body Compos. Assess. Using Deuterium Dilution Tech. Anal. Saliva Samples Fourier Transform Infrared Spectrom. IAEA Hum. Health Ser. No 12* (2010).

34. Neese, R. A. *et al.* Measurement in vivo of proliferation rates of slow turnover cells by 2H2O labeling of the deoxyribose moiety of DNA. *Proc. Natl. Acad. Sci. U. S. A.* **99**, 15345–15350 (2002).

35. Hellerstein, M. K. *et al.* Subpopulations of long-lived and short-lived T cells in advanced HIV-1 infection. *J. Clin. Invest.* **112**, 956–966 (2003).

36. Wherry, E. J. T cell exhaustion. *Nat. Immunol.* **12**, 492–499 (2011).

37. Grossman, Z., Meier-Schellersheim, M., Sousa, A. E., Victorino, R. M. M. & Paul, W. E. CD4+ T-cell depletion in HIV infection: Are we closer to understanding the cause? *Nat. Med.* **8**, 319–323 (2002).

38. Brunner, A. *et al.* Ultra-high sensitivity mass spectrometry quantifies single-cell proteome changes upon perturbation. *Mol. Syst. Biol.* **18**, e10798 (2022).

39. Lau, E. *et al.* A large dataset of protein dynamics in the mammalian heart proteome. *Sci. Data* **3**, 160015 (2016).

40. Kim, T.-Y. *et al.* Metabolic Labeling Reveals Proteome Dynamics of Mouse Mitochondria. *Mol. Cell. Proteomics MCP* **11**, 1586–1594 (2012).

41. Lam, M. P. Y. *et al.* Protein kinetic signatures of the remodeling heart following isoproterenol stimulation. *J. Clin. Invest.* **124**, 1734–1744 (2014).

4. DEUTERIUM BRAIN IMAGING AT 7T DURING DEUTERIUM-OXIDE DOSING

Published as a full-text article in *Magnetic Resonance in Medicine, 89(4):1514-1521.*, April 2023.

ABSTRACT

Purpose: To characterize the (^{2}H) deuterium MR signal measured from human brain at 7T in participants loading with D_2O to ˜1.5% enrichment over a six-week period.

Methods: ^{2}H spectroscopy and imaging measurements were used to track the time-course of ^{2}H enrichment within the brain during the initial eight-hour loading period in two participants. Multi-echo gradient echo (MEGE) images were acquired at a range of TR values from four participants during the steady-state loading period and used for mapping ^{2}H T_1 and T_2 * relaxation times. Co-registration to higher resolution ^{1}H images allowed T_1 and T_2 * relaxation times of deuterium in HDO in cerebrospinal fluid (CSF), gray matter (GM), and white matter (WM) to be estimated.

Results: ^{2}H concentrations measured during the eight-hour loading were consistent with values estimated from cumulative D_2O dose and body mass. Signal changes measured from three different regions of the brain during loading showed similar time-courses. After summing over echoes, gradient echo brain images acquired in 7.5 minutes with a voxel volume of 0.36 ml showed an SNR of ˜16 in subjects loaded to 1.5%. T_1 -values for deuterium in HDO were significantly shorter than corresponding values for ^{1}H in H_2O, while T_2 * values were similar. ^{2}H relaxation times in CSF were significantly longer than in GM or WM.

Conclusion: Deuterium MR measurements at 7T were used to track the increase in concentration of ^{2}H in brain during heavy water loading. ^{2}H T_1 and T_2 * relaxation times from water in GM, WM, and CSF are reported.

Keywords: D_2O loading; MEGE; deuterium (^{2}H); heavy water; human brain; relaxation times.

4.1 INTRODUCTION

The low natural abundance (˜0.015%) and gyromagnetic ratio (6.54 MHz/T) of deuterium (^{2}H) reduce the available NMR signal compared to ^{1}H. However, the shorter longitudinal relaxation times of ^{2}H allow faster signal averaging, partially compensating for the reduction in SNR associated with the reduced signal strength. The minimal equipment modifications required for implementing ^{2}H imaging and the simplicity of the pulse sequences that can be used, mean that ^{2}H imaging has significant potential for use in clinical applications. This has led to an increasing interest in the use of deuterium magnetic resonance in conjunction with injection or ingestion of ^{2}H-labeled compounds, as a means of monitoring cellular metabolism [1, 2, 3].

Deuterium metabolic imaging (DMI) involves using ^{2}H chemical shift imaging to map the distribution of the metabolic products of administered ^{2}H-labeled compounds. The majority of experiments in humans and animals have used [6,6′-D_2] glucose [2, 3, 4, 5, 6, 7, 8, 9, 10, 11, 12, 13, 14, 15, 16]. In this case, lactate and glutamine/glutamate (Glx) are produced alongside deuterated water (HDO), and their relative concentrations reflect the cells' preference for glucose metabolism, i.e., aerobic, anaerobic glycolysis or oxidative phosphorylation. Spatially localized, elevated, lactate production has been observed using DMI in a patient with a glioblastoma, [2] in keeping with an increased glycolysis in neoplastic cells, known as the Warburg effect [17].

DMI can provide spatially resolved measurements of metabolite concentrations and pathway fluxes, [1, 4] but this often requires knowledge of the local relaxation times of the ^{2}H signals from metabolites. The signal from naturally abundant HDO can be used in calculating absolute concentrations of other metabolites. Therefore, knowledge of the relaxation times of HDO in different tissues is important for quantitative measurements. Previous measurements of HDO relaxation times in human participants have used non-localized signals [2, 3, 11] which do not allow the variation of relaxation times across regions and compartments to be evaluated.

Oral intake of heavy water is commonly used for assessment of body composition [18] and is increasingly being applied in studies of triglyceride synthesis [19] and protein turnover [20, 21, 22]. These approaches generally involve analysis of body fluid samples or tissue biopsies. However, ^{2}H magnetic resonance allows direct, non-invasive, measurement of the concentration of HDO, deuterated lipids, and other metabolic products of ^{2}H labelled water and so could complement invasive measurements. The feasibility of imaging the distribution of HDO in the body following oral ingestion of D2O was demonstrated in animal experiments carried out in the 1980 s, [23, 24, 25, 26, 27] but has not yet been performed in humans.

Here, we implemented deuterium MRI at 7T and used it to characterize HDO signals from the human brain in four healthy participants who increased their deuterated water content to ˜1.5% for a six-week period by drinking D2O. The heavy water loading was carried out as part of a parallel study.

4.2 METHODS

Six healthy participants took part in this ^{2}H-imaging sub-study which was approved by the local institutional ethics committee with the volunteers giving informed consent. Two participants were scanned during a set-up phase in which we established the feasibility of ^{2}H imaging and identified favourable imaging parameters. Here, we report data from four participants (A-D) who were subsequently scanned using the optimized imaging protocols on a 7T Achieva scanner (Philips Healthcare), operating at 45.8 MHz for ^{2}H. A 26.4-cm-inner-diameter, dual-tuned ^{1}H/^{2}H birdcage coil (Rapid Biomedical) was used for deuterium measurements, while the standard, 32-channel Rx/2-channel Tx head coil (Nova Medical) was used for acquiring anatomical ^{1}H images.

The parallel study required an initial loading regime in which the targeted enrichment was built up in around eight hours. This involved the participants drinking between 12 and 16, ˜50 ml doses of 70% D2O/30% H2O (one dose every ˜30 minutes), with the total amount of D2O consumed adjusted according to the participant's body weight to produce 1.5% enrichment. Participants subsequently drank ˜50 ml of D2O each morning over the six-week study period to maintain 1.5% enrichment. Similar enrichment levels and durations have been used in recent studies [28, 29, 30] with no adverse events reported, however some participants experienced a brief period of dizziness during the initial loading phase due to the rapid rise in body water enrichment [28]. Saliva samples were collected from participants at regular intervals during the study and analysed using gas chromatography–mass spectrometry (GC-MS) [31] *(as previously described in Chapter II, section 3.2)*.

Two participants (A and B) were scanned during the initial eight-hour loading period to monitor the time-course of deuterated water concentration changes in the brain. A scanning protocol of ˜15 minutes duration was performed before dosing and after 30, 90, 150, 210, 270, 360, 420, and 540 minutes. The protocol comprised a ^{1}H scout scan for planning, followed by acquisition of ^{2}H pulse-acquire spectra from the whole head and from a 2-cm-thick axial slice positioned over the lateral ventricles. Both used the following scan parameters: flip angle $\alpha = 90°$, 2048 samples, bandwidth (BW) = 3000 Hz, repetition time TR = 1 s and 64 averages (scan time, Tscan = 64 s). We then acquired axial, 3D MEGE ^{2}H images (20 averages, Tscan = 453 s, FOV = 288 × 288× 80 mm3, 6 × 6 × 10 mm3 voxels, $\alpha = 33°$, TR = 62 ms, five echoes, TE1 = 8.9 ms and ΔTE = 8.4 ms). Axial ^{1}H 3D GE images (Tscan = 232 s, 32 slices, FOV = 288 × 288 × 80 mm3, 3 × 3 × 2.5 mm3 voxels, TE = 5.9 ms, TR = 39 ms) were also acquired. This scanning protocol was repeated 17 days after the initial loading to provide comparative data at steady-state enrichment. The spectroscopy measurements made before loading provided an estimate of the signal from naturally abundant deuterium in water: scaling subsequent measurements then allowed the absolute HDO concentration to be estimated at each time-point. The HDO concentration in the body was also estimated from the ratio of the total imbibed D2O volume to an estimate of total body water [32].

We used the image data to track the changes in ^{2}H signal from different tissue compartments. The ^{2}H images acquired at each time-point were summed over the five echoes, and regions of interest (ROI) were then formed for a background region, general brain tissue, the lateral ventricles and for a region of high signal intensity thought to arise from blood vessels and CSF in the superior cistern. The SNR in images acquired before loading was too low to make good estimates of natural abundance signals, so values were normalized to the signal measured in the superior cistern ROI at the last time point of the initial loading period.

^{2}H relaxation times for water in CSF, GM, and WM were calculated from data acquired during the six-week loading period using the dual-tuned ^{2}H/^{1}H coil. In each session, we acquired ^{2}H 3D sagittal MEGE images (voxels = 6 × 6 × 10 mm3, FOV = 288 × 288 × 240 mm3, slices = 24) at a range of TR values, along with ^{1}H 3D MEGE images (voxels = 3 ×3 × 5 mm3, FOV = 288 × 288 × 240 mm3, slices = 48, 15 echo times with TE1 = 2.5 ms, ΔTE = 2.34 ms, and TR = 41 ms). ^{2}H MEGE data from Participants A and B were acquired with five echoes (TE1 = 4.3 ms, ΔTE = 8.4 ms), α = 60°, and TR = 68, 136, 272, 544 ms, with 8, 4, 2, and 1 averages, so that Tscan = 487 s per image. ^{2}H MEGE data from participants C and D were acquired with six echoes (TE1 = 4.3 ms, ΔTE = 8.4 ms) and one additional TR-value (TR = 816 ms, one average, Tscan = 730 s). The number of TE and TR values were increased to improve fitting quality. The ^{2}H scanning sessions were performed twice on Participants C and D.

We also acquired ^{1}H MPRAGE images (0.7 mm resolution) and ^{1}H 3D MEGE images (3 × 3 × 5 mm3 voxels, 15 echo times, TE1 = 2.5 ms, ΔTE = 2.57 ms, and TR = 41 ms) from each participant in a separate scanning session using the Nova coil. These images were used for image segmentation and estimation of the ^{1}H T2 * values.

For calculation of maps of ^{2}H relaxation rate constants R1 and R2 *, we first estimated the variation of flip angle (α) over the image volume by summing the images across TEs, at each TR, and fitting the data voxel-wise to a saturation recovery curve (i.e., fitting signal variation with TR for α, R1, and signal amplitude). The resulting flip-angle maps were smoothed by averaging over 5 × 5 × 5 voxel neighbourhood and the α-values then used as fixed parameters in dual-fitting the variation in signal intensity Si,j across TRi and TEj values for R1, R2 * and signal amplitude, A. This involved minimisation of

$$\sum_{i=1}^{n_{\mathrm{TR}}}\sum_{j=1}^{n_{\mathrm{TE}}}\left\|\frac{A\sin\alpha(1-\exp(-R_1\,\mathrm{TR_i}))}{1-\cos\ \alpha\ \exp(-R_1\,\mathrm{TR}_i)} * \exp(-R_2^*\,\mathrm{TE_j})-S_{i,j}\right\|^2 \tag{1}$$

using the Matlab *fmincon* command. ^{1}H R2 * maps were obtained by similar fitting to the exponential signal decay with TE in the ^{1}H MEGE data acquired using the Nova coil.

To evaluate the relaxation times in different compartments, we segmented the ^{1}H MPRAGE data (FSL FAST [33]) and transformed the resulting GM, WM, and CSF masks to the space of the ^{2}H relaxation time maps. Following brain extraction (FSL

BET [34]) and bias field correction, an affine matrix was obtained from image co-registration (FSL FLIRT [35, 36]) that transformed the ^{1}H MEGE data acquired using the Rapid Biomedical coil to the space of the ^{1}H MEGE Nova Medical coil data, along with an affine matrix for the ^{1}H MEGE to MPRAGE transformation. The MEGE data were summed across echoes and repetition times before co-registration.

The brain-extracted MPRAGE image was segmented to create binary masks for GM, WM, and CSF using FSL FAST [33]. These masks were transformed to the ^{2}H space using the previously obtained affine matrices and the outer regions of the CSF mask were manually removed so that the majority of the mask comes from the lateral ventricles. The new masks were applied to the relaxation maps for calculation of mean relaxation times for CSF, GM, and WM.

4.3 RESULTS

Figure 1 shows example ^{2}H image data obtained during the steady-state loading period. Figure 1A shows 3D sagittal image data produced by summing the MEGE data over TE and TR values. The resulting images clearly depict the brain anatomy and have a similar appearance to T2 *-weighted, ^{1}H-images. The CSF in the ventricles and at the cortical surface appears hyperintense, while regions where there is little partial-voluming with CSF, such as the white matter in the corpus callosum, appear hypointense. Figure 1B shows the variation of image intensity with TE and TR in a central sagittal slice. The slower T2 * decay of the CSF signal compared with that of the GM and WM signals is evident, along with the signal saturation at reduced TR, and the reduction of contrast at low TE and TR values.

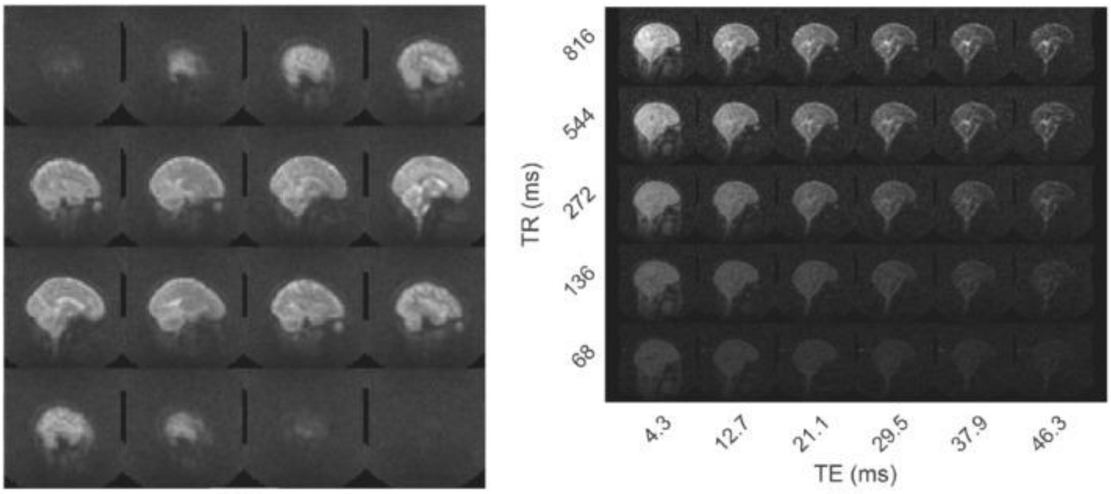

(A) (B)

Figure 1: *(A) 3D MEGE ^{2}H image data from Participant C. Images produced by summing over six TE values and five TR values. (B) 3D MEGE ^{2}H image from one slice from Participant D. Images are displayed with TE value varying horizontally and TR-value varying vertically. Voxel size = 6 × 6 × 10 mm^3, FOV = 288 × 288 mm^2 in data used for both sub-figures.*

Figure 2 shows maps of the relaxation rate constants from two participants, with the dominant feature in the ^{2}H maps being the reduced R2 * and R1 values in the ventricles. Table 1 reports the average and SDs of the ^{2}H T1 and T2 * values, along with ^{1}H T2 * values measured in GM, WM, and CSF in the four participants.

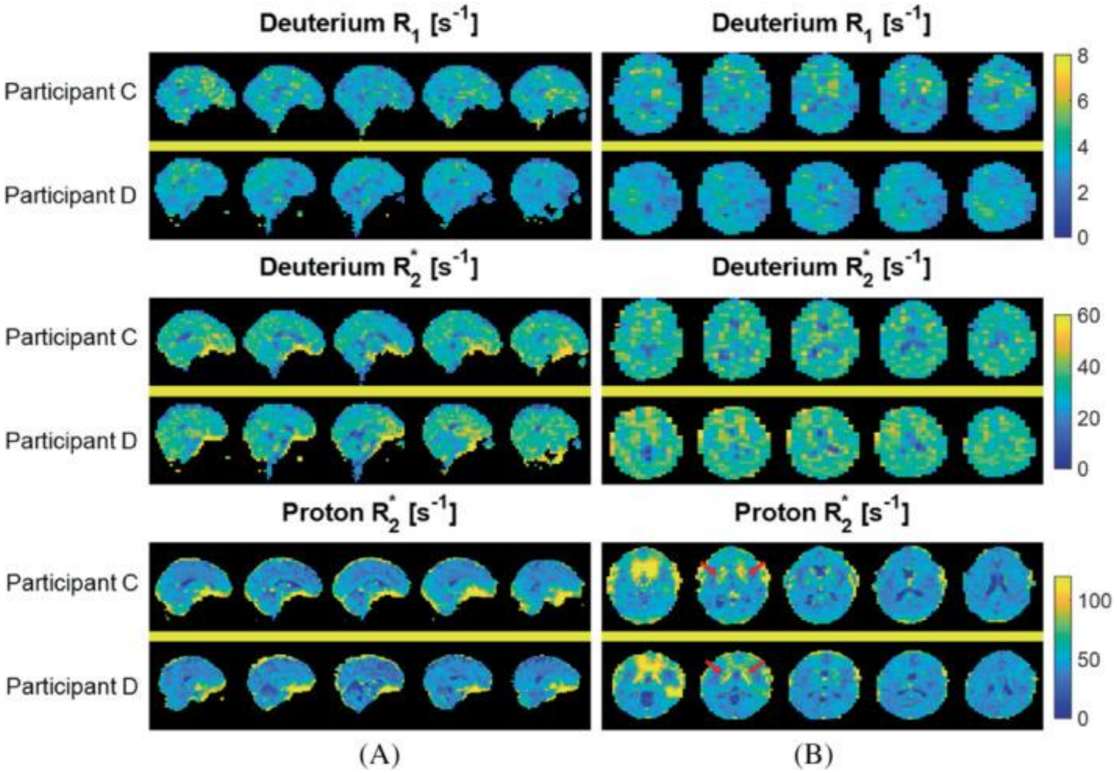

Figure 2: *^{2}H $R_2{}^*$ and R_1 maps are shown along with ^{1}H $R_2{}^*$ maps in sagittal (A) and axial (B) format. Maps show five central slices from Participants C and D. Relaxation maps were calculated from MEGE data equivalent to that displayed in Figure 1. The elevated $R_2{}^*$ in iron-rich deep GM structures is evident in the lower slices of the ^{1}H maps (red arrows), but is not seen in the ^{2}H maps. The images shown have a reduced FOV of 204 × 204 mm^2.*

TABLE 1

Average and SD of ^{2}H (T_2^* and T_1) and ^{1}H (T_2^*) relaxation times in CSF, GM, and WM for different participants and visits.

		Deuterium relaxation times [ms]						Proton relaxation times [ms]		
		CSF		**GM**		**WM**		**CSF**	**GM**	**WM**
Subject	**Visit**	**T_1**	**T_2^***	**T_1**	**T_2^***	**T_1**	**T_2^***	**T_2^***	**T_2^***	**T_2^***
A	**1**	450 ± 200	110 ± 90	280 ± 100	32 ± 8	260 ± 100	30 ± 10	106 ± 90	26 ± 20	27 ± 20
B	**1**	520 ± 200	83 ± 50	300 ± 100	33 ± 10	280 ± 100	32 ± 20	103 ± 90	25 ± 20	23 ± 10
C	**1**	460 ± 100	76 ± 40	301 ± 80	31 ± 7	290 ± 100	30 ± 10	93 ± 100	22 ± 10	21 ± 6
C	**2**	390 ± 100	82 ± 60	295 ± 90	32 ± 8	267 ± 90	32 ± 10			
D	**1**	720 ± 200	84 ± 50	420 ± 100	31 ± 6	350 ± 100	28 ± 6	87 ± 90	23 ± 10	22 ± 8
D	**2**	510 ± 100	110 ± 40	320 ± 80	31 ± 6	277 ± 80	28 ± 6			
Mean		510	90	320	32	290	30	97	24	23
SD		100	10	50	1	30	1	5	2	2

Note: *These values were produced by averaging over segmented relaxation time maps, similar to those shown in Figure 2. Average values and SDs across participants are also shown.*

Figure 3 reports example ^{2}H images acquired from Participants A and B during the loading process. The different regions of interest in which the signal changes were tracked are indicated on Figure 4A (for Participant A) and Figure 4B shows the time courses from the different ROIs, along with the steady-state values measured after 17 days of loading. Figure 4C plots the temporal variation of the absolute ^{2}H concentration estimated from the spectroscopy measurements. The concentration calculated from the cumulative D_2O dose and estimated total body water volume is shown for comparison.

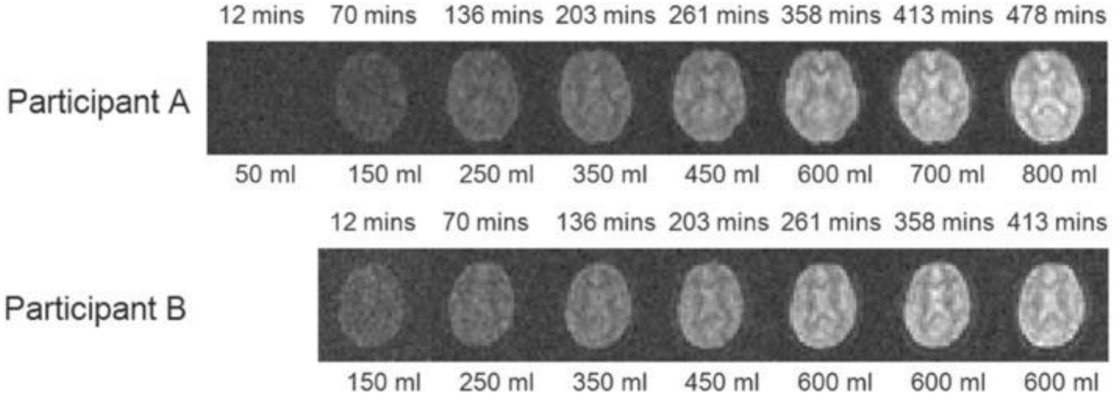

Figure 3: *^{2}H images acquired from two participants at different times during the initial, 8-h heavy water loading period. The time since the first dose is indicated above each image and the cumulative dose of heavy water is indicated below. A single axial slice spanning the lateral ventricles is shown. The images shown are formed from the average over five echoes (TE_1 = 8.9 ms, ΔTE = 8.4 ms). The images shown have a reduced FOV of 204 × 204 mm^2.*

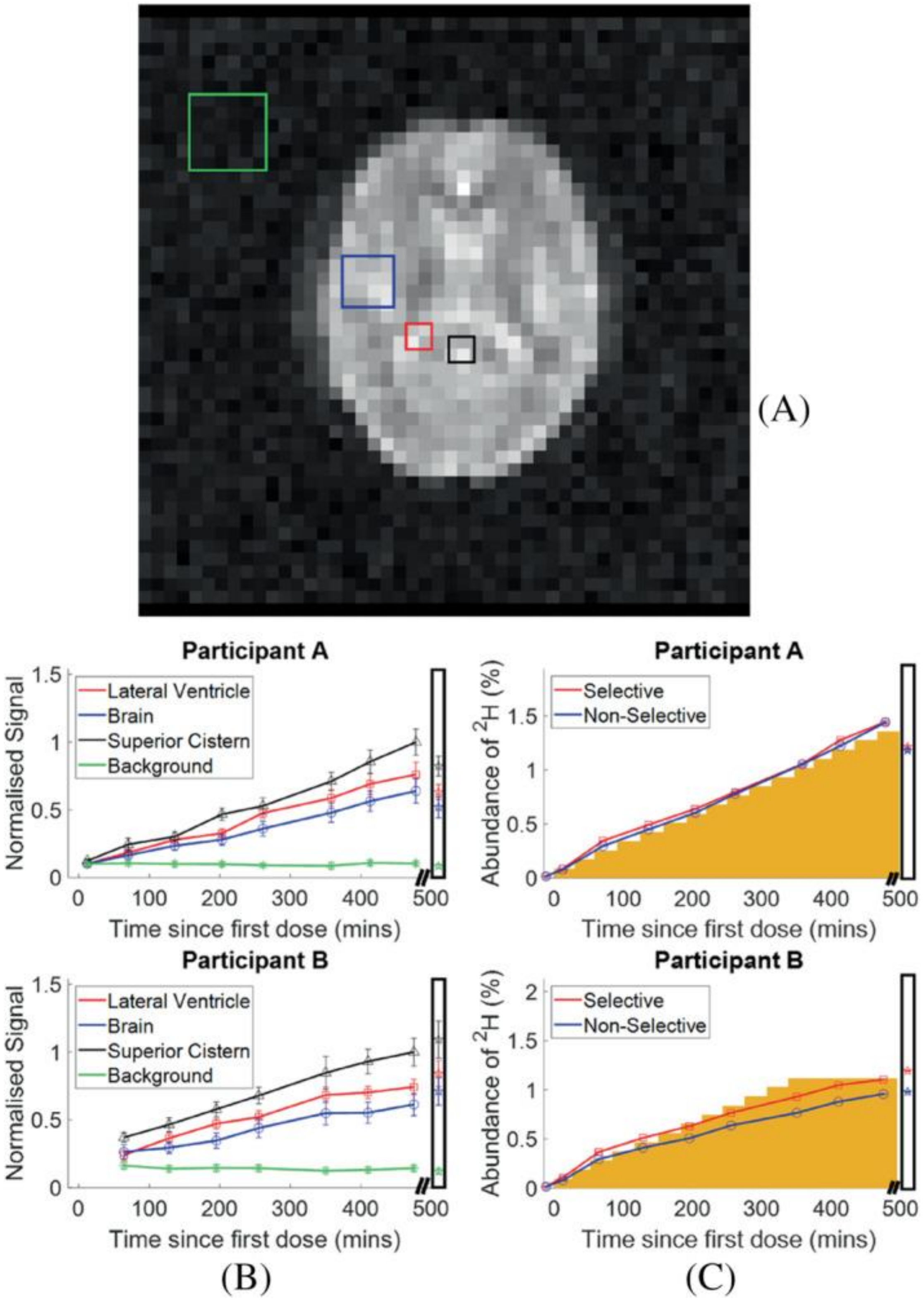

Figure 4: *(A) Regions of interest used for following the time-course of signal change during D_2O loading. Black = superior cistern; Red = lateral ventricle; Blue = brain (GM, WM, and CSF); Green = background noise. (B) Time course of average signal change in image ROIs (red = lateral ventricle; blue = brain tissue; black = superior cistern; green = background noise) in two participants. Signals from all compartments are scaled by the superior cistern signal at the final measurement time-point. Scaled signals measured at steady state (after 17-days loading) are shown in the box at the far right (C) Time course of the concentration of deuterium in the brain estimated from the ^2H spectroscopy measurements (red = from 2 cm slice at level of lateral ventricles; blue = whole head).*

Percentage estimated by scaling by the signal measured at natural abundance (assumed to be 0.015%). The orange blocks indicate the concentration estimated from the cumulative D_2O dose and body weight. The measurements made at steady state (after 17 days of loading) are shown in the box at the far right.

4.4 DISCUSSION

The results shown in Figures 1 and 3 indicate that ^{2}H images of 6 × 6 × 10 mm^3 voxel size with a useful SNR can be acquired in 7.5 minutes at 7T with a head-sized bird-cage coil, when participants have been deuterium-enriched to ˜1.5% concentration (˜100 times natural abundance). After summing over echo times these images (Figure 3) showed SNR ˜16 in brain tissue in the steady-state condition (after 17 days of loading).

The measured relaxation times were reasonably consistent across the six measurements (Table 1), with CSF having significantly higher T_1 and T_2^* values than GM or WM ($p < 0.007$ for two-sample t-test). The measured T_1 and T_2^* values were consistently higher in GM than in WM, but the differences did not reach statistical significance (T_1: $p = 0.21$; T_2^*: $p = 0.08$). The relatively coarse resolution of the ^{2}H images made it difficult to avoid the effects of partial voluming, particularly of CSF and GM, and the limited range of TE (4.3–46.3 ms) and TR (68–816 ms) values reduced the accuracy of measurement of the long T_1 and T_2^* values in CSF, as is evident from the larger SDs of these measurements (Table 1). Longer echo trains with a duration that exceed the expected T_2^* value and measurements at longer TR values should be used in future experiments targeting a better characterization of ^{2}H HDO relaxation times in CSF. For example, simulations show that inclusion of an additional measurement with a TR of 1500 ms would halve the SD of the estimated T_1 relaxation time of CSF but would also require 20 minutes of additional scanning time: use of an inversion recovery sequence may therefore be a better option. The average values of the relaxation times are consistent with values reported from non-localized measurements of HDO signals in human,[2,3,11] cat[27] and rat[1,2] brain.

Focusing on human brain measurements, De Feyter et al.[2] reported HDO T_1 of 346 ± 5 ms at 4T, while Ruhm et al.[11] measured 362 ± 6 ms at 9.4T – values which lie between the values for CSF (510 ms) and GM/WM (320/290 ms) measured here at 7T. As expected, the measured ^{2}H T_1-values are significantly shorter than the corresponding ^{1}H values at 7T,[32] due to the quadrupolar relaxation of ^{2}H. The long T_1 of HDO in CSF relative to GM/WM will lead to greater saturation in the CSF signal in short CSI measurements used for DMI (for example Ruhm et al. used TR = 155 ms[11]) which needs to be considered when quantifying signals from other ^{2}H-labeled metabolites using natural abundance HDO signals. Bi-exponential T_2 decay was previously identified at 4T[2] and 7T[37] using non-localized spin echo measurements: at 7T large (small) pools were found to have relaxation times of 29 ± 1 (412 ± 40) ms, respectively,[37] consistent with our identification of short and long T_2^* values in GM/WM (32/30 ms) and CSF (90 ms).

The TE-summed MEGE images in Figures 1A and 3 show contrast that is dominated by T_2^*-weighting, with the CSF appearing hyperintense relative to grey and white matter, as is the case in $T_2{}^*$-weighted ^{1}H images. A notable difference between the ^{1}H and ^{2}H $R_2{}^*$ maps (Figure 2) is that deep GM structures which appear with elevated $R_2{}^*$ in ^{1}H maps due to their high iron content[38] do not appear hyperintense in the ^{2}H maps. This is a consequence of the dominance of quadrupolar, rather than dipolar, relaxation in the case of ^{2}H and the relatively short T_2 relaxation times that the quadrupolar interactions produce in tissue, along with the lower ^{2}H gyromagnetic ratio. Together these mean that the large, microscopic and macroscopic field inhomogeneities generated by the iron-rich inclusions in deep GM structures regions, which increase the ^{1}H $R_2{}^*$ relaxation rate constants, do not have a significant effect on the measured ^{2}H $R_2{}^*$-values. The ^{1}H $R_2{}^*$ maps also show larger regions of hyperintensity near the frontal sinuses due to the greater field-inhomogeneity-related intra-voxel dephasing resulting from the higher γ of ^{1}H. Signals from structures outside the brain (apart from the eyeball) are only evident in the ^{2}H images acquired with the shortest TE value (Figure 1B) most likely because of the very short $T_2{}^*$ of HDO in muscle.[39, 40]

Figure 4 shows that the changes in HDO concentration during the initial heavy water loading could be readily tracked with imaging and spectroscopy. The concentrations estimated from the ^{2}H spectra are in reasonably good agreement with the values calculated from the cumulative D_2O dose and body mass (Figure 4C.) The signal amplitudes measured from ROIs in the brain images all have similar time-courses and maintain relatively constant ratios, with values that are most likely dictated by differences in $T_2{}^*$-weighting and water fraction in the different brain regions. This implies that the dispersal kinetics following oral ingestion of D_2O are rapid throughout the body on the timescale of the measurements. This is consistent with previous measurements based on blood sampling which indicate that the half-life of absorption into blood is ˜12 minutes, with similar time constants for dispersal into other body water compartments.[41, 42] In our experiments the subject came out of the magnet bore between measurements, leading to the potential for changes in signal intensity due to variation of the slice position. Nevertheless the ^{2}H signals tracked the monotonically increasing dose and the values measured at maximum dose were similar to those measured 17 days later during the steady state loading period. Although both participants had approximately the same weight and target D_2O dose, Participant B was only able to ingest 600 ml during the initial loading. The deuterium concentration measured from Participant A was consequently higher at the end of the loading period. The rest of participant B's loading was completed over the following 4 days, along with the daily 50 ml top-up and similar concentrations were measured from the two participants in the steady state (Figure 4C). The GC-MS measurements of deuterium concentrations in the saliva samples from Participant A and B were 1.51% ± 0.09%, and 1.53% ± 0.17%, respectively.

Rapid increases in body water enrichment can lead to feelings of dizziness and nausea. These symptoms can occur at relatively low enrichments while equilibrium has not yet been achieved and are thought to result from temporary effects on the vestibular system due to density changes in the semi-circular canals of the inner ear.[43] Some participants experienced these effects and so the rate of D_2O loading was slowed. The rapid loading was required for the parallel study, but a more gradual increase in heavy water uptake could be used for future MR-loading experiments to minimize these effects.

4.5 CONCLUSIONS

Deuterium MR measurements at 7T have been successfully used to track the increase in concentration of ^{2}H in brain during heavy water loading to 100 times natural abundance, in four human participants. Gradient echo images with an SNR of 16 and a voxel volume of 0.36 ml could be acquired in 7.5 minutes. ^{2}H T_1 and $T_2{}^*$ relaxation times from water in GM, WM, and CSF have also been measured at 7T. These relaxation times can be applied in research protocols using the natural abundance ^{2}H signal from water for calibration.

In future work we aim to track uptake from a single D_2O dose on a shorter time scale, using faster, interleaved acquisition of ^{2}H images and spectra. This is in light of the recent renaissance for the utility of stable isotopes within the field of metabolic imaging, in particular for its benefits regarding safety and ease of administration within clinical practice[3].

This study is the first to demonstrate the utility of DMI in human participants loaded with D_2O, and has contributed to the increased attention D_2O and deuterated-glucose are currently receiving for their application to measurements of glucose metabolism and neurotransmitter abundance implicated in several disease states[44, 45], as well as for their use in monitoring tumour progression and metabolism[46].

4.6 REFERENCES

1. Lu M, Zhu X-H, Zhang Y, Mateescu G, Chen W. Quantitative assessment of brain glucose metabolic rates using in vivo deuterium magnetic resonance spectroscopy. J Cereb Blood Flow Metab. 2017; 37: 3518-3530.

2. De Feyter HM, Behar KL, Corbin ZA, et al. Deuterium metabolic imaging (DMI) for MRI-based 3D mapping of metabolism in vivo. Sci Adv. 2018; 4: 7314.

3. De Feyter HM, de Graaf RA. Deuterium metabolic imaging – Back to the future. J Magn Reson. 2021; 326: 106932.

4. Kreis F, Wright AJ, Hesse F, Fala M, Hu D-e, Brindle KM. Measuring tumor glycolytic flux in vivo by using Fast deuterium MRI. Radiology. 2020; 294: 289-296.

5. de Graaf RA, Hendriks AD, Klomp DWJ, et al. On the magnetic field dependence of deuterium metabolic imaging. NMR Biomed. 2020; 33: e4235.

6. Riis-Vestergaard MJ, Laustsen C, Mariager CØ, Schulte RF, Pedersen SB, Richelsen B. Glucose metabolism in brown adipose tissue determined by deuterium metabolic imaging in rats. Int J Obes (Lond). 2020; 44: 1417-1427.

7. Straathof M, Meerwaldt AE, de Feyter HM, de Graaf RA, Dijkhuizen RM. Deuterium metabolic imaging of the healthy and diseased brain. Neuroscience. 2021; 474: 94-99.

8. Markovic S, Roussel T, Neeman M, Frydman L. Deuterium magnetic resonance imaging and the discrimination of fetoplacental metabolism in Normal and L-NAME-induced preeclamptic mice. Metabolites. 2021; 11: 376.

9. Peters DC, Markovic S, Bao Q, et al. Improving deuterium metabolic imaging (DMI) signal-to-noise ratio by spectroscopic multi-echo bSSFP: a pancreatic cancer investigation. Magn Reson Med. 2021; 86: 2604-2617.

10. Polvoy I, Qin H, Flavell RR, et al. Deuterium metabolic imaging-rediscovery of a spectroscopic tool. Metabolites. 2021; 11: 570.

11. Ruhm L, Avdievich N, Ziegs T, et al. Deuterium metabolic imaging in the human brain at 9.4 tesla with high spatial and temporal resolution. Neuroimage. 2021; 244: 118639.

12. Simões RV, Henriques RN, Cardoso BM, Fernandes FF, Carvalho T, Shemesh N. Glucose fluxes in glycolytic and oxidative pathways detected in vivo by deuterium magnetic resonance spectroscopy reflect proliferation in mouse glioblastoma. Neuroimage Clin. 2022; 33: 102932.

13. von Morze C, Engelbach JA, Blazey T, et al. Comparison of hyperpolarized (13) C and non-hyperpolarized deuterium MRI approaches for imaging cerebral glucose metabolism at 4.7 T. Magn Reson Med. 2021; 85: 1795-1804.

14. Wang T, Zhu X-H, Li H, et al. Noninvasive assessment of myocardial energy metabolism and dynamics using in vivo deuterium MRS imaging. Magn Reson Med. 2021; 86: 2899-2909.

15. Veltien A, van Asten J, Ravichandran N, et al. Simultaneous recording of the uptake and conversion of glucose and choline in tumors by deuterium metabolic imaging. Cancer. 2021; 13: 4034.

16. Ge X, Song K-H, Engelbach JA, et al. Distinguishing tumor admixed in a radiation necrosis (RN) background: 1H and 2H MR with a novel mouse brain-tumor/RN model. Front Oncol. 2022; 12: 885480.

17. Warburg O. On the origin of cancer cells. Science. 1956; 123: 309-314.

18. INTERNATIONAL ATOMIC ENERGY AGENCY . Introduction to Body Composition Assessment Using the Deuterium Dilution Technique with Analysis of Saliva Samples by Fourier Transform Infrared Spectrometry. Vienna: International Atomic Energy Agency; 2011.

19. Strawford A, Antelo F, Christiansen M, Hellerstein MK. Adipose tissue triglyceride turnover, de novo lipogenesis, and cell proliferation in humans measured with 2H2O. Am J Physiol Endocrinol Metab. 2004; 286: E577-E588.

20. Wilkinson DJ, Brook MS, Smith K, Atherton PJ. Stable isotope tracers and exercise physiology: past, present and future. J Physiol. 2017; 595: 2873-2882.

21. Busch R, Kim YK, Neese RA, et al. Measurement of protein turnover rates by heavy water labeling of nonessential amino acids. Biochim Biophys Acta. 2006; 1760: 730-744.

22. Sadygov RG. Using heavy mass Isotopomers for protein turnover in heavy water metabolic labeling. J Proteome Res. 2021; 20: 2035-2041.

23. Brereton IM, Irving MG, Field J, Doddrell DM. Preliminary studies on the potential of in vivo deuterium NMR spectroscopy. Biochem Biophys Res Commun. 1986; 137: 579-584.

24. Brereton IM, Doddrell DM, Oakenfull SM, Moss D, Irving MG. The use of in vivo 2H NMR spectroscopy to investigate the effects of obesity and diabetes mellitus upon lipid metabolism in mice. NMR Biomed. 1989; 2: 55-60.

25. Irving MG, Brereton IM, Field J, Doddrell DM. In vivo determination of body iron stores by natural-abundance deuterium magnetic resonance spectroscopy. Magn Reson Med. 1987; 4: 88-92.

26. Block RE, Parekh BC. Deuterium nuclear spin relaxation in biological tissues. Magn Reson Med. 1987; 5: 286-289.

27. Ewy CS, Ackerman JJ, Balaban RS. Deuterium NMR cerebral imaging in situ. Magn Reson Med. 1988; 8: 35-44.

28. Robinson MM, Turner SM, Hellerstein MK, Hamilton KL, Miller BF. Long-term synthesis rates of skeletal muscle DNA and protein are higher during aerobic training in older humans than in sedentary young subjects but are not altered by protein supplementation. FASEB J. 2011; 25: 3240-3249.

29. Burger JA, Li KW, Keating MJ, et al. Leukemia cell proliferation and death in chronic lymphocytic leukemia patients on therapy with the BTK inhibitor ibrutinib. JCI Insight. 2017; 2: e89904.

30. Loomba R, Decaris M, Li KW, et al. Discovery of half-life of circulating hepatitis B surface antigen in patients with chronic hepatitis B infection using heavy water labeling. Clin Infect Dis. 2018; 69: 542-545.

31. Yang D, Diraison F, Beylot M, et al. Assay of low deuterium enrichment of water by isotopic exchange with [U-13C3] acetone and gas chromatography-mass spectrometry. Anal Biochem. 1998; 258: 315-321.

32. Watson PE, Watson ID, Batt RD. Total body water volumes for adult males and females estimated from simple anthropometric measurements. Am J Clin Nutr. 1980; 33: 27-39.

33. Zhang Y, Brady M, Smith S. Segmentation of brain MR images through a hidden Markov random field model and the expectation-maximization algorithm. IEEE Trans Med Imaging. 2001; 20: 45-57.

34. Smith SM. Fast robust automated brain extraction. Hum Brain Mapp. 2002; 17: 143-155.

35. Jenkinson M, Bannister P, Brady M, Smith S. Improved optimization for the robust and accurate linear registration and motion correction of brain images. Neuroimage. 2002; 17: 825-841.

36. Jenkinson M, Smith S. A global optimisation method for robust affine registration of brain images. Med Image Anal. 2001; 5: 143-156.

37. Roig ES, de Feyter HM, Nixon TW, et al. Deuterium metabolic imaging of the human brain in vivo at 7 T. Magn Reson Med. 2023; 89: 29-39.

38. Peters AM, Brookes MJ, Hoogenraad FG, et al. T2 * measurements in human brain at 1.5, 3 and 7 T. Magn Reson Imaging. 2007; 25: 748-753.

39. Gursan A, Froeling M, Hendriks AD, et al. Residual quadrupolar couplings observed in 7 tesla deuterium MR spectra of skeletal muscle. Magn Reson Med. 2022; 87: 1165-1173.

40. Damion RA, Cocking DJ, Haywood B, et al. Natural abundance deuterium MRS of the human calf and T1 measurements with a surface coil at 3 T. Proc Soc Magn Reson Med. 2021; 29: 3836.

41. Davies S, Spanel P, Smith D. Rapid measurement of deuterium content of breath following oral ingestion to determine body water. Physiol Meas. 2001; 22: 651-659.

42. Péronnet F, Mignault D, du Souich P, et al. Pharmacokinetic analysis of absorption, distribution and disappearance of ingested water labeled with D2O in humans. Eur J Appl Physiol. 2012; 112: 2213-2222.

43. Money KE, Myles WS. Heavy water nystagmus and effects of alcohol. Nature. 1974; 247: 404-405.

44. Niess, F., Strasser, B., Hingerl, L., Niess, E., Motyka, S., Hangel, G., Krššák, M., Gruber, S., Spurny-Dworak, B., Trattnig, S., Scherer, T., Lanzenberger, R., & Bogner, W. Reproducibility of 3D MRSI for imaging human brain glucose metabolism using direct (2H) and indirect (1H) detection of deuterium labeled compounds at 7T and clinical 3T. NeuroImage. 2023; 277: 120250.

45. Niess, F., Hingerl, L., Strasser, B., Bednarik, P., Goranovic, D., Niess, E., Hangel, G., Krššák, M., Spurny-Dworak, B., Scherer, T., Lanzenberger, R., & Bogner, W. Noninvasive 3-Dimensional 1 H-Magnetic Resonance Spectroscopic Imaging of Human Brain Glucose and Neurotransmitter Metabolism Using Deuterium Labeling at 3T : Feasibility and Interscanner Reproducibility. Investigative radiology. 2023; 58: 431–437.

46. Wan, J., Guo, Y., Chen, H., Sun, P., Zhang, X., Ye, T., Li, L., Pan, F., & Yang, L. Application and development of Deuterium Metabolic Imaging in tumor glucose metabolism: visualization of different metabolic pathways. Frontiers in oncology. 2023; 13: 1285209.

CHAPTER III:

TECHNICAL CONSIDERATIONS AND PROSPECTS FOR SINGLE-CELL PROTEOMICS

1. REVIEW

1.1 INTRODUCTION

The development of many pathologies relates to the progressive or chronic activity of heterogenous cells that exist within a complex tissue microenvironment. For instance, in cancer it has long been recognised that tumours exist through the concerted activity of multiple cell types[1,2]. This interplay of heterogenous cell types extends to autoimmune diseases such as rheumatoid arthritis[3], where macrophage subtypes have demonstrated distinct associations with clinical state and disease remission[4,5]. In further complex tissues such as those of the musculoskeletal system, the presence of heterogenous cell types is known to be vital for homeostatic mechanisms related to healing and regeneration[6]; in particular following trauma[7] or exercise-induced muscle damage[8,9].

Recent advances in RNA sequencing technologies have enabled resolution down to a single-cell level[10,11], with these technologies presenting significant clinical value through examination of cellular heterogeneity within single-cell populations[12–14]. However, knowledge of cellular RNA profiles can only provide a proxy for protein levels within cells of interest[15] and have shown divergence once resolution reaches the level of single-cells[16]. As proteins constitute the molecular machinery for cellular metabolism, information relating to their levels of expression, turnover and modification status can provide detailed information regarding cellular function. Previously, deciphering the proteomes of single-cell subpopulations within complex biological matrices has proven incredibly difficult, due to analytical techniques requiring bulk measurements that often obscure cellular heterogeneity within complex tissues. Techniques for the isolation of cell subspecies such as magnetic-activated cell sorting (MACs) and fluorescence-activated cell sorting (FACs) have demonstrated capabilities to efficiently isolate single-cells from mixed populations[17,18], yet downstream detection of proteins with common methods such as western blotting, mass cytometry or ELISAs present limitations in their capacity for multiplexing and accurate protein quantification with such low amounts of biological material. Recent developments have increased the viability of these technologies to the study of single-cell proteomes[19,20], yet challenges remain in their widespread adoption[21].

In recent years, great advances have been made in the application of liquid chromatography tandem mass spectrometry (LC-MS/MS) proteomics capable of analysing low protein quantities, with these techniques starting to gain traction towards the study of single-cell proteomes[22]. This has primarily been achieved through recent advances in instrumentation that enable for quicker scan rates and parallel acquisition strategies[23,24], but have also been greatly contributed by developments in sample preparation[25,26], experimental optimisation of instrumentation[27–29] and bioinformatic analysis pipelines[30–32]. This review aims to provide an overview of current considerations and prospects for mass spectrometry single-cell proteome analysis.

1.2 SAMPLE PROCESSING

Sample processing represents a key step for any proteomics workflow, with this being of critical importance within single-cell proteomics where starting quantities of protein are limited and loss of sample can be particularly detrimental. While single-cell RNA sequencing technologies are able to utilise product amplification to ensure sufficient signal intensity[33], alternate strategies must be employed within single-cell MS proteomic workflows to enable detection. These commence with sample processing.

When analysing single-cells in the range of 1000-100000s of cells (generally termed, bulk analysis) only minor adjustments to standard sample preparations are necessary to enable MS analysis[29,34]. Consequently, these often still utilise detergents or chaotropic agents for cell lysis, as there is sufficient biological material to allow for subsequent sample clean-up via precipitation or desalting thereafter. These processes become less feasible as cell numbers approach 100s-10s of cells and minimisation of sample handling becomes paramount. A recent publication[35] demonstrated the efficacy of an acidification-based proteomics extraction and processing method utilising Trifluoroacetic acid, that demonstrated improved protein yield and circumnavigated the necessity for detergents or chaotropic agents while generating high quality data. Indeed, in our hands slight alterations to this protocol have resulted in significant improvements in protein extraction yield compared to more conventional detergent-based approaches, down to as low as ~3000 human T-cells (FACs: CD14- CD3+ CD45RO+ CCR7+; unpublished data). This quick and minimalist method only requires downstream removal of Tris-Trifluoroacetate that can be successfully removed with offline or online desalting via reversed-phase C18 resins. Although to the author's knowledge this approach has yet to be otherwise tested in the field of single-cell proteomics, a derivative of Trifluoroacetic acid, Trifluoroethanol, has been successfully applied to single-cell analysis in a culture model of primary leukaemia where it has demonstrated improved protein extraction compared to pure water[28] and reduced sample losses compared to detergent-based approaches that require additional sample clean-up steps[36]. Indeed, for low input proteomics where associated loss of sample via clean-up strategies must be negated, use of organic solvents have proven viable options for efficient cell lysis, protein solubilisation and denaturation that reduce the requirements for subsequent sample purification prior to MS analysis[16,28,36,37]. Pure water has alternatively been implemented as a means to remove the need for sample purification, yet usually requires additional physical disruption via either sonication[38] or heat-cool cycles[25].

Among the first of these studies was Single Cell ProtEomics by Mass Spectrometry (SCoPE-MS)[38]. This study opted for mechanical lysis through acoustic sonication[39] to circumnavigate sample clean-up and its associated losses for true single-cell analysis. Single-cell processing volumes were reduced to microlitre scale within PCR strip-tubes at 2-200ul volumes following which peptides were isobarically-labelled before being combined with 'booster' channels of 200 cells to increase MS2 signal intensities for peptide identification. Although important in ensuring sufficient signal intensities, use of a 'booster' channel also reduces single-cell peptide surface interaction through relative dilution, minimising both adsorptive losses from plastic or glassware during chemical preparation and nano liquid-chromatography (nLC). Further development of this protocol aimed to reduce processing volumes by 10-fold through Minimal ProteOmic sample Preparation (mPOP)[40], with the aims of promoting automation for higher analytical throughput and reduced sample handling, while utilising widely available equipment. mPOP demonstrated superior protein extraction via cell lysis when compared to a traditional urea-based method, confirmed by SILAC LC-MS analysis, suggesting its suitability for implementation within the SCoPE analysis framework. Adoption of this platform was further developed into the SCoPE2 framework[25], that incorporated single-cell processing within multi-well plate format utilising widely available and cost-effective PCR thermocyclers and liquid dispensers. Combined with utilisation of mass spectrometry instrumentation that has been commercially-available for over 10 years, this presents a highly accessible single-cell MS analysis platform that has demonstrated capabilities to discern cellular heterogeneity at single-cell resolution[41].

While adsorptive losses during sample preparation and chromatographic separation can be reduced within multiplexed workflows through use of a carrier channel, alternate strategies must be employed within label-free approaches to maximise the introduction of low peptide inputs for separation and detection via (nano) LC-MS. One of these strategies is through minimising sample transfer and processing volumes via a single-pot approach. While a single-pot approach was originally introduced in the field of proteomics to ameliorate issues of sample quantity [42] and has demonstrated some utility in the field of single-cell proteomics within a study of human oocytes[43], further adaptations have been implemented to facilitate the analysis of smaller mammalian cell types of lower protein content that may not tolerate the losses inevitable during sample clean-up within these workflows. To this end, a recent publication investigated the use of 1µl single-pot sample preparation for label-free single-cell proteomics[44]. Utilising the CellenONE automated liquid handling system, they observed substantial benefits in protein identifications through enhanced recovery and digestion efficiency when sample hydration was maintained via addition of water every 15 minutes during tryptic digest. This, along with the addition of 5% DMSO to aid hydrophobic peptide solubilisation, significantly reduced adsorptive peptide losses from plastic or glassware and translated directly to increased protein identifications[44]. This was further enhanced when samples were injected directly from the 384-well plate formats used for single-pot processing, reinforcing the importance of minimal sample transfer during preparation.

Alternative protocols utilising greater levels of miniaturisation into the nanolitre scale have also proven successful, with the aim of maximising sample recovery and enabling enzymatic digestion to occur at comparable concentrations relative to bulk analyses[22]. Originally implemented using custom nano well or chip designs[26,45,46], nanodroplet approaches have also been successfully automated via the liquid handling system, CellenONE[47–51]. This increased level of miniaturisation has enabled identification of 100-1000s proteins from single-cells using both label-free and multiplexed experimental designs, with application of nano-PrOteomic sample Preparation (nPOP) within the SCoPE2 framework demonstrating improved proteomic profiling of HeLa and U-937 monocytic cell lines during cell cycle division compared to the previously adopted mPOP protocol[40]. However, comparable results have recently been achieved with use of processing volumes ~2ul in conjunction with low protein-binding microwell plates[16,28,37,41], representing an attractive and accessible approach to single-cell analysis utilising widely available equipment and MS instrumentation. The viability of these approaches, however, is arguably contributed by the integration of ion mobility (TIMS/FAIMS) within these workflows that improve signal: noise ratios (akin to the aim of nanodroplet processing) which will be discussed in further detail below. Reducing spectral complexity appears key to improving protein identifications with current LC-MS technologies, whether this is achieved through nanodroplet approaches or downstream ion mobility filtering.

1.3 CHEMICAL LABELLING VS LABEL-FREE APPROACHES

Both label-free and chemical labelling strategies have been applied to the proteomic analysis of single-cells. Label-free proteomic techniques represent a minimalist approach that do not require the introduction of isobaric or non-isobaric mass tags, simplifying the workflow and reducing sample handling. Labelling strategies seek to chemically modify samples in order to improve the chances of peptide identification and quantification but have the potential to impact sample processing, chromatographic separation and MS analysis. However, both techniques present benefits and limitations for the identification and quantification of proteins within single-cells.

Isobaric labelling originally gained traction in the field of proteomics as an alternative method for protein quantification due to the limitations of stable isotope approaches currently employed at the time. Although *in vitro* stable isotope labelling approaches[52,53] demonstrated some utility for quantitative proteomics as long as the model organism was compatible with the necessary culture conditions, *in vivo* labelling approaches were more difficult to implement due to limitations in accurate prediction of isotope incorporation or for their laborious and expensive nature[54]. Alternatively, chemical derivatisation techniques using stable isotopes can present their own constraints[55,56], in particular when deuterium is the stable isotope label of choice. Although the mass modification following deuterium-labelling is small, it has been shown to increase mobility of deuterated peptides during high performance reversed-phase liquid chromatography to the point that they often elute as a separate fraction[55,57]. This poses problems in treating the ‘heavy’ (deuterated) and ‘light’ peptides as internal standards for one another during relative protein quantification, as these peptides do not co-elute for integrated detection of ion intensities and therefore it is possible that they are differentially suppressed during ionisation by interfering compounds. Although for deuterium-labelled compounds this appears less problematic with HILIC separations[58,59], stable isotopes are further capable of being incorporated at multiple sites within a peptide of interest. As a result, the discrepancy between the extent of isotopic labelling among ‘heavy’ and ‘light’ peptide pairs can differentially alter the charge state of peptides during electrospray ionisation, further reducing the confidence in peptide quantification[57,60].

Tandem mass tags (TMT) were introduced as a solution to some of these limitations in isotope labelling strategies and involve the incorporation of multiple 'tags' - present as amino acids – that label peptides with a sensitisation group, mass normaliser and cleavage enhancer[61]. These tags are analysed using MS2 data acquisition, where their design facilitates the collision-induced dissociation (CID) of the TMT fragment from the precursor ion in a manner that enables its detection as a reporter at a specific mass-charge ratio. Tags can be designed for reactive specificity to label a variety of nucleophile target sites and therefore are capable of targeting distinct peptides with a high level of accuracy. Through the use of a mass normalisation group, pairs of TMT labelled peptides have the same mass and chemical composition, thus ensuring comigration during chromatographic separation to provide more accurate internal standards for peptide quantification. Additionally, as these peptides coelute and share the same chemical properties, they are detected as one peak during MS1. This provides a clear benefit for low-input proteomics, as there is an increased chance of peptide detection through greater cumulative ion intensities. This is in juxtaposition to stable isotope labelling where peptide pairs are separated into two peaks (or more) and respective ion intensities will therefore be weaker. With peptide pairs sharing a peak in MS1, they can also be isolated together more accurately for quantification via MS2 acquisition, which provides an improved signal-noise ratio due to the absence of non-specific peptides or compounds.

Within the field of single-cell proteomics the use of TMT labelling has become an attractive option for protein identification and quantification, where it has demonstrated high analytical throughput and deep proteome coverage[28,38]. Single-cell isolations are separately lysed and digested, before being differentially labelled with isobaric mass tags. Samples are then pooled together, with detection of these low abundance samples being augmented by their further combination with a carrier sample that typically comprises hundreds of cells from the experimental populations of interest[62]. Multiplexed analysis of single-cells in this way circumnavigates some of the innate difficulties of detecting such low intensity ions, thus improving detection in MS1 and subsequent selection for and improved sequencing in MS2. Use of a carrier channel has successfully enabled analysis of >100 cells per day from up to 16 multiplexed single-cell samples, achieving >1000 protein group identifications per cell and thus representing a powerful tool for single-cell MS proteomics[28,41].

Control and consideration of the carrier channel is, however, vitally important as alterations to this channel will directly impact intensities and therefore detection of sample peptides[63]; although this also presents an opportunity to enrich detection of specific sample peptides through adjustments to the quantities of these same peptides in the carrier. To avoid quantification bias, carrier channels are generally limited to no more than 200-cells within analytical workflows[28,38], with reductions to 20-100 cell carriers appearing optimal for true single-cell analysis[63,64]. With the aim to further reduce bias effects, use of linear ion traps have been implemented to separate sample and carrier precursors prior to their introduction to the Orbitrap[63], while experimental removal of a carrier channel altogether has been achieved through miniaturised sample analysis using nanolitre volumes[50]. Although use of nanolitre preparation showed an improved reporter ion signal: noise ratio when assessed with 16-plex TMT labelling (although this appears in part to be contributed by the choice of TMT reagent) lack of a 20x carrier channel reduced average PSMs, peptides and proteins identified (from ~2000 protein groups to ~1500), suggesting a potential trade-off between quantitative accuracy and rates of identification[50]. However, these identifications with removal of a carrier are still comparable to other reported rates in single-cell experiments[37,65], suggesting the viability of nanolitre workflows to improve quantitative accuracy while maintaining relative levels of protein identification.

Current applications of isobaric labelling to single-cell proteomics provide some of the highest rates of identification and analytical throughput, but there are still drawbacks to this approach. Although labelling is generally highly efficient, it can be impacted by contaminating primary amino groups contained within the sample that interact with the amine-reactive mass tags[66,67]. For this reason, sufficient sample clean-up is imperative prior to isobaric labelling or alternatively avoidance of amine-containing buffers such as Tris and ammonium bicarbonate[68]. Additionally, isotopic impurities of isobaric labels can impact MS quantification through their cross-detection within alternate channels, necessitating data correction via computational methods[69]. Both of these present challenges for single-cell proteomics, at the level of both sample processing and data interpretation. At serial bulk dilutions aimed at reflecting single-cell quantities, application of isotopic impurity correction factors have been shown to increase quantitative error[63], suggesting currently employed computational strategies that are successful for bulk analyses may not be as suitable for single-cell proteomics. Cross-channel contributions from isotopic impurities have been shown to result in reductions in quantitative precision within single-cell workflows[28,63,70] and appear to be exacerbated by increased carrier: single-cell channel ratios[70]. Additional issues are known to arise from the co-isolation of peptide fragments, where ratio compression may undermine the ability to accurately distinguish quantitative differences between samples[71]. Within single-cell frameworks that utilise a carrier channel, this proves particularly problematic, as single-cell reporter ion intensities may be saturated by the carrier and collected as noise within the MS spectrum[70]. As a result, CVs for single-cell channels have been shown to increase inversely with signal: noise at both PSM and protein levels[63,70]. At such low relative signal intensities, it is possible single-cell analysis may result in increased missing values not observed with bulk analysis[63], presenting further difficulties for downstream statistical analysis. As a result, label-free quantification (LFQ) likely presents a more robust method for peptide quantification at either MS1 or MS2 level, due to not being constrained by the biases and extenuating considerations of isobaric labelling approaches and for minimal sample handling. However, the need for increased analytical throughput is still a prominent issue within single-cell proteomics, especially if the technology is to become suitable for routine clinical applications and keep pace with other current single-cell sequencing technologies, particularly where parallel single-cell experiments are required.

1.4 DATA ACQUISITION

1.41 DDA Or DIA

Choice of quantification via LFQ or chemical labelling will influence the choice of data acquisition during single-cell proteomic analysis, namely the selection of data-dependent acquisition (DDA) or data-independent acquisition (DIA). DDA has traditionally been employed within chemical labelling workflows in order to select the most abundant precursors for fragmentation. However, as precursors are isolated individually for fragmentation prior to MS2, this invariably leads to increased analytical times in order to achieve deep proteome coverage when using Orbitrap instrumentation[72]. Non-isobaric labelling (such as mTRAQ or dimethyl labelling) enables sample multiplexing to improve throughput but as a result increases precursor numbers and therefore requires longer cycle times in MS1 for sufficient resolution[56,73]. High resolution is often necessary at both MS1 and MS2 to enable accurate peptide identifications with the low signal intensities of single-cell peptides but invariably such a multiplex approach increases spectrum complexity, challenging data interpretation. Alternatively, as discussed earlier within this review, isobaric labelling enables comigration of multiplexed sample peptides, enabling greater throughput by selection of a higher pooled signal precursor for fragmentation (albeit with drawbacks in the quantitative accuracy henceforth). Due to the limitations of co-isolation with isobaric labelling, techniques such as TMT labelling are generally constrained to DDA, as simultaneous isolation of multiple peptide precursors within an isolation window will result in indistinguishable reporter ions during MS2 quantification. Computational developments are now facilitating greater implementation of DIA as a powerful tool for deep and robust proteome analysis to interpret the chimeric complexity of spectra obtained via DIA[24,31,32,74]. Recent reports into the application of DIA with TMT labelling demonstrated improved data completeness and improved precision without compromising identification rates[64,75], yet did not necessarily resolve the concerns regarding co-isolation within these workflows. However, replicability was high across runs of low sample inputs (0.5ng, 1ng, 5ng, 10ng), potentially as a result of more consistent signal: noise intensities that henceforth enable for the consistent detection of precursor and reporter ion intensities[75]. This was further complemented by this study's observation that data point generation was reproducible across samples when applying their DIA isolation scheme. This suggests that DIA may be possible for TMT experiments and presents an augmentation to the multiplex capabilities of isobaric labelling strategies to further increase throughput, however, likely requires further validation to confirm its quantitative accuracy.

In an attempt to circumnavigate the underlying quantitative issues of isobaric labelling while maintaining or increasing analytical throughput by taking advantage of the multiplicative nature of DIA, recent studies have employed alternative methods utilising novel isotopic[76] or mTRAQ[51] non-isobaric tags for triplex analysis. The first method involves use of an isotopically labelled acetyl-isoleucine-proline (Ac-IP) tag[76], that applies a minor modification to peptides resulting in incremental 1 Da shifts for separate precursor detection and quantification via MS1. Fragmentation of the Ac-

IP tag induces dissociation by neutral loss that leads to its detection at a defined m/z within MS2, minimising the complexity of resulting MS2 spectra during peptide identification. Together, this enables for use of modest resolution at both MS1 (70,000) and MS2 (17,500) level, which for Orbitrap instruments enables cycle times to be kept at an acceptable level, therefore retaining the benefits in throughput from DIA. This is an improvement on previous methods for multiplex DIA utilising neutron-encoded mDa shifts with ^{13}C or ^{15}N that require use of ultra-high resolution at MS2 (>120,000) and in comparison reduced acquisition rates through longer Orbitrap cycle times[77–79]. Although promising, Ac-IP has yet to be applied to the study of single-cell proteomes. An alternate triplex non-isobaric labelling approach with mTRAQ[51] has, however, been successfully applied to the study of single-cells. This method was implemented following observation of the benefits from DIA strategies employed in recent LFQ workflows[16,24] that have enabled throughput and identifications similar (or superior) to previously reported isobaric labelling approaches[32,80], while avoiding the inherent quantitative limitations of isobaric labelling to present improved quantitative accuracy. This triplex non-isobaric DIA method termed plexDIA[51] similarly utilises MS1-based peptide quantification, while incorporating the benefits of DIA to increase quantitative accuracy and reduce missing values. However, this results in minor trade-offs in protein identifications under similar chromatography and instrument times when compared to previous TMT-DDA methods using the same Orbitrap instrument[41]. Utilisation of a timsTOF mass spectrometer within this workflow (opposed to a Q Exactive Classic Orbitrap) did however return identifications approximate to those identified with TMT-DDA[51]. This choice, again, has likely been largely influenced by the introduction and success of DIA-timsTOF workflows within low-input LFQ[24,32,81], whose benefits will be discussed in further detail below. Regardless of quantification strategy, DIA presents many opportunities for the study of single-cell proteomes and will likely undergo further developments in the coming years.

1.42 Optimising Data Acquisition

For single-cell proteomic analysis, both DDA and DIA approaches pose the potential to increase the accumulation of precursor ions for improved signal, through either pooling isobarically-labelled peptides from multiple samples within DDA or multiplying precursor peptide selection via wider m/z isolation windows from single (or multiple) samples within DIA. As previously discussed within this review, this is essential for single-cell proteomics, where increased signal: noise ratios are integral to successful peptide identification through either acquisition or preparation strategies (such as nanoscale preparation). However, further adjustments to instrument set-up and utilisation can have profound effects on data generation, precursor detection, peptide identification and subsequent quantification. Indeed, many of the advances already described within this review have only become possible through considerable optimisation of their associated instrumentation, that cumulatively represent further vital considerations for the MS analysis of low input samples and true single-cell proteomics. These are routinely characterised by increased ion accumulation times, high resolution MS1 and MS2 (with options for deep MS3 and beyond), adjustments to *n* precursor selection within DDA, increased injection times, low-flow nano liquid chromatography, optimisation of data points per peak and adjustments to automatic gain control (AGC) targets. These key ingredients must be balanced relative to the experimental parameters of single-cell studies and minor alterations to only a few of these parameters can already demonstrate notable benefits within bulk analysis of up to as many as 10,000 cells[29]. Where analysis involves 1000s - true single-cells, the influence of these alterations becomes increasingly profound.

1.43 Nanoflow Liquid Chromatography

Following sample preparation, separation of the resultant complex peptide mixtures prior to measurement via MS is instrumental to enable detection across the dynamic range of proteins present within limited samples[22,82]. Due to the reduced protein quantities present within single-cells and the synonymous elongated injection and accumulation times required to reach sufficient AGC targets for sequencing, nanoflow systems implementing reduced flow rates have demonstrated benefits in the optimisation of ion flux prior to subsequent nano electrospray ionisation[83]. Due to such low flow rates (typically 100-250nl/min[16,25,28,51], chromatography is generally employed using columns with inner diameters of 50-100µm and particle sizes ranging from 1.6-2µm[16,38,51,75,84]. As sensitivity in proteomics is largely a function of concentration and dependent on the optimal ionisation and subsequent delivery of ions through the vacuum system for detection within the instrument, use of low flow nLC increases sensitivity by increasing the relative concentration of peptides delivered to the nESI source[85]. Simultaneously, nESI enables the formation of smaller droplets, reducing the influence of contaminants that may suppress peptide ionisation, in particular non-volatile salts[86,87]. A drawback of low-flow nLC systems, however, is the difficulty in their maintenance and robust operation, partly due to the consequent increases in back-pressure as a result of such narrow columns and fine particles. However, steps towards the robust implementation of nanoflow liquid chromatography systems are being realised. A recent publication utilised an offline EvoTip trap column coupled to the EvoSep One liquid chromatography system for sample separation through use of a single-pump across a pre-formed beta gradient to great success[16]. Sample peptides were concentrated into 20nl packages during elution from the offline trap column for direct introduction into the separation system, facilitating miniaturised sample clean-up without additional processing steps. This liquid chromatography system standardised for reproducible results at a flow rate of 100nl/min (although as low as 25nl/min was performed successfully) and its application for analysis of 1ng HeLa digest produced a 10-fold increase in MS signal using DDA detection coupled with a timsTOF instrument compared to 1µl/min separations, with further benefits in MS detection observed following the use of DIA within this workflow[16]. Invariably synonymous with signal: noise when assessing the analytical input of nLC efficiency is the generation of sharp peaks through contracted ion elution profiles. To this end, as well as the low flow rate, the design of this liquid chromatography system enabled concentration of separated peptides within a pre-formed gradient prior to their separation through the analytical column[88]. Peptides eluted from the EvoTip trap with an organic solvent (<35% organic) were then offset by a gradient that reduced organic solvent composition, focusing sample peptides within a storage loop at the set organic content from which they will subsequently elute. Formation of a chromatographic gradient within a storage loop henceforth facilitates the use of a high-pressure single-pump to transfer peptides onto the analytical column for further separation, which results in very narrow peak widths for MS detection[16,88]. An added benefit to this approach is that washing of the column is integrated within the composition of the pre-formed gradient and therefore does not require separate loading of a wash buffer into the system, increasing analytical throughput by reducing wait times between sample loading. Such advancements will be necessary if routine proteomic analysis of low input biological samples is to become viable within the field of clinical proteomics.

Further developments in column composition, diameter and reductions in nanoflow rate have been implemented for low input or single-cell proteomics. Among these involve microfluidic pillar array column designs (µPAC)[89,90]; ordered non-porous columns that boast reproducible retention times, sharp peak capacities, minimal on-column losses and whose optimal operation at low flow rates naturally lends itself to single-cell MS analysis. Indeed, application of µPAC columns has demonstrated improved protein identifications for low input samples[90,91] and has successfully been applied to the proteomic analysis of single-cells[37]. Its inherent low-binding capacity is well-suited to single-cell applications and will likely receive further attention as a column of choice as a result. Among other recently employed options are use of porous layer open tubular (PLOT) columns[92], which have been successfully employed to the analysis of ~50-100 spiked MCF-7 cells from whole blood isolations where they identified ~1300-2000 protein groups respectively[93], while employing a low flow rate of 20nl/min across a 4-hr gradient using a 4m column with an inner diameter of 10µm and porous permeability of ~1 µm. Use of narrow-bore columns <50µm have also been successfully employed with standard 3µm C18 porous particles through custom column packing, where use of narrow-bore columns of inner diameter (ID) 20µm demonstrated improved rates of protein identifications over 30µm, when flow rates of 20nl/min and 50nl/min were employed respectively[94]. This was observed for both low input proteomics of 0.2-2ng HeLa digest and single HeLa cell proteomic analysis, where use of a 20µm ID column resulted in identification of ~300 protein groups compared to ~200 protein groups when applying a 30µm ID column[94]. Further application of this custom 20µm narrow-bore column for chromatography within an expanded proteomics workflow utilising field-asymmetric ion mobility spectrometry (FAIMS) for filtration of ion precursors prior to detection with a Thermo Scientific Orbitrap Eclipse Tribrid MS instrument enabled identification of >1000 protein groups from a single HeLa cell[95], representing one of the most in-depth label-free single-cell measurements of a mammalian cell type to date while demonstrating the utility of this column type for single-cell proteomics experiments.

1.44 Ion Mobility Spectrometry

Among the great developments in the field of single-cell proteomics in recent years has been the successful implementation of trapped ion mobility spectrometry (TIMS, Bruker instrumentation)[96] or Field Asymmetric Ion Mobility Spectrometry (FAIMS, Thermo instrumentation)[97] techniques. Although mass spectrometry instrumentation is generally set-up to disregard singly-charged contaminant species, these can still influence ion flux and may be co-isolated along with target peptides, increasing spectral complexity and reducing the ability to efficiently identify peptides. While perhaps negligible with bulk analyses, these effects become exaggerated with the inherently low signal: noise of single-cell peptide abundances. This has been evidenced within a study whereby use of a FAIMS device to quantify single HeLa cell proteomes resulted in an approximate doubling (~100% increase) of both unique peptides and protein groups[95]. Designed to omit singly-charged species, FAIMS achieves reduced spectral complexity and poses the possibility to perform gas-phase fractionation in real-time to assist deeper targeted sequencing via MS2 or MS3[28,37] or alternatively to minimise the need for MS2 acquisition through utilisation of ion mobility values that provide sufficiently robust and detailed information for three-dimensional matching with MS1 and chromatographic retention times[98].

A peptide's ability to traverse the gas phases of either TIMS or FAIMS instruments is relative to its size and chemical composition, from which a value denoting its collisional cross section can be calculated[99]. Peptide collisional cross section values increase specificity through the capability to differentiate amino acid sequences based on both length and structure to the point where isobaric peptides can be distinguished[100,101], with the integration of this data dimension into the MaxQuant analytical software demonstrating improved precision for MS1 label-free quantification[30]. As one can imagine, this technology can pose a multiplicative benefit via matching ion mobility values across analytical runs, where it has demonstrated greater reproducibility than liquid chromatography retention times across experimental batches[102]. Indeed, detailed information can be garnered from collisional cross section measurements with TIMS instrumentation, which demonstrate good agreement with standard drift-tube ion mobility measurements, and when TIMS is applied in conjunction with a parallel accumulation-serial fragmentation approach (PASEF)[103] it has demonstrated approximately a 10-fold analytical improvement to sequence peptides[102]. While TIMS separation improves peptide identifications through enhanced signal: noise and reduced spectral complexity, it also poses the possibility to further optimise the delivery of analyte ions for detection. Ions are separated and accumulate via a counteracting electrical field that retains ions in the gas phase prior to their sequential release through stepped decreases in the electrical current (an inverse mechanism to drift tube IMS) and this enables delivery of ions as concentrated packages to increase sequencing speed without compromising sensitivity within MS/MS analysis[103]. Naturally, this is an exciting option for low input and single-cell proteomics as a means to further optimise ion delivery to the MS instrumentation for improved signal detection and naturally parallelises well to both DDA and DIA acquisition methods[24,103]. This has resulted in the application of DIA-PASEF TIMS-TOF analysis to successfully identify thousands of proteins from low input and single-cell samples[16,32,104], which currently represent the deepest proteomic profiling of single-cells achieved to date.

Further advancements towards increasing throughput are also being realised, drawing upon the principles introduced in SONAR[105] and Scanning SWATH[106], whereby precursor ions are isolated by a quadrupole across a continuous DIA selection window (opposed to traditional stepped isolations) enabling for the direct determination of precursor-fragment relationships through time-dependent signal intensity calculations. This generates an additional data dimension (termed Q1) aimed at facilitating high analytical throughput without compromising quantitative precision and was successfully able to differentiate COVID-19 disease severity based on plasma proteome measurements using microflow chromatography gradients as short as 60 seconds[106]. Applied within the context of two DIA-PASEF TIMS-TOF workflows[107,108], quadrupole 'slicing' increased precursor sampling efficiency, speed and signal intensities, extending this data acquisition strategy to six dimensions: retention time, ion mobility, quadrupole selection, Q1 profile, m/z and intensity. Applied to the analysis of 200pg HeLa cell tryptic digest (approximate to single-cell quantities[109]) this approach enabled the quantification of ~1400 proteins from a 2µl/min gradient employed at 200 samples per day throughput on the EvoSep One chromatography system paired with a timsTOF Pro 2 instrument[108]. This poses an exciting technological advance that will likely receive considerable attention in the coming years towards the realisation of high throughput quantitative proteomics compatible with single-cell and clinical applications.

1.45 Linear Ion Traps

Although advancements to enable single-cell proteomics began with the use of orbitrap mass analysers[26,38] and TIMS-TOF instruments currently enable some of the deepest proteomic profiling for low input omics[16,32], linear ion trap mass analysers have recently gained attention for their speed and sensitivity in measuring low input samples[110,111]. Current advanced instrumentation additionally supports switching between orbitrap and linear ion trap acquisition schemes for both standard tandem MS/MS as well as deeper MSn sequencing[37,84], thus facilitating utilisation of this acquisition strategy without the need to acquire further instruments within the laboratory. This has consequently enabled internal instrument comparisons between orbitrap and linear ion trap acquisition schemes.

Investigation of differences in peptide and protein identification rates (as well as quantitative accuracy) from MS2 data acquired via orbitrap vs linear ion trap for low input samples was first employed for serial bulk dilutions of HeLa digests using an Orbitrap Fusion Lumos Tribrid (ThermoFisher) in DIA mode[110]. When analysing 10ng or lower, use of a linear ion trap resulted in improved peptide identifications and CVs compared to the orbitrap while decreasing cycle times. Increasing the precursor isolation windows, while removing the benefit of reduced cycle times, further increased peptide precursor identifications to approximately double that of the DIA-orbitrap acquisition scheme at 10ng and 1ng analytical loads[110]. A further study extended investigation into the benefits of linear ion traps for low input proteomics, again utilising a serial bulk HeLa dilution[111]. This study similarly observed benefits for peptide identifications with linear ion traps once sample loads decreased to 10ng or less, additionally observing minimal increases in identification rates when analysing loads above 5ng[111]. This suggests the innate suitability of linear ion traps for low input proteomics as both studies observed an earlier plateau in identifications relative to sample concentration for linear ion trap methods compared to orbitrap, which demonstrated superior identification rates at higher sample loads[110,111]. These studies attributed these differences to the reduced specificity of linear ion traps driven by their low resolution capabilities, resulting in their associated DIA-generated spectra being more complex, and affirming the benefit of small isolation windows for DIA-LIT. An interesting observation to this effect was the influence of injection time on spectrum complexity and consequently peptide identifications. Increased injection times resulted in improved peptide coverage[110,111] and quantitative accuracy[111] when isolation windows were maintained resulting in longer cycle times, with peptide identifications decreasing when cycle time was matched through use of larger isolation windows. This iterates the specific suitability of linear ion traps for low input proteomics, as it appears that increased ion flux or complexity arising from larger isolation windows or bulk digests is problematic for DIA-linear ion trap analysis, as the time required for proper resolution would become impractical or impossible at these loads. Indeed, at 1ng inputs linear ion traps exhibited peptide identifications and CVs superior to orbitrap analysis unless analytical resolution at MS2 was massively increased to 120,000 (and by association cycle times)[111], reinforcing their superior sensitivity. With analytical throughput posing a constant consideration for the practical implementation of single-cell proteomics, particularly within clinical settings, the rapid scan rates possible with linear ion traps may complement the increased injection times required to achieve deep proteomic profiling.

Linear ion traps have successfully been applied to the study of single-cell proteomes; with a study utilising nanoPOTS preparation, low flow nanoLC separation at 100nl/min and an Orbitrap Eclipse Tribrid interfaced with a FAIMSpro (Thermo Instrumentation) enabling detection of ~3000 proteins at single-cell level[84]. Data was acquired with DDA and matching to a spectral library of 11 cells proved highly successful for peptide and protein identifications, as previously alluded to for low input samples analysed via linear ion trap[111]. This supports the effective use of both DDA and DIA acquisition strategies with linear ion traps for MS2 peptide identification, with 6-plex TMT-labelled quantification having additionally been achieved via linear ion trap MS3[112] (although this has yet to be applied within the context of single-cell proteomics). Indeed, due to the high sensitivity and reduced specificity of linear ion traps DDA acquisition strategies may prove preferable, particularly in scenarios where parallel acquisition can be performed to parallelise high-resolution orbitrap MS1 with increased MS2 injection times for linear ion trap sequencing[84]. Use of linear ion traps for MS2 real-time peptide searches (RTS) prior to successive MS2 or MS3 quantitative orbitrap scans has also been successfully employed for single-cell MS[37] (again with use of an Orbitrap Eclipse Tribrid instrument). Although the linear ion trap scans employed were rapid (23ms and 46ms max injection times respectively), inclusion of on-the-fly RTS-enabled precursor matching led to substantial improvements in spectra interpretation and subsequent protein identification rates, in particular when performed within an RTS-MS3 protocol[37]. It is likely further development of low input linear ion trap acquisition strategies will drive new progress within the field of single-cell proteomics.

1.5 DATA PROCESSING AND ANALYSIS

Spectral processing and statistical inference are key parameters in the interpretation of single-cell proteomics data, and within the context of the reduced: signal noise present within low input MS spectra, optimisation of these parameters is often inherent to the choice of search engine, algorithm, spectral library and limits of statistical probability, that determinatively impress upon the ensuing data analysis and research outputs. While analytical incorporation of further data dimensions has shown to result in improved spectral interpretation[28,37,98], increased data parameters are secondary to the functional paradigm of computational analysis which must be implemented appropriately relative to the experimental design.

Matching between runs is a feature that was first incorporated into the MaxQuant software algorithm in order to tackle the missing value problem recurrent within -omics technologies[113]. Through accounting for variation in liquid chromatography retention times, features can be matched between experimental runs by accurate mass to increase identification rates in cases where MS2 data may not have been generated. Naturally, this would be particularly suited to low input proteomics, where a DDA acquisition strategy is unlikely to uniformly sample the same MS1 precursors relative to retention time. The proposed benefits of the MBR feature within MaxQuant processing have been repeatedly demonstrated for low input and single-cell proteomics, where they have shown the capacity to increase identifications by >2-fold[26,45,95]. This was achieved through both matching across single-cell samples and to a bulk sample composed of greater cell numbers from the population of interest. Although false transfer rates from MBR are generally at a minimum when applied in the context of LFQ[114], recent application of FDR-controlled MBR with IonQuant[115](as part of the FragPipe analytical suite) demonstrated some benefits in improving quantitative accuracy during the re-analysis of two single-cell proteomics experiments[95,116]. With FDR-controlled MBR also being successfully employed in one of the deepest proteomic profiling of single-cells to date with DDA[84], use of FDR-controlled MBR may be prudent and viable for similar single-cell proteomics experiments without being overtly detrimental to identification rates. However, this study employed a relatively high MBR-FDR (0.05)[84] that may not necessarily provide a drastic reduction in FDR-derived identifications[115], in conjunction with the bulk-generated (11 cells) spectral library that was used for matching to experimental runs.

Experiment-specific bulk spectral libraries can be applied both individually, in combination with library-free database searches or in multiplicity. In another study of single-cells[98], FAIMS was used to fractionate high-input bulk samples into up to 4-gas phase fractions at different compensation voltages (CV) in order to generate in-depth DDA spectral libraries for subsequent matching to experimental LC-MS runs of single-cells in which multiple CV settings were cycled through sequentially. This resulted in the successful identification and label-free quantification of >1000 proteins from single HeLa cells[98]. While the use of experimentally-derived spectral libraries has been adopted to great success within these single-cell DDA workflows[84,98], use of bulk spectral libraries may present the greatest benefit for DIA workflows where there is increased spectral stochasticity. Here, generation of spectral libraries poses the benefit of providing experimentally accurate spectra; foregoing the need for theoretical reference spectra that may deviate in their predicted (vs observed) fragmentation intensities[117]. In a study that generated a spectral library from DDA-PASEF TIMS-qTOF analysis of bulk HeLa cells, searching against this experimental spectra enabled the identification of ~4000 proteins with a significantly reduced 20-minute gradient when analysing 10ng HeLa digest using single-shot DIA analysis[104]. This study similarly utilised 4-phase gas fractionation via TIMS to increase spectral library proteome coverage, a strategy that poses an attractive avenue in order to reduce analytical time per sample for low input proteomics and may prove suitable for single-cell DIA. Although highly successful, DDA spectral libraries are often experiment and instrument dependent, which may necessitate the time-consuming and costly repeated generation of spectral libraries for every project. Coupled with their limited capacity for novel identifications when matching to experimental runs, there has been a drive in recent years towards the implementation of deep learning approaches capable of generating *in silico* spectral libraries comparable or superior in performance to those derived experimentally[118,119].

An exciting implementation of this outlook for fast and robust DIA analysis of low input samples is the application of deep neural network modelling to augment identification and quantitative performance through deconvolution of spectra signal: noise, as well as additional interference correction strategies; termed DIA-NN[74]. Within this approach, deep neural networks are trained for the calculation of target and decoy elution peak discriminant scores to generate subsequent q-values that determine the statistical significance of precursor matches. Through incorporation of both peptide-[120] and spectrum-centric approaches[121], DIA-NN improves identification performance at strict FDR through extensive peak scoring at the peptide level to iteratively train a classifier, before incorporating an evaluation of potential precursor interference in cases where multiple precursors map to the same retention time; selecting only those identifications best supported by the model. Additionally, implementation of an interference-removal algorithm to select the most suitable fragment ions based on their respective peak elution's (with the aim to minimise co-elution interference) demonstrated improved quantitative precision when compared to other common software tools, such as Spectronaut[74]. DIA-NN is consequently being increasingly applied to the analysis of low input or single-cell proteomics[16,32,51,104]. Among these developments is the implementation of DIA-NN to single-cell multiplex and low input label-free workflows aimed at increasing analytical throughput[51,108], with further capabilities for the analysis of post-translational modifications (PTMs) being developed[122,123]. Extension of DIA-NN to the re-analysis of low input (10-100ng) HeLa digest collected via DIA PASEF on a timsTOF Pro[32] demonstrated significant increases in protein identifications of 28-56% compared to the original report[24]. Additional incorporation of the recently introduced timsTOF Pro 2 within a comparable DIA-PASEF workflow utilising DIA-NN further enabled this research group to identify 7442 proteins from a single injection of 10ng HeLa digest and 3651 proteins from a single injection of 1ng HeLa digest[32], demonstrating the ability to generate deep proteome coverage while maintaining quantitative performance at low sample inputs[32]. Adoption of DIA-NN for single-cell proteomics collected via DIA PASEF on a timsTOF Pro[16] resulted in improved performance compared to Spectronaut processing, enabling the identification of ~2000 proteins per single HeLa cell[16]. Deep-learning strategies are continuing to grow at a rapid pace, similar to the field of single-cell proteomics, and their expansion will likely continue to improve our ability to interpret the complex experimental data sets arising from these investigations.

1.6 SUMMARY

MS single-cell proteomics is developing at a rapid rate, and with it, our understanding of processes central to cellular biology[16,41] and disease[28,37]. Technical advancements have been driven by several factors; in particular the miniaturisation of sample preparation to nanoscale volumes, automation of sample handling, parallelised data acquisition and novel analytical strategies to optimise and uncover the data complexity awaiting discovery within single-cells. As throughput and analytical sensitivity improve, it is likely single-cell MS proteomics technologies will be increasingly implemented within clinical research applications, where they pose the complementary potential to those observed via the RNA landscape for diagnostics and investigations into disease pathology.

1.7 REFERENCES

1. J, M. & K, M. Steps in metastasis: an updated review. *Med. Oncol. Northwood Lond. Engl.* **38**, (2021).

2. Hinshaw, D. C. & Shevde, L. A. The Tumor Microenvironment Innately Modulates Cancer Progression. *Cancer Res.* **79**, 4557–4566 (2019).

3. Giat, E., Ehrenfeld, M. & Shoenfeld, Y. Cancer and autoimmune diseases. *Autoimmun. Rev.* **16**, 1049–1057 (2017).

4. Alivernini, S. *et al.* Distinct synovial tissue macrophage subsets regulate inflammation and remission in rheumatoid arthritis. *Nat. Med.* **26**, 1295–1306 (2020).

5. Boutet, M.-A. *et al.* Novel insights into macrophage diversity in rheumatoid arthritis synovium. *Autoimmun. Rev.* **20**, 102758 (2021).

6. Chazaud, B. Inflammation and Skeletal Muscle Regeneration: Leave It to the Macrophages! *Trends Immunol.* **41**, 481–492 (2020).

7. Sass, F. A. *et al.* Immunology Guides Skeletal Muscle Regeneration. *Int. J. Mol. Sci.* **19**, 835 (2018).

8. Dueweke, J. J., Awan, T. M. & Mendias, C. L. Regeneration of skeletal muscle following eccentric injury. *J. Sport Rehabil.* **26**, 171–179 (2017).

9. Saclier, M. *et al.* Differentially activated macrophages orchestrate myogenic precursor cell fate during human skeletal muscle regeneration. *Stem Cells Dayt. Ohio* **31**, 384–396 (2013).

10. Shapiro, E., Biezuner, T. & Linnarsson, S. Single-cell sequencing-based technologies will revolutionize whole-organism science. *Nat. Rev. Genet.* **14**, 618–630 (2013).

11. Slovin, S. *et al.* Single-Cell RNA Sequencing Analysis: A Step-by-Step Overview. in *RNA Bioinformatics* (ed. Picardi, E.) 343–365 (Springer US, 2021).

12. Eppert, K. *et al.* Stem cell gene expression programs influence clinical outcome in human leukemia. *Nat. Med.* **17**, 1086–1093 (2011).

13. Boufea, K. *et al.* Single-cell RNA sequencing of human breast tumour-infiltrating immune cells reveals a γδ T-cell subtype associated with good clinical outcome. *Life Sci. Alliance* **4**, e202000680 (2020).

14. Maynard, A. *et al.* Therapy-Induced Evolution of Human Lung Cancer Revealed by Single-Cell RNA Sequencing. *Cell* **182**, 1232-1251.e22 (2020).

15. Vogel, C. & Marcotte, E. M. Insights into the regulation of protein abundance from proteomic and transcriptomic analyses. *Nat. Rev. Genet.* **13**, 227–232 (2012).

16. Brunner, A. *et al.* Ultra-high sensitivity mass spectrometry quantifies single-cell proteome changes upon perturbation. *Mol. Syst. Biol.* **18**, e10798 (2022).

17. Ravelo, K. M., Andersen, N. D. & Monje, P. V. Magnetic-Activated Cell Sorting for the Fast and Efficient Separation of Human and Rodent Schwann Cells from Mixed Cell Populations. *Methods Mol. Biol. Clifton NJ* **1739**, 87–109 (2018).

18. Tripathi, H. *et al.* Isolation Methods for Human CD34 Subsets Using Fluorescent and Magnetic Activated Cell Sorting: an In Vivo Comparative Study. *Stem Cell Rev. Rep.* **16**, 413–423 (2020).

19. Hughes, A. J. *et al.* Single-cell western blotting. *Nat. Methods* **11**, 749–755 (2014).

20. McCarthy, R. L., Mak, D. H., Burks, J. K. & Barton, M. C. Rapid monoisotopic cisplatin based barcoding for multiplexed mass cytometry. *Sci. Rep.* **7**, 3779 (2017).

21. Levy, E. & Slavov, N. Single cell protein analysis for systems biology. *Essays Biochem.* **62**, 595–605 (2018).

22. Kelly, R. T. Single-cell Proteomics: Progress and Prospects. *Mol. Cell. Proteomics MCP* **19**, 1739–1748 (2020).

23. Kelstrup, C. D. *et al.* Rapid and Deep Proteomes by Faster Sequencing on a Benchtop Quadrupole Ultra-High-Field Orbitrap Mass Spectrometer. *J. Proteome Res.* **13**, 6187–6195 (2014).

24. Meier, F. *et al.* diaPASEF: parallel accumulation–serial fragmentation combined with data-independent acquisition. *Nat. Methods* **17**, 1229–1236 (2020).

25. Petelski, A. A. *et al.* Multiplexed single-cell proteomics using SCoPE2. *Nat. Protoc.* **16**, 5398–5425 (2021).

26. Zhu, Y. *et al.* Proteomic Analysis of Single Mammalian Cells Enabled by Microfluidic Nanodroplet Sample Preparation and Ultrasensitive NanoLC-MS. *Angew. Chem. Int. Ed Engl.* **57**, 12370–12374 (2018).

27. Bruderer, R. *et al.* Optimization of Experimental Parameters in Data-Independent Mass Spectrometry Significantly Increases Depth and Reproducibility of Results*. *Mol. Cell. Proteomics* **16**, 2296–2309 (2017).

28. Schoof, E. M. *et al.* Quantitative single-cell proteomics as a tool to characterize cellular hierarchies. *Nat. Commun.* **12**, 3341 (2021).

29. Maes, E., Cools, N., Willems, H. & Baggerman, G. FACS-Based Proteomics Enables Profiling of Proteins in Rare Cell Populations. *Int. J. Mol. Sci.* **21**, E6557 (2020).

30. Prianichnikov, N. *et al.* MaxQuant Software for Ion Mobility Enhanced Shotgun Proteomics. *Mol. Cell. Proteomics MCP* **19**, 1058–1069 (2020).

31. Röst, H. L. *et al.* Publisher Correction: OpenSWATH enables automated, targeted analysis of data-independent acquisition MS data. *Nat. Biotechnol.* **38**, 374 (2020).

32. Demichev, V. *et al.* dia-PASEF data analysis using FragPipe and DIA-NN for deep proteomics of low sample amounts. *Nat. Commun.* **13**, 3944 (2022).

33. Ziegenhain, C. *et al.* Comparative Analysis of Single-Cell RNA Sequencing Methods. *Mol. Cell* **65**, 631-643.e4 (2017).

34. Sielaff, M. *et al.* Evaluation of FASP, SP3, and iST Protocols for Proteomic Sample Preparation in the Low Microgram Range. *J. Proteome Res.* **16**, 4060–4072 (2017).

35. Doellinger, J., Schneider, A., Hoeller, M. & Lasch, P. Sample Preparation by Easy Extraction and Digestion (SPEED) - A Universal, Rapid, and Detergent-free Protocol for Proteomics Based on Acid Extraction. *Mol. Cell. Proteomics MCP* **19**, 209–222 (2020).

36. Wang, H. *et al.* Development and evaluation of a micro- and nanoscale proteomic sample preparation method. *J. Proteome Res.* **4**, 2397–2403 (2005).

37. Furtwängler, B. *et al.* Real-Time Search-Assisted Acquisition on a Tribrid Mass Spectrometer Improves Coverage in Multiplexed Single-Cell Proteomics. *Mol. Cell. Proteomics MCP* **21**, 100219 (2022).

38. Budnik, B., Levy, E., Harmange, G. & Slavov, N. SCoPE-MS: mass spectrometry of single mammalian cells quantifies proteome heterogeneity during cell differentiation. *Genome Biol.* **19**, 161 (2018).

39. Dhabaria, A., Cifani, P., Reed, C., Steen, H. & Kentsis, A. A high-efficiency cellular extraction system for biological proteomics. *J. Proteome Res.* **14**, 3403–3408 (2015).

40. Specht, H. *et al.* Automated sample preparation for high-throughput single-cell proteomics. 399774 Preprint at https://doi.org/10.1101/399774 (2018).

41. Specht, H. *et al.* Single-cell proteomic and transcriptomic analysis of macrophage heterogeneity using SCoPE2. *Genome Biol.* **22**, 50 (2021).

42. Hughes, C. S. *et al.* Ultrasensitive proteome analysis using paramagnetic bead technology. *Mol. Syst. Biol.* **10**, 757 (2014).

43. Virant-Klun, I., Leicht, S., Hughes, C. & Krijgsveld, J. Identification of Maturation-Specific Proteins by Single-Cell Proteomics of Human Oocytes. *Mol. Cell. Proteomics MCP* **15**, 2616–2627 (2016).

44. Matzinger, M., Müller, E., Dürnberger, G., Pichler, P. & Mechtler, K. Robust and easy-to-use one pot workflow for label free single cell proteomics. 2022.10.03.510693 Preprint at https://doi.org/10.1101/2022.10.03.510693 (2022).

45. Zhu, Y. *et al.* Nanodroplet processing platform for deep and quantitative proteome profiling of 10–100 mammalian cells. *Nat. Commun.* **9**, 882 (2018).

46. Li, Z.-Y. *et al.* Nanoliter-Scale Oil-Air-Droplet Chip-Based Single Cell Proteomic Analysis. *Anal. Chem.* **90**, 5430–5438 (2018).

47. Leduc, A., Huffman, R. G. & Slavov, N. Droplet sample preparation for single-cell proteomics applied to the cell cycle. 2021.04.24.441211 Preprint at https://doi.org/10.1101/2021.04.24.441211 (2021).

48. Woo, J. *et al.* High-throughput and high-efficiency sample preparation for single-cell proteomics using a nested nanowell chip. *Nat. Commun.* **12**, 6246 (2021).

49. Leduc, A., Huffman, R. G., Cantlon, J., Khan, S. & Slavov, N. Exploring functional protein covariation across single cells using nPOP. 2021.04.24.441211 Preprint at https://doi.org/10.1101/2021.04.24.441211 (2022).

50. Ctortecka, C. *et al.* An automated workflow for multiplexed single-cell proteomics sample preparation at unprecedented sensitivity. 2021.04.14.439828 Preprint at https://doi.org/10.1101/2021.04.14.439828 (2022).

51. Derks, J. *et al.* Increasing the throughput of sensitive proteomics by plexDIA. *Nat. Biotechnol.* 1–10 (2022).

52. Ong, S.-E. *et al.* Stable Isotope Labeling by Amino Acids in Cell Culture, SILAC, as a Simple and Accurate Approach to Expression Proteomics. *Mol. Cell. Proteomics* **1**, 376–386 (2002).

53. Zhu, H., Pan, S., Gu, S., Bradbury, E. M. & Chen, X. Amino acid residue specific stable isotope labeling for quantitative proteomics. *Rapid Commun. Mass Spectrom. RCM* **16**, 2115–2123 (2002).

54. Wu, C. C., MacCoss, M. J., Howell, K. E., Matthews, D. E. & Yates, J. R. Metabolic Labeling of Mammalian Organisms with Stable Isotopes for Quantitative Proteomic Analysis. *Anal. Chem.* **76**, 4951–4959 (2004).

55. Gygi, S. P. *et al.* Quantitative analysis of complex protein mixtures using isotope-coded affinity tags. *Nat. Biotechnol.* **17**, 994–999 (1999).

56. Hsu, J.-L., Huang, S.-Y., Chow, N.-H. & Chen, S.-H. Stable-Isotope Dimethyl Labeling for Quantitative Proteomics. *Anal. Chem.* **75**, 6843–6852 (2003).

57. Zhang, R., Sioma, C. S., Wang, S. & Regnier, F. E. Fractionation of Isotopically Labeled Peptides in Quantitative Proteomics. *Anal. Chem.* **73**, 5142–5149 (2001).

58. Guo, K., Ji, C. & Li, L. Stable-isotope dimethylation labeling combined with LC-ESI MS for quantification of amine-containing metabolites in biological samples. *Anal. Chem.* **79**, 8631–8638 (2007).

59. Di Palma, S., Raijmakers, R., Heck, A. J. R. & Mohammed, S. Evaluation of the Deuterium Isotope Effect in Zwitterionic Hydrophilic Interaction Liquid Chromatography Separations for Implementation in a Quantitative Proteomic Approach. *Anal. Chem.* **83**, 8352–8356 (2011).

60. Cho, K.-C., Kang, J. W., Choi, Y., Kim, T. W. & Kim, K. P. Effects of peptide acetylation and dimethylation on electrospray ionization efficiency. *J. Mass Spectrom.* **51**, 105–110 (2016).

61. Thompson, A. *et al.* Tandem Mass Tags: A Novel Quantification Strategy for Comparative Analysis of Complex Protein Mixtures by MS/MS. *Anal. Chem.* **75**, 1895–1904 (2003).

62. Specht, H. & Slavov, N. Optimizing Accuracy and Depth of Protein Quantification in Experiments Using Isobaric Carriers. *J. Proteome Res.* **20**, 880–887 (2021).

63. Cheung, T. K. *et al.* Defining the carrier proteome limit for single-cell proteomics. *Nat. Methods* **18**, 76–83 (2021).

64. Ctortecka, C., Stejskal, K., Krššáková, G., Mendjan, S. & Mechtler, K. Quantitative Accuracy and Precision in Multiplexed Single-Cell Proteomics. *Anal. Chem.* **94**, 2434–2443 (2022).

65. Dou, M. *et al.* High-Throughput Single Cell Proteomics Enabled by Multiplex Isobaric Labelling in a Nanodroplet Sample Preparation Platform. *Anal. Chem.* **91**, 13119 (2019).

66. Li, J. *et al.* TMTpro reagents: a set of isobaric labeling mass tags enables simultaneous proteome-wide measurements across 16 samples. *Nat. Methods* **17**, 399–404 (2020).

67. Ross, P. L. *et al.* Multiplexed Protein Quantitation in Saccharomyces cerevisiae Using Amine-reactive Isobaric Tagging Reagents *. *Mol. Cell. Proteomics* **3**, 1154–1169 (2004).

68. Armenta, J. M., Hoeschele, I. & Lazar, I. M. Differential Protein Expression Analysis Using Stable Isotope Labeling and PQD Linear Ion Trap MS Technology. *J. Am. Soc. Mass Spectrom.* **20**, 1287–1302 (2009).

69. Searle, B. C. & Yergey, A. L. An efficient solution for resolving iTRAQ and TMT channel cross-talk. *J. Mass Spectrom.* **55**, e4354 (2020).

70. Ye, Z., Batth, T. S., Rüther, P. & Olsen, J. V. A deeper look at carrier proteome effects for single-cell proteomics. *Commun. Biol.* **5**, 150 (2022).

71. Rauniyar, N. & Yates, J. R. Isobaric Labeling-Based Relative Quantification in Shotgun Proteomics. *J. Proteome Res.* **13**, 5293–5309 (2014).

72. Bekker-Jensen, D. B. *et al.* An Optimized Shotgun Strategy for the Rapid Generation of Comprehensive Human Proteomes. *Cell Syst.* **4**, 587-599.e4 (2017).

73. Mertins, P. *et al.* iTRAQ Labeling is Superior to mTRAQ for Quantitative Global Proteomics and Phosphoproteomics. *Mol. Cell. Proteomics MCP* **11**, (2012).

74. Demichev, V., Messner, C. B., Vernardis, S. I., Lilley, K. S. & Ralser, M. DIA-NN: Neural networks and interference correction enable deep proteome coverage in high throughput. *Nat. Methods* **17**, 41–44 (2020).

75. Ctortecka, C. *et al.* Comparative Proteome Signatures of Trace Samples by Multiplexed Data-Independent Acquisition. *Mol. Cell. Proteomics MCP* **21**, 100177 (2021).

76. Tian, X., Vries, M. P. de, Permentier, H. P. & Bischoff, R. The Isotopic Ac-IP Tag Enables Multiplexed Proteome Quantification in Data-Independent Acquisition Mode. *Anal. Chem.* **93**, 8196 (2021).

77. Minogue, C. E. *et al.* Multiplexed Quantification for Data-Independent Acquisition. *Anal. Chem.* **87**, 2570 (2015).

78. Di, Y., Zhang, Y., Zhang, L., Tao, T. & Lu, H. MdFDIA: A Mass Defect Based Four-Plex Data-Independent Acquisition Strategy for Proteome Quantification. *Anal. Chem.* **89**, 10248–10255 (2017).

79. Zhong, X. *et al.* Mass Defect-Based DiLeu Tagging for Multiplexed Data-Independent Acquisition. *Anal. Chem.* **92**, 11119–11126 (2020).

80. Muntel, J. *et al.* Comparison of Protein Quantification in a Complex Background by DIA and TMT Workflows with Fixed Instrument Time. *J. Proteome Res.* **18**, 1340–1351 (2019).

81. Mund, A. *et al.* Deep Visual Proteomics defines single-cell identity and heterogeneity. *Nat. Biotechnol.* **40**, 1231–1240 (2022).

82. Røberg-Larsen, H., Lundanes, E., Nyman, T. A., Berven, F. S. & Wilson, S. R. Liquid chromatography, a key tool for the advancement of single-cell omics analysis. *Anal. Chim. Acta* **1178**, 338551 (2021).

83. Schmidt, A., Karas, M. & Dülcks, T. Effect of different solution flow rates on analyte ion signals in nano-ESI MS, or: when does ESI turn into nano-ESI? *J. Am. Soc. Mass Spectrom.* **14**, 492–500 (2003).

84. Fulcher, J. M. *et al.* Parallel measurement of transcriptomes and proteomes from same single cells using nanodroplet splitting. 2022.05.17.492137 Preprint at https://doi.org/10.1101/2022.05.17.492137 (2022).

85. Wilm, M. & Mann, M. Analytical properties of the nanoelectrospray ion source. *Anal. Chem.* **68**, 1–8 (1996).

86. Juraschek, R., Dülcks, T. & Karas, M. Nanoelectrospray--more than just a minimized-flow electrospray ionization source. *J. Am. Soc. Mass Spectrom.* **10**, 300–308 (1999).

87. Wilm, M. Principles of Electrospray Ionization. *Mol. Cell. Proteomics MCP* **10**, M111.009407 (2011).

88. Bache, N. *et al.* A Novel LC System Embeds Analytes in Pre-formed Gradients for Rapid, Ultra-robust Proteomics. *Mol. Cell. Proteomics MCP* **17**, 2284–2296 (2018).

89. De Malsche, W. *et al.* Pressure-Driven Reverse-Phase Liquid Chromatography Separations in Ordered Nonporous Pillar Array Columns. *Anal. Chem.* **79**, 5915–5926 (2007).

90. Stejskal, K., Op de Beeck, J., Dürnberger, G., Jacobs, P. & Mechtler, K. Ultrasensitive NanoLC-MS of Subnanogram Protein Samples Using Second Generation Micropillar Array LC Technology with Orbitrap Exploris 480 and FAIMS PRO. *Anal. Chem.* **93**, 8704–8710 (2021).

91. Stadlmann, J. *et al.* Improved Sensitivity in Low-Input Proteomics Using Micropillar Array-Based Chromatography. *Anal. Chem.* **91**, 14203–14207 (2019).

92. Yue, G., Luo, Q., Zhang, J., Wu, S.-L. & Karger, B. L. Ultratrace LC/MS proteomic analysis using 10-microm-i.d. Porous layer open tubular poly(styrene-divinylbenzene) capillary columns. *Anal. Chem.* **79**, 938–946 (2007).

93. Li, S. *et al.* An Integrated Platform for Isolation, Processing, and Mass Spectrometry-based Proteomic Profiling of Rare Cells in Whole Blood. *Mol. Cell. Proteomics MCP* **14**, 1672–1683 (2015).

94. Cong, Y. *et al.* Improved Single-Cell Proteome Coverage Using Narrow-Bore Packed NanoLC Columns and Ultrasensitive Mass Spectrometry. *Anal. Chem.* **92**, 2665–2671 (2020).

95. Cong, Y. *et al.* Ultrasensitive single-cell proteomics workflow identifies >1000 protein groups per mammalian cell. *Chem. Sci.* **12**, 1001–1006 (2021).

96. Silveira, J. A., Ridgeway, M. E. & Park, M. A. High resolution trapped ion mobility spectrometery of peptides. *Anal. Chem.* **86**, 5624–5627 (2014).

97. Barnett, D. A., Ells, B., Guevremont, R. & Purves, R. W. Application of ESI-FAIMS-MS to the analysis of tryptic peptides. *J. Am. Soc. Mass Spectrom.* **13**, 1282–1291 (2002).

98. Woo, J. *et al.* Three-dimensional feature matching improves coverage for single-cell proteomics based on ion mobility filtering. *Cell Syst.* **13**, 426-434.e4 (2022).

99. Gabelica, V. *et al.* Recommendations for reporting ion mobility Mass Spectrometry measurements. *Mass Spectrom. Rev.* **38**, 291–320 (2019).

100. Wu, C., Siems, W. F., Klasmeier, J. & Hill, H. H. Separation of isomeric peptides using electrospray ionization/high-resolution ion mobility spectrometry. *Anal. Chem.* **72**, 391–395 (2000).

101. Srebalus Barnes, C. A., Hilderbrand, A. E., Valentine, S. J. & Clemmer, D. E. Resolving Isomeric Peptide Mixtures: A Combined HPLC/Ion Mobility-TOFMS Analysis of a 4000-Component Combinatorial Library. *Anal. Chem.* **74**, 26–36 (2002).

102. Meier, F. *et al.* Deep learning the collisional cross sections of the peptide universe from a million experimental values. *Nat. Commun.* **12**, 1185 (2021).

103. Meier, F. *et al.* Parallel Accumulation-Serial Fragmentation (PASEF): Multiplying Sequencing Speed and Sensitivity by Synchronized Scans in a Trapped Ion Mobility Device. *J. Proteome Res.* **14**, 5378–5387 (2015).

104. Guergues, J., Wohlfahrt, J. & Stevens, S. M. Enhancement of Proteome Coverage by Ion Mobility Fractionation Coupled to PASEF on a TIMS-QTOF Instrument. *J. Proteome Res.* **21**, 2036–2044 (2022).

105. Moseley, M. A. *et al.* Scanning Quadrupole Data-Independent Acquisition, Part A: Qualitative and Quantitative Characterization. *J. Proteome Res.* **17**, 770–779 (2018).

106. Messner, C. B. *et al.* Ultra-fast proteomics with Scanning SWATH. *Nat. Biotechnol.* **39**, 846–854 (2021).

107. Skowronek, P. *et al.* Synchro-PASEF allows precursor-specific fragment ion extraction and interference removal in data-independent acquisition. *Mol. Cell. Proteomics MCP* 100489 (2022).

108. Szyrwiel, L., Sinn, L., Ralser, M. & Demichev, V. Slice-PASEF: fragmenting all ions for maximum sensitivity in proteomics. 2022.10.31.514544 Preprint at https://doi.org/10.1101/2022.10.31.514544 (2022).

109. Kulak, N. A., Pichler, G., Paron, I., Nagaraj, N. & Mann, M. Minimal, encapsulated proteomic-sample processing applied to copy-number estimation in eukaryotic cells. *Nat. Methods* **11**, 319–324 (2014).

110. Borràs, E., Pastor, O. & Sabidó, E. Use of Linear Ion Traps in Data-Independent Acquisition Methods Benefits Low-Input Proteomics. *Anal. Chem.* **93**, 11649–11653 (2021).

111. Phlairaharn, T. *et al.* High Sensitivity Limited Material Proteomics Empowered by Data-Independent Acquisition on Linear Ion Traps. *J. Proteome Res.* **21**, 2815–2826 (2022).

112. Liu, J. M., Sweredoski, M. J. & Hess, S. Improved 6-Plex Tandem Mass Tags Quantification Throughput Using a Linear Ion Trap–High-Energy Collision Induced Dissociation MS3 Scan. *Anal. Chem.* **88**, 7471–7475 (2016).

113. Tyanova, S., Temu, T. & Cox, J. The MaxQuant computational platform for mass spectrometry-based shotgun proteomics. *Nat. Protoc.* **11**, 2301–2319 (2016).

114. Lim, M. Y., Paulo, J. A. & Gygi, S. P. Evaluating False Transfer Rates from the Match-between-Runs Algorithm with a Two-Proteome Model. *J. Proteome Res.* **18**, 4020–4026 (2019).

115. Yu, F., Haynes, S. E. & Nesvizhskii, A. I. IonQuant Enables Accurate and Sensitive Label-Free Quantification With FDR-Controlled Match-Between-Runs. *Mol. Cell. Proteomics MCP* **20**, 100077 (2021).

116. Williams, S. M. *et al.* Automated Coupling of Nanodroplet Sample Preparation with Liquid Chromatography-Mass Spectrometry for High-Throughput Single-Cell Proteomics. *Anal. Chem.* **92**, 10588–10596 (2020).

117. Röst, H. L. Deep learning adds an extra dimension to peptide fragmentation. *Nat. Methods* **16**, 469–470 (2019).

118. Tiwary, S. *et al.* High-quality MS/MS spectrum prediction for data-dependent and data-independent acquisition data analysis. *Nat. Methods* **16**, 519–525 (2019).

119. Gessulat, S. *et al.* Prosit: proteome-wide prediction of peptide tandem mass spectra by deep learning. *Nat. Methods* **16**, 509–518 (2019).

120. Reiter, L. *et al.* mProphet: automated data processing and statistical validation for large-scale SRM experiments. *Nat. Methods* **8**, 430–435 (2011).

121. Wang, J. *et al.* MSPLIT-DIA: sensitive peptide identification for data-independent acquisition. *Nat. Methods* **12**, 1106–1108 (2015).

122. Steger, M. *et al.* Time-resolved in vivo ubiquitinome profiling by DIA-MS reveals USP7 targets on a proteome-wide scale. *Nat. Commun.* **12**, 5399 (2021).

123. Zeng, W.-F. *et al.* AlphaPeptDeep: a modular deep learning framework to predict peptide properties for proteomics. *Nat. Commun.* **13**, 7238 (2022).